RUI MIGUEL DOS SANTOS MARTINS

IN-SITU X-RAY DIFFRACTION STUDIES DURING GROWTH OF Ni-Ti SHAPE MEMORY ALLOY FILMS AND THEIR COMPLEMENTARY *EX-SITU* CHARACTERIZATION

Thesis submitted to the Faculty of Sciences and Technology of the New University of Lisbon for the degree of Doctor in Materials Engineering-Metallurgical Technologies.

This thesis was prepared in the framework of the collaboration between the Forschungszentrum Dresden-Rossendorf (FZD) and CENIMAT/FCT/UNL in the Rossendorf Beamline (ROBL) at the European Synchrotron Radiation Facility (ESRF) and at FZD.

LISBOA
2008

This thesis is dedicated

to my parents, Jaime and Júlia

and to my sister, Vanda

ACKNOWLEDGEMENTS

The research work described in this thesis was carried out at the Forschungszentrum Dresden-Rossendorf (Institute of Ion Beam Physics and Materials Research / Rossendorf Beamline), and I would like to acknowledge all those people who helped to make this thesis possible. I am indebted especially to a number of people for scientific, theoretical, experimental, and moral support:

Firstly, many thanks to my supervisor Professor Francisco Manuel Braz Fernandes, my official supervisor at FCT/UNL. We were always in touch and I knew I always could come and discuss or ask him for help. His door was always open for discussions on both scientific and personal issues. I believe that this is the best what a student could have from the supervisor. Additionally he has initiated the international collaborations, which were indispensable in the success of this thesis.

I must give a special acknowledgement also to my supervisor Dr. Norbert Schell. Without his support, I would not have never came to FZD and made my PhD study. I am very grateful for all time that we have spent together. I am impressed by his ultimate patience and devotion for excellence. All these years spent with him were very enriching from both personal and professional point of view. I am grateful to Norbert for all that hard work he has done while working with me and trying to understand my way of thinking and being. He has been and is a true friend.

I would like to thank the FZD for funding my PhD work and the Portuguese Foundation for Science and Technology (FCT/MCTES) for a PhD individual grant since March 2006 (POCI 2010/FSE).

It is particular a pleasure for me to thank Dr. Johannes Borany, head of the Department for Structural Studies (FWIS), for the fruitful stays in Dresden. He provided excellent conditions, candid support and encouragement during this work.

Among the many colleagues at FZD that I have had the pleasure of meeting, I am particularly grateful to Manfred and Valentina for many discussions and their kind support. Furthermore, for creating a unique working atmosphere within our group. I can never thank you enough.

A particular thanks to Udo and Manuela, my colleagues at ROBL, for the technical support, the prompt settlement of any kind of administrative problem and, above all, their friendship.

I owe a huge debt of gratitude to Dr. Arndt Mücklich for engaged TEM analysis, for answering all my questions regarding the TEM technique and, especially, for his kindness and support during my stays at FWIS. For TEM observations it has also been essential the technical support given by Frau Martina Missbach and Frau Annette Kunz on the preparation of the samples for X-TEM. They have performed a great work.

I would like to thank Dr. Helfried Reuther and Frau Elfi Christalle for the technical support during SEM analyses carried out on my samples as well as their kind support during my stays at the department.

I am also grateful to Frau Elke Quaritsch for the big amount of AES measurements performed on my samples.

I would like to acknowledge the support of Dr. Frank Eichhorn who was an invaluable source of knowledge concerning XRD. I appreciate his time and patience with our measurements at the FWIS XRD laboratory. I would also like to thank Frau Andrea Scholz for all the XRD measurements that she performed for me in Dresden when I was working on different tasks in Grenoble. She was always very kind to me.

I must mention here the support of Dr. Shengqiang Zhou when, just before a beamtime at ROBL, I needed some RBS measurements. Shengqiang immediately performed the work at FZD and sent me the fitted data to ESRF. His wife was just living the last days of her pregnancy.

I would also like to acknowledge the support of other members of our group in Dresden, who have made my experience at FZD truly special: Dr. Kurt Walther, Frau Birgit Gebauer, Dr. Natalia Shevchenko, Joachim Kreher, Dr. Jörg Grenzer, Dr. Friedrich Prokert, Rene Weidauer.

Winfried Oehme and Siegfried Dienel, from the Department of Research Technology (at FZD), involved in the scientific and technical programme of ROBL, were responsible for technical improvements that led to successful beamtimes.

It is also a pleasure to acknowledge the support of Professor Rui Silva (from CENIMAT). Working with Rui has been a rewarding and enjoyable experience. It has been extremely important for me his support, especially on those countless sleepless nights at the beamline.

At CENIMAT, Luís Pereira also carried out complementary resistivity measurements, which resulted on a very nice observation of the phase transformation characteristics as a function of the processing parameters. Dr. Karimbi Mahesh went several times to Grenoble to give precious support during the beamtimes. Dr. Andersan Paula was always somehow present when I needed her. Márcia Silva has been in Grenoble during the first beamtime for my PhD thesis work. I cannot forget her important support. They are much more than colleagues - they are good friends.

My deepest gratitude to Dr. Carla Santos who gave me confidence in my abilities during the thesis writing.

Finally, this thesis would not have been possible without the tremendous support and encouragement from my parents and my sister who have always encouraged me to follow my dreams and happiness.

SUMMARY

Shape Memory Alloy (SMA) Ni-Ti films have attracted much interest as functional and smart materials due to their unique properties. However, there are still important issues unresolved like formation of film texture and its control as well as substrate effects. Thus, the main challenge is not only the control of the microstructure, including stoichiometry and precipitates, but also the identification and control of the preferential orientation since it is a crucial factor in determining the shape memory behaviour.

The aim of this PhD thesis is to study the optimisation of the deposition conditions of films of Ni-Ti in order to obtain the material fully crystallized at the end of the deposition, and to establish a clear relationship between the substrates and texture development. In order to achieve this objective, a two-magnetron sputter deposition chamber has been used allowing to heat and to apply a bias voltage to the substrate. It can be mounted into the six-circle diffractometer of the Rossendorf Beamline (ROBL) at the European Synchrotron Radiation Facility (ESRF), Grenoble, France, enabling an *in-situ* characterization by X-ray diffraction (XRD) of the films during their growth and annealing. The *in-situ* studies enable us to identify the different steps of the structural evolution during deposition with a set of parameters as well as to evaluate the effect of changing parameters on the structural characteristics of the deposited film. Besides the *in-situ* studies, other complementary *ex-situ* characterization techniques such as XRD at a laboratory source, Rutherford backscattering spectroscopy (RBS), Auger electron spectroscopy (AES), cross-sectional transmission electron microscopy (X-TEM), scanning electron microscopy (SEM), and electrical resistivity (ER) measurements during temperature cycling have been used for a fine structural characterization.

In this study, mainly naturally and thermally oxidized Si(100) substrates, TiN buffer layers with different thicknesses (i.e. the TiN topmost layer crystallographic orientation is thickness dependent) and MgO(100) single crystals were used as substrates. The chosen experimental procedure led to a controlled composition and preferential orientation of the films. The type of substrate plays an important role for the texture of the sputtered Ni-Ti films and according to the ER results, the distinct crystallographic orientations of the Ni-Ti films influence their phase transformation characteristics.

SUMÁRIO

O fabrico de películas finas de ligas Ni-Ti com memória de forma tem atraido especial interesse na área dos materiais funcionais e inteligentes, sobretudo devido às suas características peculiares. No entanto, existem ainda questões importantes que requerem resolução, como a identificação dos diferentes factores que influenciam o tipo de orientação preferencial da película depositada, um possível controlo da mesma, bem como a influência do tipo de substrato utilizado. Deste modo, não só se apresentam como factores preponderantes aqueles mais vezes mencionados (o controlo da microstrutura, incluíndo estequiometria e formação de precipitados), mas também se apresenta com particular ênfase, a identificação e controlo do tipo de orientação preferencial das películas de Ni-Ti, uma vez que, no caso das aplicações recorrendo ao efeito de memória de forma, existe uma relação entre a textura e a extensão da deformação recuperável.

Este trabalho teve por finalidade estudar as condições de optimização da produção (por pulverização catódica) de películas finas de Ni-Ti com memória de forma, de modo a obter material cristalino durante o processo de deposição (sem tratamentos térmicos adicionais), e sobretudo estabelecer uma relação entre o tipo de substrato usado e a evolução da orientação preferencial das películas. De forma a atingir este objectivo, foi utilizada uma câmara de deposição que permite a co-deposição a partir de dois alvos, bem como a deposição em substrato aquecido e polarizado. Este equipamento foi especialmente projectado para poder ser montado no círculo φ do goniómetro de 6 círculos existente na Rossendorf Beamline (ROBL), no European Synchrotron Radiation Facility (ESRF), permitindo assim a caracterização do processo de deposição por difracção de raios-X (DRX) *in situ*. Este tipo de estudo permite, por isso, acompanhar a evolução estrutural da película à medida que o processo de deposição vai avançando, bem como correlacionar as condições de deposição (fixas ou variáveis) com a microestrutura final da película. Após o processo de deposição, as películas foram estudadas *ex situ*, recorrendo-se a ensaios de DRX a nível laboratorial, espectroscopia de retrodispersão de Rutherford (RBS), espectroscopia electrónica de Auger (AES), microscopia electrónica de transmissão (TEM – amostras preparadas em secção transversal), microscopia electrónica de varrimento (SEM) e medidas da resistividade eléctrica durante ciclos térmicos, o que permitiu uma caracterização estrutural mais fina das películas.

Neste estudo foram usadas como substrato placas (15×15 mm^2) extraídas de bolachas de Si(100), com óxido nativo, bem como de bolachas oxidadas termicamente. Revestimentos de TiN com diferentes espessuras (ou seja, existe uma dependência entre a orientação cristalográfica da camada mais superficial de TiN e a espessura do revestimento) foram também utilizados, assim como substratos MgO(100). O procedimento experimental adoptado permitiu o controlo e a manipulação da composição e do tipo de orientação preferencial das películas de Ni-Ti. O tipo de substrato condiciona o tipo de orientação preferencial da película e, segundo as medidas de resistividade eléctrica, o tipo de textura influencia o seu comportamento característico durante o processo de transformação de fase.

RÉSÚME

Les couches minces en Alliage à Mémoire de Forme (AMF) Ni-Ti ont attiré l'intérêt comme matériaux intelligent et adaptatif grâce à leurs propriétés uniques. Cependant il y a encore de nombreuses difficultés non résolues comme la formation texture et son contrôle dans les couches minces ainsi que les effets du substrat. Donc le principal challenge n'est pas seulement le contrôle de la microstructure, incluant la stoechiométrie et les précipités mais aussi l'identification et le contrôle des orientations préférentielles puisqu'elles sont un facteur crucial pour déterminer le comportement de la forme mémorisée.

L'objectif de ce travail de thèse est d'étudier l'optimisation des conditions de dépôt de couches minces de Ni-Ti dans le but d'obtenir un matériau entièrement cristallisé et d'établir un lien évident entre le substrat utilisé et le développement de la texture. Pour accomplir cet objectif une chambre de dépôts par pulvérisation magnétron (à 2 cibles) permettant de chauffer et d'appliquer une tension sur le substrat a été utilisée. Cette chambre peut être monté sur le diffractomètre à 6-axes de la ligne de lumière de Rossendorf (ROBL) à l'European Synchrotron Radiation Facility (ESRF) à Grenoble, France. Cette installation permet de caractériser *in-situ* par diffraction de rayon X les couches minces pendant leur croissance et recuit. Les études *in-situ* nous permettent soient d'identifier les différentes étapes de l'évolution structurale pendant les dépôts avec des paramètres fixés, soient d'évaluer l'effet du changement des paramètres sur les caractéristiques structurales des couches minces déposées. A la suite de ces études *in-situ*, d'autres techniques complémentaires *ex-situ* ont été utilisées pour une caractérisation plus fine. Ces techniques sont la diffraction de rayons X de laboratoire, la spectrométrie de rétrodiffusion Rutherford (RBS), la spectrométrie par électrons Auger (AES), la microscopie à transmission (X-TEM), à balayage (SEM) et les mesures de résistance électrique pendant des cycles thermiques.

Dans cette étude, du Si(100) naturellement et thermiquement oxydés, des couches tampons en TiN de différentes épaisseurs (c'est-à-dire que l'orientation cristallographique de la couche supérieure en TiN est dépendante de son épaisseur) et des monocristaux de MgO(100) sont principalement utilisés comme substrats. La procédure expérimentale choisie guide la manipulation contrôlée de la composition et des orientations préférentielles des couches minces. Le type de substrat joue un rôle important dans la texture des couches de Ni-Ti pulvérisées et selon les résultats des mesures de résistances électriques, les orientations cristallographiques distinctes des couches minces de Ni-Ti influencent le comportement de leur transformation de phase.

LIST OF SYMBOLS AND ABREVIATIONS

α	deposition angle (relative to the substrate normal)
a_0	lattice parameter
AES	Auger electron spectroscopy
α_f	expansion coefficients of the film
A_f	austenite-finish temperature
A_s	austenite-start temperature
α_s	expansion coefficients of the substrate
β	angle of orientation of the film columns (relative to the substrate normal)
B19'	martensite
B2	austenite
BF	bright field
CEFITEC	Centro de Física e Investigação Tecnológica
CENIMAT	Centro de Investigação de Materiais
d	interplanar distance
DC	direct current
DCM	double-crystal monochromator
DF	dark field
DSC	differential scanning calorimetry
E	Young's modulus
EDX	energy dispersive X-ray spectroscopy
ER	electrical resistivity
ESRF	European Synchrotron Radiation Facility
FZD	Forschungszentrum Dresden-Rossendorf
GIXD	X-ray diffraction in grazing incidence geometry off-plane
GIXS	grazing exit in-plane large angle scattering
GP	Guinier-Preston
h	distance target/substrate
HR	high resolution
IBA	ion beam analysis
IC	integrated circuit
k	Boltzmann constant
l	mean free path
λ	wavelength
MC	Monte Carlo
MD	molecular dynamics
MEMS	micro-electro-mechanical system
M_f	martensite-finish temperature
MRH	Materials Research Hutch
M_s	martensite-start temperature
ν	Poisson ratio
Ni-Ti	Nitinol

p	pressure
PVD	phase vapour deposition
RF	radio frequency
R'_f	R-phase-finish temperature on heating
R'_s	R-phase-start temperature on heating
RBS	Rutherford backscattering spectroscopy
R_f	R-phase-finish temperature on cooling
RHEED	reflection high-energy electron diffraction
ROBL	Rossendorf beamline
R_s	R-phase-start temperature on cooling
RT	room temperature
σ	cross section for the collision
SAED	selected area electron diffraction
SE	superelasticity
SEM	scanning electron microscopy
SMA	Shape Memory Alloy
SME	shape memory effect
σ_{th}	thermal stress
T	temperature
T_d	deposition temperature
TEM	transmission electron microscopy
T_m	melting temperature
UHV	ultra high vacuum
V_b	substrate bias voltage
XRD	X-ray diffraction
XRR	X-ray reflectivity
X-TEM	cross-sectional transmission electron microscopy

TABLE OF CONTENTS

LIST OF FIGURES

LIST OF TABLES

Introduction

INTRODUCTION

The combination of attractive properties like the shape-memory effect (SME), superelasticity (SE), high damping capacity, biocompatibility, high specific energy output, and excellent mechanical properties, as well as a very high resistance to corrosion has made Ni-Ti alloys one of the most technologically important Shape Memory Alloys (SMAs). The basic phenomenon enabling the SME and SE is related to the thermoelastic martensitic transformation. In the Ni-Ti system, while cooling, the high temperature phase (austenite - B2 structure, of the CsCl type) transforms into monoclinic B19' martensite phase either directly or via intermediate rhombohedral R-phase transformation. The R-phase ⇔ B2 transformation is very useful for actuator applications because it is associated with a small temperature hysteresis, when compared to that of the B19' ⇔ B2 transformation.

SMAs have been attracting attention as smart materials because they can work as sensors and actuators at the same time. Ni-Ti films are considered to be attractive candidates for micro-electro-mechanical system (MEMS) applications, since they can be patterned with standard lithography techniques and fabricated in batch processes. Furthermore, when compared with the bulk material, Ni-Ti films demonstrate fast cooling rates because of their higher surface/volume ratio, increasing substantially the heat transfer rate. Usually, Ni-Ti films are prepared using a sputtering method (on Si and on SiO_2/Si wafers) although a number of different fabrication methods are being tried. The composition and structure of the deposited films are significantly affected by the sputtering conditions (target power, gas pressure, target to substrate distance, deposition temperature, substrate bias voltage *etc*). Composition shifts can occur resulting from differences in sputtering yield, angular flux distribution, and lateral diffusion of the sputtered species because of atomic collisions with Ar and residual gases. A small deviation from stoichiometry can give rise to a significant precipitation of second phases. If the substrate is not heated during deposition, as-sputtered films are amorphous. These films need a post-deposition heat treatment in order to crystallize and be able to exhibit a thermally induced phase transformation.

For MEMS integration, there is a need for an electrically and thermally insulating or sacrificial layer. Thus, the study of Ni-Ti film deposition on different types of substrates is important for its successful MEMS applications. In a previous work (MSc thesis), Ni-Ti films have been prepared by DC magnetron sputtering on Si(100) and poly-Si/Si(100) substrates to elucidate the influence of the substrate on the crystallization of these films. The relationship

between the intermediate layer of poly-Si and the crystallization behaviour, as well as the final structure of the deposited films, was discussed. It has been shown that the presence of a poly-Si buffer layer enhances the crystallization process of the Ni-Ti films, because of the higher number of nucleation sites provided by the rougher surface morphology of the poly-Si layer, when compared with a naturally oxidized Si(100) substrate. The *in-situ* studies of the structural development have been limited to post-deposition heat treatments and it seems essential to follow *in situ* the evolution of the structure of the growing film. Nowadays, despite several methods proposed for resolving some of the processing difficulties, the deposition of Ni-Ti films with definite stoichiometry and high purity remains a challenge. Moreover, it is clear from the published works that important issues like the formation of film texture and its control are still unresolved.

The aim of this PhD thesis is to study the optimisation of the deposition conditions for the formation of Ni-Ti films in order to obtain the material fully crystallized at the end of the deposition, and to establish a clear relationship between the substrates and texture development. In order to achieve this goal, a two-magnetron sputter deposition chamber has been used allowing to heat and to apply a bias voltage to the substrate. This equipment can be mounted into the six-circle diffractometer of the Rossendorf Beamline (ROBL) at the European Synchrotron Radiation Facility (ESRF), enabling an *in-situ* characterization by X-ray diffraction (XRD) of the films during their growth and annealing. In addition to the *in-situ* studies, complementary *ex-situ* characterization techniques such as XRD at a laboratory source, Rutherford backscattering spectroscopy (RBS), Auger electron spectroscopy (AES), cross-sectional transmission electron microscopy (X-TEM), scanning electron microscopy (SEM) and electrical resistivity (ER) measurements during temperature cycling have been used for a fine structural characterization.

The thesis consists of five principal chapters: (1) Background and literature review, (2) Experimental details, (3) Results, (4) Discussion and (5) Conclusions and future work.

Chapter 1 is divided into three sections. First a brief overview of the Ni-Ti system is given that supports future discussions on the composition control, the phases present in the films and phase transformations. In this section, the SME and the SE are also described. The second section is dedicated to the phenomena involving the deposition of thin films in general by sputtering. A short background of the sputtering process, including growth and morphology of the films is presented. The effects of ion bombardment and some considerations about stress in the films are also presented. In this thesis, since, the relationship

between the substrates and texture development in the Ni-Ti films is highlighted, the essential points related with texture in films, like the different types of textures and the driving forces involved are described. This topic includes a review concerning texture development on TiN films due to the importance of the TiN layers for the present study. In the last section, several aspects regarding the production and characteristics of Ni-Ti films are discussed. Therefore, the importance of the composition control, the crystallization of the films and phenomena associated, the oxidation behaviour, as well as film/substrate interfacial reactions and the role of the thickness on the properties of the Ni-Ti films are presented. Further, a brief literature review related to texture in Ni-Ti materials (bulk and films) is also given. Finally, a short review about NiTiHf films is given to support the preliminary results obtained during the first tests of the deposition of this type of films at ROBL, with a view to explore the feasibility of the *in-situ* sputtering equipment for the future study of ternary alloys.

The equipment used to produce and to study *in situ* the evolution of the structure of the films during growth and annealing by synchrotron radiation scattering is discussed in chapter 2. The *in-situ* studies enabled to evaluate the structural evolution during deposition at fixed deposition parameters, as well as to identify the effect of changing parameters (Ti power target) on the structural characteristics of the film. A brief overview of the complementary *ex-situ* characterization techniques, such as XRD at a laboratory source, RBS, AES, X-TEM, SEM and ER measurements is also given.

The studies have focused on the following points:

- deposition of Ni-Ti films on different types of substrates, such as naturally and thermally oxidized Si(100) substrates and MgO single crystal substrates;
- analysis of the role of a TiN buffer layer on the growth of the Ni-Ti film;
- influence of the bias voltage applied to the substrate during Ni-Ti growth;
- the characterization of graded films (controlled change of the Ti:Ni ratio *during* deposition).

For each situation, special attention is paid to the stability of the preferential orientation of the austenitic phase during the deposition process, trying to answer the question of how and when the different textures generate.

Chapter 3 includes the *in-situ* X-ray studies performed during the deposition (and subsequent annealing) of Ni-Ti films and their complementary *ex-situ* studies. Results obtained on near equiatomic films as well as the study of the effect of the controlled change of

the Ti:Ni ratio during the deposition of Ni-Ti films are presented (the first reported studies on the topic). During the *in-situ* study, the evolution of the intermediate structural "states" of the growing film has been identified, which cannot be seen/revealed *ex-situ*, because those states occurred only during the growth but were no longer detectable after deposition.

Chapter 4 discusses the preferential orientation of the films, the interface analysis and their link with the phase transformation characteristics.

In chapter 5, conclusions are presented based on the *in-situ* and *ex-situ* characterization of the samples studied during the present work. Furthermore, suggestions for future work are given.

Chapter 1

Background and Literature Review

1. BACKGROUND AND LITERATURE REVIEW

In the first section of this chapter, an overview of the Ni-Ti alloy system is given in relevance to the discussions on the composition control, the phases present in the films and phase transformation. The Shape Memory Effect (SME) and Superelasticity Effect (SE) are also explained.

The second section of this chapter is dedicated to the phenomena involving the deposition by sputtering of thin films in general. A short introduction to the sputtering process, which includes the growth and morphology of the films, is given. The ion bombardment effects and various considerations about stress in the films are also presented. It is as well described important points related to texture in films like the types of textures and the driving forces involved. TiN sputtered films are frequently mentioned in this section due to their importance for the present study.

In the last section of chapter 1, several aspects concerning the production and characteristics of Ni-Ti films are reviewed. Hence, the importance of the composition control, the crystallization of the films and related phenomena, the oxidation behaviour, as well as the interfacial film/substrate reactions and the role of the thickness on the properties of the Ni-Ti films are discussed. A brief review of texture in Ni-Ti SMA materials (bulk and films) is also given, as it assumes an important role. At the end, a short review about NiTiHf films is given to support the preliminary results obtained during the first tests regarding the deposition of ternary SMA alloys at ROBL.

1.1. Ni-Ti SHAPE MEMORY ALLOY

Ni-Ti alloys became one of the most technologically important SMAs due to the excellent combination of attractive properties like the SME, SE, high damping capacity, biocompatibility, high specific energy output and excellent mechanical properties, as well as a very high resistance to corrosion [1]. The thermoelastic martensitic transformation enables the SME and SE.

Crystallized binary Ni-Ti SMAs transform martensitically from cubic B2 (CsCl type) austenite phase into monoclinic B19' martensite either directly or via rhombohedral R−phase [2]. The intermediate transformation to a rhombohedral R-phase before achieving

the monoclinic martensitic phase has been a subject of study for several researchers [3-8]. It can be observed if the alloy is subject to specific processing conditions like: variation of Ni content, introduction of a ternary element, thermal annealing, thermal cycling or cold working. The R-phase ⇔ B2 transformation is associated with a small temperature hysteresis, when compared to that of the B19' ⇔ B2 transformation. The R-phase presents other attractive features like stability against thermal cycling and negligible strain-recovery fatigue, although the associated strain is smaller (0.5 %-1 % instead of 6.5 %-8.5 % of that of the later).

The capability to transmit particularly high forces along with a large stroke make SMAs a material with the greatest specific work output of several actuation mechanisms (Fig. 1.1) [9]. For comparison, bulk piezoelectric materials produce a large force over extremely small displacements, while piezo-bimorphs have large displacements but produce small forces.

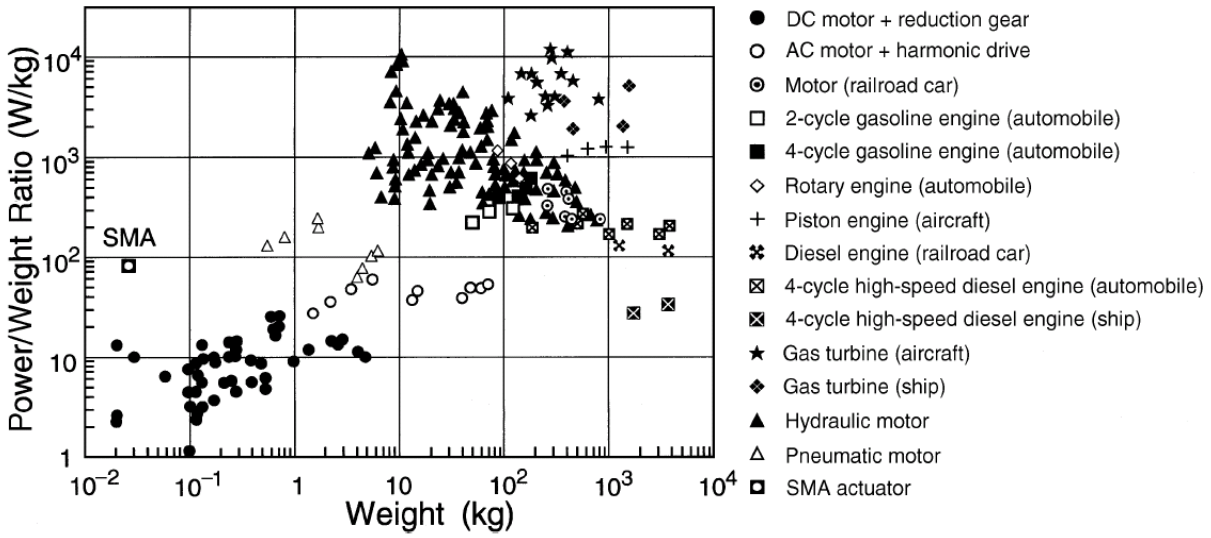

Fig. 1.1: Power/weight ratio *versus* weight for SMA actuators as compared with other devices, demonstrating the relatively large output of SMA actuators given their small size [9].

Ni-Ti SMA thin films have been recognised as promising high performance materials in the field of micro-electromechanical system (MEMS). However, although the deposition of Ni-Ti films has matured into an advanced technology during the last years, there are still important issues unresolved [10].

1.1.1. Phase diagram and crystal structures

The Ni-Ti alloy system is very attractive, since the alloy can be improved by utilizing various phase transformations, both diffusional and diffusionless. The SME and SE occur in near equiatomic Ni-Ti alloys with compositions ranging from ≈ 45-55 at.% Ni. Observing the Ni-Ti binary phase diagram in Fig. 1.2 [1], it is visible that the solubility in Ni-Ti changes gradually with temperature on the Ni-rich side, while it has a steep solvus boundary on the Ti-rich side. A small deviation from stoichiometry in Ni-Ti alloys can give rise to a significant precipitation of second phases. It was found that in Ni-rich Ni-Ti alloys, diffusional transformations take place during aging or slow cooling from high temperature. The precipitation sequence can be written as B2→Ni_4Ti_3→Ni_3Ti_2→Ni_3Ti (stable) [11]. The Ni_4Ti_3 metastable phase (rhombohedral until cell) appears at lower temperatures and at shorter aging times. The presence of Ni_4Ti_3 is especially important for improving shape-memory characteristics and strength, since it precipitates on a very fine scale. The inset of Fig. 1.2 shows the metastable equilibrium between Ni-Ti and Ni_4Ti_3.

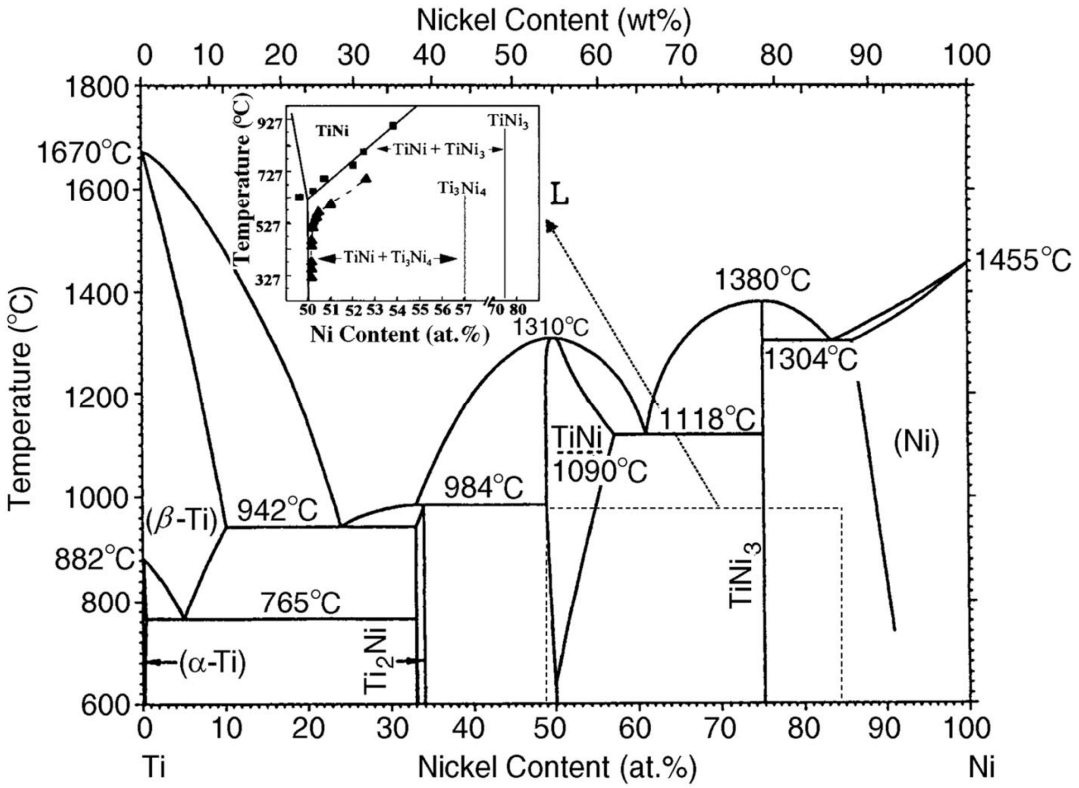

Fig. 1.2: Phase diagram of a Ni-Ti alloy to which the phase equilibrium between the B2 and Ni_4Ti_3 phases are added. [1].

Nishida *et al.* [11] have studied the precipitation processes in Ni-rich Ni-Ti alloys and reported the TTT (time-temperature-transformation) diagrams for several composition alloys. At lower aging temperature and shorter aging time, Ni_4Ti_3 phase appears, while at higher aging temperature and longer aging time Ni_3Ti phase appears and at intermediate temperature and time Ni_3Ti_2 phase appears (Fig. 1.3). Further studies [12] were conducted in an aged Ti-52 at% Ni alloy in order to clarify details of the microstructural aspects of the Ni_3Ti_2 phase using optical and electron microscopy and electron diffraction. It has been found that the Ni_3Ti_2 precipitate exhibits a phase transformation. The sequence of transformation events was described as occurring in two-step transformations: parent phase (tetragonal) ⇔ intermediate phase (orthorhombic) characterized by antiphase-like domain morphology ⇔ low temperature phase characterized by antiphase and needle-like domains morphology (monoclinic). Later, Hara *et al.* [13] have performed a study to determine the crystal structure of the Ni_3Ti_2 precipitate and to clarify the characteristics of the transformation from the crystallographic point of view. The crystal structure of the high and low temperature phases, and twinning in the low-temperature phase were studied in detail. The crystal structure of the high-temperature phase is tetragonal with Pd_3Ti_2 type (space group: *I4/mmm*). The values determined by the Rietveld method for the lattice parameters were: $a = 0.3095(38)$ and $c = 1.3585(169)$ nm. The low-temperature phase exhibits an orthorhombic structure with Al_3Os_2 type (*Bbmm*). The lattice parameters obtained were: $a = 0.4398(49)$, $b = 0.4370(48)$, and $c = 1.3544(150)$ nm.

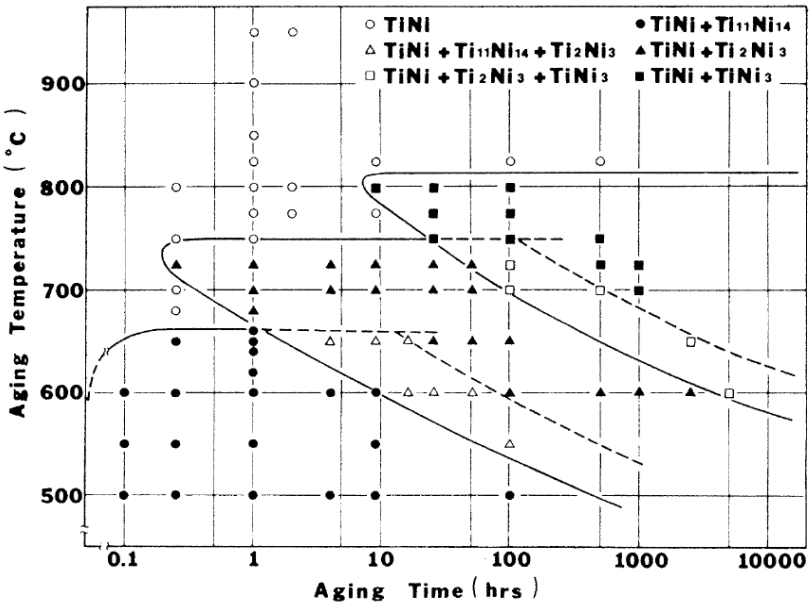

Fig. 1.3: TTT diagram describing aging behaviour for Ti-52 at% Ni [11].

Commercially used Ni-Ti alloys frequently contain a small volume fraction of intermetallic precipitate phase, normally Ni_4Ti_3 or Ti_2Ni, distributed in the B2 matrix. It is known that these phases can produce coherency strains and affect the transformation and mechanical characteristics of the alloy. However, in the Ti-rich side the solubility limit is almost vertical and the manipulation of the Ti_2Ni precipitates cannot be easily employed to improve the properties of the alloy. This situation changes in crystallized films via amorphous state, which is a non-equilibrium state, and even microstructures quite different from those of bulk materials can appear. This subject will be discussed in more detail in section 1.3.2.

The martensitic transformation in Ni-Ti SMA is a first order phase transformation that does not require long-range atomic migration to form the new crystal structure. When the high temperature B2 austenite phase is undercooled to a certain temperature (martensite start), it becomes unstable and transforms to a lower symmetry martensite (B19') by a shear-dominated, cooperative movement of atoms.

The parent phase of equiatomic Ni-Ti is a CsCl-type B2 cubic structure with a lattice constant of 0.3015 nm and the space group is Pm $\bar{3}$ m. The crystal structure is shown in Fig. 1.4(a). The low-temperature phase which can form with the same composition as the parent phase with a diffusionless transition has a monoclinic structure (AuCd type), denoted B19', as shown in Fig. 1.4(b) [14]. It belongs to space group $P2_{1/m}$. Kudoh *et al.* [15] found the following lattice parameters for the martensite phase: $a = 0.2898$ nm, $b = 0.4108$ nm, $c = 0.4646$ nm, and $\beta = 97.78°$ (Ti-49.2at% Ni alloy tested at 50°C).

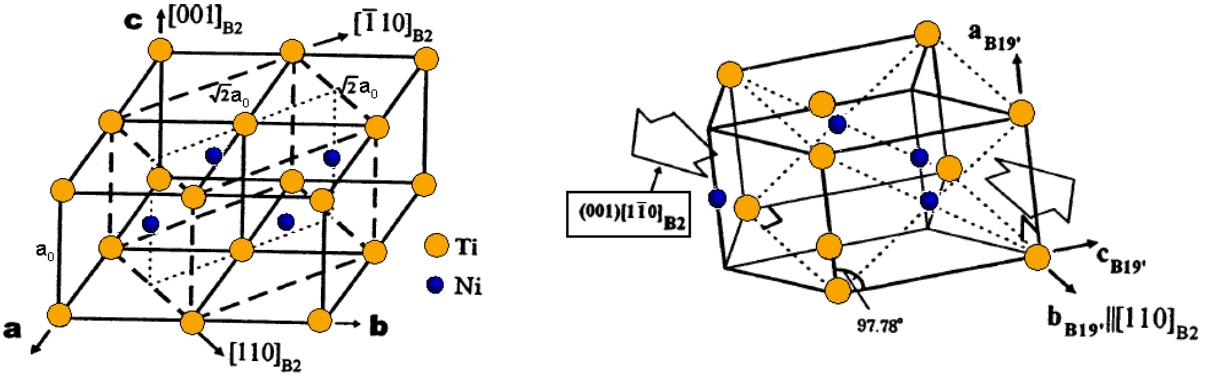

(a) (b)

Fig. 1.4: (a) B2 austenite phase, (b) B19' martensite phase [14].

As mentioned before, under certain conditions the R-phase can appear upon cooling and heating prior to martensite and austenite transformation, respectively. The R-phase transformation is recognized as a martensitic transformation (martensite plates are clearly

observed by electron microscopy) [16]. R-phase was reported as a rhombohedral distortion and the lattice can be described by stretching the cubic parent lattice along the <111> diagonal direction. If we define the corner angle α, which is 90° in B2 parent phase, as shown in Fig. 1.5, it deviates from 90° with changing temperature.

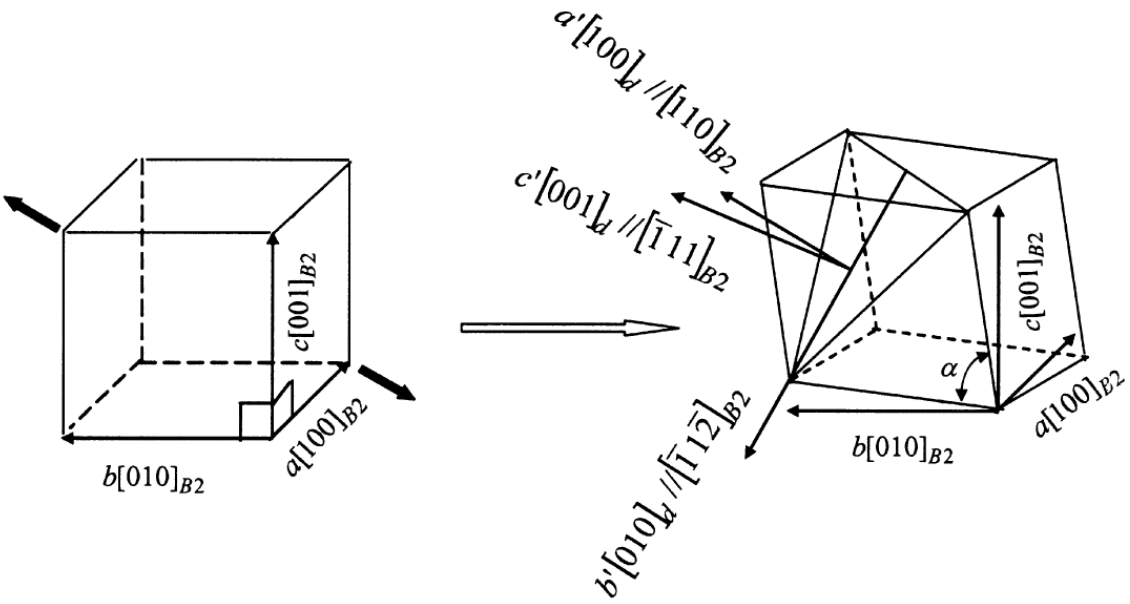

Fig. 1.5: Transformation of cubic (B2) austenite to rhombohedral (R) phase [17].

The SME and the SE are linked with the thermoelastic transformation. One of the most important characteristics of SMAs is the temperature at which it changes from one crystalline structure to the other. The characteristic temperatures of a phase transformation will be referred as follows:

- M_s : martensite-start temperature (upon cooling);
- M_f : martensite-finish temperature (upon cooling);
- A_s : austenite-start temperature (upon heating);
- A_f : austenite-finish temperature (temperature at which martensite becomes completely unstable upon heating);
- R_s : R-phase-start temperature on cooling;
- R_f : R-phase-finish temperature on cooling;
- R'_s : R-phase-start temperature on heating;
- R'_f : R-phase-finish temperature on heating.

The transformation temperatures are greatly dependent on composition, alloying elements and heat treatment processes [16]. The application of an external stress also influences the transformation temperatures. An effective way of changing the transformation temperatures is by changing the composition. In several cases, one percent change in

composition can change the transformation temperatures by more than 100°C. In the Ni-Ti system, the Ni-rich side has some solubility at high temperature (Fig. 1.2) and the transformation temperatures are strongly dependent on the Ni concentration. Increasing Ni causes a drastic decrease in the transformation temperatures. The martensitic transformation temperature drops to below 100 K for a Ni content exceeding 51.5 at.% (Fig. 1.6). On the Ti-rich side the transformation temperatures do not exhibit such dependence with composition, probably due to the fact that the solubility limit of Ni-Ti phase on the Ti-rich side is almost vertical.

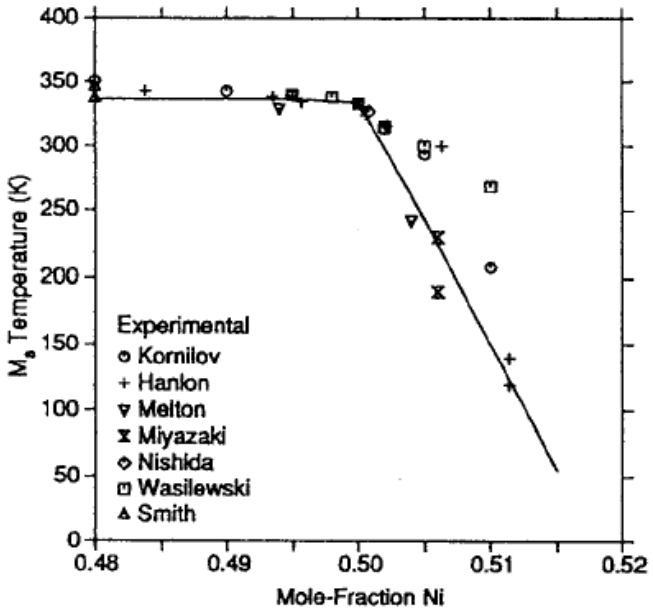

Fig. 1.6: M_s as a function of Ni content for binary Ni-Ti SMA. The different symbols represent data from different authors and the solid line is given by thermodynamic calculations [18].

The phase transformations can be investigated by measuring some physical properties such as electrical resistivity (ER) as a function of temperature. This technique was chosen in order to study the Ni-Ti films produced during this PhD work. Figure 1.7 shows the temperature dependence of the resistivity for a Ni-Ti bulk sample heat-treated at 380°C, obtained by Uchil *et al.* [19]. During cooling from B2-phase, the resistivity value decreases linearly with the temperature down to R_s. Self-accommodated R-phase transformation starts at R_s and the austenite parent phase (B2) transforms to the twinned R-phase with further decrease of the temperature. Twinning in an alloy matrix results in electron scattering that in turn leads to the increase of the ER [17]. The twinned structure density in B2 phase increases with the decrease of the temperature (due to the B2 $\Rightarrow$ R-phase transformation), producing a higher ER as a result of the more pronounced increase of lattice imperfections. R-phase transformation ends once the temperature decreases to R_f. An additional cooling promotes the R-phase distortion and, at M_s, the R-phase starts transforming to monoclinic B19' martensite,

which exhibits less lattice distortion. The martensite transformation finishes when the temperature reaches M_f, and, cooling below M_f, does not result in more phase changes. On heating, the authors did not identify the R-phase reverse transformation. The transformation to cubic B2 austenite parent phase is completed at temperature A_f and the microstructure completely reverses to the original microstructure consisting of single cubic B2 austenite.

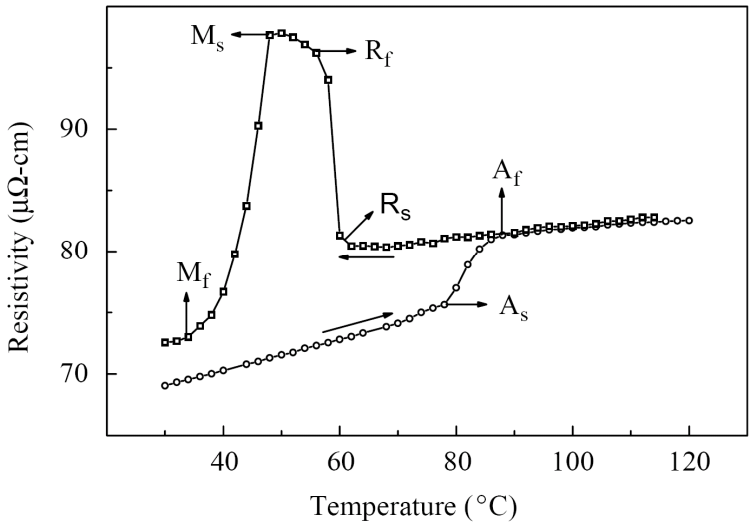

Fig. 1.7: Temperature dependence of electrical resistivity of a Ni-Ti sample, heat-treated at 380°C, in a complete thermal cycle [19].

1.1.2. Shape memory effect (SME) and superelasticity effect (SE)

The SME in Ni-Ti alloy was discovered in the 1960s at the Naval Ordnance Laboratory [20], hence the acronym Nitinol is commonly used in referring to the Ni-Ti system (Nickel Titanium Naval Ordnance Laboratory). The SME is a result of the change in crystalline structure as the material is heated and cooled. The martensitic transformation is a displacive type solid-state transformation and atoms are cooperatively rearranged or shifted into a new structure (without diffusion). The displacement of each atom is not large but since all of the atoms move in the same direction in a domain or variant, the transformation results in a macroscopic change in shape. This phenomenon may lead to unique properties such as the SME and SE. The martensitic transformation is described by a shear-like mechanism, as shown schematically in Fig. 1.8(a) and (b) [1]. When the B2 parent phase in Fig. 1.8(a) is cooled below M_s, the structure changes into martensite, as in Fig. 1.8(b). The formation of martensite is normally referred to as athermal transformation, since the amount of new phase present is typically dependent only upon temperature, but not upon the length of time at the transformation temperature. In the case of Ni-Ti, twinning is the dominant accommodation process for martensite transformation. It can accommodate shape changes in a reversible way

that is necessary for the SME. Twin boundaries are of very low energy and quite mobile, thus favouring the formation of martensite. When the temperature is raised above A_s and the martensite becomes unstable, the reverse martensitic transformation occurs [Fig. 1.8(b) to (a)]. However, if in the martensitic state, a stress is applied, the twin boundary movement results in a new shape [Fig. 1.8(b) to (c)]. The deformation of the martensite in Ni-Ti is accomplished by the motion of these twin boundaries producing coalescence or growth and shrinkage of variants. In Ni-Ti alloys, the growth of variants that produces a shape change in the direction of applied stress can accommodate strains of approximately 10%. Heating the sample to a temperature above A_f, the martensite variants revert to their original orientation in the parent phase [Fig. 1.8(c) to (a)].

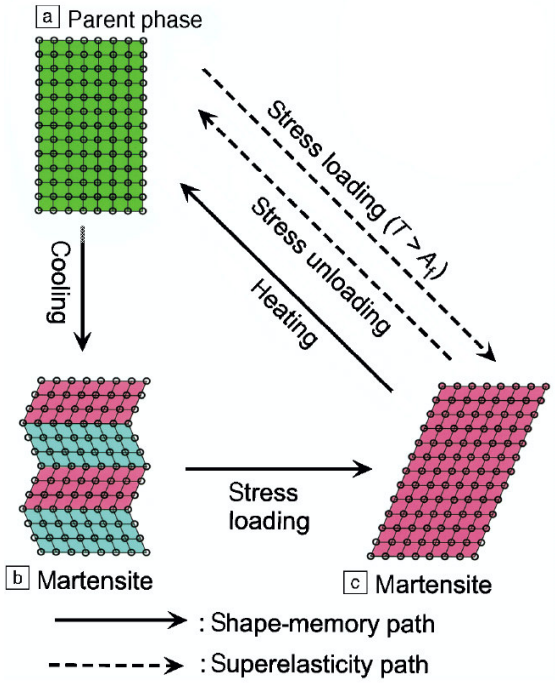

Fig. 1.8: (a)-(c) Schematic illustration of the mechanism of the SME and SE. The solid lines represent the SME and the dotted lines represent the SE path [1].

A transformation hysteresis is observed for this type of phase transformation, i.e., the heating and cooling paths do not overlap. The reduction in hysteresis allows for higher frequency actuation by shortening the temperature range, and resulting heating and cooling time, between the A_s and M_f temperatures. The R-phase transformation exhibits an extremely small temperature hysteresis, which could be beneficial for many MEMS applications (e.g. actuators).

Ni-Ti in the austenitic phase can exhibit apparently plastic deformations that are fully recoverable when the applied stress is removed. This phenomenon is named superelasticity (SE), whose mechanism can be described by using Fig. 1.8(a) and (c). It is defined as the

recovery of the strain upon unloading for the stress-induced martensitic transformation above A_f (if slip does not occur under the applied stress). Due to the fact that martensitic transformation occurs by a shear-like mechanism, it is possible to induce it even above M_s if a stress is applied. However, the martensite is completely unstable at a temperature above A_f in the absence of stress. Therefore, the reverse transformation must occur during unloading in this case, and the strain completely recovers in the thermoelastic transformation.

In the SME phenomenon discussed above, what is remembered is the shape of the austenitic phase. The shape change associated with phase transformation only occurs during the heating process. This is very often called the *one-way SME.* However, it is possible to remember the shape of martensite under certain conditions, i.e. both austenite and martensite can be "memorized". Briefly speaking, the shape change is purely a result of changing the temperature without the application of external stresses. This is called the *two-way SME*. The *one-way SME* is due to the strong reversibility and unique lattice correspondence upon reverse transformation, while *two-way SME* is due to the selective nucleation of certain martensite variants.

Since the *two-way SME* requires special procedures for the alloy to be able to exhibit it and since it is not as well understood as that of the *one-way SME*, the use of the one-way-effect with external reset force in many cases is chosen as the more economical solution. Nevertheless, especially in the field of MEMS, it can be advantageous to use the intrinsic *two-way SME* to realize a reversible shape change. It is easier to optimise the design regarding size and weight if no consideration has to be paid to a resetting spring. In order to realize the shape of martensitic phase certain martensite variants need to be selected. It is known that the martensitic transformation strongly interacts with stress, and the stress selects certain variants of martensite in the nucleation process in order to lower the energy of the system, thus contributing to create a certain shape of martensite [16]. Several reports concerning the procedures to obtain the *two-way SME* include: (1) introduction of plastic deformation; (2) constraint aging; (3) thermal cycling; (4) utilization of precipitates; (5) martensite aging due to symmetry-conforming short range order *etc.*

Freestanding Ni-Ti films usually show intrinsic *two-way SME*, with large displacement, but relatively small force in actuation [10]. The nature of this *two-way SME* could be due to: (1) intrinsic residual stress in Ni-Ti films [21]; (2) compositional gradient through film thickness [22]; (3) precipitates formation along some preferential planes by an appropriate heat treatment [23, 24]. The constrained film/substrate actuators could provide

large actuation force, but sacrifice the deflection (or strain). On the other hand, the substrate may act as an effective biasing force, thus creating a mechanical *two-way SME*.

During previous work on Ni-Ti films (MSc thesis [25]) we have performed *in-situ* annealing experiments, using a Be-dome furnace installed into the six-circle diffractometer of the Rossendorf Beamline (ROBL-CRG) at the ESRF, Grenoble, which allowed us to determine the kinetics of the phenomena and to identify the sequence of precipitation [26], [27]. The *two-way SME* has been observed in freestanding films removed from the substrate after the annealing process. When heated above room temperature (RT) the film presents a bent shape, memorized during annealing, as seen in Fig. 1.9.

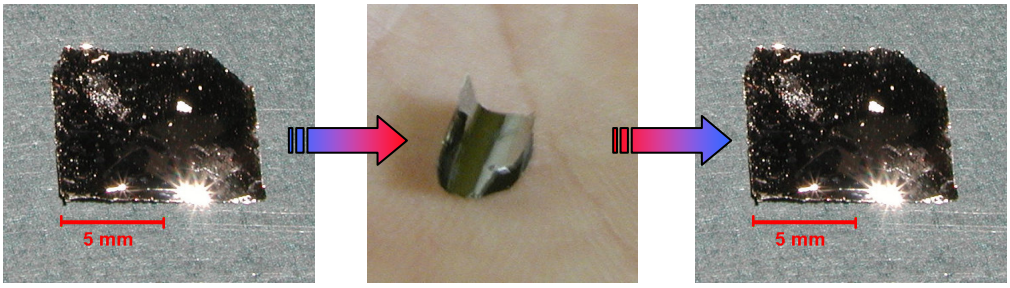

(a) (b) (c)

Fig. 1.9: Free-standing film after crystallization exhibiting the *two-way SME*; (a) flat on a table, (b) bent after phase transformation on a human hand, (c) again flat on the table [27].

During cooling it recovers its flat shape. This effect can be applicable in micro-sensors, micro-switches or micro-positioners. The nature of this *two-way SME* could be due to the Ni_4Ti_3 precipitates that formed during the heat treatment [26] and the presence of R-phase. At RT the film exhibits the R-phase structure and just the contact with a human body is then enough to induce the R-phase $\Rightarrow$ B2 transformation [27].

1.2. THIN FILMS IN GENERAL

Many concepts using bulk Ni-Ti were implemented and grew to successful applications but in some specialized applications bulk material has experienced only limited success (such as temperature sensitive switches and robotic manipulators) due to the limitation of the heating/cooling rate. Thus, thin wires and especially films are explored for potential use in micron- to millimetre- scale microelectromechanical systems and miniature robotics. They can be heated resistively, and the small thermal mass and the large surface to

volume ratios allow a rapid heat transfer improving thus response speed. As films they have the additional potential for batch fabrication and, correspondingly, Ni-Ti films are attractive materials for microfabrication and integration in micro-miniature systems composed of mechanical elements, actuators, sensors and electronics made on *one* chip [28-30]. Due to their high power density, and due to the large displacement and actuation force, most applications of Ni-Ti films are focused on micro-actuators, such as micropumps, microgrippers, microvalves, micropositioners *etc.* [10]. Because of their sensitivity to environmental changes, e.g. thermal, and/or to stress they are also ideal materials for applications in microsensors [31].

In a general way, for the production of films of a certain material, the choice of the deposition technique is normally based on fulfilling the requirements put forth by the sample properties as well on practical limitations such as cost, area of coverage and vacuum requirements. In this study, magnetron co-sputtering has been applied for depositing the Ni-Ti samples.

Nonthermal growth techniques, such as sputtering, have proved to be among the most promising regarding the control of morphology and crystalline quality during film growth. This technique can lead to unusual and often advantageous growth kinetics and can force a film to grow under conditions far from thermal equilibrium. Melt-spinning is considered as well a non-equilibrium technique (the result may strongly depend upon the cooling rate) and it has been used by some researchers for the production of Ni-Ti ribbons [32, 33]. It allows also to obtain fine grains (rapid quenching) but it may be difficult to obtain reproducible results among different apparatus or among different researchers. Typically the thickness of melt-spun ribbons is 30-40 μm. It is also possible to make strips as thin as 30 μm by cold rolling and, thus, melt-spinning technique and rolling technique may become competitive in the future [16]. Nevertheless, considering potential applications in the field of MEMS, sputter deposition technique is much more suited because the Ni-Ti films can be deposited directly on semiconductors or IC, and patterning can be as well incorporated using photoresist technique.

A brief introduction to the sputtering technique, including growth and morphology of films in general, is presented in this section. There are also some considerations concerning the effects of ions bombardment, which are linked to this deposition technique, as well as the occurrence of stress in the films. Furthermore, the type of texture and their driving forces are discussed.

1.2.1. Sputtering process

Through the application of a negative potential to the magnetrons (creating a voltage between the target material and the grounded substrate plate), the target material is bombarded with ions (Ar^+ in this work) extracted from an electropositive plasma. A small current is created by the small number of charge carriers initially present in the sputtering gas when the voltage is applied to the electrodes. An increase of the applied negative potential of the target leads to an increase in the current density. This is in part a result from the creation of a large density of charge carriers, e.g. secondary electrons. The electrons move towards the anode (sample) while an ion flux is generated towards the cathode (target). This behaviour continues for voltages up to the breakdown voltage and is named the *Townsend discharge region*. Once electrical breakdown occurs, the concurrent increased charge-carrier density increases the current density and decreases the electrode voltage. The applied voltage is now so high that the number of Ar^+ ions produced by collisions with one secondary electron is enough to produce another secondary electron. In this way the plasma is self-sustaining *(normal discharge region)*. An illustration of the sputtering process is presented in Fig. 1.10.

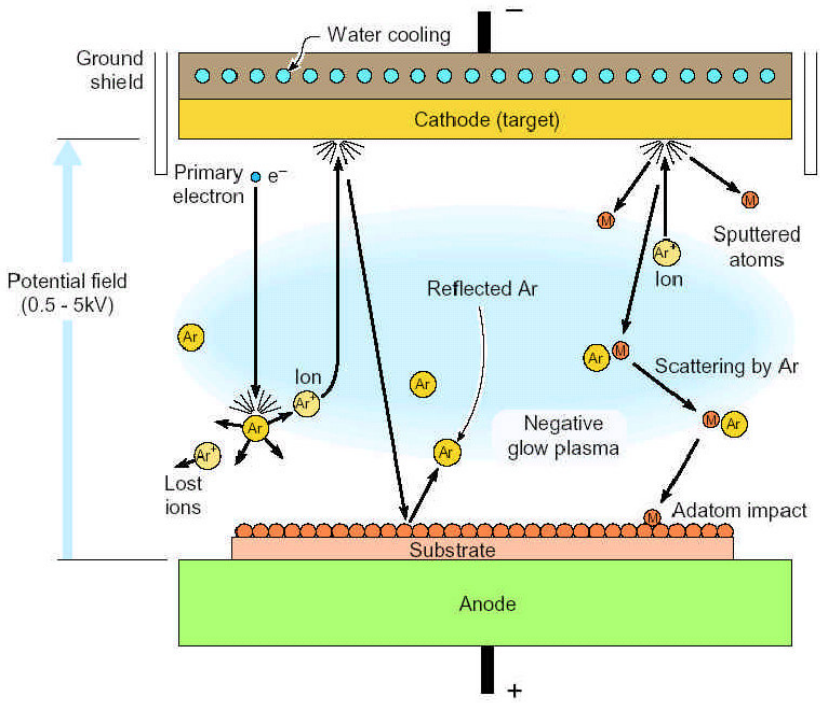

Fig. 1.10: Scheme of the sputtering deposition process [34].

Since it is not the scope of this thesis to discuss the plasma in detail, more important details can be found in Refs [35, 36]. Nevertheless, various characteristics of the plasma are essential in order to comprehend the flux of bombarding particles at the growing films, which

is one of the main parameters for explaining the observed morphology. One of them is an excess of positive charge carriers in the space near to the negative cathode. This is related to the attraction (repulsion) of the ions (electrons) and leads to a sheath voltage that is about the same as the electrode voltage, V_{CA}. The total difference in a potential between the electrodes is confined to this sheath close to the cathode, which is named the cathode sheath or *Crooke's dark space*. The Ar^+ ions are accelerated through this sheath, gaining an energy of eV_{CA}, and create secondary electrons upon colliding with the target material. The electrons are accelerated back through the Crooke's dark space before they ionise or excite the Ar atoms in the negative *glow space*. Only parts of the cathode area in the low-current end of the normal discharge region are covered by the negative glow discharge space. This coverage increases as the applied voltage is increased until the entire cathode-area is covered, which is the end of the normal discharge region. Throughout the lateral expansion of the negative glow discharge the current density stays constant. An increase of the voltage further increases the current density and the *abnormal discharge region* is entered.

A high ion current is necessary in order to have a reasonable sputtering rate, which explains why the abnormal discharge region is used for sputtering. The collision of Ar^+ ions with the target surface causes:

- sputtering of the target material;
- emission of secondary electrons;
- electron capture and backscattering of neutral Ar atoms;
- implantation of Ar^+ ions into the target.

The number of gas atoms between the sample and the magnetrons should be low allowing the sputtered atoms to arrive at the sample without any major collisions that would redirect the sputtered atoms way from the sample and thus decrease the deposition rate. The mean free path (l) is given by

$$l = (kT/(\sqrt{2}.\sigma.p) \qquad (1.1)$$

where σ is the cross section for the collision, k the Boltzmann constant, T the temperature and p the pressure. This equation shows that the pressure has to be lower than a certain maximum to fulfil this condition. On the other hand, in order to guarantee that secondary electrons produce ionising collisions, a constraint for having a self-sustaining plasma, the total thickness of Crooke's space and the negative glow space must be less than the electrode separation. This total thickness increases with decreasing sputtering pressure and thus defines a minimum pressure.

A simple sputtering system is based on a cathode (the target) and an anode facing each other *(Planar Diode Glow Discharge Sputter Deposition).* The target is not only the source of coating material but also the source of secondary electrons sustaining the glow discharge (the target is normally water-cooled). Several factors determine the deposition rate such as: the power density at the target surface, source-substrate distance, working gas pressure, size of the erosion area, and source material. Various factors are interrelated, such as pressure and power density. Consequently, the optimum operating condition is achieved by controlling the parameters to get the maximum power which can be applied to the target without causing cracking, sublimation or melting.

In order to increase significantly the ionisation efficiency near the target, magnetic fields are frequently employed for the diode sputtering process *(Magnetron Sputter Deposition).* Due to the fact that ions are generated relatively far from the target in the conventional planar diode process, the probability for ions to lose their energy to the chamber walls is large. Additionally, the number of primary electrons hitting the anode at high energies without experiencing collisions is increased as the pressure decreases, thus reducing ionisation efficiency. In the magnetron sputter deposition process, an applied magnetic field parallel to the cathode surface forms electron traps and restricts the primary electron motion to the vicinity of the cathode. The magnetic field strength is in the range of a few hundred gauss and consequently, it can influence the plasma electrons but not the ions. The electrons trapped on a given field line can advance across the magnetic field to an anode or walls by making collisions (mainly with gas atoms). As a result, their chances of being lost to the walls or anode without collisions are very little. Due to the higher efficiency of this ionisation procedure, the process can be operated at low pressures (around 0.13 Pa) with high current densities at low voltages, hence providing high sputtering rates.

Depending on the configuration of the magnetic fields, there is a distinction between *balanced* and *unbalanced magnetrons*. The magnetic field in a *normal/balanced magnetron* is designed to maintain the electrons, and, therefore, the plasma in the vicinity of the substrate. The configuration of the balanced magnetron was developed for specific applications such as microelectronics, due to the fact that the bombardment of the growing film by energetic particles was to be avoided. However, there are situations where it is necessary to bombard the growing film with energetic particles (for example in the deposition of hard coatings). For that it can be used a secondary plasma near the substrate as a source of energetic particles or use a separate ion gun. Nevertheless, there is also the possibility to alter the magnetic fields between the inner, and the outer sets of magnets in the sputtering cathode, so as to permit the

plasma to extend to the region of the substrate (increasing the efficiency of the ionisation) and, thus, a greater number of ions are directed toward the growing film *(unbalanced magnetron)*.

There are several configurations of magnetron sputter deposition technologies like the cylindrical magnetron and the planar magnetron. In applications where the substrate needs to be coated from all sides simultaneously, a cylindrical target accomplishes the task in one easy step. With the sputtered flux arriving from the inner surface of the cylindrical target this type of sources keep the entire substrate surface "in the plasma" during the deposition for highly uniform film properties. In the present work, planar magnetron sputtering (the sputter target is placed above a configuration of permanent magnets that produce a magnetic field over the target surface) was used for the deposition of the Ni-Ti films (Fig. 1.11).

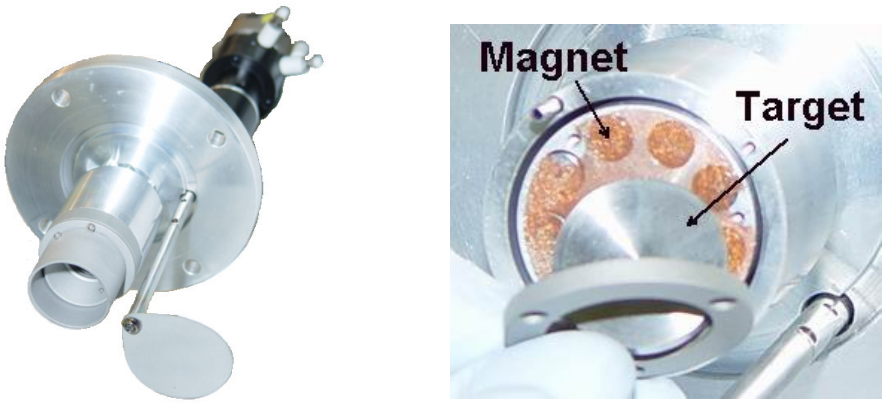

Fig. 1.11: Overview of an *unbalanced* miniature magnetron, commercially available from AJA International [37] (type A4001) and a detail of the localization of the target (Ti target in the photo).

The sputter deposition chamber has been developed for the *in-situ* study of film growth by synchrotron XRD and X-ray reflectivity (XRR) and, therefore, to fit into the Huber six-circle goniometer of the ROBL beamline, which is used, as a multipurpose instrument for many other experiments. These were main points that have been considered during the project of the chamber. A detailed description of the apparatus used is given in the experimental chapter.

1.2.2. Growth and morphology

The growth and morphology of films become dependent on the used deposition technique because each deposition technique has a characteristic set of deposition parameters. However, the process of film growth as a result of sputter deposition has various aspects in common with other PVD techniques such as evaporation. The growth of films is usually

described as proceeding in three steps. *Step I* consists on the transport of the target material to the substrate. The mechanisms on the substrate/film surface such as surface chemistry and surface diffusion are covered by *step II,* and *step III* includes these mechanisms in the bulk, i.e. bulk chemistry and bulk diffusion. Temperature has a major role on the rate of the mechanisms taking place in *step II* and *step III*. The typical ratio of activation energies for surface, grain boundary and bulk diffusion is 1:2:4 [38], which means that *step II* will dominate over *step III* at lower temperatures. Ballistic motion on a small scale on the surface can be created by bombarding the growing film with high-energy atoms/ions, increasing the surface diffusion and consequently *step II* is promoted. The energies of the bombarding species and their flux ratios to the target materials are key parameters for growth and morphology of the resulting film. In particular, these parameters are important at lower homologous temperatures ($T/T_m < 0.35$; T_m represents the melting temperature) where the surface diffusion is slow. An illustration of the atomic-scale phenomena affecting the nucleation and growth of films is shown in Fig. 1.12.

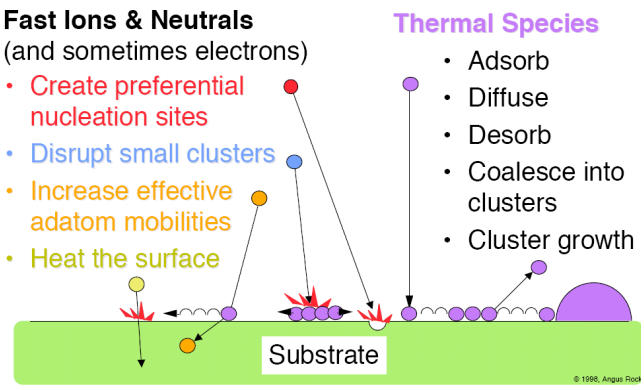

Fig. 1.12: Schematic illustration of the film growth process: atomic-scale phenomena affecting nucleation and growth [34].

Movchan and Demschichin [39] have built a structure-zone model to describe the observed morphology as a function of the substrate temperature for evaporated films. They have studied the influence of base temperature on the condensation, structure and properties of thick (up to 2 mm) polycrystalline condensates of Ni, Ti, W, Al_2O_3 and ZrO_2. Three structure-zones with their own structure and properties were found, with boundary temperatures T_1 and T_2 (Fig. 1.13). For the metals T_1 and T_2 were 0.3 and 0.45-0.5 T_m, respectively, and for the oxides 0.22-0.26 and 0.45-0.5 T_m. In *zone I*, films have a voided columnar structure with many dislocations. This is related to the small diffusion length on the surface during *step II* resulting in grain boundaries with very low densities. The increase of

temperature above T_1 leads to *zone II*, in which a high surface diffusion creates a good order across each column' widths and partly to the grain boundaries, being more dense. In *zone III* the temperature is high enough to allow bulk diffusion and an equiaxed grain structure evolves.

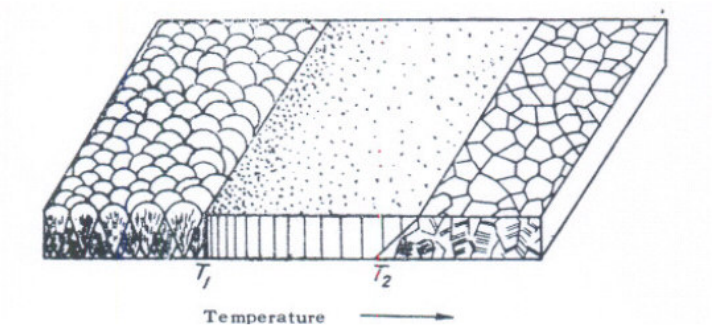

Fig. 1.13: Diagram of structural zones revealed as a function of the base temperature [39].

Thornton [40] extended the model proposed by Movchan and Demschichin to comprise sputtering. In his representation four structures are present. The resulting film morphology is dependant on the substrate temperature, melting temperature, and argon pressure [Fig. 1.14(a)]. The model is also based on experimental results and gives a good reference for the determination of the expected morphologies when the substrate is heated to specific substrate temperature/melting temperature ratios. In this model the pressure becomes as well a key parameter. The mean free path of the sputtered atoms and fast neutrals decreases with increasing pressure and, therefore, the energy of the bombarding species becomes dependent on the pressure. As a consequence, the rate of *step II* depends on the pressure. There is also an increase of the oblique component of the deposition flux due to collisional scattering by the inert gas, and the self-shadowing effect decreases the density at the grain boundaries (*zone I* is promoted). The insertion of the pressure as a major parameter introduces an extra zone, *zone T* or *transition zone*, between *zones I* and *II*.

Later, Barna *et al.* [41], after analysing the structure zone models published in the literature, suggested that the various structure zones could be characterised as it is shown in Fig. 1.14(b).

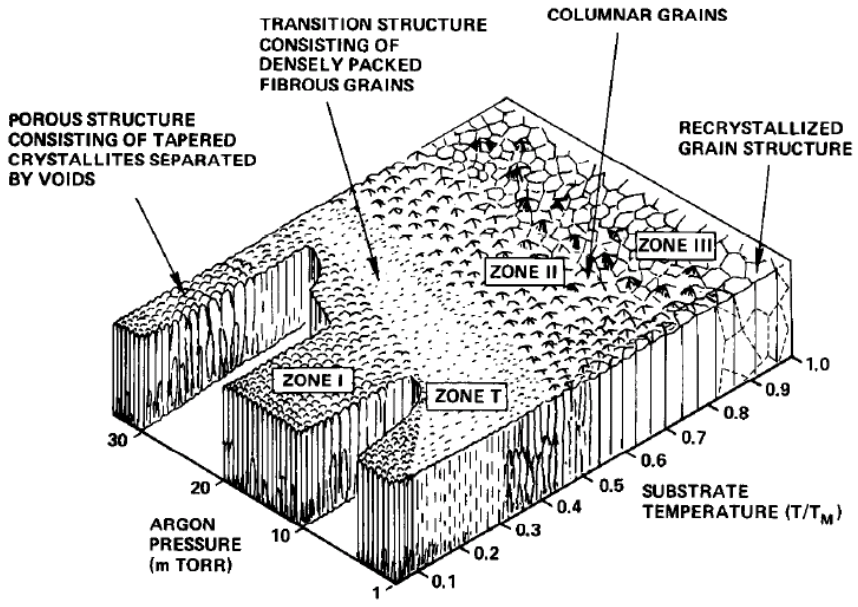

(a)

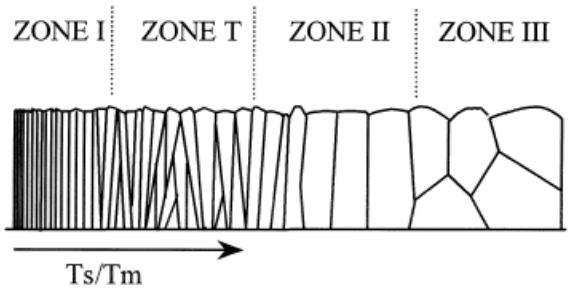

(b)

Fig. 1.14: (a) Microstructure zone diagram for metal films deposited by magnetron sputtering showing the influence of the deposition pressure and homologous temperature on the morphology of films (*T* is the substrate temperature and T_m is the melting point of the coating material) [40]. (b) Main characteristics of structure zones used in the literature [41].

In *zone I*, the film is composed of fibrous grains and the grain boundaries are porous. Shadowing effects caused by an oblique component of the deposition flux and substrate roughness can play an important role. In this zone, neither the bulk diffusion nor the self-surface diffusion have a remarkable influence in the resulting structure due to low atomic mobility. The crystalline fibres grow out of the primary nuclei and advance to the top of the film. The orientation of fibres follows the random orientation of the nuclei. An increase in T/T_m leads to an increase in the diameter of the fibres.

In *zone T*, the morphology is characterized by being fibrous without having a large fraction of voids. At low pressure the energetic bombardment promotes the mobility on the surface, and the structure thus becomes denser since *step II* is promoted. However, in the lower part of this temperature interval, no grain boundary migration can be expected. As a result, the lateral size of competing crystals at the substrate is determined by the nucleation

density and the crystals are in random orientation. For the higher temperatures grain boundaries can become mobile leading to the lateral growth of grains situated on the substrate. The structure of *zone T* is known to be inhomogeneous along the film thickness. It is fine crystalline at the substrate, composed of V-shaped grains in the subsequent thickness range (competition taking place among the differently oriented neighbouring crystals) while it can be columnar in the upper part of thicker films. In this zone (*T*), a weak preferred orientation develops strengthening gradually with temperature and is changing with thickness.

Zone II is dominated by surface diffusion with a homogeneous structure along the film thickness, which is composed of columns that penetrate from the bottom to the top of the film (columnar crystals with similar orientation). Grain boundaries nearly normal to the film plane are expected (minimisation of the grain boundary energy). This zone is associated with high substrate temperatures ($T/T_m > 0.4$). The lateral size of the grains increases with increasing temperature.

In *zone III*, the high substrate temperature leads to equiaxed (globular) three-dimensional grains, which is an indication that the crystal growth has been blocked periodically.

At this point it seems important to summarize the kinetic factors and process parameters that affect the evolution of the structure of polycrystalline films. Table 1.1 gives an overview on this topic [42].

Factors affecting the structure evolution in polycrystalline films
Kinetic factors affecting the structure evolution Adatom diffusivities on the substrate surface Adatom self-diffusivities on island surfaces Self-diffusivities in grain boundaries Grain boundary mobilities Adatom cluster nucleation rates Adatom desorption rates
Process parameters Deposition rate *(affects adatom arrival rate, affects adatom diffusion time before cluster nucleation or desorption, affects film purity)* Substrate temperature *(affects all kinetic processes, increasing rates with increasing temperature)* Background pressure *(affects film and surface purity)* In sputter deposition: sputtering gas pressure and substrate bias *(affect the angular distribution and energies of arriving adatoms)*
Factors affecting zone models Deposition technique Materials class Impurities incorporation

Tab. 1.1: Factors affecting structure evolution in polycrystalline films [42].

Apart from the *factors affecting zone models* mentioned in Tab. 1.1, Hultman and Sundgren [43] referred that though the structure zone models seem to be adequate in giving a qualitative classification of film microstructure formation, they do not include effects from the *substrate material* itself on the film growth mode. It has been found that the observed microstructure of hard coatings is not simply dependent on process parameters such as temperature and energetic particle bombardment during growth, but also significantly dependent on the substrate crystal structure, morphology, composition and/or surface contamination, all of which have important influences on the nucleation. For example, substrate surface roughness often exists at the same time on several size scales. This roughness can be reproduced in exaggerated form on the coating surfaces in *zone I* structures, due to superimposed shadow growth. Open boundaries are associated with coarse surface irregularities. In the presence of severe surface irregularities *zone I* structures can persist into the *zone II* and *zone III* regions as T/T_m is increased. It is also essential to choose the substrate material carefully since preferred crystallographic orientation in coatings have been associated with effects such as minimization in surface energies and a variation in condensation coefficients.

It should be clear now that in PVD deposition processes the atoms are deposited from a gas phase onto a substrate and the deposition parameters play an important role in determining the microstructure and physical properties of PVD-grown films. Parameters including the deposition rate, deposition angle (i.e., the angle the velocity vector of a depositing atom makes with the substrate normal), the distribution of deposition angles (i.e., the degree of collimation of the deposition beam), the kinetic energy of the depositing atoms, and the substrate temperature must be taken in consideration. As described before, considering the structural zone models, for lower substrate temperatures the films tend to exhibit a porous columnar microstructure. With the increase of deposition angle this porous structure is promoted (i.e., increasingly oblique). In these named *zone I* microstructures, experimental observations suggest that the angle of orientation of these columns (relative to the substrate normal) β, is normally smaller than the deposition angle (relative to the substrate normal) α. The columnar structure is oriented more nearly perpendicular to the substrate than the deposition flux.

Nieuwenhuizen and Haanstra [44] described the relationship between the column orientation and the deposition angle in their experimental results using the following empirical relation:

$$\tan \alpha = 2 \tan \beta \qquad (1.2)$$

This equation is known as the *tangent law* and it is found to be valid for deposition angles $\alpha \leq 60°$. An increase in film density is expected when the substrate temperature is increased or the deposition angles decrease. On oblique depositions, increasing temperature leads to a continuous transition from a porous film with a columnar microstructure to a densely packed film. The transition temperature increases with the deposition rate.

Many atomistic simulation studies of film growth have been performed by Monte Carlo (MC), molecular dynamics (MD) and ballistic deposition models. Here an overview of results obtained by Dong *et al.* [45] is given. They have employed atomistic, molecular dynamics simulations to study the role of several PVD deposition parameters (deposition angle, kinetic energy, and substrate temperature) on the microstructure (density, roughness, and column orientation) of the growing films. The effects of temperature and deposition kinetic energy on film growth at fixed deposition angle were investigated, since these deposition parameters are known to have a pronounced effect on the roughness and porosity of the growing film. The role of deposition angle on the roughness and porosity of the film was also examined. Their results have shown that an increase in substrate temperature and deposition kinetic energy leads to fewer voids, smaller voids, smoother surfaces, and higher film density. The similarity between the variation in microstructure with temperature and deposition kinetic energy suggests that these two physical parameters play a similar role in the deposition process: namely, changing the atomic mobility on the growing surface. On the other hand, the film microstructure changes from a dense film, with few voids, to a microstructure in which nearly collinear tracks of elongated voids form and, finally, to a highly porous structure of well-formed columns if the deposition angle is increased. Void formation, void alignment into tracks, and the columnar structure are all attributable to shadowing effects. The change of the column/void track angle β with deposition angle α can be described by the classical tangent law at low angles, but is generally predicted to be higher by the tangent law for $\alpha > 60°$ than experimentally found. Due to increased surface mobility the column angle β decreases slowly with increasing deposition kinetic energy.

1.2.3. Energetic ion bombardment

In a PVD process like magnetron sputtering, it has been observed that along with other deposition parameters, the effect of the ion bombardment also plays an important role on the properties of the growing film. Ion bombardment influences film properties such as packing

density, surface roughness, and crystallinity. Energetic ion, electron, or neutral bombardment of the growing film surface can alter the mobility of film atoms, resulting in changes in film structure or density.

Nowadays, there is a constant demand towards the use of lower processing temperatures. This means that in several cases the deposition has to be done at low T/T_m where the adatom mobility is limited. A columnar growth structure defined by voided open boundaries is normally expected for vapour deposited coatings grown under such conditions *(zone I)*. As mentioned before, this structure is essentially a consequence of atomic shadowing acting in concert with the low adatom mobility and tends to be exacerbated by the non-uniform surface topography encountered. An advantage of the sputtering technique is that a depositing atom brings along kinetic energy of about a few electron volts and in some cases up to 20 eV or even more resulting in additional local rearrangement of the atoms at the film surface. This rearrangement results in less self-shadowing and denser film structure. In addition, at the low working pressures typically used in magnetron sputtering, energetic neutral working gas atoms (ions that are neutralized and reflected at the sputtering target) having energies as high as several hundred eV can reach the substrates with a substantial fraction of their energy. The energy flux carried to the substrate by the neutralized and reflected ions depends on the target mass relative to that of the working gas, the cathode shape (due to the scattering directions of the reflected species relative to the emission directions of the sputtered species), and the working gas pressure. In *unbalanced* magnetron sputtering, due to the magnetic field configuration, some of the ions from the glow discharge are directed toward the substrate, which can be been utilized to modify the properties of the growing film. Thornton [46] concludes that the existence of a *zone T* structure in films deposited by extended magnetron sources is largely a consequence of the bombarding effect of working gas ions which are neutralized and reflected at the cathode surface. The *zone I/zone T* boundary can thus be envisioned as resulting from a competition between the effects of energetic particle bombardment which tends to create a dense microstructure, and oblique deposition which tends to produce an open structure.

Nevertheless, in several cases the bombardment that results from ions that are neutralized and reflected at the cathode using magnetron sputtering sources at low pressures is not enough to suppress a *zone I* structure. Thus, a more energetic process is required such as the intense ion bombardment that can be produced by bias sputtering. For example, by applying a bias to the substrate, more ions can be accelerated toward the substrate with sufficient energy to assist the growing film. In addition to bombardment by ions from the

adjacent plasma, an independent ion source can also be used. The intense energetic ion bombardment during deposition can largely suppress the development of open *zone I* structures at low T/T_m. The relevant parameters are the ion energy and the ion flux relative to the coating flux [46]. An illustration of the role of the ion bombardment during film growth is presented in Fig. 1.15.

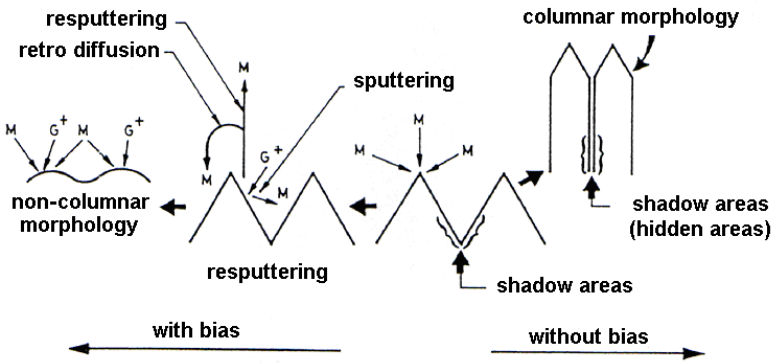

Fig. 1.15: Model of the modification of the growth mode of a film by ion bombardment [47].

It seems that the superposition of an additional physical process, such as energetic particle bombardment or surface chemistry reactions, can dominate the low temperature growth process. Computer simulations have been employed [46]. The energetic particles incident on the surface of the growing film must transfer energy and momentum to the atoms in the film lattice while they slow down. This results in enhanced mobility of the atoms and there is a propensity to fill the microvoids that appear to be an inherent consequence of low T/T_m deposition. Bridging is seen to develop between the columns at high degrees of ion bombardment. Although, ion bombarding appears to be a precious tool, several points should be considered. High-energy bombardment can lead to composition modifications in multi-components-materials due to the difference in sputtering yields. Film atoms may also be resputtered from the film surface altogether (decreasing deposition rate) for high incident particle energy. Chemical reactions between the arriving film particles, the surface, and background gas atoms can alter the composition of the growing film (which can also be deliberate). Finally, for microstructure modifications at low T/T_m by energetic particle bombardment, working gas entrapment can occur. For example, Ar bubbles were observed by TEM in Ag films deposited (at ROBL) with bias voltages of −150 and −250 V (Fig. 1.16) during the studies performed by Almtoft *et al.* [48]. Furthermore, the *in-situ* XRD experimental Ag data show that the rate of grain growth [and the intensity of the (111) Bragg-peak] depends on the bias voltage applied during growth. Significant grain growth, for example, was observed at an annealing temperature of 81°C in a film grown with a bias

voltage of −50 V, while the grain growth in films grown with the higher bias voltages of −150 V and −250 V was significantly reduced. The build-up of Ar atoms, which formed Ar bubbles, is probably dominating the reduction of the grain growth. Some of the Ar bubbles were spread over the interior of the grains, slowing down the recrystallization process, while other decorated the grain boundaries, reducing the grain boundary mobility due to pinning.

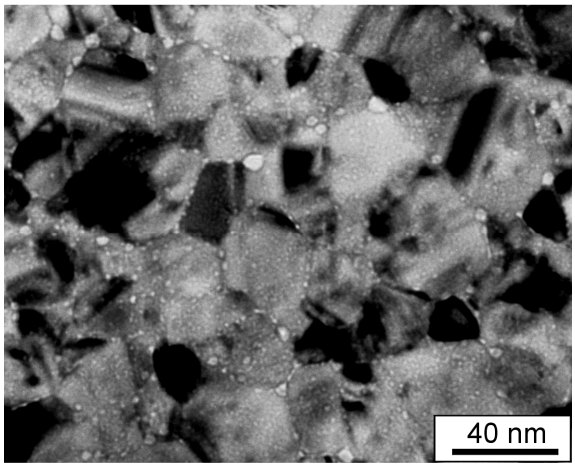

Fig. 1.16: Plan-view, bright-field under-focused TEM image of a Ag film as deposited at −250 V bias showing white Ar bubbles [48].

1.2.4. Stress in the films

In a general way, the stress state of a material is described by the stress tensor, containing the directional stress components of a differential volume:

$$s_{ij} = \begin{pmatrix} s_{11} & s_{12} & s_{13} \\ s_{21} & s_{22} & s_{23} \\ s_{31} & s_{32} & s_{33} \end{pmatrix} \tag{1.3}$$

The normal contributions of the stress in a Cartesian coordinate system is represented by the diagonal elements, and the shear stresses by the off-diagonal elements. A biaxial state of stress is defined by the components:

$$s_{11},\ s_{22},\ s_{12} = s_{21} \text{ and } s_{33} = s_{13} = s_{31} = s_{23} = s_{32} = 0 \tag{1.4}$$

A state of stress can be transformed to be aligned along with the principal directions, where the shear components vanish. The principal stresses are denoted S_i. Since in a film, the lateral dimensions are much larger than the total thickness of film and substrate and as the film thickness is much smaller than the substrate thickness, the state of stress is biaxial and the stress tensor can be written as [49]:

$$S_i = \begin{pmatrix} S_1 & 0 & 0 \\ 0 & S_2 & 0 \\ 0 & 0 & 0 \end{pmatrix} \tag{1.5}$$

where S_1 and S_2 are the principal stresses in the plane of the film and S_3, which is the principal component normal to the plane, is zero (assuming that there are no constraints on the expansion/contraction in this direction). Moreover, in-plane elastic isotropy is assumed in a film so that $S_1 = S_2$.

A strain ϵ that is imposed to the film (e.g. due to the introduction of defects, change of the temperature or a phase transformation) will lead, according to Hooks law, to a stress S that is:

$$S = S_1 = S_2 = Y\,\epsilon \tag{1.6}$$

where Y (biaxial modulus) is given by $Y = E/(1-\nu)$. E and ν are the Young's modulus and the Poisson ratio of the film, respectively. In a film attached to the substrate, a stress in the film will lead to a bending of the substrate and the film. This is schematically shown in Fig. 1.17.

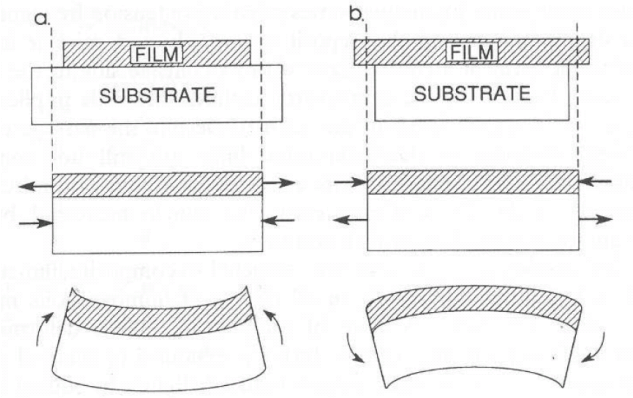

Fig. 1.17: Sequence of events leading to (a) residual tensile stress in the film, (b) residual compressive stress in the film [50]. Bending of a film/substrate compound induced by biaxial stress in the thin film.

Thermal stresses are extrinsic and arise from differences in thermal expansion coefficients of the film (α_f) and the substrate (α_s). When changing the temperature from T_d to T_0, e.g. from deposition temperature to ambient temperature, a thermal stress is produced (in the following σ_{th} is used), given by:

$$\sigma_{th} = \frac{E_f}{1-\nu_f} \times (\alpha_f - \alpha_s)(T_d - T_0) \tag{1.7}$$

E_f and ν_f are the Young's modulus and the Poisson ratio of the film, respectively. The coefficient of thermal expansion for Ni-Ti is $\alpha = 11\times10^{-6}\ K^{-1}$ [51] in the austenitic phase, $\alpha = 6.6\times10^{-6}\ K^{-1}$ [51] in the martensitic phase, and for Si it is $\alpha_{298.2} = (2.59\pm0.05)\times10^{-6}\ K^{-1}$ [52]. Using the elastic modulus and the Poisson ratio given in appendix A ($E_{B2\ phase} \approx 83$ GPa and $\nu = 0.33$), and $\Delta T = 470 - 20 = 450°C$, one can estimate the thermal stress contributions as ≈ 0.47 GPa.

A tensile stress is present in the film when the coefficient of thermal expansion of the film is larger than that of the substrate. This is seen by the concave up shape of the film/substrate system [Fig. 1.17 (a)]. On the contrary, if the substrate has a higher coefficient of thermal expansion, the film/substrate system will experience a compressive stress and be concaved down [Fig. 1.17 (b)]. However, a main part of stress is built in during the film growth, and this is denoted as *intrinsic stress* (not attributed to the thermal stress). The mechanism causing intrinsic stress is not well understood like in the case of thermal stress, because of the complex behaviour of different mechanisms participating during the growth. Although it is often called intrinsic stress, it is not an intrinsic property of the film but is a result of subsequent rearrangement during and after growth. Several mechanisms can contribute for this type of stress in films like annihilation of vacancies, dislocations and grain boundaries, phase transformation, precipitation and compositional and structural changes.

The pressure is considered to be a fundamental parameter in sputtering deposition processes and Hoffman's grain-boundary relaxation model [53] is usually cited for the justification of the observed tensile stress encountered in films deposited without a concurrent bombardment of the surface with energetic species. This model considers that the intrinsic structure of the film contains grain boundaries in which the atoms are less densely packed, exhibiting an atomic separation larger than the equilibrium distance, consequently resulting in a tensile stress. As described before, the energy of the target atoms and the high-energy reflected Ar neutrals are controlled by the pressure in the sputtering system. For a sufficiently high pressure, the flux of atoms and neutrals becomes thermalized which, combined with the flux having an increased oblique part, results in an extremely open *zone I* microstructure that exhibits tensile stress. With a decrease of the pressure, the flux arriving at the film surface is more energetic, originating an increased mobility on the surface and a less open *zone T* structure. In this case, the structure contains a less tensile state of stress and as the deposition pressure decreases more, the stress may become compressive due to recoil implantation of film atoms into volumes that are smaller than their atomic volumes. Since the atoms in the

bulk film have a smaller atomic separation than the equilibrium distance due to this recoil implantation (caused primarily by the neutral Ar bombardment), compressive stress is observed for the sample having a *zone T* microstructure.

In the early 1990's Davis developed a theoretical model for cathodic arc deposition that relates the stress in films with the energy of incident ions [54]. This type of empirical theory reproduces the common experimental observation of a stress level which, with increasing energy, changes from tensile to compressive, reaches a maximum compressive value and with further increase in energy shows a steady decrease.

During the deposition of films by sputtering using unbalanced magnetrons, the plasma extends to the region of the substrate and, consequently, a greater number of ions are directed toward the growing film. When positive bias voltage is applied to the substrate, the energy of bombarding ions decreases. Conversely, when negative bias is applied, ion bombardment energy increases resulting in an enhanced surface-atom mobility. Therefore, a controlled negative substrate bias voltage can be applied in order to reach a lower biaxial stress state.

1.2.5. Texture in films

An important characteristic of the microstructure of poly-crystalline films is their texture (the statistical distribution of grain orientations). For each grain, two degrees of freedom for translation that determine its location on the substrate can be distinguished, and three degrees of freedom for rotations that determine its orientation.

For bulk materials, texture is known to be influenced by cold work, recrystallization and grain growth. For films, preferential orientation usually originates from the formation of the layer (e.g. film deposition or a solid state reaction between a film and a substrate), although texture changes during post-deposition annealing treatments can also occur. Texture is known to influence the mechanical, magnetic and thermoelectrical properties of the films. Therefore, controlling texture is important for many applications.

Although XRD and orientation imaging microscopy are normally used for texture characterization in bulk samples, measurements for films are typically more challenging because of the small grain size (typical of the order of the film thickness) and the limited amount of material usually encountered in these samples. Besides this, films are often reported as exhibiting a pronounced depth dependence of their preferential orientations. Several methods have been introduced in order to determine the texture gradient. The

preparation of a set of samples under identical deposition conditions, but of various thicknesses, followed by the measurement of each sample separately is usually the choice. Nevertheless, it is desirable to monitor the film growth *in situ* to avoid the exposition of the material to external atmospheric contamination. This would allow a direct correlation between processing parameters and film properties as well to determine the most favourable conditions for the growth of high quality films. However, *in-situ* analysis techniques are rare for sputter-deposited films due to probe absorption and scattering by the sputtering gas and plasma environment. Under the operating pressures of sputter-deposition, X-ray radiation seems to be a logical choice to monitor the growth. It is known that photon scattering is relatively small in a gaseous atmosphere, when compared to that of electron beam probes, and photon are not sensitive to magnetic fields or charged particles. XRD with an X-ray tube poses some limitations for real-time investigations due to the measurement times required for serial data collection. Yet, Malhotra *et al* [55] and Lee *et al* [56] have developed sputtering deposition systems to be used into laboratory X-ray diffractometers. They have minimized data acquisition time through the use of optimised detectors. Alternatively, XRD with a synchrotron radiation source has been used since the 1990's for *in-situ* investigations of film growth. Je *et al* [57] have reported a series of real-time synchrotron X-ray measurements to reveal the nature of the growth morphology of TiN films grown by radio frequency (RF). The chamber used during their work had only one magnetron available. Later, Matz *et al* [58] have developed a two-magnetron sputter deposition chamber for *in-situ* observation of film growth by synchrotron radiation scattering at ROBL/ESRF.

Thus, the use of synchrotron radiation allows the *in-situ* monitoring of selected Bragg peaks or even whole diffraction patterns *during* the deposition process and important investigations have been made with this tool in the last few years [48, 59-61].

1.2.5.1. Types of texture

Here, a classification of the type of textures reported for films is given and various terminologies are discussed (random, fibre texture, and biaxial texture).

Random: a homogeneous distribution of the diffracted intensity across pole figures is observed in the case of a random texture, since no restrictions are imposed on grain orientation. It can be expected that, for a sample with a fully random grain orientation, the intensity ratios of the different peaks observed in a $\theta/2\theta$ XRD measurement correspond to ratios found in the powder diffraction database.

Fibre texture: vapour deposited metallic films very often exhibit a strong crystallographic texture. In the case of a typical fibre texture, a particular (hkl) plane is preferentially aligned parallel to the film surface. The direction normal to the surface is generally referred to as the fibre axis. A dominating very intense peak is present at a θ/2θ XRD measurement, result of the diffraction from the lattice plane that is preferentially parallel to the surface of the film and, in pole figure measurements, a spot in the centre of the pole figure is observed [see Fig. 1.18(a)].

In some cases, a variant of the standard fibre texture is found, which is denominated *tilted texture*. The preferred orientation of the crystallites is inclined with respect to the sample surface. It means that the fibre axis is not perfectly perpendicular to the sample surface. In Fig. 1.18(b) it is shown a (200) pole figure for a MgO film, which was deposited without substrate rotation. The direction of the vapour flux is shown by the arrow [62]. The pole figure from Fig. 1.18(c) shows the (200) pole figure for a TiN/TiAlN multilayer coating deposited on WC-Co with substrate rotation [63]. Under such deposition conditions, circles centred near the middle of the pole figures are encountered in pole figure measurements. Due to the fact that the orientation of the grains is only subject to a single constraint, there is a remaining degree of freedom for rotation around the surface normal, leading in the circular region of highly diffracted intensity on the corresponding pole figure.

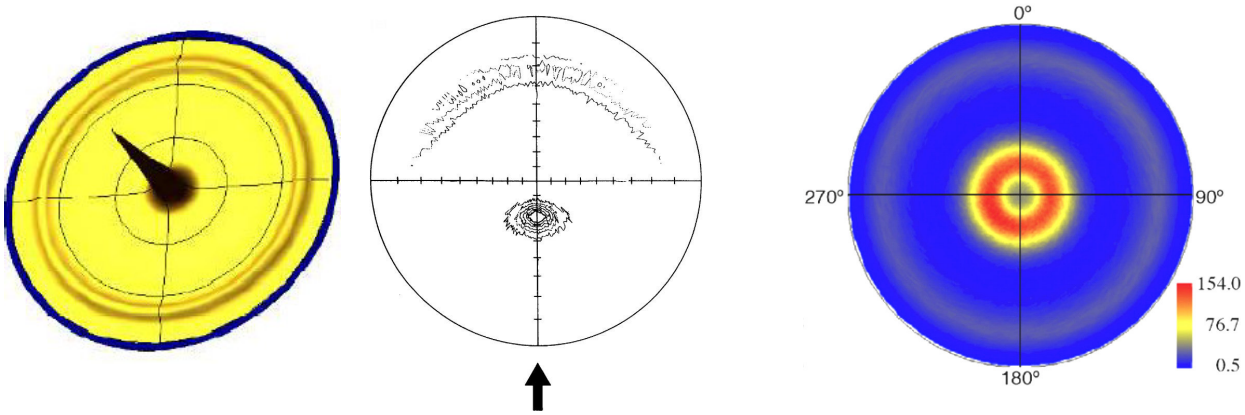

(a) (b) (c)

Fig. 1.18: Pole figures; (a) Permalloy ($Ni_{80}Fe_{20}$) film exhibiting a strong <111> fibre texture [64], (b) (200) pole figure for a MgO film (without substrate rotation - the direction of the vapour flux is shown by the arrow) [62] (c) (200) pole figure for TiN/TiAlN multilayer coating deposited on WC-Co (with substrate rotation) [63].

Biaxial texture, also known as in-plane texture for films deposited onto amorphous or polycrystalline substrates, and epitaxy or epitaxial alignment for films that are deposited or formed onto single crystal substrates. This type of texture is characterized by an orientation of

the grain completely fixed with respect to the substrate (a combination of out-of-plane and in-plane alignment).

1.2.5.2. Driving forces

After the classification of different types of film textures described above, one should consider the reasons why a certain crystallographic orientation is preferred. The selection of a specific texture during film growth and the texture evolution during heat treatments is very often explained by thermodynamic arguments. The predominance of a certain crystallographic orientation is commonly attributed to a smaller surface energy, strain energy and/or interface energy, leading to an energetic advantage of a preferred orientation. It is often mentioned that this growth preference may be related to the thermodynamic preference of deposited atoms to condense on low, instead of on high-energy surfaces in order to minimize the surface energy. This statement is consistent with the observations that the typically observed out-of-plane orientations correspond to the lowest-energy surfaces. Although these thermodynamic models appear to have success, it should be noted that growth kinetics might also play an important role (e.g. growth anisotropy or secondary nucleation during solid-state reactions, resputtering and shadowing effects during film deposition [65]). Growth velocity anisotropies can as well lead to competition of grains at the surface of the thickening film and a *through-thickness evolution* of the in-plane grain size and the average crystallographic texture of the grains at the surface. The model proposed by Van der Drift [66], is frequently used to explain the formation of fibre texture. According to the model, this type of texture results from the difference in growth rates between different crystal faces of the grains at the surface of the film. The vertical growth rates of the crystals depend on their orientations and selection takes place because of the differences of the growth rates. This process was named evolutionary selection and is considered to be the cause for the increase of the orientation sharpness during vertical growth. In the case of vapour-deposited layers, the bigger the vertical growth rate of the individual crystals, the greater the probability of survival. Therefore only a few favoured orientations (with nearly maximum vertical growth rate) will be left over at the end, all other orientations gradually dying out. Figure 1.19 shows the case of a two-dimensional space (on the page) in which one-dimensional crystals grow on a one-dimensional substrate. It is assumed that the vertical growth rate is bigger the steeper the orientation. *If two crystals meet, the less steep one ends in the flank of the steeper one leading to the survival of the fastest* [66]. Although things are a bit more complicated in a real layer, the principle is valid.

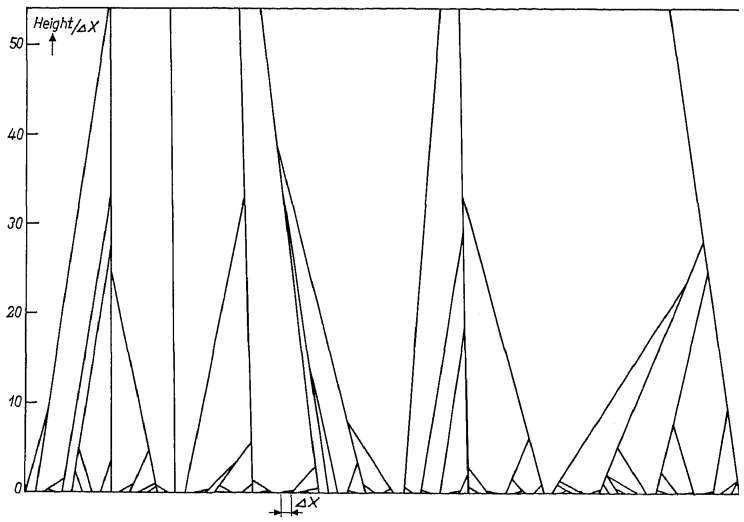

Fig. 1.19: Evolutionary selection during growth starting from randomly orientated equidistant nuclei on a one-dimensional substrate (bottom line) in a two-dimensional space. The height above the substrate is expressed in the unit Δx, the distance between two nuclei. The assumption is that the vertical component of the growth rate is larger at steeper orientations of the crystal [66].

1.2.5.3. Examples of texture selection on amorphous or polycrystalline substrates

As mentioned before, a qualitative explanation for fibre texture is recurrently based on the surface energy arguments. For example, in the case of fcc metals on amorphous substrates, surface and interface energies appear to be minimized for grains with (111) texture, whereas strain energies are minimized for grain with (100) texture. Zhang *et al.* [67] have calculated the surfaces energies for 38 surfaces of fcc metals Cu, Ag, Au, Ni, Pd, Pt, Al, Pb, Rh and Ir by using the modified embedded-atom method. The results show that, for all the fcc metals, the close-packed (111) surface has the lowest surface energy. There is a linear increase of the surface energies with increasing angle between the surface (hkl) and (111) for the other surfaces. In the case of the bcc metals Li, Na, K, V, Nb, Ta, Cr, Mo, W and Fe, the surface energies for 24 surfaces have also been calculated [68]. The results show that for most bcc metals the lowest surface energy corresponds to the (110) surface, as predicted from the bcc lattice, and the highest surface energies correspond to the (433) surface. As expected from surface energy minimization, the (110) texture should thus be favoured in bcc films.

Efforts have also been carried out to obtain more detailed models in order to explain the development of (out-of-plane) fibre textures during deposition of films onto amorphous substrates by taking in consideration not only the differences in surfaces energies, but also anisotropy in crystallographic growth rates, preferential (re)sputtering and shadowing effects [65].

In the present study, the effect of a TiN buffer layer deposited on top of the SiO_2/Si(100) substrate prior to the deposition of the Ni-Ti films was among other influences on texture analysed. The TiN intermediate layer acts not only as a diffusion barrier but also induces different crystallographic orientations on the Ni-Ti film deposited on top, which depends on the preferential orientation of the topmost TiN layer. Due to the importance of the TiN material to the present study a short literature review concerning texture development on this type of films is presented.

For TiN films the most often reported orientations are <100> and <111> fibre textures. Since TiN has anisotropic mechanical properties, a change in preferred orientation may improve its coating performance even further. E.g., (111) oriented TiN shows the largest wear resistance [69]. Therefore, a great deal of interest has been put into describing and controlling the preferred orientation of sputter-deposited nitride films. Despite extensive research, however, reported results are scattered and sometimes even conflicting due to the large variety of deposition parameters such as substrate temperature [70-72], energy and flux of bombarding particles [73-75], bias voltage [76-78], magnetron power [71, 79], partial pressure [70, 79] and species of the sputtering gas [80-81].

In order to generalize experimental results, Pelleg *et al.* [70] developed a thermodynamic model to describe the preferred orientation in TiN. It is based on the frequently observed ‘‘orientational cross-over’’, i.e. a change in crystallographic texture with thickness. TiN growth sets in with random nucleation followed by an intermediate layer with a <100> fibre texture, which, starting at a thickness of ≈ 100 nm, gradually evolves into a (111) orientation. Pelleg *et al*. attributed this behaviour to a competition between surface and strain energy as follows. Strain/stress in films arises by ion peening during film growth, leading to trapping of gas ions and defect incorporation. At low thicknesses this stress can be neglected. The growth, therefore, is determined by the surface energy and a preferred orientation of the low surface energy (100) planes [82] is to be expected. At higher thicknesses the stress contribution dominates, and since the film seeks to minimize it’s overall energy, the growth of low strain energy planes is preferred, which is the (111) orientation in the TiN case [83-84]. Although this model explains the observed cross-over, it is still subject to controversy. Other effects, like recrystallization [85] or mechanisms of kinetic nature like competitive grain growth are likely to take place and to compete with the thermodynamic effects described above.

In a series of publications [73-75] collaborating research groups demonstrated that low energy ion-irradiation during magnetron sputtering of TiN films can change their preferred

orientation. They highlighted that a (111) orientation does not require the presence of strain and does not result from changes in strain state with increasing film thickness. The experimental results were supported by *ab-initio* calculations and *in-situ* high temperature Scanning Tunneling Microscopy [86-88]. It was shown that for ion-irradiation at a low energy of 20 *e*V, preferred orientation develops by a competitive growth between (100) and (111) based on adatom mobilities, and, therefore, *rather by kinetics than by thermodynamics*.

Beckers *et al.* [59] have presented XRD data of $Ti_{1-x}Al_xN$ films with low Al concentration taken with synchrotron radiation at ROBL *during* the growth process in vacuum. In this way it was possible to study in *real-time* the development of microstructure and preferred orientation of these films *in situ* in dependence of the film thickness under changing parameters like substrate temperature, growth rate and substrate bias voltage. The results confirm and extend the kinetic model mentioned above. For high deposition rates the cross-over from initial (100) to final (111) preferred orientation is observed, which has often been reported for TiN. Decreasing the deposition rate by increasing the N_2 partial pressure leads to a denser film with an almost complete (100) preferential orientation, nearly independent of substrate temperature and Al concentration (see Fig. 1.20). This change in preferential orientation is not accompanied by a significant change in film microstructure, and it does not originate from different stress states. The results are interpreted by a competitive growth process in which the (100) orientation is promoted by atomic nitrogen that is delivered mainly by molecular nitrogen ions from the plasma.

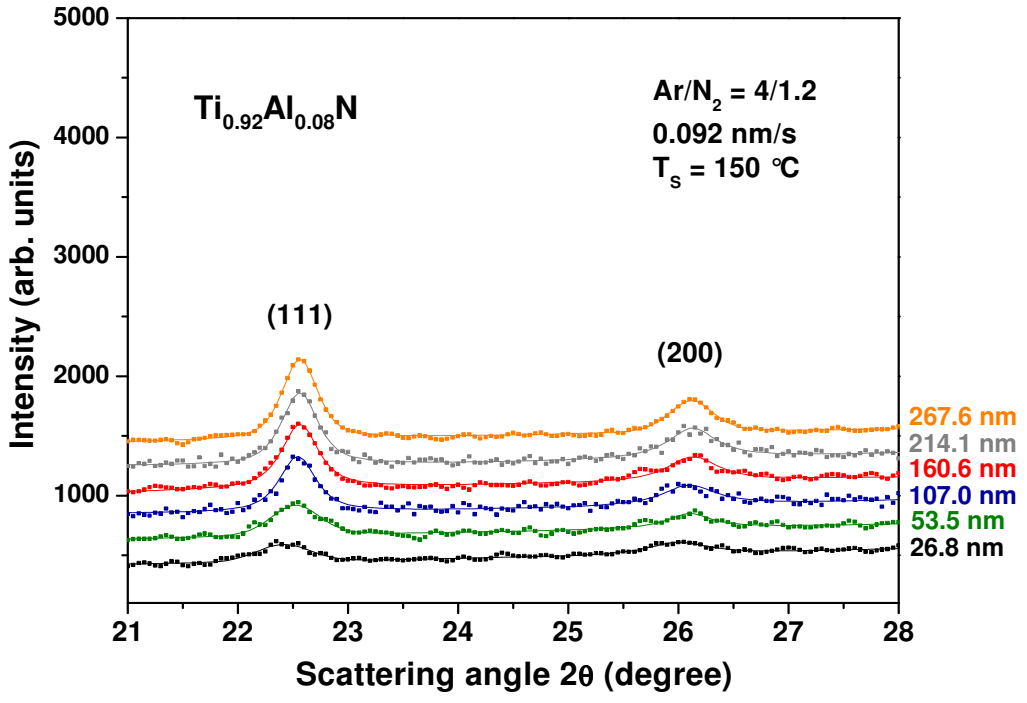

(a)

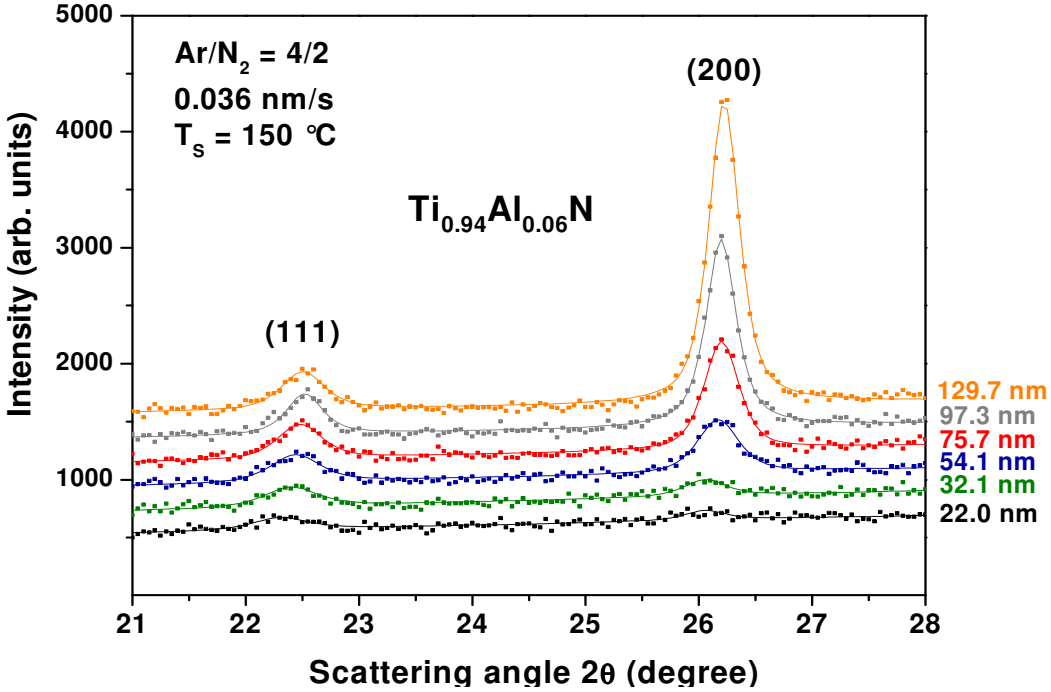

(b)

Fig. 1.20: Thickness dependent *in-situ* XRD spectra of $Ti_{1-x}Al_xN$ samples deposited at different growth rates; (a) 0.092 nm/s, (b) 0.036 nm/s. A lower growth rate favours (100) preferred orientation [59].

In the case of *tilted textures* in TiAlN coatings, Falub *et al.* [63] explained the phenomenon by the evolutionary selection model of van der Drift. Using some assumptions concerning the sticking factor of the landing molecules as a function of the crystal orientation and some extreme cases (e.g. zero, infinite) of the surface diffusion, the model of van der Drift can predict that the fastest vertical growth (and hence the fibre texture) occurs at an angle that is related to the angle of incidence on the substrate. However, these authors also consider that other mechanisms could also play a role in determining the fibre texture. For instance, applied bias voltage influences the surface mobility of adsorbed atoms and, due to this, a different texture can be formed. Due to the variable incidence angle of the incoming ions during deposition, the change of the sputtering yield between aligned and misaligned grains may also influence the fibre texture. A tilted texture in TiAlN deposited by UHV dual-target magnetron sputtering was also found by Wahlström *et al.* [89]. This preferred orientation was explained by the oblique paths between the substrate and the Ti/Al targets.

In their work, Falub *et al.* [63] concluded that it is still unresolved whether it is the stress that influences the texture, or inversely the texture developing the stress. They have observed that fibre texture can be influenced by geometry of the deposition and some additional deposition parameters and, thus, texture may influence the stress as different crystallographic directions have distinct elastic constants. However, the strain energy in the

films can be controlled via enhancement / reduction of the intrinsic stress through ion bombardment, controlling in this way the fibre texture in the film.

1.2.5.4. Examples of texture selection on single crystal substrates

The study of interfaces is very important for different types of applications. For example, metal/ceramic interfaces are important in magnetic storage media and supported catalysts. It is fundamental to understand how the crystallography and microstructure of metallic films deposited onto ceramic substrates depend on growth and/or annealing conditions so that their physical properties can be tailored for specific applications. The production of epitaxial single-crystal films has attracted considerable attention. For the deposition of magnetic films, MgO substrates are very often chosen.

It is usually supposed that the main factor in determining the occurrence of epitaxial alignment on single crystal substrates is the interface energy; even though surface energy and strain energy may also play a role. Through the optimisation of the bonding across the interface, a minimization of the interface energy is achieved. This phenomenon can take place by interface reconstruction, whereby the atoms in the first few atomic layers close to the interface are re-arranged, similar to surface reconstruction at the crystal/vacuum interface. The bonding can only be optimised in a methodical way across the entire area of the interface if the interface structure is periodic, considering both the grain and the substrate to have periodic crystal structures. This way, the theory of periodicity in the plane of the interface may as a result be used as a guiding principle for studying "matching" interfaces. It should be mentioned that for epitaxial alignment, a certain fixed (hkl) plane is preferentially parallel to the surface of the film.

To accomplish a more detailed understanding of the processes governing the growth, i.e. nucleation and subsequent coalescence of islands, some techniques have been developed. These methods can be used to obtain information on film thickness or surface roughness. Nevertheless, not all techniques allow to measure the surface morphology during vacuum deposition in real-time. Ellipsometry is a nondestructive method and can be used for real-time measurements. However, its accuracy depends on the optical parameters used to interpret the data, which are strongly dependent on the morphology of the film. Reflection high-energy electron diffraction (RHEED) can be used to observe changes in the surface morphology during growth on an atomic scale [90]. Oscillations in the electron reflectivity are studied and from the period and shape of these oscillations (as a function of film thickness), information

on the growth mode of the developing film can be derived. Quantitative treatment of the RHEED oscillations is difficult due to the large scattering cross-sections between electrons and atoms, which lead to multiple-scattering effects. Unlike RHEED, XRR is characterized by single scattering of the materials, which simplifies the analysis of the acquired data. Usually, XRR is measured as a function of the scattering vector, either by varying the scattering angle (angular resolved) or the wavelength (energy-dispersive mode). Lee *et al* [91] have reported a novel set-up for measuring the surface roughness of the film with the detector positioned at a fixed 2θ angle and the sample fixed at θ angle during film growth. Intensity oscillations could be observed as a function of deposition time. The oscillation amplitude is damped as the film thickness increases indicating that the surface roughness of the film increases. Thus, the study of crystal growth using surface sensitive X-ray scattering techniques with high-brilliance X-ray beams can lead to important achievements in the investigation of growing interfaces/surfaces at an atomic scale. Using harder X-rays, the geometry of the low incident angle is improved for *in-situ* observation and a thicker film can be studied due to the greater penetration of hard X-rays.

The evolution of the intensity oscillations with time during hetero-epitaxial growth can be used to determine the growth mode of the growing film. When the film grows layer-by-layer, the intensity oscillates over time. A hint that the surface becomes rough, i.e., three-dimensional (3D) islands form, comes by a drop of the intensity. Bøttiger *et al.* [92] presented one of the first studies on the direct observation of the growth mode during heteroepitaxial growth of TiN on MgO(100) substrates. Real-time specular XRR measurements using synchrotron radiation were used during reactive magnetron sputtering, obtaining intensity oscillations as a function of time. The results revealed that TiN grew in a layer-by-layer mode and the surface became rougher faster during growth at lower temperatures. In a recent work [93], the first *in-situ* studies of the growth of Ti_2AlN by real-time specular XRR have been performed at ROBL. The films were epitaxially grown onto single MgO(111) and MgO(100) substrates by DC reactive magnetron co-sputtering from Al and Ti targets in an Ar/N_2 gas mixture at 690°C. A fcc $(Ti_{0.63}Al_{0.37})N$ seed layer was deposited to promote the nucleation of Ti_2AlN on top of it. It was observed that the seed layer shows no roughening until its final thickness of approximately 10 nm, independent of substrate orientation, indicating pseudomorphic layer-by-layer growth (Fig. 1.21). The Ti_2AlN film shows heteroepitaxial layer-by-layer growth on MgO(111), with increased surface roughening up to approximately 20 nm, whereas on MgO(100) the growth mode changes to Volmer-Weber-type already after three monolayers.

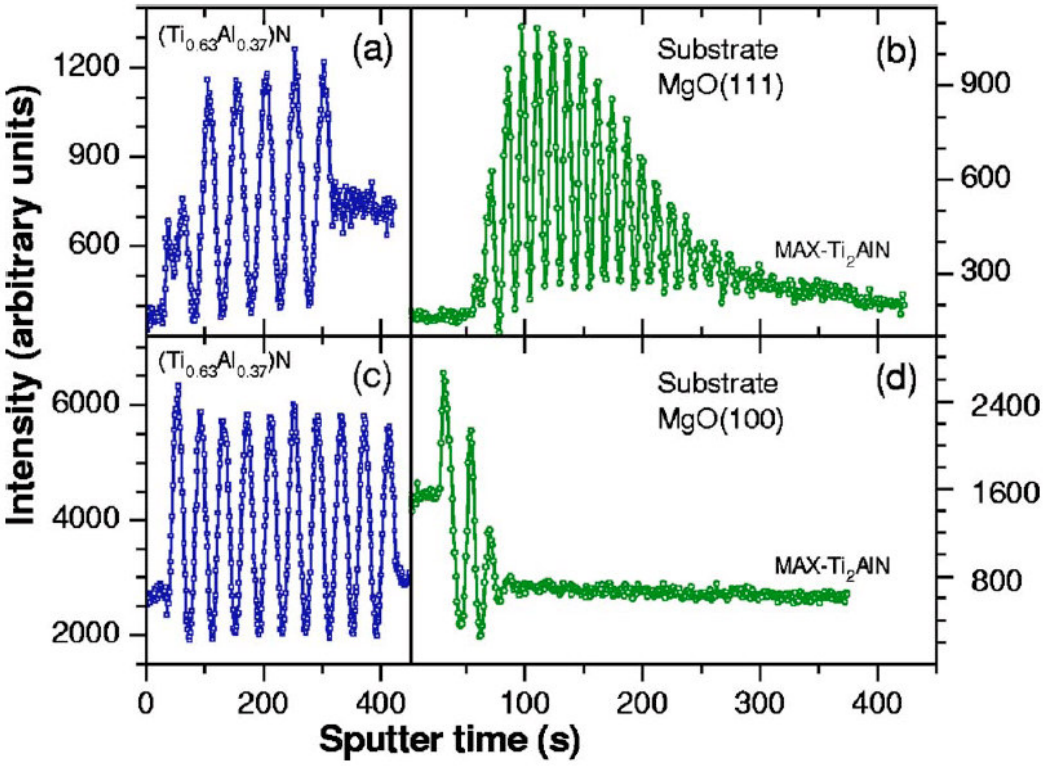

Fig. 1.21: Time-dependent *in-situ* specular X-ray reflectivity of fcc $(Ti_{0.63}Al_{0.37})N$ seed layers [(a) and (c)] and *MAX* phase Ti_2AlN [(b) and (d)] on substrates MgO(111) [(a) and (b)] and MgO(100) [(c) and (d)]. The incidence and scattering angles were fixed at $\theta/2\theta$ = 1.8° / 3.6° [(a) and (b)] and θ / 2θ=2.1° / 4.2° [(c) and (d)]. The oscillatory behaviour for the deposited seed layers as well as the Ti_2AlN films on top are a fingerprint of *layer-by-layer* growth. The decreasing amplitudes of those oscillations reveal increasing roughness or island growth, which is more pronounced for the Ti_2AlN film on MgO(100) (d) [93].

1.3. SPUTTER DEPOSITION AND MICROSTRUCTURAL DETAILS OF Ni-Ti FILMS

In the nineties several papers appeared on Ni-Ti films obtained by sputter deposition. A first work on shape memory films integrated with the Si micromachining process was presented in 1990 by Walker *et al.* [94]. Busch *et al.* [95] in the same year focused on the shape memory properties of Ni-Ti sputtered deposited films. They have obtained amorphous films (confirmed by XRD) and the as-deposited films did not exhibit the SME. After crystallization, however, the films showed transformation temperatures much lower than the target material. In later work the group has presented great advances in the field [96]. In 1990, Jardine *et al.* [97] also presented their work on the preparation of Ni-Ti films and posterior publications have made clear that their early difficulties were overcome [98, 99].

Ni-Ti films are quite sensitive to diverse process conditions like target power, gas pressure, distance target/substrate, deposition temperature, substrate bias voltage as well as contamination, thermo-mechanical treatments, annealing and aging processes *etc*. Although a dependence on all those features appears to be a disadvantage, this phenomenon can also be useful in order to manipulate the properties of the films in an intentional way for different applications. Nevertheless, it is necessary, at first, to reach the optimal deposition parameters. The first difficulties in film processing arrived from porosity, oxygen contamination, and composition deviation [9].

The composition and structure of the films are drastically affected by the sputtering conditions. A high gas pressure results in a porous columnar structure leading to brittleness. The incorporation of oxygen also originates the brittleness and, due to Ti-rich oxide formation, leads to a shift in composition. A high-vacuum-system is thus required. The precise control of the Ti:Ni ratio is essential but difficult due to the difference in sputtering yields of Ti and Ni at a given sputtering power density [100], as well as wear, erosion and roughening of the targets during sputtering [101]. Several solutions were proposed to overcome this problem: adding Ti plates on the Ni-Ti target to compensate the loss of Ti [23], co-sputtering from Ni-Ti and Ti targets [101] or from two separate single element (Ni and Ti) targets [102, 103], as well as varying the Ni-Ti target temperature since a heated target reduces the loss of Ti [104].

If the substrate is not heated during sputtering deposition, as-sputtered Ni-Ti films are amorphous [26], [105-107] requiring a post-sputtering annealing, since the thermally induced phase transformation occurs only in crystalline materials. On the other hand, films sputtered at elevated temperatures (typically above 400°C) are crystalline as deposited. In that case, and depending on the substrate type, specific fibre textures can be obtained [108] and fine-grained structures are also observed [109].

Several considerations about these and other topics will be presented in the following subsections. Despite several methods proposed to resolve some of the processing difficulties, the deposition of Ni-Ti films with definite stoichiometry and high purity remains a challenge [110]. Furthermore, it is clear by the published works that important issues like formation of film texture and its control are still unresolved [10].

1.3.1. Composition control

In sputtering deposition, if a Ni-Ti alloy target is used, the compositions of the sputtered films are Ni-richer when compared to the composition of the target. A shift of 2–4 at.% occurs which can lead to a reduction of the transformation temperatures by more than 100°C. This phenomenon is normally attributed to the higher sputtering yield of Ni, differences in angular flux distributions, and lateral diffusion of sputtered species due to the collision with Ar gas atoms [9]. The Ti losses can also occur due to easy oxidation of Ti but if a UHV environment is used the concern for oxidation effects is eliminated leaving the angular distribution as the main factor.

An initial sputtering of the Ni-Ti target with the substrates masked by the shutter (pre-sputtering) must be performed to enable the adjustment of the deposition parameters and stabilization of the discharge, to suppress contaminants from the target's surface and to reduce the partial pressure of oxygen in the chamber (due to the getter effect of Ti).

The ratio of the number of atoms ejected from the target to the number of incident bombarding particles is commonly denominated by sputter yield. The sputter yields of the constituents of an alloy target are usually different leading to a higher presence of one of the elements in the deposited film. The element with the higher sputter yield will sputter at a higher rate leaving a larger area on the target surface enriched with the element of the lower sputter yield. Theory predicts that after the target has reached a steady state, the film will finally reach the original composition of the target. In the case of an equiatomic Ni-Ti target, initially a Ni-rich film will form as Ti has a greater sputter resistance relative to Ni, thus leading to a gradient film composition.

Additionally, the film composition is also affected by the distance target/substrate and pressure in the sputtering system. In previous research [111], the variation of the gas pressure has been used to adjust the composition ratio. However, this is not the best solution because sputtering at a high pressure can result in a porous structure and, as a consequence, in film brittleness. Bendahan *et al.* [111] have shown that they were able to control *in situ* the composition of RF sputtered Ni_xTi_{1-x} ($0.476 < x < 0.531$) films, so that the SME is shown above RT by varying the product of sputtering gas *p* and distance target/substrate *h*. Their pressure measurements gave a good sensitivity for the control of Ti-rich films and in the case of Ni-rich films a better sensitivity was achieved with optical emission spectroscopy of the sputtering plasma. Another important conclusion of this study is that the peak intensity ratio

of the optical emission spectra does not depend on the *substrate* and the *Ar flow rate*. They have not seen any difference in the composition of the samples by varying these two parameters. The optical emission results have shown that the peak intensity ratio I_{Ni}:I_{Ti} decreases when increasing $p \bullet h$ (Fig. 1.22). Equivalence between the chemical composition and the peak intensity ratio was also found.

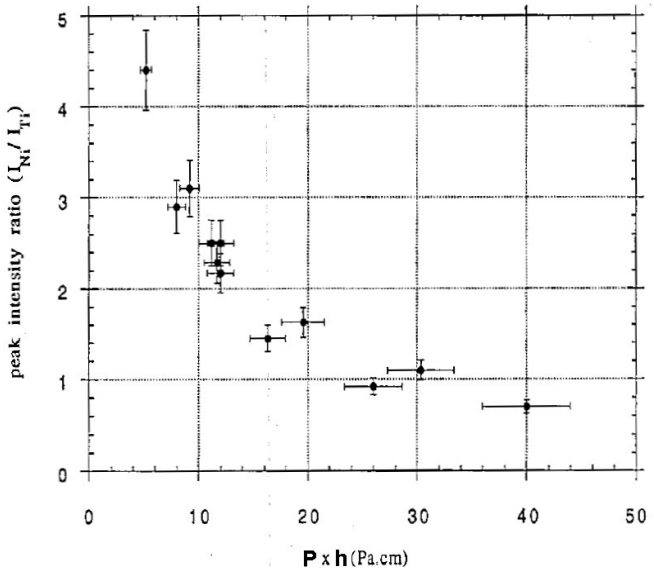

Fig. 1.22: Ratio of the optical emission intensity of Ni to Ti *versus* the product of pressure and distance target/substrate [111].

These results suggest that for the same experimental conditions, Ni atoms are thermalized at a smaller distance than Ti atoms. In the high $p \bullet h$ regime the Ni atoms have a higher probability for not being deposited on the substrate since they leave the target with a lower energy than Ti atoms and are thus more rapidly thermalized [111].

Optical emission spectroscopy of the sputtering plasma was tested at CEFITEC during the MSc thesis work of R.M.S. Martins [25] and follow-up work has shown the benefit of this technique [112].

A common and simple way to solve the problem of the shift in film composition is to add pieces of pure Ti (or Ni) onto the target alloy in order to achieve the correct film stoichiometry [23]. However, this method is not possible for controlling the composition of the film *during* the deposition process. There are also several drawbacks with this method to reach a flexible composition adjustment with high repeatability, like controlling the number, size, position and geometry of the additional plates (or meshes). Nevertheless, the reproducibility of the results using this procedure has proven to be acceptable for laboratory production. Surbled *et al.* [113] have used a Ti mesh (diameter = 40 mm, wire diameter = 0.5 mm) covering 35% of the target (100 mm) in order to obtain Ti-rich films. They also

reported that the films facing the target are poor in Ti for a low $p \cdot h$. An enrichment in Ti was obtained for the films deposited on substrates placed away from the target, i.e., with an offset between centres of the Ni-Ti target and the substrate. They not only attributed the stronger concentration of Ti on the substrates far from the target to the thermalization of Ni atoms but also referred a larger angular distribution for Ti and mentioned that Ni is sputtered closer to the surface normal. One explanation for this difference in the ejection angle between the elements can be the existence of a concentration gradient in the near surface of the target. Due to the fact that recoiling atoms have randomly oriented momenta, the atoms of the surface of the target, which is richer in Ti, are ejected in many directions. This phenomenon involves a wider angular distribution compared to the atoms from the deeper layers richer in Ni.

Ho *et al.* [104] presented a novel method for depositing Ni-Ti films by sputtering with transformation temperatures very close to the target without requiring compositional modification of the Ni-Ti alloy target. The compositional modification could be produced by varying the target temperature. Depositions with hot targets (poor thermal contact between the target and the copper chill block, which led to temperatures above 600°C) resulted in compositions similar to the target while "cold" targets (225°C) lead to Ti deficiency. These researchers studied the angular sputtering profile of Ni-Ti using substrates attached in a semicircular arc, 60 mm from the centre of the target and 18° apart [100]. The composition of the films produced with cooled target varies as a function of the polar angle, showing that more Ti is ejected at higher angles from the target normal. The increase of the target temperature resulted in a less severe composition dependence on the angle (Fig. 1.23). An explanation hypothesized by the authors is a possible difference in the composition of the target top altered layer in the cooled and hot targets resulting from diffusion processes or a reduction in the binding energy.

However, they conclude that the increase in Ti for films sputtered with hot targets was due to an increase in the sticking coefficient at the substrate relative to Ni. This suggestion was advanced after concluding that the net atomic flux of Ti *versus* Ni being sputtered remains equivalent to the ratio in the target, whether or not the target is heated.

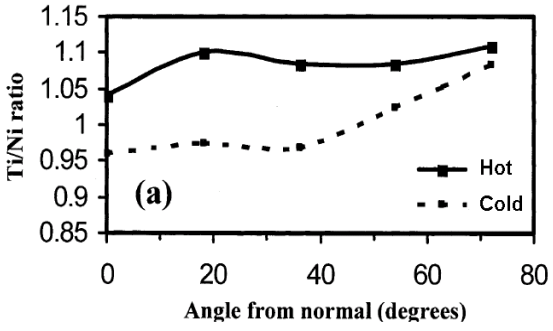

Fig. 1.23: RBS results of composition *versus* sputtering angle (using a hot and a "cold" target) [100].

Apart from the methods cited above, it has been successfully demonstrated that co-sputtering could be used to deposit equiatomic Ni-Ti films. Ohta *et al.* [102] (RF magnetron sputtering) and later, Sanjabi *et al.* [114] (DC magnetron sputtering), produced films by simultaneous sputter deposition from separate elemental Ni and Ti targets. By adjusting the power to each target the desired composition could be obtained. The use of Ni-Ti and Ti targets for co-sputtering rather than Ti and Ni elemental targets has been preferred by Shih *et al.* [101]. They have observed that additionally to the development of circular grooves on the flat metallic targets in DC magnetrons, roughening of the surface of the targets also takes place during service, which is more marked for Ni than for Ti (Fig. 1.24). Since the evolution of surface morphology could vary the vapour flux of metal atoms contributed by each target at a constant power during use, they have preferred Ni-Ti and Ti targets for co-sputtering rather than Ti and Ni elemental targets (the relative change in vapour flux at constant target power is larger for Ni than for either Ti or Ni-Ti.).

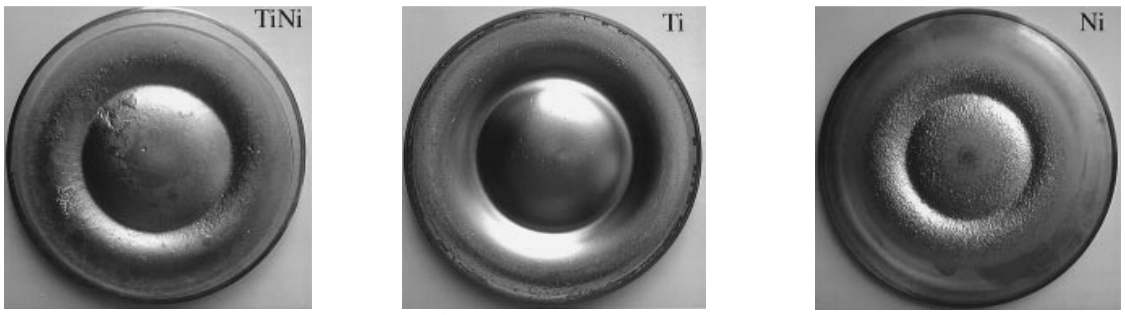

Fig. 1.24: Grooves present in used sputtering targets; (a) Ni-Ti, (b) Ti, (c) Ni [101].

This subsection has been focusing on the importance and difficulties of the control of film composition. The deviation of film composition from the target and its variation both in the plane and across the thickness are identified inconveniences. The martensitic transformation temperature can be largely affected by a small shift of film composition. Nevertheless, future directions include the production of functionally graded films by changing deliberately the Ti:Ni ratio across their thickness. The main goal is the fabrication of films with a two-way reversible actuation (films with a combination of superelasticity and shape memory characteristics [10]). However, for the successful development of this type of graded films, it is important to characterize, model and control the variations in composition, crystalline structure and transformation temperatures. The growth process is a highly complex phenomenon controlled by many parameters requiring the application of several experimental tools to understand the physical processes occurring during deposition.

Despite this difficulty, Gill *et al.* [22] have manufactured microwrappers and have demonstrated that the curvature in a microwrapper arms could be induced using either a bi-layer material (i.e. polyimide and Ni-Ti) or a functionally graded Ni-Ti film through the thickness (Fig. 1.25). When the temperature approaches A_f, the arms of the microwrapper flatten to open up. When it cools, the arms curl up to form the cage-like structures.

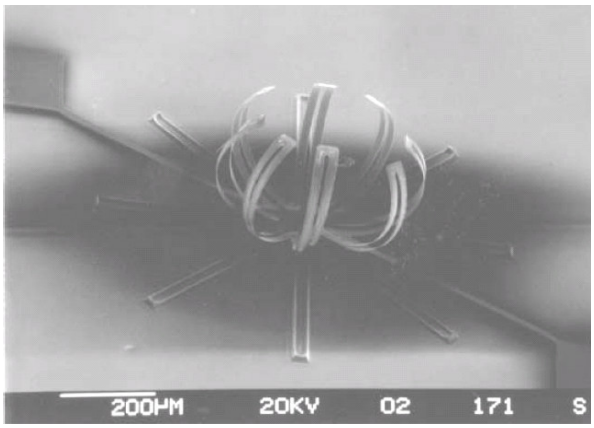

Fig. 1.25: Photograph of a microwrapper fabricated using a Ni-Ti graded film [22].

The returning process to the cage-shaped configuration requires residual stress using a bias spring mechanism (polyimide) or a shape memory material exhibiting the *two-way* SME (Ni-Ti graded film).

Figure 1.26 illustrates the functional grading through the thickness of the film used in the fabrication of the microwrapper. The Rutherford Back Scattering (RBS) results presented in Fig. 1.26(a) were obtained for the first ≈ 600 nm Ni-Ti layer deposited onto the Si substrate. The Ni-Ti layer adjacent to the substrate is Ni-rich (it is known that Ni-rich Ni-Ti films can exhibit the SE phenomenon). The enrichment in Ni decreases the transformation temperature and, even at RT, the Ni-rich Ni-Ti film is in the austenite phase and subsequently thought to be superelastic. The RBS measurements carried out on the Ni-Ti layer (≈ 800 nm thick) obtained on top of the Ni-rich Ni-Ti layer demonstrate that it has a near equiatomic composition Fig. 1.26(b).

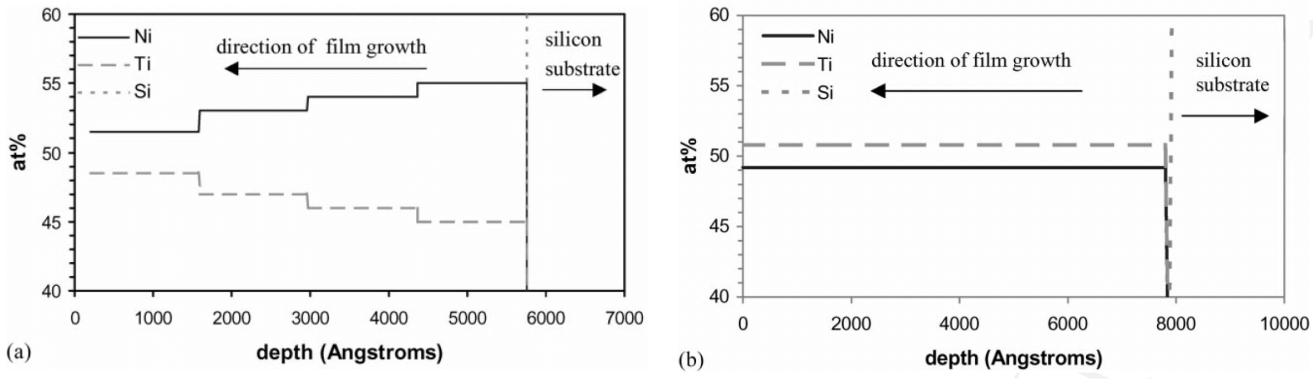

Fig. 1.26: RBS measurements; (a) initial 600 nm thick Ni-Ti layer deposited on the Si substrate, (b) Ni-Ti layer deposited on the Ni-rich Ni-Ti layer (*Y*-axis: atomic composition of Ni and Ti, *X*-axis: thickness of Ni-Ti layer) [22].

The combination of different phase transformation temperatures, i.e. different compositions, along the Ni-Ti membrane thickness appears to be an efficient tool to create the mechanism inducing the *two-way* SME. This compositional difference between the top and bottom Ni-Ti fractions serves as a functionally graded bimorph inducing a curvature in the microwrapper arm. In order to determine the existence of a possible effect of tensile stresses, together with the material grading properties, on the induction of the *two-way* SME, Gill *et al.* [22] performed a complementary experiment. They shielded the Si substrate during the first 5 min of the Ni-Ti deposition and thus, when the shutter is open (after 5 min) only the near equiatomic composition is obtained (the deposition rate is 220 nm/min). It has been observed that the film deposited without a Ni-rich fraction does not exhibit the *two-way* SME. They have concluded that the Ni-rich superelastic layer is the dominant mechanism originating the *two-way* SME. The microwrapper fabricated based on the functionally graded Ni-Ti film represents a significant improvement over the one with double layers of polyimide and Ni-Ti due to the absence of discrete property changes and thus the larger inclination to failure.

1.3.2. Heat treatments

In this work the chosen deposition conditions allowed to obtain films fully crystallized at the end of the deposition (substrate temperature ≈ 470°C). When the substrate is not heated during deposition, as-sputtered films are amorphous. These films need a post-deposition heat treatment in order to crystallize and be able to exhibit a thermally induced phase transformation. This was not the case in the present work. During the last years different techniques such as XRD, Differential Scanning Calorimetry (DSC), *in-situ* TEM have been used to examine the initial crystallization of these films, the development of the microstructure from the amorphous phase and their link to transformation properties. Although post-deposition heat treatments were not required in the present study to crystallize the films, a review of a few works focusing the subject is presented in this subsection in order to show a link between the transformation temperatures, microstructure, composition, and the development of precipitates. In the last part of this subsection there is an introduction to depositions on *heated substrates*.

A standard method for Ni-Ti film production is sputtering deposition onto *an unheated substrate*. The as-deposited films are amorphous and the SME does not occur. Therefore, a proper thermal annealing process is necessary in order to crystallize the films and obtain the desired microstructure and shape memory behaviour. During the annealing process the film is

heated above its crystallization temperature allowing the amorphous film to crystallize. The films can also be aged for an extended period of time below the crystallization temperature for grain and precipitation development. Understanding the interplay between nucleation and growth processes during the crystallization step is fundamental to determine the final microstructure. As observed in Fig. 1.2, the phase diagram of Ni-Ti has a very narrow intermetallic region and a small deviation in composition can change drastically the mode of crystallization and result in a different microstructure. It is known that there is a link between martensitic phase transformation and the microstructure. Since the actuation properties of Ni-Ti films are based on their crystallographic phase changes, the study of the crystallization behaviour of these materials is a great benefit for the development of devices based on them.

Chen and Ting [105, 115] performed a detailed study to investigate the effect of pressure, electrode distance, and sputter power (DC) on the composition of films deposited on Si(100) and Corning glass substrates. The as-deposited Ni-Ti films exhibited an amorphous structure, which crystallized upon heat treatment at 550 or 600°C. The deposition rates and the composition of the films were examined and a dependence of the deposition rate as well as of the composition on the deposition pressure was determined. The deposition rate was found to decrease with pressure. However, it has been observed that the dependence of the deposition rate on pressure is linear at an electrode distance of 90 mm but non-linear at an electrode distance of 50 mm. Ti content increases with increasing pressure and a higher increase is detected for lower pressures than for higher pressures. The other objective of their study was to investigate the crystallization behaviour of the films, in particular the activation energies of Ni-Ti films with 4 different compositions near $Ni_{50}Ti_{50}$ ($Ni_{49.41}Ti_{50.59}$, $Ni_{49.86}Ti_{50.14}$, $Ni_{49.98}Ti_{50.02}$, and $Ni_{50.32}Ti_{49.68}$) using the Kissinger method. It was found that the crystallization temperature increases with pressure for the same heating rate (Fig. 1.27).

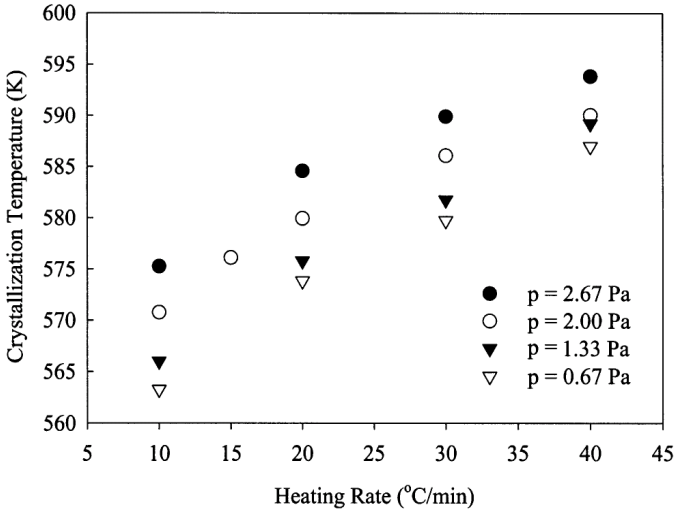

Fig. 1.27: The crystallization temperature of the Ni-Ti films increases with Ar working pressure for the same heating rate [115].

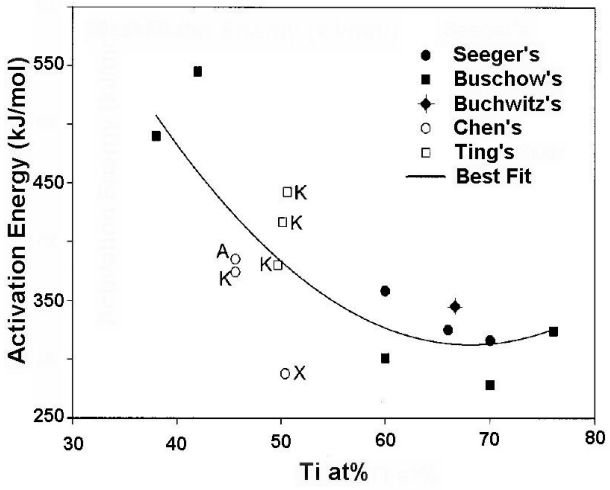

Fig. 1.28: Comparison of activation energies: open symbols are data from Ni-Ti films and closed symbols from bulk Ni-Ti (K: Kissinger's method, A: Avrami's method, and X: X-ray method) [105].

Calculations of the activation energies for crystallization of the different samples result in the following values: 380.1, 401.33, 416.6 and 442.1 kJ/mol for Ni-Ti films obtained at 0.67 Pa, 1.33 Pa, 2.00 Pa, and 2.67 Pa, respectively. Thus, a linear increase of the activation energy with pressure is observed. They believe that a lower pressure favours a lower activation energy due to the initial presence of higher compressive stress, smaller nuclei, and higher defect concentrations. The activation energies obtained in this study (Ting's) were furthermore compared to literature data, which is exposed in Fig. 1.28. The authors suggested that the use of bulk data for films might not be appropriate.

The effect of isothermal devitrification temperature (between 390 and 450°C) on the reaction kinetics and the microstructure of Ni-Ti freestanding films have been studied by Vestel *et al.* [116]. Low annealing temperatures would be favourable for their CMOS compatibility and thus are important to the applications of MEMS structures. The study shows that the minimum temperature for complete crystallization of amorphous as-sputtered films (in a reasonable length of time) is at least 400°C. The experimental procedure included annealing (isothermal or isochronal) in a power-compensated DSC under nitrogen atmosphere in Al container pans as well as TEM observations on partially crystallized films to address the microstructural development. Figure 1.29 shows the DSC isothermal plots obtained during crystallization of equiatomic Ni-Ti films released from stainless steel substrates. The lowest crystallization temperature at which an exothermic peak could be easily distinguished was 420°C. An increase of the temperature from 420 to 440°C leads to a decrease in the incubation time. No identifiable crystallization exothermic peak could be produced with an

annealing at 400°C for 400 min and 390°C for 600 min. They have found activation energies between 347 and 435 kJ/mol.

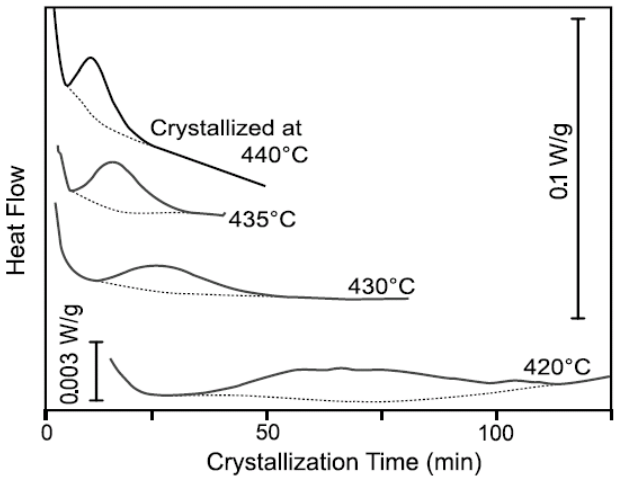

Fig. 1.29: DSC isothermal plots equiatomic Ni-Ti films (≈22 µm) released from a stainless steel substrate showing broadening of crystallization peaks and an increase in incubation times as the crystallization temperature is lowered [116].

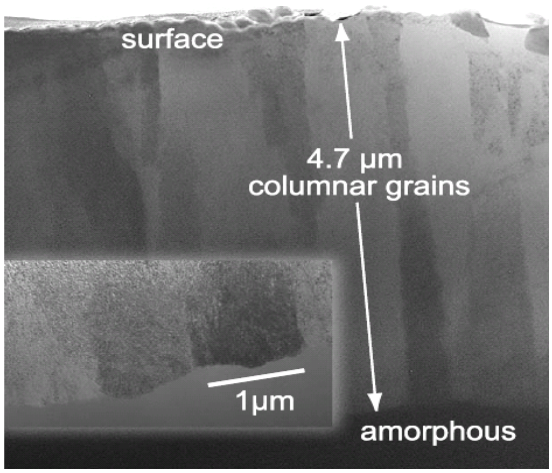

Fig. 1.30: TEM micrograph of one of the two surfaces of a Ni-Ti film crystallized at 430°C and quenched in liquid nitrogen after 25 min. It shows the microstructure resulting from surface nucleation of columnar grains (top) growing into remnant amorphous phase (bottom). The inset with a close-up of the interface reveals a grain size of approximately 1 µm [116].

TEM studies allowed them to conclude that the crystalline phase always nucleated first at free surfaces, grew laterally until impingement, and then grew inward to form columnar grains. Nucleation takes place almost simultaneously at both free surfaces (for free-standing films) and leads to impingement of columnar grains near the centre of the film when crystallization is complete. However, roughened surfaces appear to delay the onset of surface nucleation. The grains are equiaxed (in-plane profile) and are elongated in the film growth direction. In Fig. 1.30 a TEM micrograph of a Ni-Ti film (22.4 µm) annealed at 430°C during 25 min is shown as an example of nucleation at free surfaces. A 4.7 µm deep crystalline zone at one of the two surfaces where the nucleation occurred is exposed (two crystalline fractions of 4.7 µm represents 42 % crystallization, agreeing well with what is expected using the relative area model on the DSC curve). In the inset, a higher magnification image of the crystalline/amorphous interface shows a faceted shape but all the grains appear to be growing into the amorphous phase at approximately the same rate.

Additionally to nucleation at free surfaces, bulk nucleation events are also found to take place, leading to stratified regions of crystalline material with relatively shallow, wide grains, in sharp contrast to the high aspect ratio and orientation of the surface-nucleated

grains. This nucleation process occurs in the interior of the film (without a link to the surface-nucleated columnar grains), resulting in multi-directional laminar microstructures, which may account for the observation of multiple martensitic transformation events.

Vestel *et al.*, in a later work [117], studied the details of the crystallization process in Ti-rich Ni-Ti films (390-450°C), including the precipitate formation. The nucleation in high concentrations of Ti-rich particles (Ti_2Ni) at the columnar grain interface was notorious for films with a complete crystalline structure (which is not the case for partially crystallized films). A higher density of precipitates was detected at the columnar/plate grain interface. The authors propose that during the crystallization process, excess Ti is driven into the amorphous region ahead of the crystal/amorphous interface, leading to Ti-rich precipitates preferentially at the columnar/plate grain interface.

Although for Ti-rich compositions higher transformation temperatures can be achieved compared to equiatomic or Ni-rich compositions, it is necessary to have in mind that a non-controlled growth of Ti_2Ni precipitates can disturb or even impede the growth of martensite plates [118]. On the other hand, it has been shown that Ti-rich Ni-Ti thin films crystallized from the amorphous state exhibit fine flake-like microstructures that have never been reported in bulk materials [118]. Guinier-Preston (GP) zones (submicrometric plate precipitates) and homogeneously distributed Ti_2Ni precipitates inside a grain cause different shape memory behaviour from those of bulk Ni-Ti. The GP zones can be deformed elastically during martensitic transformation or mechanical deformation, and, thus, they do not affect the growth of martensite plates during martensitic transformations or mechanical twinning shear in the martensite. This assures that the film can obtain a large shape recovery strain. The relation between composition, heat-treatment temperature and resulting microstructures are shown in Fig. 1.31 for a Ni-Ti film (Ti-48.2at.%Ni) heat-treated for the period of 1 h [9]. During heat-treatment of the amorphous film, the microstructure in the B2 matrix changes in the sequence of plate precipitates along {100} planes of the matrix [Fig. 1.31(e) and (d)], plate precipitates and spherical Ti_2Ni precipitates with moiré fringes [Fig. 1.31(c)], and spherical Ti_2Ni precipitates [Fig. 1.31(b)] with increasing processing temperature.

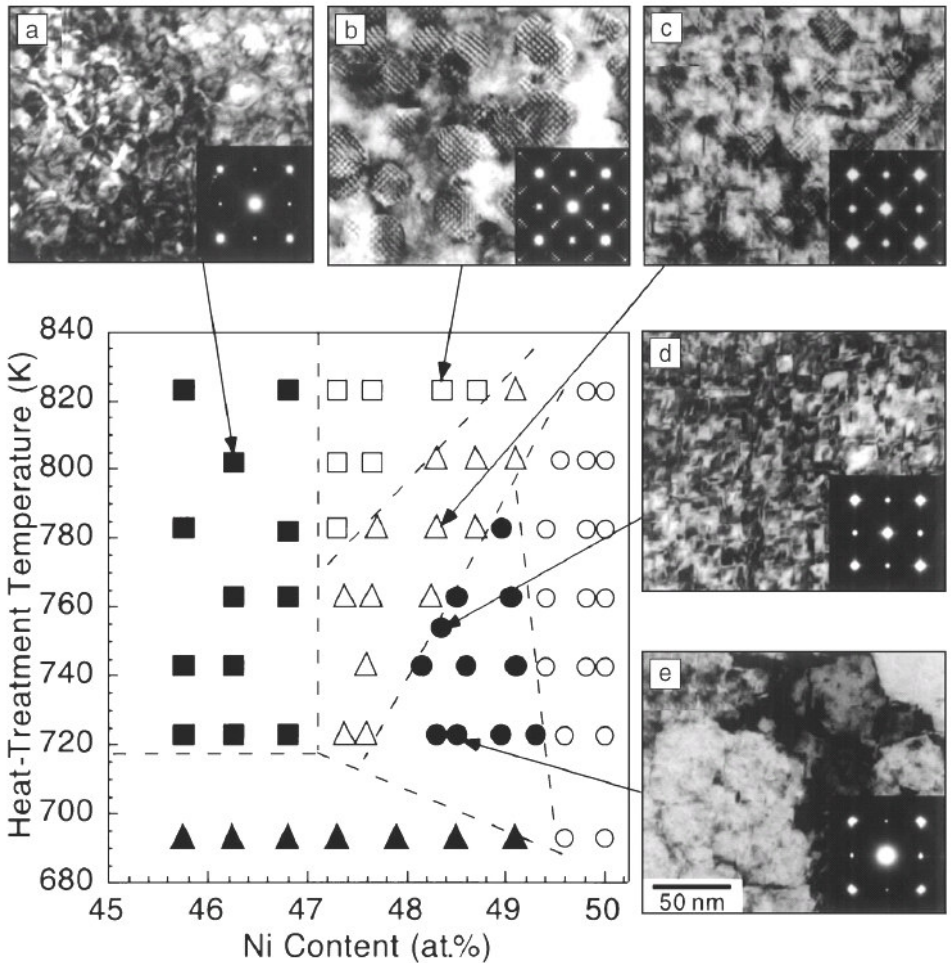

Fig. 1.31: Precipitation in the Ni-Ti matrix of Ti-rich Ni-Ti film (Ti-48.2at.%Ni) heat-treated for 1 h at various temperatures: (■) are Ti_2Ni particles with random orientation; (□) are Ti_2Ni precipitates with the same orientation as that of the matrix; (Δ) are plate precipitates and oriented Ti_2Ni precipitates; (●) are plate precipitates – d) high temperature form, e) low temperature form; (O) indicate no precipitates; (▲) indicate amorphous films [9].

The heat-treatment temperature has an important role on the distribution of the plate precipitates. For high temperatures, supersaturated B2 phases appear in the amorphous matrix with the same composition as the amorphous phase and, after that, plate precipitates are created uniformly in the B2 grains. For low temperatures, B2 phase with a near equiatomic composition crystallizes in the amorphous phase, expelling excess Ti atoms into the amorphous matrix (as proposed by Vestel *et al.* [117]), leading to a localized distribution of plate precipitates. Although the structure of this type of plate precipitates raises still some questions, two types of structures have been reported: a GP-zone-type structure in which excess Ti atoms are clustered on B2 {100} planes; and a $C11_b$-type ordered structure, which differs from that of Ti_2Ni. The TEM observations have shown a coherency between the plate precipitates and the matrix. Concerning the Ti_2Ni particles, in this temperature regime two situations with respect to the orientation relationship with the B2 matrix were identified. For a

Ti content lower than 53%, Ti_2Ni precipitates have a specific orientation relationship with the matrix (B2 phase), because the precipitates are formed after the crystallization of the B2 matrix. In this case it is expected that the crystal axes of Ti_2Ni and those of B2 are parallel to each other. On the contrary, when the Ti content is higher, the Ti_2Ni phase is formed first, and then crystallization occurs and no orientation relationship between the precipitate and the matrix could be identified. For both cases, the studies report granular Ti_2Ni precipitates.

As an example, the microstructure of a sample (Ti-48.2 at. %) annealed at 500°C for 1 h was reported to have a dispersion of Ti_2Ni inside the Ni-Ti grains, as well as GP zones. The Ti_2Ni have partial coherency with the matrix and the misfit is considerably relaxed. They found a close relationship between the Ti_2Ni precipitates and the Ni-Ti matrix, and observed some similarity between the unit cells of both phases. A high magnification image of the interface in their study revealed that some of the {110} planes are continuous through the precipitate and the matrix. Since the d-spacing of $Ti_2Ni(400)$ is 0.283 nm and for B2(100) is 0.301 nm (considering the JCPDS cards shown in appendix B), if the Ti_2Ni precipitate is coherent with the matrix at the beginning of the precipitation process, a tensile stress field is formed around the precipitate.

Although the high quality works performed using several *ex-situ* techniques provide important information to understand the crystallization behaviour of Ni-Ti films, there had been a demand for more direct observations and an independent method of measuring the crystallization evolution. Recently, the crystallization and phase transformations of amorphous Ni-Ti thin films have been studied using *in-situ* TEM [106, 107, 119]. The microstructural evolution was monitored and recorded. This method allows the determination of kinetic parameters such as the nucleation rate, growth rate, and area-fraction transformed by noting the number of grains per frame and their change in size. Using the Johnson-Mehl-Avrami analysis, fitted kinetic parameters were calculated and they were consistent with the TEM observations (showing that Ni-Ti is a model system). Furthermore, to explore the compositional sensitivity of crystallization, near equiatomic (Ti 50.4 at.%) and slightly Ti-rich (Ti 52.6 at.%) samples were studied with those methods [119].

Martins *et al.* [26] have also demonstrated the benefit of *in-situ* XRD for the study of the crystallization process of Ni-Ti films. Amorphous films were deposited using target/substrate distances *(h)* of 70 mm ($Ni_{50.7}Ti_{49.3}$) and 40 mm ($Ni_{50.2}Ti_{49.8}$). The Ni-Ti films were deposited on Si(100) substrates with and without an intermediate layer of poly-Si [prepared by low-pressure chemical vapour deposition (LPCVD) under two conditions: 600

and 675ºC]. The structural development of the films during crystallization (at a constant temperature of 430ºC) has been studied by XRD in grazing incidence geometry off-plane (GIXD) at the synchrotron radiation beamline ROBL (BM20 at ESRF) allowing to establish a correlation between the deposition conditions and the kinetics of crystallization. During the annealing process, besides the B2 phase, precipitation of Ni_4Ti_3 was detected (Fig. 1.32). The results have also shown that the crystallization process of Ni-Ti SMA is significantly enhanced for low *h* distances of 40 mm instead of 70 mm for Si(100) substrates (Fig. 1.33).

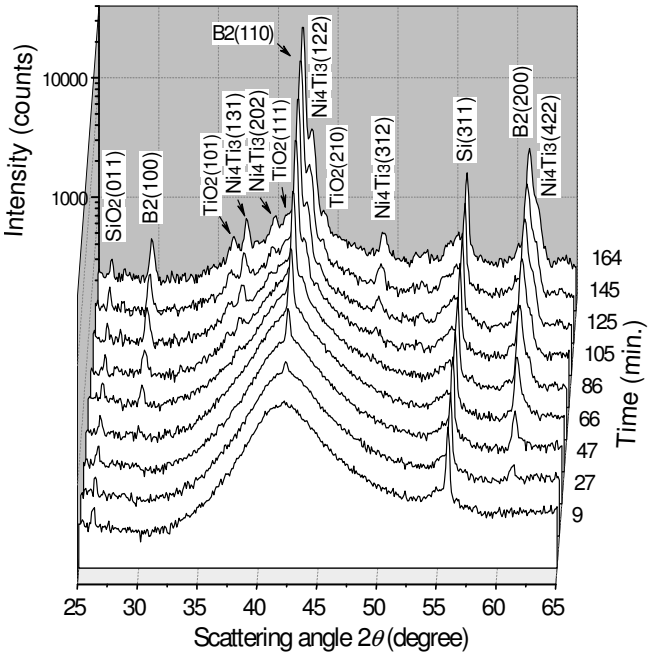

Fig. 1.32: GIXD patterns of Ni-Ti films during crystallization at an annealing temperature of 430ºC deposited on a Si(100) substrate at 70 mm – the indicated annealing time corresponds to the time when half a scan is completed [26].

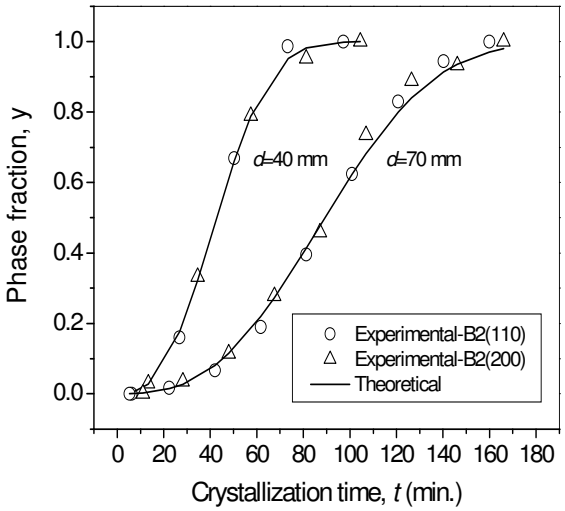

Fig. 1.33: Crystallized phase fraction *versus* crystallization time for Ni-Ti films deposited directly on Si(100) wafers (*h* = 40 and 70 mm). The experimental data correspond to integrated peak intensities of Ni-Ti B2(110) and (200), the theoretical values are obtained by using the Johnson-Mehl-Avrami equation [26].

The presence of an intermediate layer of poly-Si furthermore drastically enhances the crystallization process (see Fig. 1.34), because of the higher number of nucleation sites provided by the rougher surface morphology of the poly-Si layer. Additionally, *ex-situ* annealing of identical samples at 500°C during 1 h and complementary characterization of the structure and morphology of the films by X-TEM and Selected Area Electron Diffraction (SAED) were performed. Results obtained by GIXD and XRR have given an indication of the precipitation behaviour in the films (identification and dispersion of the precipitates), suggesting that during crystallization excess Ni is driven into an amorphous region ahead of

the crystal/amorphous interface, thus leading to a higher concentration of Ni closer to the surface region and further precipitation of Ni-rich precipitates (Ni_4Ti_3).

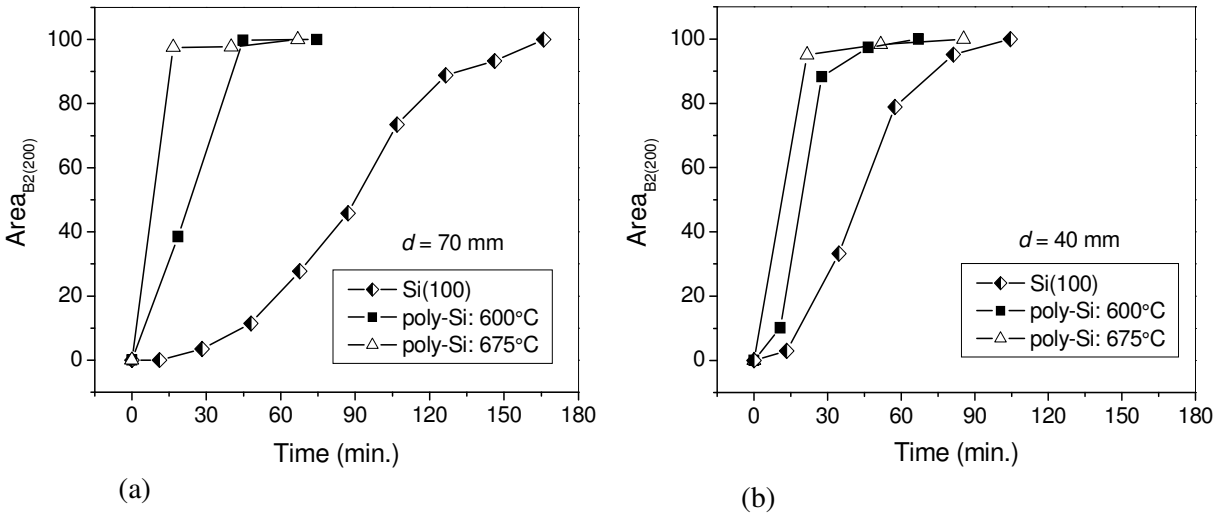

Fig. 1.34: Development of the B2(200) diffraction peak area during crystallization of the Ni-Ti films, deposited on Si(100) with and without an intermediate poly-Si layer; (a) Ni-Ti deposited at 70 mm, (b) Ni-Ti deposited at 40 mm [26].

The temperature dependence of the ER during thermal cycles was also measured (using the van der Pauw configuration [120, 121]), identifying the temperature ranges of the phase transformations. An increase of the overall resistivity with the precipitation of Ni_4Ti_3 has been detected as well as an increase of R_s for the samples with the poly-Si layer. This could be explained by the joint effect of depletion of Ni from the matrix, due to the formation of Ni-rich precipitates, and the interfacial coherency stresses associated with these precipitates.

Mohanchandra *et al.* [122] have also tested the sensitivity of ER measurements (using a four-point probe method) in order to detect phase transformations and the presence of precipitates (and their effect) in the film. Typically, they deposit Ti-rich films on Si(100) wafers at 225 nm/min and crystallize them by heating to 500°C for 20 min *in situ* prior removal from the sputtering system. In view of the fact that the crystallization process is very sensitive to temperature and duration, they have chosen these parameters in order to be able to control the precipitation and produce a high-quality film exhibiting SME. The existence of defects in the films such as vacancies, and also very small grain sizes and related large numbers of grain boundaries after crystallization, leads to an easier diffusion of atoms and precipitation occurs faster than in the bulk material. These authors have in this particular study annealed films at three different temperatures to determine the effects of heat treatment on the Ni-Ti films. Different films have been annealed at 550, 600 and 650°C for 20 min.

They rule out the possibility of precipitates inside grains for a temperature of 650°C. The resistivity of all phases increased significantly for the film annealed at 650°C, which is believed to be due to the increase in precipitate density near the grain boundary. Together with the resistivity changes, a shift in some of the transformation temperatures is also observed. With increasing temperature a decrease in the transformation temperatures is observed for R_s, R_f and M_s (negligible small shifts are observed in other transformation temperatures). This decrease may be attributed in part to the growth of Ti_2Ni precipitates within grain boundaries because a slight increase in Ni in the matrix is well known to decrease the transformation temperatures.

As mentioned earlier, the aim of this PhD thesis is to study the optimisation of the deposition conditions of films of Ni-Ti in order to obtain the material fully crystallized at the end of the deposition. The deposition on *heated substrates* is a way to create crystallized films without a further annealing step. *In-situ* crystallization reduces the risk of oxidation and leads to a reduction in the crystallization temperature. Gisser *et al.* [96] observed that Ni-Ti films could be crystallized during deposition on Si(100) substrates heated to 460°C. However, this method has yet not been a main focus of research with the exception of a few works. Gill *et al.* [22] during the investigation of manufacturing issues related to a Ni-Ti microwrapper found that the patterned Ni-Ti film breaks at the sacrificial layer step. Scanning Electron Microscopy (SEM) observations have shown that a hole is produced during etching at the interface Ni-Ti/sacrificial layer (deposited on unheated substrates). The hole enlarges and ultimately breaks the film. The breakage of the Ni-Ti film was attributed to residual stresses in the film. The Ni-Ti film had a tensile stress of 310 MPa in the austenite phase and 200 MPa in the martensite phase. In order to reduce the residual stress they have deposited Ni-Ti films on heated substrates (350°C). They state that when the Ni and Ti atoms arrive on a heated substrate, the atoms have more thermal energy to rearrange themselves and relieve the stress (higher mobility of atoms). After repeating the same etching procedure, SEM pictures have shown the presence of the etch hole but this time it is considerably smaller in size when compared to the film deposited onto an unheated substrate. Nevertheless, according to the authors, the *in-situ* heating temperature should not exceed 500°C in order to minimize the number of precipitates (partial crystallization of the films starts at ≈ 400°C).

Liu *et al.* [109] have studied the microstructure and characteristics of Ti-rich Ni-Ti films deposited onto single crystal Si substrates at RT and high temperature (≈ 500°C) by using the magnetron-sputtering technique. Differences in grain size, growth texture, stress

range, and transformation behaviour were identified. For the films crystallized *in situ*, the grain size was only several tenths of a micrometer, one order of magnitude less than for the film deposited on the unheated substrate. A post-deposition annealing of amorphous Ni-Ti films leads in many cases to a weak texture or almost none [23], probably due to a homogeneous nucleation mechanism by which the crystalline phase forms [123]. For films crystallized during deposition, a strong <110> fibre texture is commonly observed for the B2 cubic structure [96].

Rumpf *et al.* [124] have sputtered Ni-Ti films from melt-cast disc targets on Si substrates at 450°C in the crystalline state. The films revealed a dense microstructure due to the high volume diffusion of the atoms deposited (*zone III* in the general classification from Thornton). The sputtered Ni-Ti films exhibited superelastic properties at 37°C and an astonishing high ultimate tensile strength of 1180 MPa at a strain of 11.5%. This notable improvement in the mechanical properties could be, according to the authors, correlated to the small grain sizes (50-200 nm), to texture (which does not appear when typical subsequent crystallization is applied, 500°C for 1 h *ex-situ*) and a single-phase microstructure. The study has shown that the preparation method used by the authors lead to a microstructure responsible for the remarkable improvement of mechanical properties in comparison with previous studies.

1.3.3. Oxidation

A dominant issue involved in determining the quality of Ni-Ti films is the extreme reactivity of the Ti atoms. Therefore, a very low base pressure is necessary in the sputtering chamber before the admittance of the Ar sputtering gas, in order to reduce contaminants (principally Ti oxide precipitates) in the film, which could adversely affect the SME. Also the post-deposition heat treatments at high temperatures in atmosphere containing oxygen will result in the oxidation of Ni-Ti films.

There had been an effort on the characterization of the surface oxidation of bulk Ni-Ti SMA since these alloys have attracted considerable attention as materials for medical implants. Their biocompatibility depends on a corrosion resistant Ti oxide layer avoiding the allergic and toxic effects of Ni. It is necessary to use the appropriate conditions for the oxidation of Ni-Ti medical implants that will ensure the surface formation of a protective layer of Ti oxides with the minimal release of Ni through it. One of the earliest works on the oxidation behaviour of equiatomic Ni-Ti alloy in high temperature air environment was

presented by Chu *et al.* [125]. They have studied the isothermal oxidation behaviour of the alloy in dry air from 550 to 1000°C. Experimental results have shown that a multi-layered scale is formed, composed of an outer rutile layer, a porous intermediate layer of TiO_2 and Ni(Ti), and a thin inner Ni_3Ti layer. Moreover, a stripe-like lamellar structure in the intermediate layer is detected at the Ni_3Ti interface. The authors proposed a schematic oxidation mechanism of the Ni-Ti alloy to explain the observed results (Fig. 1.35).

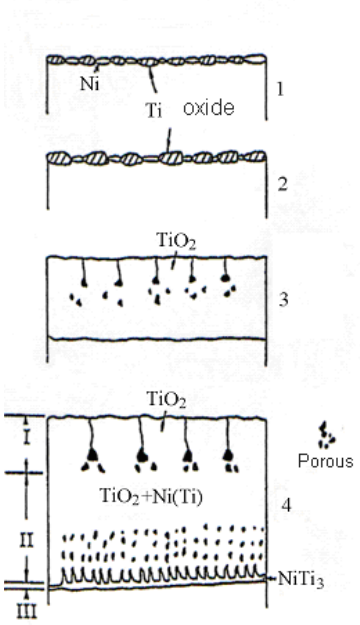

Fig. 1.35: Schematic representation of oxidation of an equiatomic Ni-Ti alloy [125].

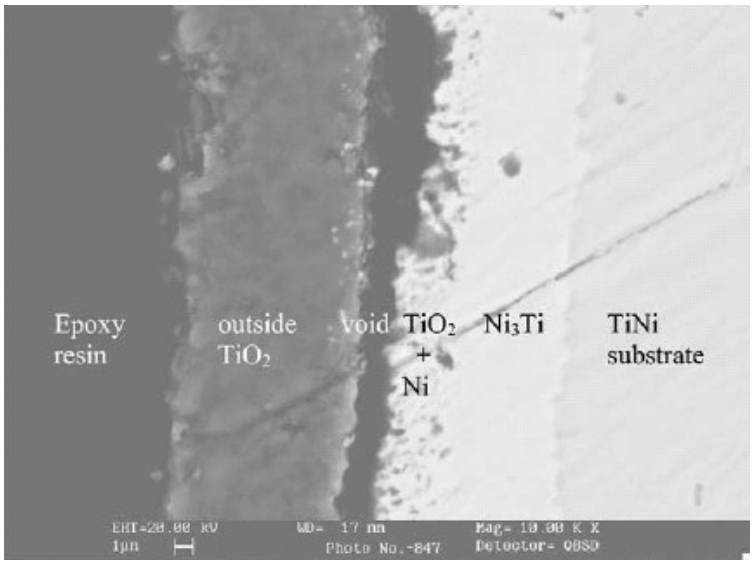

Fig. 1.36: Multi-layered structure seen in cross-section of a specimen oxidized at 750°C [126].

In the early stage of oxidation Ti is oxidized first while Ni remains unchanged (*stage 1*-Fig. 1.35). While the Ti oxide is formed becoming a continuous outer oxide layer, the high temperature atmosphere converts the transient Ti oxides (TiO and Ti_2O_3) to TiO_2 (which is the more stable oxide). The crystals of rutile grow, both in the horizontal and vertical direction, leading to a rutile enriched layer and a local enrichment of Ni just beneath the TiO_2 layer (*stage 2*-Fig. 1.35). With progressing oxidation, Ti atoms diffuse outward while oxygen atoms diffuse inward (the diffusivity of Ti in rutile is expected to be faster than that of oxygen). This leads to an outward growth of rutile and an inward growth of Ni-rich phases such as Ni(Ti), *stage 3* of Fig. 1.35. The formation of voids near the interface between the rutile (*layer I* in Fig. 1.35) and beneath *layer II* could be due to the difference between the vertical and lateral growth rates of rutile crystals. The study also revealed that oxidation at temperatures between 550 and 1000°C in dry air follows approximately a parabolic law. An effect on the M_s and M_f transformation temperatures of the bulk Ni-Ti near the oxide layer is

also clearly detected. They are suppressed after the alloy is oxidized at temperatures above 550°C, most likely due to the interstitial oxygen absorbed in the Ni-Ti lattice.

In a later work, Xu *et al.* [126] have shown that the kinetics of Ni-Ti alloy at 450°C in pure oxygen for 4 h obeys a logarithmic growth law. For the temperature range 550-750°C it obeys a parabolic law. It was also demonstrated that the oxide formed on the surface of the Ni-Ti alloy at 550-750°C is rutile (TiO_2). A multilayer structure – TiO_2 oxide, mixture of Ni(Ti)-TiO_2 and Ni_3Ti layer – was formed on the surface of the Ni-Ti samples (Fig. 1.36). The spalling of the external TiO_2 layer occurred maybe due to high stresses developed at the interface.

The oxidation behaviour of bulk Ni-Ti alloys appears to be well understood, however, it should be pointed out that the structure of Ni-Ti films differs from that of bulk alloys. When compared with reasonably dense bulk materials, sputter deposited Ni-Ti films are often porous exhibiting microcracks and voids, which provide short circuit pathways for the inward diffusion of oxygen during oxidation. As a consequence, the formation and growth of the oxide layer, the in-depth diffusion of oxygen and the distribution of oxides may differ from that of bulk Ni-Ti materials. The isothermal oxidation kinetics of sputter-deposited equiatomic Ni-Ti films in pure oxygen from 550 to 650°C has been studied using thermo-gravimetric analysis by Zhang *et al.* [127]. The oxidation kinetics of Ni-Ti films at 550, 600 and 650°C also obeys a near-parabolic law. The oxidized Ni-Ti films exhibit rutile (TiO_2), Ni_3Ti and B2 phases. With the increase of the isothermal oxidation temperature, the TiO_2 phase enhances and the B2 phase decreases. The authors have also mentioned that the phase distribution in the oxidized film differs from that in oxidized bulk materials. The oxide scale of bulk Ni-Ti alloys includes an outermost rutile layer and a thin inner pure Ni_3Ti layer, which cannot be found in oxidized Ni-Ti films. Instead, a double-layered scale including the outermost layer and the Ni-rich layer is formed outside the B2 matrix of oxidized Ni-Ti films. Also observed are particles of TiO_2 phases distributed in both layers, which decrease with increasing depth. The thickness of the outermost layer and the Ni-rich layer increase with the oxidation temperature. A surface smoothening of the Ni-Ti films is induced by the thermal oxidation and the surface roughness decreases with increasing oxidation temperature.

Although the oxidation and formation of a protective oxide layer on the bulk materials appear to be a plus for biocompatibility improvement, special care is needed in the case of films. Since the Ni-Ti films required for MEMS applications are usually a few micrometers thick, a relatively thin oxide layer could have significant adverse effects on shape memory

properties. The surface oxide layer restricts the phase transformation, alters stoichiometry of the remaining Ni-Ti film, and reduces volume of the material available for phase transformation. The film thickness on the shape memory behaviour of Ni-Ti films will be discussed in a later subsection. This subject is of extreme importance since for very thin films the surface oxide and interfacial diffusion layers exert a dominant constraining effect that renders a high residual stress and a low recovery stress in the film.

1.3.4. Interfacial film/substrate reactions

During this thesis work, the analysis of the interfacial reaction products also assumed special importance. In this subsection, mainly information published concerning the Ni-Ti/Si(100) interface is presented.

Ni-Ti films are typically deposited on Si as well as on SiO_2/Si wafers. This is in part due to the fact that in the field of MEMS, an important goal is the integration of mechanical elements, sensors and electronics on a common Si substrate through Si microfabrication technology. The development of "intelligent" products is expected by augmenting the computational ability of microelectronics with the control and perception capabilities of microactuators and microsensors [30]. Several groups have considered the use of a thermally grown SiO_2 layer because it can act as an electrical and thermal insulating layer to prevent silicide formation, and also as a sacrificial layer in surface micromachining processes. The study of Ni-Ti film deposition on different substrates (such as poly-Si, TiN, Si_3N_4 *etc*) is thus important for the development of suitable microdevices [10].

Miniaturization of mechanical devices is evolving toward nanometer scale but shrinking this technology to sub-micron dimensions raises important questions in the properties of Ni-Ti films. In very thin Ni-Ti films it is essential to investigate the microstructure to understand the mechanism and origin of the thickness limit. This includes grain size, grain structure, twin size twinning configuration, and reactions layers. The reaction layer could affect film properties significantly when its thickness is comparable to film thickness [128]. Previous studies have shown that there exist interfacial diffusion and chemical interactions at the Ni-Ti/Si(100) interface whereby Ni and Ti silicides may form [129, 130]. The interfacial phases are formed through diffusion and reactions of atoms at certain temperature ranges during high temperature deposition or post-deposition annealing. Wu *et al.* [130] have illustrated in a schematical way the microstructural evolution of interfacial reaction layers of Ni-Ti deposited on Si(100) and annealed at 400-700ºC for

30 min (Fig. 1.37). The Ni atoms are the primary diffusing species and $NiSi_2$ begins to form (30 min annealing at 400ºC) from the interface to the Si substrate [Fig. 1.37(b)]. The development of $NiSi_2$ instead of NiSi or Ni_2Si might be due to the (Si, O)-rich layer (native silicon oxide layer), which reacts against the diffusion of Ni atoms, resulting in a lower Ni supply rate. The (Si, O)-rich amorphous layer also appears to be a good diffusion barrier to Ti and Si at low temperatures. The formation of nickel silicide is less sensitive to the O-rich layer than the formation of titanium silicide in the Ti/Si-substrate system [131].

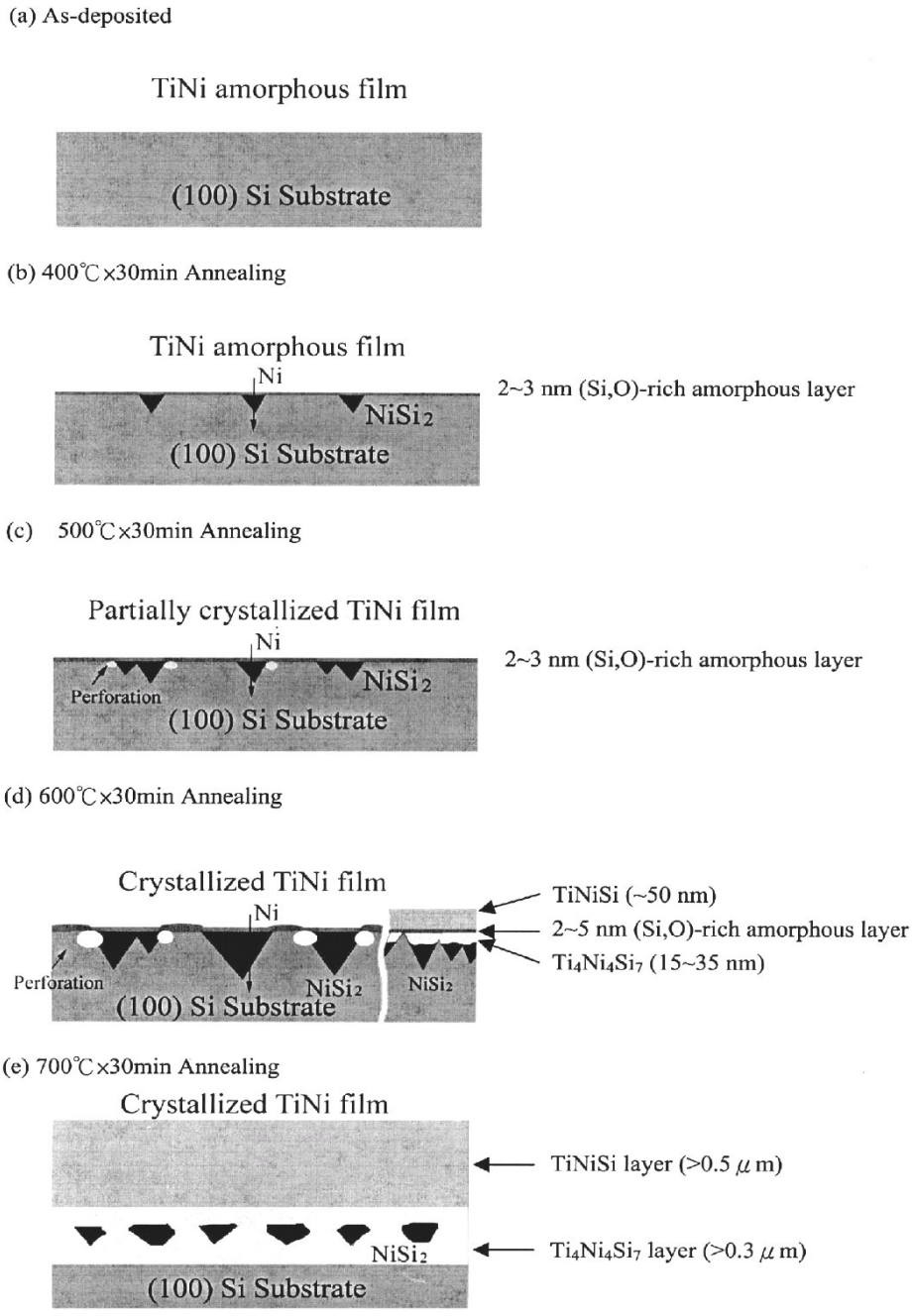

Fig. 1.37: Schematic diagrams of the microstructural evolution of interfacial reaction layers of Ni-Ti/Si(100) annealed at 400-700°C for 30 min [130].

An annealing at 500ºC for 30 min results in the grow of $NiSi_2$ into the Si substrate and the Ni-Ti film begins to crystallize as a $Ni_{50}Ti_{50}$ B2 phase [Fig. 1.37(c)]. At 600ºC the Ti and Si atoms penetrate the (Si, O)-rich amorphous layer leading to the formation of Ti-Ni-Si compounds, observed in some areas of the Ni-Ti/Si interface [Fig. 1.37(d)]. A near-$Ti_4Ni_4Si_7$ compound nucleates at the interface and grows into the Si substrate and the triangular $NiSi_2$. The nucleation of a near-TiNiSi compound, which grows into the Ni-Ti films, was also observed. For the samples annealed at 700ºC [Fig. 1.37(e)] the $Ti_4Ni_4Si_7$ and TiNiSi ternary compounds have formed two layers between the crystallized Ni-Ti film and the Si substrate. $NiSi_2$ appears embedded in the $Ti_4Ni_4Si_7$ layer forming isolated islands. The (Si, O)-rich amorphous layer could not be detected. The Si-rich ternary phase ($Ti_4Ni_4Si_7$) is placed in the vicinity of the Si substrate and the TiNiSi grows on the Ni-Ti film's side.

As mentioned earlier, the inclusion of a buffer layer like SiO_2 is usually expected to act as an electrical and thermal insulating layer to prevent silicide formation, or also as a sacrificial layer. However, it was reported by Fu *et al.* [132] that a SiO_2 buffer layer serves as an effective diffusion barrier but the existence of a large amount of oxygen on the SiO_2 layer promotes the oxidization of the incoming Ti atoms arriving onto the SiO_2 surface during deposition forming a TiO_2 layer. A detailed analysis of the NiTi/SiO_2 interface has been performed by Jarrige *et al.* [133] using Electron-induced X-ray emission spectroscopy (EXES) to characterize the physicochemical environment around the Si atoms at the interface, and to obtain information about the interfacial reactivity. They have found the existence of a transition layer <5 nm thick at the interface between the Ni-Ti film and the SiO_2 buffer layer. The interfacial chemical processes comprise the reduction of SiO_2 by Ti, resulting in the formation of Ti oxides, sub-stoichiometric silicon oxide in low quantity and Ni silicides (Ti silicides formation is not expected). The sequence of formation of Ni silicides during the reaction process is $NiSi_2 \rightarrow NiSi \rightarrow Ni_2Si$, which is the reverse of what is observed for the binary system Ni/Si. This is probably due to an effect of the presence of Ti and O on the kinetics of formation of Ni silicides. The presence of a passivation layer at the surface of Ni-Ti was also confirmed, containing mainly Ti oxides (and Ni oxides only in small quantity), showing the diffusion of Ti atoms towards the surface.

There had also been studies of the Ni-Ti/Si_3N_4 interface [134, 135]. A few nanometers thick-mixed layer composed of $TiSi_2$, TiN and $NiSi_2$ forms at the Ni-Ti/Si_3N_4 interface. During annealing this interface exhibits an intermediate reactivity between that of Ni-Ti/SiO_2 and Ni-Ti/Si [134].

1.3.5. Film thickness effects

In this work, the optimum production of ≤1 μm thick Ni-Ti films was investigated in order to increase the actuation frequency of SMAs. A study of the thickness effect on the shape memory behaviour of Ti-50.0 at.%Ni films was carried out by Ishida *et al.* [136], using films with various thicknesses (ranging from 0.5 to 7 μm). A schematic illustration of the cross-sections based on TEM observations is presented in Fig. 1.38. The films exhibit an equiaxed structure with an average grain size of about 5 μm. When the film thickness is less than the average grain size the transformation strain and residual strain under a constant stress are very sensitive to the film thickness. They have reported that strains were affected by two kinds of constraints (1) from the *surrounding grains*, and (2) from the *oxide layers*.

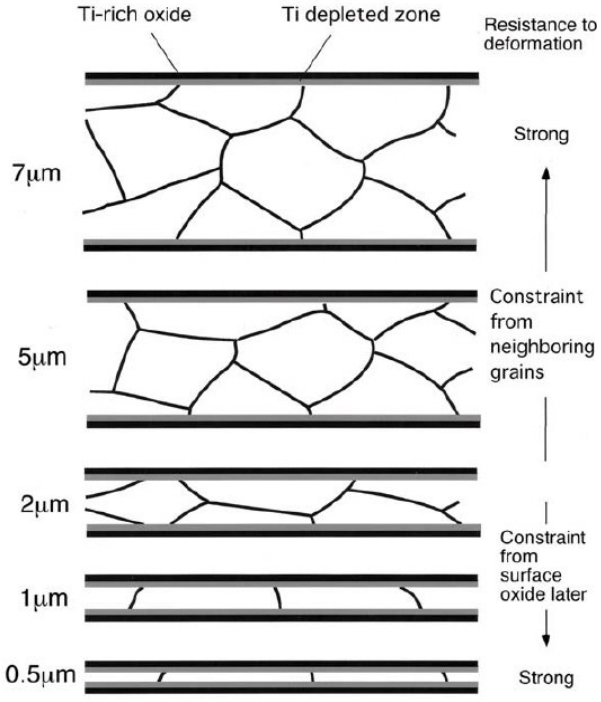

Fig. 1.38: Cross-sections of crystallized Ti-50.0at%Ni films with different thicknesses and strengthening mechanisms of films [136].

With decreasing thickness, the effect from the surrounding grains becomes weaker, but the effect from oxide layers becomes larger. With a decrease in thickness from 5 μm, the transformation strain and residual strain increase progressively and then decrease rapidly after exhibiting a maximum around 1-2 μm. The surface oxidation affects also the transformation temperature when the thickness is less than 1 μm. A decrease in the transformation temperature and an increase in the temperature range between the transformation start and finish are attributed to surface oxidation as a result of heat treatments. Although the observed

oxide layer had a 7 nm thickness, the affected zone beneath the surface oxide exhibited a thickness of approximately 50 nm. This should not be negligible for very thin films as for example 0.5 μm. It is very important to state that the study was based on freestanding Ni-Ti films.

In the case of films on thermally Si oxidized substrates (200 nm SiO_2 layer), Su *et al.* [137] observed (by X-TEM) a Ni-Ti interlayer adjacent to the substrate, which never transforms to martensite even when the above layer shows a clear transformation microstructure, presumably due to the mechanical constraints imposed by the substrate. The untransformed interlayer – consisting of the parent phase and being about 50-100 nm thick – has been found in films of various thicknesses. Fu *et al.* [128] studied the effects of film thickness on phase transformation of constrained $Ni_{49.8}Ti_{50.2}$films deposited onto Si(100) substrates. They have found a minimum thickness (about 100 nm for the Ni-Ti film) necessary to guarantee apparent phase transformation behaviour in the films. For very thin films *the surface oxide* and *interfacial diffusion layers* exert a dominating constrained effect that renders high residual stress and low recovery stress in the film. These layers restrict the phase transformation, modify the stoichiometry of the remaining Ni-Ti film, and diminish the volume of the material available for phase transformations. Figure 1.39 shows the measured residual stress at RT of the as-annealed Ni-Ti films.

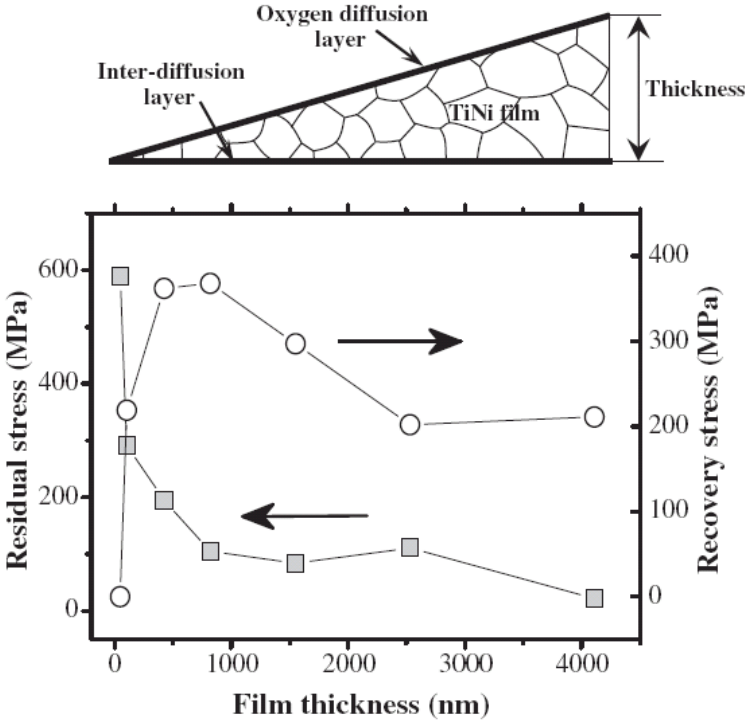

Fig. 1.39: Residual stress and recovery stress for Ni-Ti films with different thicknesses [128].

A maximum residual stress (590 MPa) is obtained for the thinnest film (48 nm) and with increasing film thickness, the residual stress decreases progressively, and then stabilizes at a low value. In the figure, the recovery stresses of the fabricated films are also represented. They are defined as the difference between the maximum and minimum stresses during phase transformation. Their results point towards a maximum recovery stress and actuation speed for a thickness value of approximately 800 nm.

In order to examine the film thickness effect on thermally induced phase transformation in nanometer-thick Ni-Ti films, Wan and Komvopoulos [17] have chosen ER measurements (in the temperature range of −150 to +150°C). The characteristic increase of the ER values associated with the B2 $\Rightarrow$ R-phase transformation was observed for film thicknesses superior to 300 nm. This phenomenon is reduced for thicknesses below 300 nm, and the R-phase transformation was even fully suppressed in a Ni-Ti film less than ≈ 50 nm. The constraints introduced by the film surface and film/substrate interface produce an opposing force, preventing lattice distortion and twinning, which are dominant mechanisms in self-accommodation R-phase transformation. It is believed that the inhibition of these mechanisms leads to the suppression and possible disappearance of the SME for thickness values below ≈ 100 nm.

1.3.6. Texture

In most polycrystalline materials, many material properties (Young's modulus, Poisson's ratio, strength, ductility, toughness, electrical conductivity *etc*) depend on the average texture. In the case of a Ni-Ti SMA, Shu *et al.* [138] using "recoverable strain" as a measure of SME have shown that texture is also a crucial factor in determining the SME in polycrystals. The study of the crystallographic texture of the Ni-Ti films assumes in this way major importance, since it has a strong influence on the extent of the strain recovery and strong textures may lead to anisotropic shape memory behaviour.

Near equiatomic Ni-Ti alloys derive their unique mechanical behaviour from the coordinated atomic movements in their phase transformations. Consequently, any significant alignment of the atomic planes from texture in the polycrystalline material can have a noticeable influence on the mechanical response by either promoting or limiting that phase transformation.

Recently, Robertson *et al.* [139] have conducted a study to seek further understanding of how processing and heat treatment can affect the texture in Ni-Ti bulk material, specifically by quantifying the texture of a variety of raw material forms, and to determine if annealing heat treatments can be utilized to change the strength and orientation of the texture in order to vary the mechanical response. They have shown that Ni-Ti does exhibit crystallographic orientation resulting from its forming and processing, which cannot be eliminated by annealing at high homologous temperatures up to $\approx 0.85\,T_m$ (with T_m the melting temperature).

Thus, due to the importance of the present topic, several researchers have studied the influence of cold work, annealing and precipitation kinetics during aging, on the martensitic transformation in Ni-Ti alloys.

Ni-Ti SMAs have a bcc superlattice structure in the B2 phase and, for that reason, common bcc textures are presented in Tab. 1.2.

Fibre	**Fibre axis**	**Relevant components associated with the fibre**
α-fibre I	<110>‖RD	{001}<110> - {112}<110> - {111}<110>
α-fibre II	<110>‖RD	{111}<110>-{110}<110>
γ-fibre	<111>‖ND	{111}<110>-{111}<112>
η-fibre	<100>‖RD	{001}<100>-{011}<100>

Tab. 1.2: Typical fibre textures observed in bcc metals and alloys (RD - rolling direction, ND - normal direction). The α-fibre II is not common in general but is observed in SMAs [138].

The calculated lattice correspondence between parent phase and martensite was proposed by Miyazaki *et al.*, [140]:

- $(110)[1\ \bar{1}\ 0]$ parent phase variant gives rise to {111}<211> and {002}<002> martensite variants,
- $(111)[1\ \bar{1}\ 0]$ parent phase variant gives rise to {210}<211> and {210}<002> martensite variants.

It has been shown that in the case of textured SMA rolled sheet, there is a considerable difference in plateau-strain and shape recovery strain when tested along different directions. For a rolled sheet, the direction where the highest shape recovery strain is obtained corresponds to the direction where the longest stress-plateau is obtained in the stress-strain curve during the martensite deformation. Least shape recovery is obtained for the test direction where the martensite stress-strain curve has no stress-plateau [141]. The α-fibre I is

desirable for unixial applications and, on the other hand, the γ-fibre exhibits the least anisotropy being preferred when recoverable strain is required in every direction of the rolled sheet.

Aging conditions giving rise to three or four steps during the martensitic transformation have been reported by Favier *et al.* and Allafi *et al.* [142, 143]. Deformation of martensite up to 6 % macroscopic tensile strain results in reoriented martensite by twinning process that is fully recoverable by heating [144]. Above 6 % strain, the deformation starts by slip that introduces dislocations, which stabilizes the configuration of martensite at temperatures above A_f. The stress fields around the stabilized martensite induce preferred martensitic variants during cooling.

The evolution of texture during annealing, before and after thermomechanical processes, becomes also a very important phenomenon to be analysed. Several studies are dedicated to the influence of texture on the thermomechanical response of the SMAs bulk materials, mainly using *in-situ* neutron diffraction to follow the structural evolution. These studies are usually carried out on Ni-rich Ni-Ti alloys at RT where the B2 phase is stable. A first high temperature texture determination for polycrystalline Ni-Ti reported in the literature [145] has been made at 120ºC. After that, Paula *et al.* [146, 147] have tested the feasibility of the determination of high-temperature pole figures using ROBL at ESRF, and showed that there is a relationship between the changing preferential orientation and the structural evolution taking place during annealing of as-received material. The effect of different thermal/mechanical treatments was also discussed regarding the structural evolution during annealing up to 800°C.

Furuya *et al.* [148] have produced and characterized melt-spun ribbons of Ni-Ti alloys and, after suitable heat-treatment, large transformation strains were observed (compared to those of the bulk materials), which has been attributed to the texture of the ribbons. The material exhibited a {200} texture for the B2 phase. The observed texture is coherent with the melt-spinning technique since crystals grow normal to the ribbon surface and the growth direction with the high growth rate in the cubic system is typically the <100>.

Concerning the texture of Ni-Ti films deposited by sputtering on Si(100) substrates, different behaviour has been observed between amorphous films post-sputtering annealed and those sputtered at elevated temperatures (> 350°C) where the films are crystalline as deposited. A post-deposition annealing of amorphous Ni-Ti films leads in many cases to a weak texture or almost none [23], probably due to a homogeneous nucleation mechanism by

which the crystalline phase forms [123]. For films crystallized during deposition, a strong <110> fibre texture is commonly observed for the B2 cubic structure [96], suggesting that the crystalline phase nucleates on the surface of the heated substrate assuming an orientation that minimizes surface energies [65, 109]. Miyazaki and Ishida [23] have study the texture in films deposited on unheated and heated substrates. Figure 1.40 show pole figures of Ni-Ti B2 phase nominally measured in the Bragg peaks B2(110) and B2(200): (a) Ti-52.2at%Ni film which was crystallized at 700°C for 1 h (deposited at RT); (b) Ti-51.6at%Ni film heat-treated at 400°C for 1 h (the film was sputtered at 350°C).

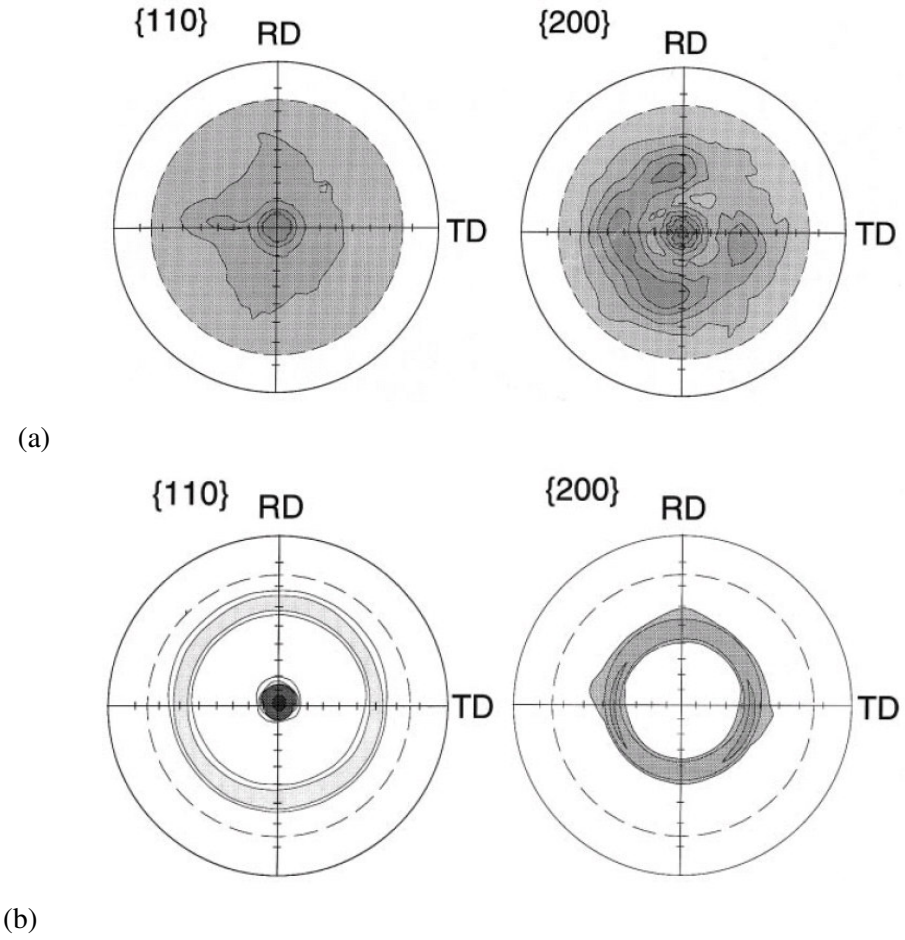

Fig. 1.40: Pole figures of Ni-Ti B2 phase nominally measured in the Bragg peaks B2(110) and B2(200); (a) Ti-52.2at%Ni film which was crystallized at 700°C for 1 h, (b) Ti-51.6 at%Ni film heat-treated at 400°C for 1 h (the film was sputtered at 350°C) [23].

The Ti-52.2at%Ni film exhibits a considerably uniform orientation distribution of grains with a maximum axis density of only 3.9 [Fig. 1.40(a)]. In contrast, the Ti-51.6 at%Ni film [Fig. 1.40(b)] shows a maximum axis density of 110. The second strongest peak density is observed on a circle with 60° apart from the centre of the {110} pole figure. This unique axis density distribution demonstrates a typical <110> fibre texture with a fibre axis

perpendicular to the film surface. In order to investigate the transformation strain anisotropy, the deformation behaviour of the Ni-Ti films was measured along different tensile axes in the film plane by cooling and heating under a variety of constant stresses (specimens were previously wire-cut from the films at 15° intervals from the long direction of substrate). It has been found that the strain is almost constant irrespective of the angle for both films. Since the fibre axes are both normal to film planes, the crystallite orientation distribution is uniform on each film plane so that transformation strain anisotropy is week on the film planes. The transformation strain increased with increasing stress, yet, it is almost constant for each stress irrespective of angle. The isotropic nature in the transformation strain on the film plane is suitable for designing microactuators of Ni-Ti films.

In the case of films deposited on thermally Si oxidized substrates, Su *et al.* [137] observed a strongly (110)-textured B2 on films presenting a good adhesion to the SiO_2/Si substrate (200 nm SiO_2 layer). These films were deposited at RT and subject to an annealing at 560ºC. On the other hand, Kim *et al.* [108] have mentioned the formation of an (200)-oriented Ni-Ti film (100 nm thick) deposited at 550ºC on a Si oxide/Si substrate (300 nm thick Si oxide layer). This work has also shown that (110)-oriented Ni-Ti films (also 100 nm thick) are obtained when a Pt random-oriented layer is deposited on top of the Si oxide substrate (at RT) before the deposition of the Ni-Ti film at high temperature. In view of those previous works, new studies are required to establish a clear relationship between the substrates and texture development.

1.3.7. Ternary system NiTiHf

A group of alloying additions, namely Hf, Zr, Au, Pd and Pt, have been found to increase the transformation temperatures of NiTi-based alloys. NiTiHf SMA materials are considered promising candidates for high-temperature applications due to their higher transformation temperatures and lower cost (when compared to the addition of precious metals). Works have already been performed on the fabrication of NiTiHf films. First studies [149] reported a difficulty on the composition control of the films (like in the case of Ni-Ti). Again, as a simplest and most common solution to compensate the deficiency of a component in the film, the addition of small pieces of the element (e.g. in this case, Hf or Ti) onto the target can be used to achieve the correct film stoichiometry. As it has been described before for the production of Ni-Ti, this is not an optimal technique. The manufacturing of a NiTiHf alloy target is also complicated because the as-cast alloy is brittle. Deposition of NiTiHf films

by sputter deposition in a clean environment (UHV) reduces problems of oxidation and contamination and the use of separate targets avoids the complexity of alloy target preparation.

Sanjabi *et al.* [103, 150] used a novel method to fabricate $Ni_{50}Ti_{50-x}Hf_x$ films using simultaneous sputter deposition from three separate elemental targets. This technique allows direct control over the film composition. $Ni_{50}Ti_{50-x}Hf_x$ alloy films have been fabricated increasing the Hf content up to 28.7 at.%. The influence of Hf on the phase transformation characteristics is shown in Fig. 1.41. The substitution of Ti by Hf considerably raised the transformation temperatures (e.g. above 300°C for > 20 at.% Hf), whereas lower Hf addition (e.g. 5 at.%) led to a decrease in transformation temperature. High temperature XRD evaluation confirmed the presence of martensite at higher temperatures.

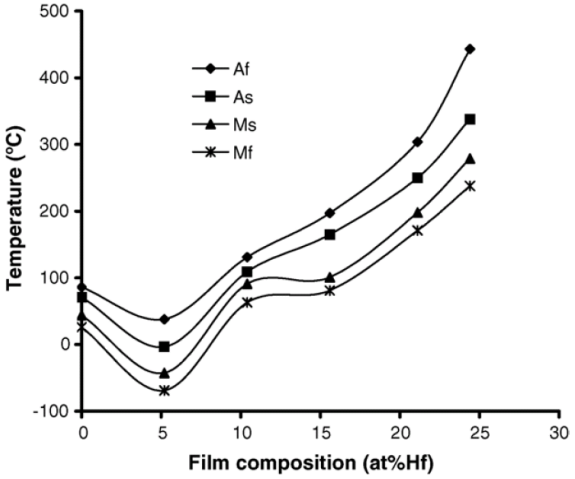

Fig. 1.41: Transformation temperature of the films as a function of Hf content [150].

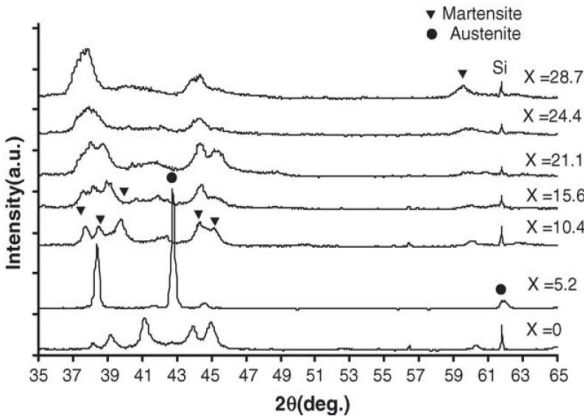

Fig. 1.42: Room temperature XRD of $Ni_{50}Ti_{50-x}Hf_x$ films after annealing at 550°C as a function of Hf content [150].

Figure 1.42 shows the XRD results obtained at RT for annealed films as a function of Hf content (deposited on Si substrates). The films exhibit a martensitic structure for 0 at.% Hf and greater than 10 at.% Hf. A mixture of austenite and martensite phases is found for the film with 5.2 at.% Hf. Apparently, considering the peak positions of martensite, probably, like in the case of bulk material, NiTiHf undergoes a martensite transformation from B2 (austenite) to B19´(monoclinic) when the Hf content is below 15 at.%, and from B2 (austenite) to B19 (orthorhombic) when the Hf content is above 15 at.%. The R-phase was observed during cooling for a Hf content below 16 at.%.

The effects of deposition temperature on the surface and cross-sectional microstructures of NiTiHf films containing 9 at% Hf (deposited from a NiTiHf single target) have been investigated by Zhang *et al.* [151]. The substrate temperature during deposition was varied between 300°C to 700°C and the post-deposition heat treatment temperature was varied between 300°C and 800°C at 100°C intervals. The microstructure analyses demonstrate that NiTiHf films have a relatively fine grain size ranging from 0.2 μm to 2.5 μm, and the grain size increases with increasing substrate deposition temperature. They also reported that the grain size is not affected by post-deposition heat treatment temperature. This is probably because the as-deposited films are already in the crystalline state before the post heat treatment. Nevertheless, an increase of deposition and post heat treatment temperatures can lead to the annealing of more and more dislocations. On the other hand, the precipitation of secondary phases can easily occur and the martensite can be suppressed if the precipitation process is not controlled.

In the last section of the chapter dedicated to the presentation of results obtained during this PhD thesis work, results obtained for the NiTiHf ternary system are shown. Although the aim of the present work was not the optimisation of the production of NiTiHf SMA films, first tests concerning the deposition of this type of films have been performed. They demonstrate the feasibility of the *in-situ* sputtering equipment for future study of this type of ternary alloys and, thus, a short discussion is presented.

Chapter 2

Experimental Details

2. EXPERIMENTAL DETAILS

In Chapter 2 it is presented the equipment used to produce and to study *in situ* the evolution of the structure of the films during deposition and annealing by synchrotron radiation scattering, as well as the techniques used for their complementary *ex-situ* characterization. Thus, besides the equipment available at ROBL, a brief overview of the techniques such as XRD at a laboratory source, RBS, AES, X-TEM, SEM and ER measurements is given. These facilities are installed at the Forschungszentrum Dresden-Rossendorf (FZD) in Germany (ER measurements have also been performed at CENIMAT as well as a complementary experiment concerning texture measurements).

General working procedure:

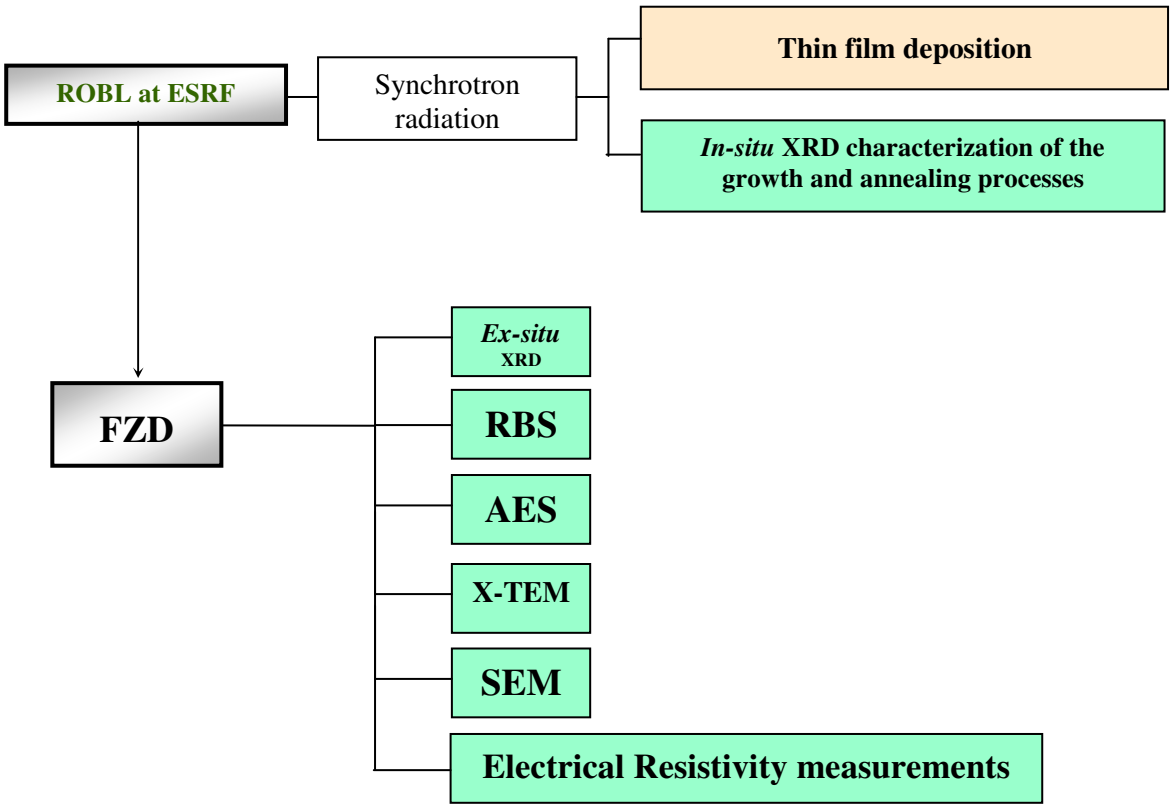

2.1. FILM DEPOSITION AND XRD CHARACTERIZATION AT ROBL

The Rossendorf Collaborating Research Group beamline (ROBL-CRG) at bending magnet BM20 at the ESRF was built and is operated by FZD located near Dresden, Germany. It is also available to outside users to perform experiments either in collaboration with the FZD or by submitting a proposal to the ESRF: one-third of the ROBL beamtime is allocated by the ESRF for peer-reviewed experiments. It uses horizontally a fan of 2.8 mrad of synchrotron radiation from a bending magnet hard edge and has been designed for performing experiments on two different alternatively running experimental stations [152]. One is a radiochemistry hutch, which employs X-ray absorption techniques for the chemical speciation of radionuclides, the other is a general-purpose materials research hutch (MRH) using various XRD techniques and reflectivity (Fig. 2.1).

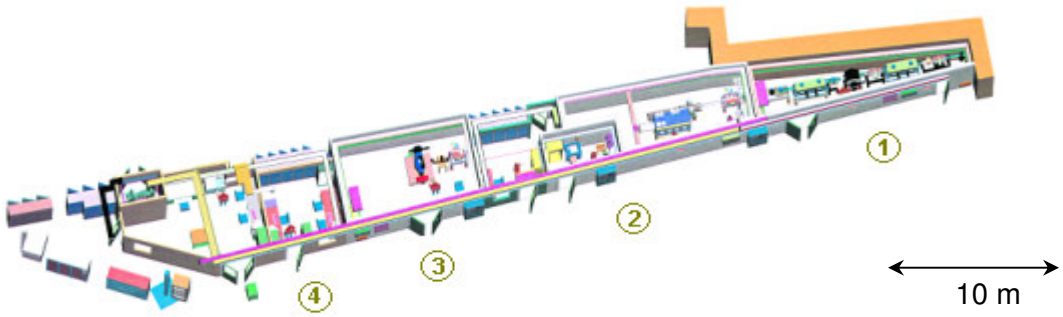

Fig. 2.1: General layout of ROBL (BM20) at ESRF. The X-ray optics in the first hutch (1) delivers monochromatic radiation either to the radiochemistry hutch (2) or to the MRH (3). A total of three cabins are available for beamline and experiments control [(4) control cabine for MRH] as well as for minor (non-radioactive) sample preparation and maintenance work.

The layout of the optics is sketched in Fig. 2.2. The basic elements are a fixed-exit double crystal Si monochromator located between two mirrors with Si and Pt surface coatings, respectively. The double-crystal monochromator (DCM) provides a fixed-exit beam with a vertical offset of 18 mm. It operates with either Si(111) or Si(311) crystal sets. The mechanical construction allows 25 keV to be reached using Si(111) crystals, and 35 keV using Si(311) crystals. The beamline is designed for an energy range from 5 to 35 keV, where in the lower range up to 12 keV the Si coated mirrors are used. The lower energy limit is given essentially by the mandatory Be-windows. The energy resolution is around 2×10^{-4} for Si(111) crystals as monochromator and better than 1×10^{-4} with Si(311) crystals.

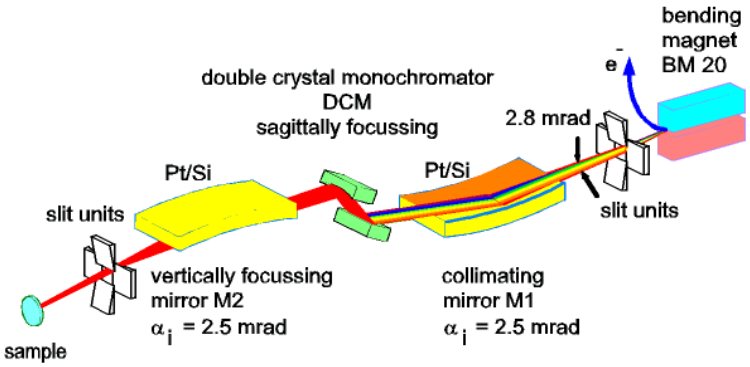

Fig. 2.2: Schematic layout of the ROBL optics [153].

The two mirrors suppress the higher-order harmonics in the monochromatic beam, reduce the heat load on the monochromator and provide a parallel or vertically focused beam at the experimental stations. With a fixed angle of incidence of 2.5 mrad and a length of 1200 mm, the first mirror intercepts only 3 mm of the vertical beam divergence corresponding to about 55% at 12 keV and about 72% at 25 keV of the incoming photons. The calculated spectral flux for the two different mirror coatings is shown in Fig. 2.3. The intensity decrease below 10 keV is due to the absorption of the beryllium windows. For the main applications of ROBL the energy regions of interest are 6 to 10 keV and between 16 and 22 keV.

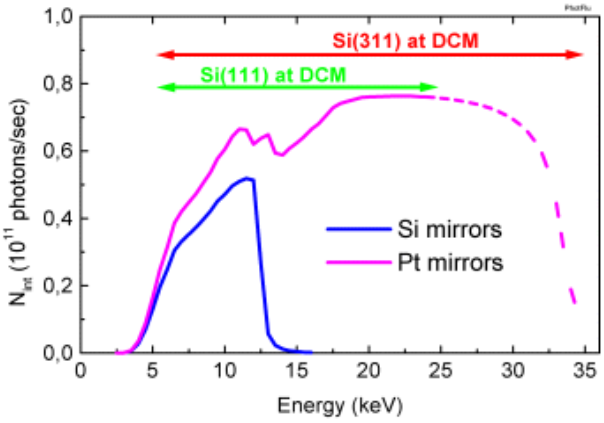

Fig. 2.3: Calculated integrated photon flux for the different mirror coatings (incidence angle 2.5 mrad) and the Si(111) crystals in the double-crystal monochromator. The maximum energy of 35 keV can be realized only with Si(311) monochromator crystals. Geometrical constraints of the DCM design limit the accessible energy range for Si(111) crystals to about 25 keV [152].

The design of the DCM is mainly a commercial one (Oxford Instruments, ATG): the axis of a high-precision rotation table is fed into a vacuum vessel. A crystal cage mounted on this axis carries both crystals. The first crystal is mounted with the rotation axis on the reflecting surface. The second crystal can be moved relative to the first one, parallel and perpendicular to the beam direction. The combined motion of both drives realizes a fixed-exit beam. The first crystal position can be adjusted only manually, while all movements of the

second crystal are motorized and remote controlled, allowing both alignment with the beam and a fine-tuning by piezoelectric translators. In addition to the mirrors and the monochromator, the optics contains various slit units, filters and beam-position monitors. The slit units have independently moveable blades (tungsten carbide), with accuracy better than 10 μm. The filter unit has six absorber foils to attenuate the white beam. The beam-position monitors consist of scanning wires. The motions of nearly all optical components are motorized, mostly with stepper motors, controlled by a UNIX workstation-based system. Many standard ESRF software applications are used in the control programs, which utilize the SPEC code package [154]. The control system also includes interlock components for the vacuum, beam shutters and the cooling of components exposed to the white beam.

2.1.1 Materials Research Hutch: diffractometer and sputtering chambers

The MRH combines the reliable and stable general X-ray source characteristics of *high flux*, *low divergence*, *energy tunability* in a wide range of hard X-rays with an extremely *free and precise sample positioning*, enhanced by *special sample environments*.

The main equipment of the MRH is a special six-circle diffractometer built from modular components (Huber) for heavy duty (Fig. 2.4) [155]. The arrangement of two parallel circles each with horizontal and vertical axes, respectively, allows experiments in both scattering planes. The sample position can be equipped with an *x*-*y*-*z* slide or, alternatively, with special sample environment chambers which are mounted directly on the φ-circle (inner diameter 80 mm). The layout is designed for a load up to 15 kg at the sample position and the χ-circle has an inner diameter of 400 mm so that relatively big chambers (e.g. a high-temperature chamber, sputtering chamber *etc*) can be used. All axes are equipped with stepping motors and gearboxes, which allow a minimum angular step of 0.001°. The *z*-translation of the *x*-*y*-*z* slide has an accuracy of 1 μm while the two other translations have an accuracy of 10 μm. The goniometer is fully computer controlled by a workstation and the programs are based on the SPEC code [154]. Different detection systems can be mounted at the detector arm. As standard, a high-load high-linearity scintillation detector (Bede ERD) was used in this work. In front of the detector, interchangeable fixed single or Soller slits can be mounted. The intensity of the incident beam for each acquisition point is controlled by a monitor because the necessary time to reach the desired intensity is dependent of the beam quality, filling mode and lifetime of the storage ring (6 GeV electrons and a 844 m circumference).

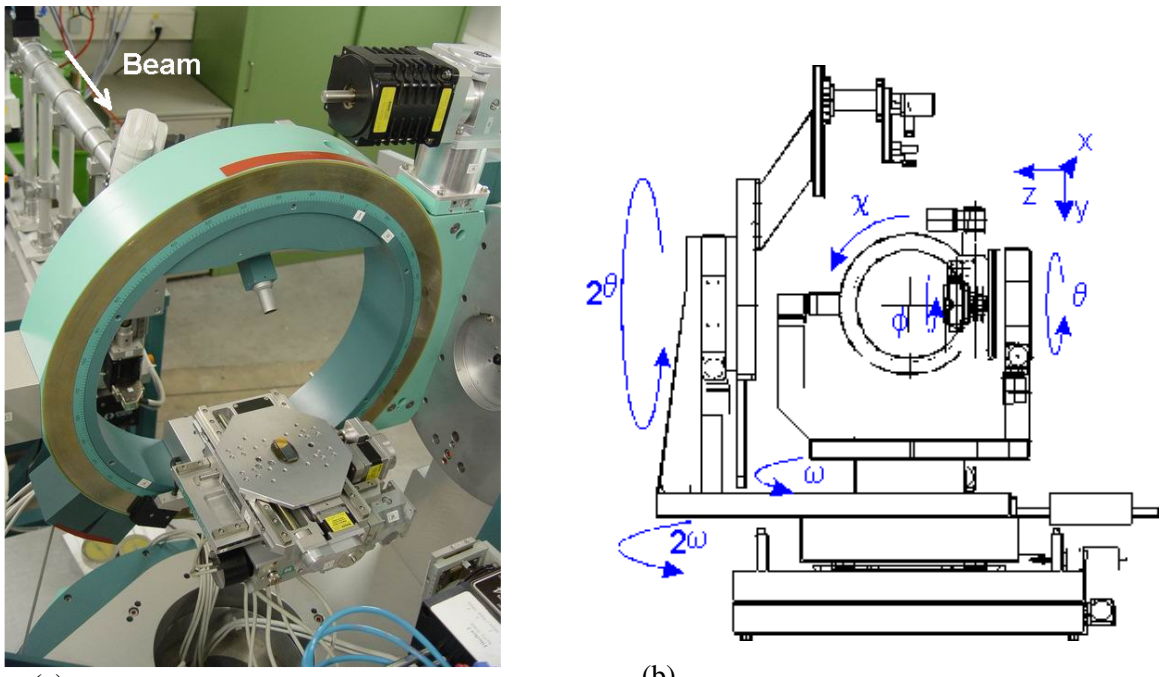

(a) (b)

Fig. 2.4: Six-circle diffractometer in the MRH of ROBL; (a) view of the χ-circle (Eulerian cradle with inner diameter of 400 mm) with the *x*-*y*-*z* slide mounted directly on the azimuthal φ-circle (front view: detector side), (b) scheme of the diffractometer with identification of the axes (view from back: beam direction).

In order to follow *in situ* the film growth and post-deposition annealing, Matz *et al.* [58] have designed a sputtering chamber that fits into the Huber six-circle diffractometer. Since the diffractometer is used as a multi-purpose instrument for many other experiments, the chamber has to be removed always after the beamtimes dedicated to this type of studies. During the period of this thesis work, a new chamber was built by Schell *et al.* [156] and was also tested and used in the deposition of the Ni-Ti films. The results were reproducible with both chambers and the main advantage of the new chamber for this work are the enlarged windows allowing the study of a higher number of Bragg peaks of the phases present in the sample. The "old" set-up (equipped with Kapton-capped flanges as X-ray entrance and exit windows) and the "new" set-up (sealed with Be foils) are described below.

The chambers have been designed to be mounted on the φ-circle and limited in weight to 15 kg in order to guarantee the high precision of the goniometer settings of 0.001°. The other geometrical limitation results from the χ-circle perpendicular to the φ-circle. The χ-circle has an inner diameter of 400 mm but is located 85 mm off-centre of the φ-circle. Taking those limitations into account one can use all existing instalments/equipment at the diffractometer like detectors, slits, collimators, and filter units without additional modifications. The Eulerian cradle is fitted to the θ circle and with an identical rotation axis

the 2θ circle is independently mounted. All four circles described rest on two other circles, ω and 2ω, with the same vertical rotation axis. The inner circles φ and χ are used for sample orientation together with the chamber. The goniometer itself allows equally vertical as well as horizontal scattering geometries. Figure 2.5 shows the actual mounting of the deposition chambers in the Huber goniometer at ROBL.

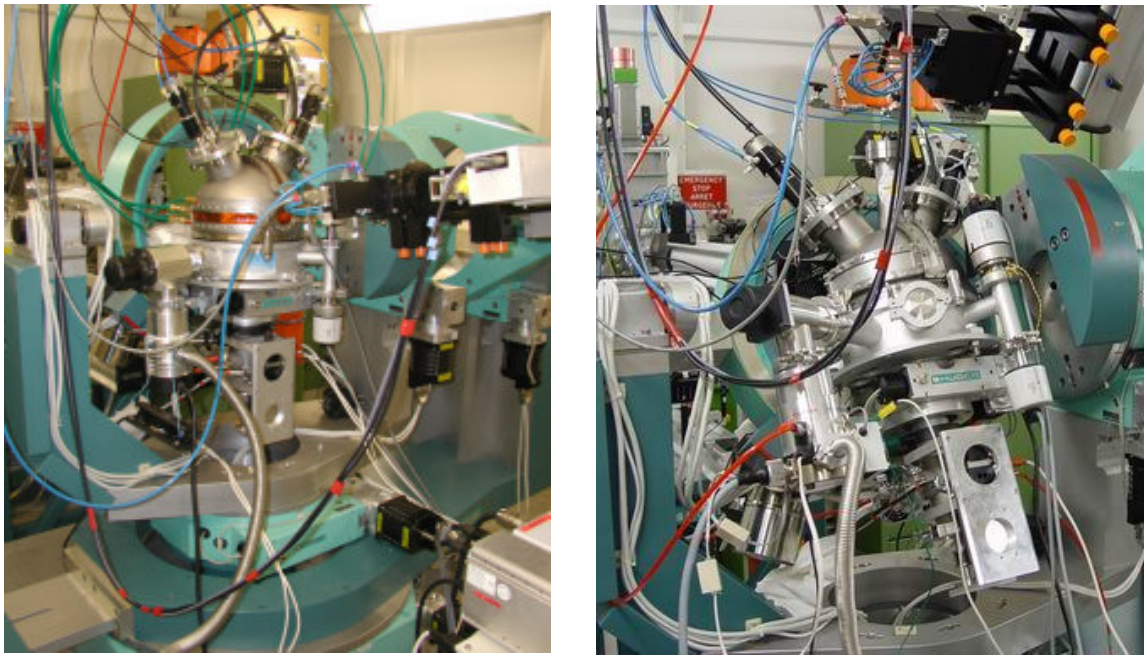

(a) (b)

Fig. 2.5: Deposition chamber mounted into the six-circle diffractometer of ROBL at ESRF (front view-detector side); (a) "old" set-up, (b) "new" set-up.

Figure 2.6(a) shows a drawing and Fig. 2.6(b) a cross-section of the interior centre plane of the chamber designed by Matz *et al.* [58] (Kapton windows). The chambers consist mainly of three separable parts. The central one is a flat cylinder, which is connected to the φ-circle of the goniometer and equipped with different flanges on the circumference and one bigger flange in the bottom. The latter flange goes through the opening of the φ-circle and connects the demountable substrate carrier to the chamber. The flanges on the circumference are for turbo-molecular pumps (connected via throttle valves), for vacuum gauges, and a liquid nitrogen trap. The trap is a copper disk or fork inside the chamber connected by a copper rod of 20 mm diameter through a bellow feedthrough to an assembly of copper chords outside the chamber. The chords are put directly into a small Dewar filled with liquid nitrogen and the cooling is achieved by conduction. This solution was adapted in order to avoid vibrations that might occur when liquid nitrogen is circulated through tubes into the inside of the chamber. The hemispherical top of the chamber is equipped with four radiation windows, two flanges for the magnetron, and a quartz viewport to inspect the sample and the plasma.

The radiation windows are made from 125 μm thick Kapton (initially chosen due to the higher cost of Be). The windows are sealed with viton o-rings. In order to reduce any influence of higher temperatures arising from the substrate heater, all the radiation window flanges are water cooled by outside copper tubes. In the new set-up sealed with Be foils this additional apparatus for cooling is not necessary. Thin aluminium foils (1 μm) are also mounted on the inner side of the windows in order to protect the Kapton or Be from thermal radiation and contamination by sputtered material.

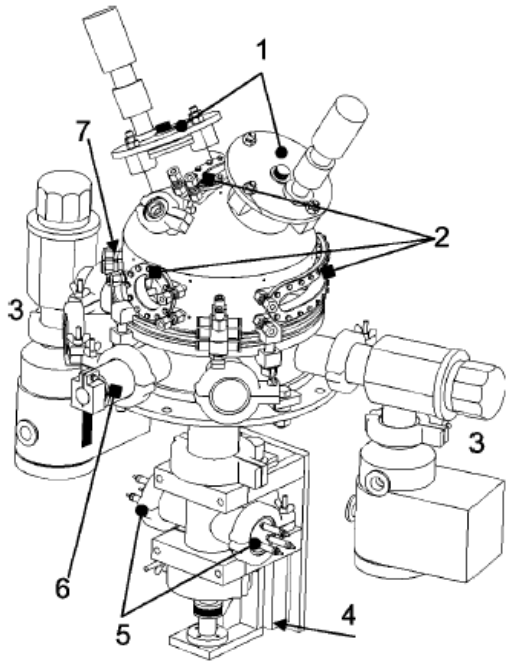

1. magnetrons;
2. X-ray windows with outside cooling tubes;
3. throttle valves and turbomolecular pumps;
4. precision *z*-drive for substrate height alignment;
5. electrical feedthroughs for heater, bias voltage, and thermocouple;
6. liquid nitrogen trap;
7. additional gas inlets.

(a)

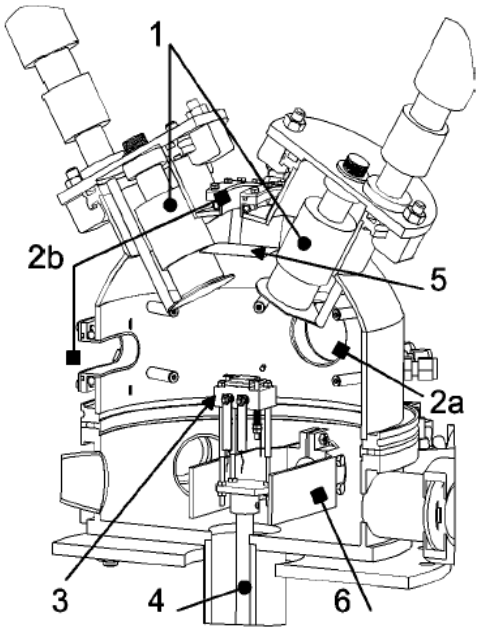

1. magnetrons with shutters;
2a. entrance window for the incoming beam;
2b. exit windows for the diffracted beams;
3. substrate carrier with heater and bias voltage;
4. tube to the *z* drive;
5. window protection foils (Al: 1 μm) fastened at inside protruding bolts;
6. copper fork from liquid nitrogen trap.

(b)

Fig. 2.6: Sputtering chamber; (a) Perspective view, in the direction of the incident beam, of the sputter deposition chamber for synchrotron X-ray scattering, (b) Cross-section with interior view of the sputter deposition chamber in a central plane [58].

The sputtering chamber is equipped with two unbalanced commercial miniature magnetrons from AJA International (type A4001) [37]. They are each positioned at a distance of 100 mm from the substrate and tilted 30° away from the substrate normal. To avoid cross contamination of the two targets, each with a diameter of 25.4 mm, cylindrical chimneys are mounted on the magnetron. Air-pressure-controlled shutters are placed in front of the

chimneys to enable sputter cleaning of the targets prior to deposition. A sputtering gas inlet for each magnetron separately is located on its corresponding flange.

The design is made in such a way that the change of the substrate can be performed by disconnecting only the substrate carrier unit at the bottom flange of the chamber while the chamber itself remains in place on the diffractometer. By flooding the chamber with dry nitrogen during the substrate change, the contamination of the inner walls of the chamber with moisture or oxygen when opening the bottom flange is considerably reduced. The substrate holder is mounted on a 300 mm long inside tube. The lower end of this tube is connected to a precision slide driven by an outside stepper motor via a bellow that allows the sample height to be adjusted in a range of ±7 mm. This wide range was chosen in order to allow for substrates of different thicknesses. Above the slide, a cross flange is mounted where the two side flanges are used for electrical feedthroughs of wires for sample heating, substrate bias voltage, and a thermocouple temperature sensor (compare Fig. 2.6). The sample carrier on top of the tube is made from boron-nitride (BN) ceramics and separated from the tube by three stainless steel screws giving thermal insulation and an additional rough sample height adjustment. The resistivity heater is located inside a Cu plate on top of the BN block and temperatures up to 700 °C can be reached. The sample substrate with a typical size of $15\times15 mm^2$ is spring-loaded to the Cu plate by two clamps, one of which is acting as the bias contact (see Fig. 2.6(b) – zone 3). The type-*K* thermocouple is located directly on the surface of the sample holder, near a corner of the substrate (protected with Mica). The sample height adjustment and the magnetron (power, sputter gas flow, shutter movements) are remote controlled from the control cabin outside the experimental hutch (Fig. 2.1).

Figure 2.7(a) shows the vertical scattering plane for the "old" set-up. In this scattering plane, the two symmetrically arranged circular windows with a diameter of 40 mm each are for beam entrance and exit. The height level of the sample to be investigated is 6 mm above the lower edge of those windows. This asymmetrical arrangement thus allows incidence and exit angles from –2° up to +16°. Those windows are used for reflectometry (with total scattering angles 2θ usually less than 10°) and symmetric large angle diffraction (with total scattering angles 2θ of maximum 32°). In the same plane, a second long window is located on the circumference with an angular range from 33° to 100°. It is foreseen for wide-angle vertical diffraction study under grazing incidence.

Despite the angular limitations one can study a large number of substances with widely varying crystal lattice parameters in this deposition chamber. The wavelength

tunability allows for an optimal adaptation to the substance under study. The absorption of X-rays by the windows is another point to be taken into experimental consideration. With the applied solution the X-rays have to penetrate 250 µm Kapton and 2 µm Al. The transmission coefficient for this combination is 0.78 at 8 keV (0.154 nm) and 0.98 at 17 keV (0.0709 nm) [58]. Thus, one has good conditions for diffraction studies even on very thin layers of low scattering power.

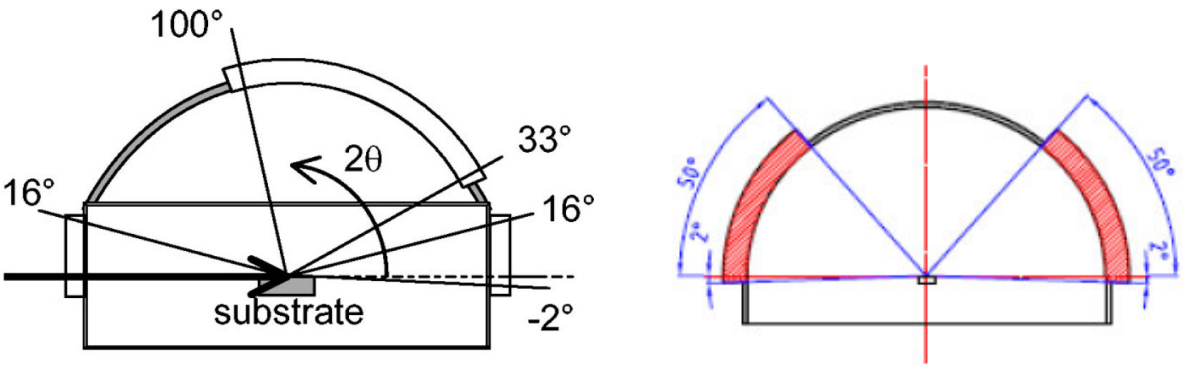

(a) (b)

Fig. 2.7: Scheme of the accessible angles in off-plane scattering geometry;
(a) "old" set-up [58], (b) "new" set-up [156].

With the new chamber, the base pressure was improved due to the Be windows. The enlarged windows of the "new" set-up also allow unhindered scattering access of –2 up to +50° off-plane [Fig. 2.7(b)]. This allowed studying for example the evolution of both the B2(211) and B2(310) peaks during deposition and further annealing, which was not possible before.

2.1.2. Experimental parameters at ROBL

The experimental studies performed during the present work have focused the following points:

- deposition of Ni-Ti films on different types of substrates, such as naturally and thermally oxidized Si(100) substrates, and MgO single crystal substrates;
- analysis of the role of a TiN buffer layer;
- influence of the presence of a bias voltage applied to the substrate;
- the characterization of graded films (controlled change of the Ti:Ni ratio *during* deposition).

For each situation, special attention was paid to the stability of the preferential orientation of the B2 phase along the deposition process, trying to answer the question of how and when the different textures generate. The introduction of Hf on the Ni-Ti system, in order to explore the feasibility of the *in-situ* sputtering equipment for future deposition of this type of ternary alloys has also been carried out.

In Tab. 2.1 are presented some processing parameters adopted in the present work. Further complementary information related with processing conditions will be given in the respective sections of Chapter 3 (Results).

Targets	Ni-Ti deposition	Ni-Ti (49 at% Ni - 51 at% Ti) and Ti (99.99%)
	NiTiHf deposition	Ni-Ti (51 at% Ni - 49 at% Ti) and Hf (99.99%)
Substrate bias voltage: V_b (V)	TiN deposition	−30
	HfN deposition	−30
Power applied to the magnetrons (W)	Near equiatomic Ni-Ti deposition	40 (Ni-Ti target) and 20 (Ti target)
	TiN deposition	80 (Ti target) : Ar/N_2 gas flow of 2/0.5 sccm
	HfN deposition	80 (Hf target) : Ar/N_2 gas flow of 2/0.5 sccm
Substrate temperature (°C)	≈ 470	
Base pressure/Working Ar pressure (Pa)	2×10^{-5} / 0.42	

Tab. 2.1: Processing parameters used in the present study.

A preliminary study has been performed (*ex situ*) to test the effect of different powers applied to the magnetrons on the film composition, which was obtained by RBS. Later, *in-situ* experiments were carried out focusing on the parameters selected on the basis of the RBS results. The RBS data obtained for the different samples allowed to find a relationship between the power applied to the magnetrons and the composition of the films. In Fig. 2.8 is shown the variation of the Ti content in function of the power applied to the Ti magnetron (for a constant power of 40 W applied to the Ni-Ti magnetron). These results have shown that a near equiatomic composition could be obtained using a power of 40 W for the Ni-Ti magnetron and a power of 20 W for the Ti magnetron. The growth rate was estimated as ≈ 0.1 nm/s and mainly near equiatomic Ni-Ti films with a thickness of ≈ 800 nm have been produced. The study of the power applied to the magnetrons on the NiTiHf film composition is shown in section 3.6.1. The parameters used for the TiN depositions were found based in

previous experiments performed at ROBL [59-61]. The substrate temperature and working pressure were chosen based in the previous work [25, 26].

Fig. 2.8: Atomic content of Ti in the Ni-Ti film *versus* DC sputtering power applied to the Ti magnetron (with a constant power of 40 W applied to the Ni-Ti magnetron).

The X-rays were monochromatized to $\lambda = 0.0675$ nm (18.367 k*e*V) in order to bring the relevant Bragg peaks of the B2 phase into the window openings and to reduce the time of the motor movements (reducing λ, the Bragg peaks fit in a shorter angular range – see Fig. 2.9). During film deposition and during subsequent annealing, repeated Bragg-Brentano, i.e. coupled θ–2θ scans were carried out, thus probing the diffraction vector situated in a plane perpendicular to the plane of deposition. These measurements can be used as an important indicator to study the degree of preferential orientation in the films. Planes parallel to the film surface are probed, thus the ratio of the intensity of different diffraction peaks can be utilized to determine whether a certain lattice plane is preferentially parallel to the surface of the film. In the case of a film with a random grain orientation, the obtained intensity ratios should be similar to what is tabulated in the powder diffraction database. The absence of certain peaks, or the detection of very intense peaks are normally associated with a preferred grain orientation in the film. In this work, these scans are intended to reveal the type of preferential orientation during the deposition process and to determine off-plane lattice parameter variations.

Low angle specular reflectivity time resolved at a fixed incidence angle was also employed to analyse the growth mode for the deposition on MgO single crystals. Thus, specularly reflected X-rays were measured in real-time with sensitivity for surface roughness. In the case of step-flow growth arriving adatoms are incorporated at existing step edges leading to a constant reflected intensity. When the atoms nucleate on a flat terrace and form two-dimensional (monolayer height) islands, the growth proceeds in a layer-by-layer fashion. This yields intensity oscillations due to the destructive interference between islands and terraces. The damping of these intensity oscillations is a measure of the quality of the layer-by-layer growth, i.e. its roughening. When no interlayer diffusion occurs, three-dimensional islands are created and 3D growth causes a monotonously decaying reflectivity.

Angular-resolved XRR has been used for growth rate calculations of the TiN buffer layers. From the Kiessig fringes (a sign of small surface and interface roughness) the film thickness could be determined. This was achieved using the Bede REFS computer code to fit the data [157]. Typically, due to increase surface roughness with film thickness, the Kiessig fringes vanish and the intensity decreases steeply already for low incidence angles on thicker films.

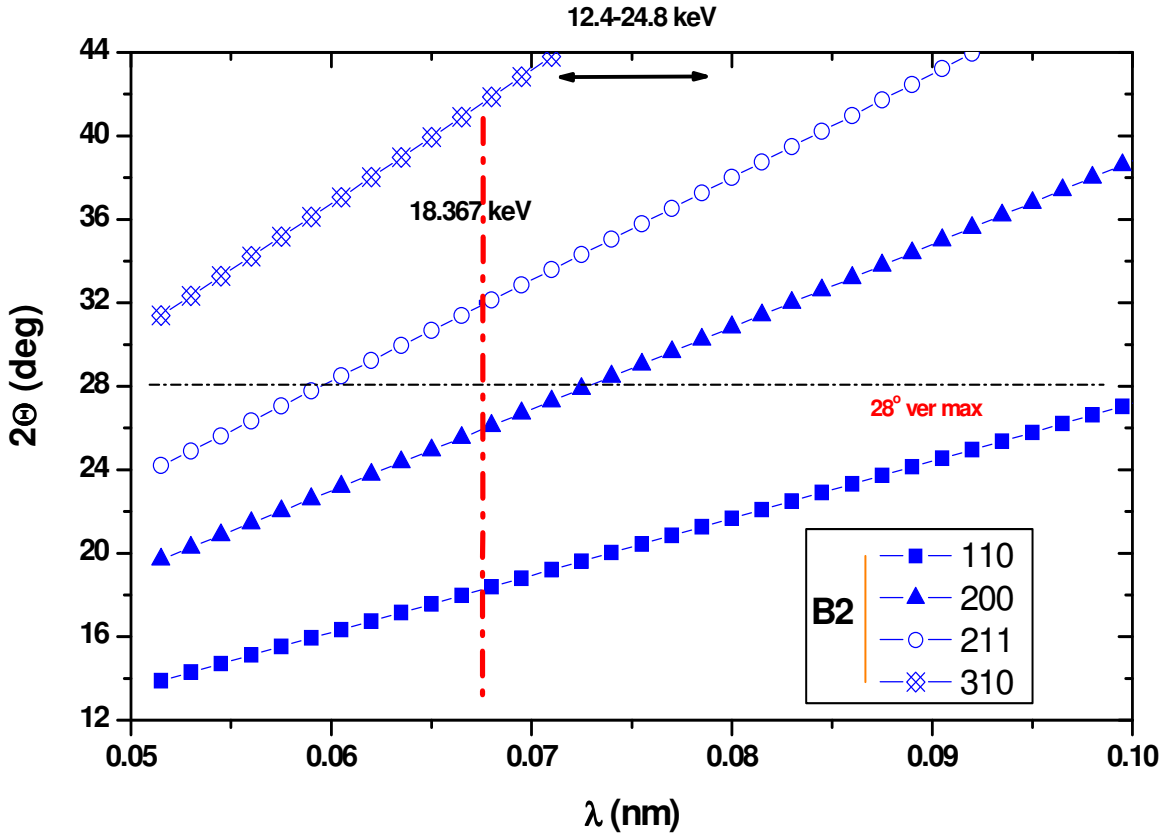

Fig. 2.9: Scattering angle 2θ *versus* wavelength/energy.

Brief overview of some selected topics analysed in this study:

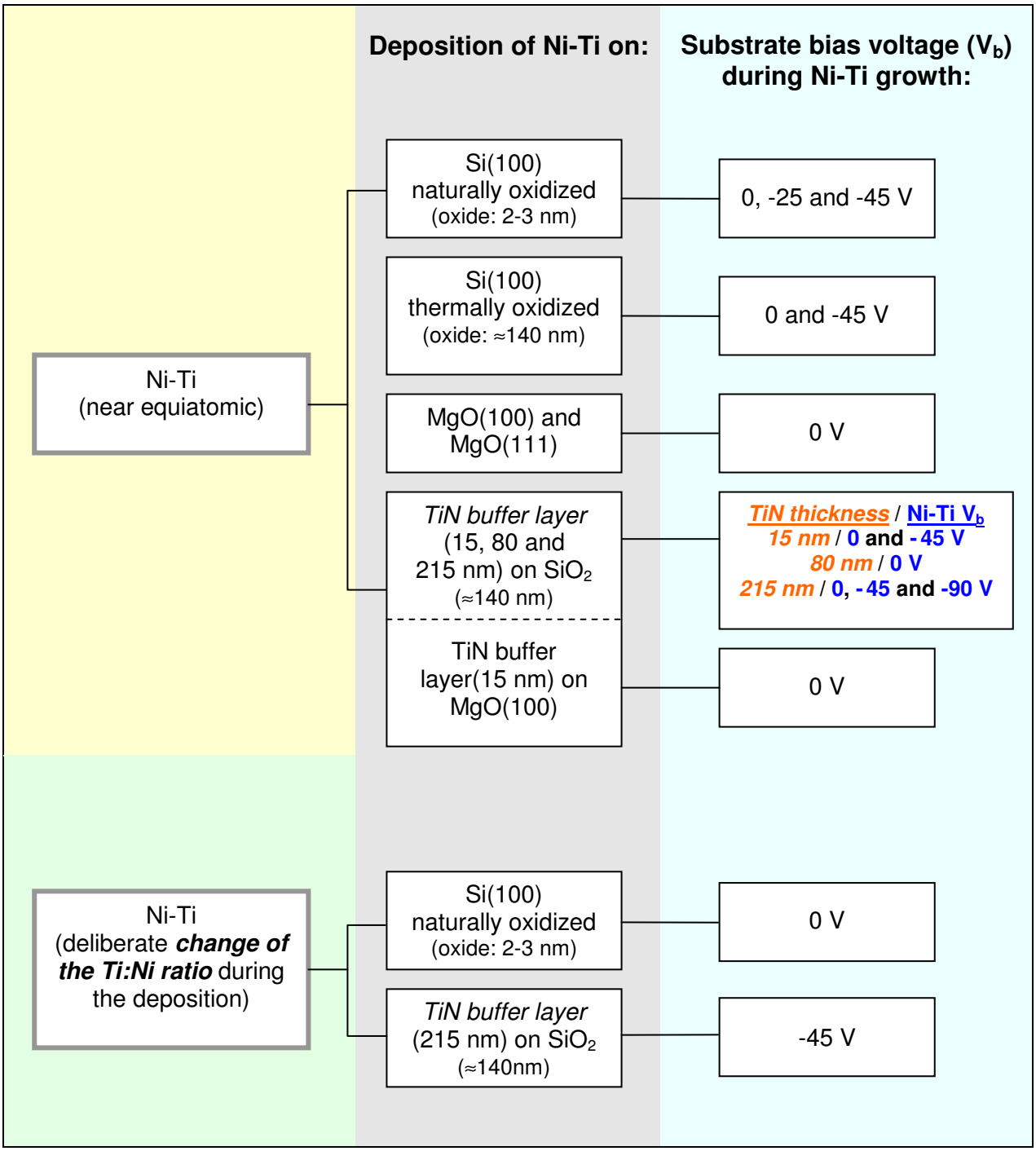

The parameters used for the measurements at ROBL are summarized in Tab. 2.2.

Energy (keV)	18.367
λ (nm)	0.0675
Standard beam size (mm)	20 (w) × 3 (h)
Beam aperture (mm)	XRR: 0.2 × 4 Bragg-Brentano: 0.4 × 4
Detector Slit (mm)	XRR: 0.22 Bragg-Brentano: 0.44

Tab. 2.2: Parameters used for the measurements at ROBL.

2.2. *EX-SITU* XRD CHARACTERIZATION

At the XRD laboratory of the Institute of Ion Beam Physics and Materials Research (at FZD), two equipments were also very useful for this work:

- Diffractometer D-5000 (BRUKER AXS);
- Diffractometer D-5005 (BRUKER AXS) with quarter-circle Eulerian cradle for powder diffraction, orientation of single crystals, and texture studies.

A series of samples was investigated by complementary *ex-situ* experiments at RT on the BRUKER AXS D5000 (Fig. 2.10) using Cu-K_α radiation. The diffraction experiments were performed in grazing incidence (incidence angle = 1º) geometry off-plane (GIXD), to control the penetration depth and to increase the sensitivity.

Fig. 2.10: Diffractometer D-5000 (BRUKER AXS).

Ni-Ti samples were also investigated by *ex-situ* XRD experiments at RT and 100°C on the BRUKER AXS D5005 diffractometer (Fig. 2.11) using Cu-K_α radiation in off-plane Bragg-Brentano geometry.

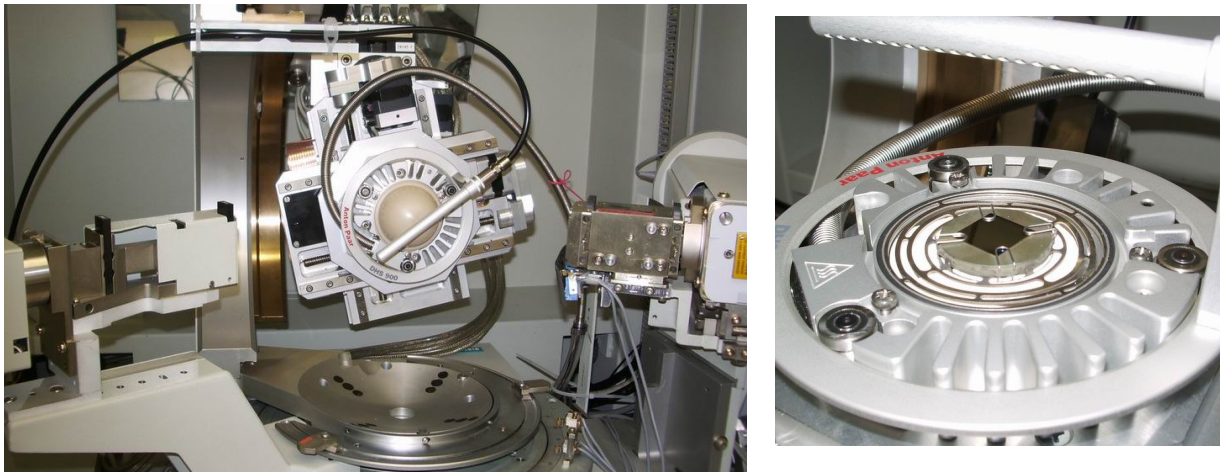

Fig. 2.11: Diffractometer D-5005 (BRUKER AXS) with an enlargement of the sample holder – configuration for XRD measurements at T≥ RT.

Texture measurements have been used to determine the preferential orientation of the grains in the samples. The result of a texture measurement can be plotted in a pole figure. This is often represented in polar coordinates consisting of the tilt (χ) and the rotation (φ) angles. A pole figure is measured at a constant 2θ scattering angle (corresponding to the Bragg diffraction angle of a certain (hkl) lattice plane) and consists of a series of φ-scans (azimuth in-plane rotation around the normal to the sample surface) at different tilt χ-(Eulerian) angle. The pole figure data is displayed as contour plots or elevation graphs with zero angle in the centre. Nevertheless, a single pole figure does not represent the complete texture information.

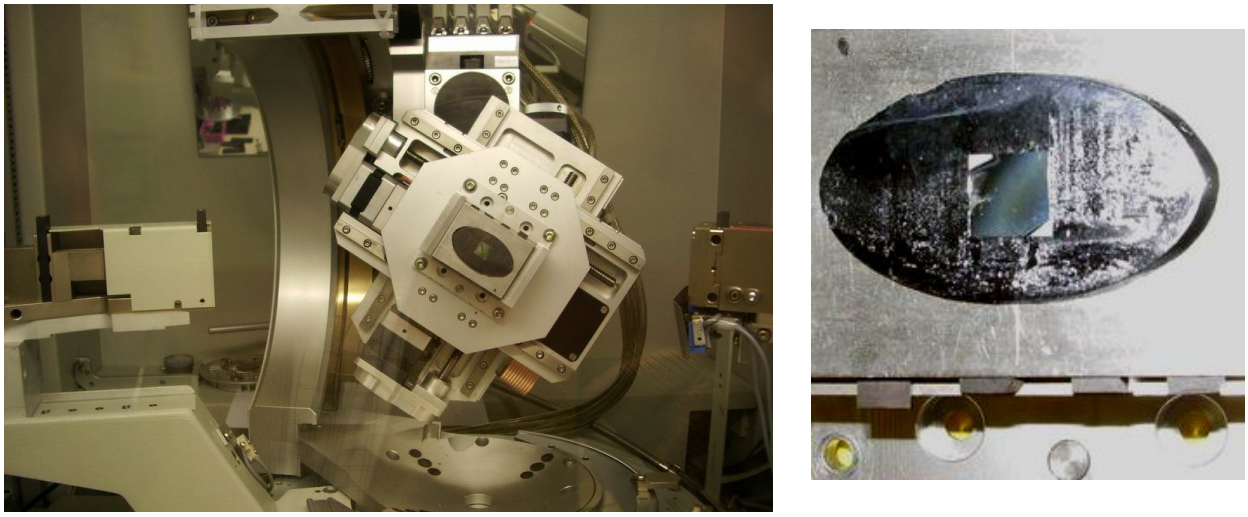

Fig. 2.12: Diffractometer D-5005 BRUKER AXS with enlargement of the sample holder – configuration for texture measurements. Picture taken during the determination of pole figures for a Ni-Ti film on MgO(100).

The pole figures have been determined for $0^\circ < \chi < 85^\circ$ and φ-scans in the range $0^\circ < \varphi < 360^\circ$, both with increments of 5°, at the laboratory source (BRUKER AXS D5005) with Cu-K_α radiation (Fig. 2.12) at FZD. A complementary experiment was also performed at CENIMAT using a diffractometer D-5000 BRUKER to identify the effect of the tilt of the magnetrons relative to the substrate.

2.3. RUTHERFORD BACKSCATTERING SPECTROSCOPY (RBS)

Rutherford Backscattering Spectroscopy (RBS) is a subset of what is commonly known as ion beam analysis (IBA). It is performed with energetic (typically a few hundred keV to a few MeV) ion beams from accelerators. RBS is based on elastic Coulomb scattering between the projectile and the target nuclei, and is usually applied to obtain data for most if not all elements present in the specimen. In a typical RBS analysis the scattered beam particles are usually detected at "back angles" (> 90° with respect to the beam direction) using a surface barrier detector.

During the RBS measurements the film was irradiated with 1.7 MeV He ions at normal incidence, and the backscattered primary ions were detected in a semiconductor detector set at 170° scattering angle according to their energy (set-up shown in Fig. 2.13). To analyse the data obtained, the spectra were simulated with the RUMP code [159].

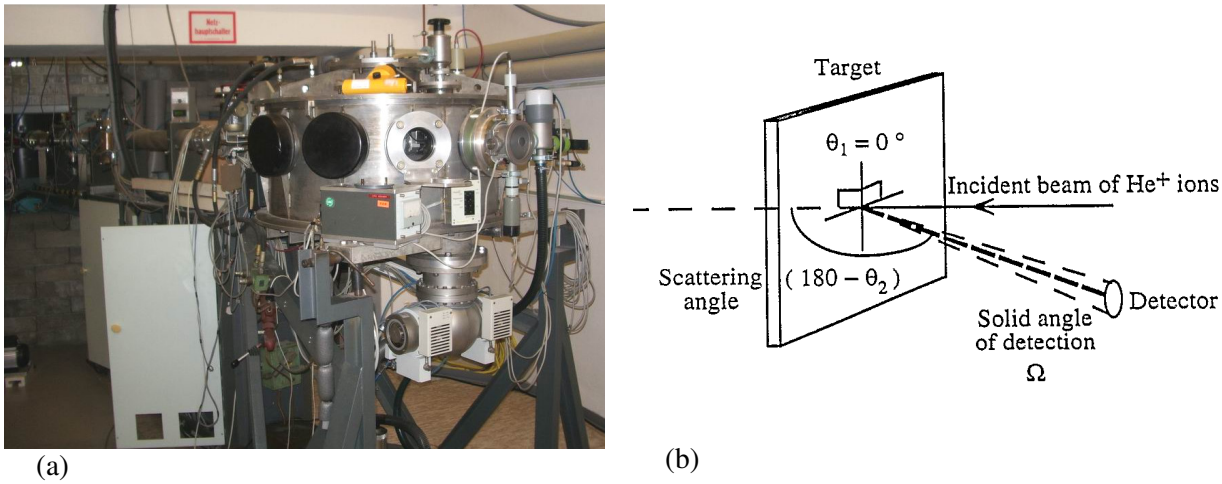

(a) (b)

Fig. 2.13: (a) RBS equipment, (b) Geometry of the RBS experiment [158].

This technique, usually non-destructive, can be very useful to examine the final composition of a sample. However, RBS could not be always successfully employed to analyse the final composition of the films deposited at ROBL during the *in-situ* studies. The thickness of the Ni-Ti films is typical around 800±80 nm after 2 h of deposition. Due to the

proximity of the Ni and Ti peaks and corresponding overlapping in the backscattering spectra, the simulation results do not exhibit enough resolution. Goldberg *et al.* [158] reported that for Ni-Ti films (100 nm or less), the backscattering spectra show separate peaks for each element (with He^+ at 4 MeV), i.e. no steps on the spectrum. In this case, the ratio of Ni and Ti in the sample can be obtained with excellent resolution simply by using the total number of counts under the peak corresponding to each element. They have even mentioned that since this technique is satisfactory only to the thinnest films, it can hardly be used for practical devices. Nevertheless, RBS was very useful, in the present work, to determine the deposition parameters to be used in the *in-situ* studies. *Ex-situ* depositions were performed to test the effect of different powers applied to the magnetrons on the film composition, which was obtained by RBS. For this purpose films (≈148-215 nm thickness) were deposited on graphite substrates in order to avoid the signal from Si substrates on the backscattering spectra. The depositions took place at ≈70°C to avoid interfacial reactions. Later, *in-situ* experiments were carried out at ROBL focusing on the specific parameters selected on the basis of the RBS results.

2.4. AUGER ELECTRON SPECTROSCOPY (AES)

Auger Electron Spectroscopy (AES) in conjunction with ion sputtering can be used to obtain depth profiles of elemental distribution in films. Depth profiling uses an ion beam to sputter the specimen surface. The surface sensitivity of AES means that only the top few monolayers that have been exposed by the ion beam are analysed, and as the ion beam erodes the sample, the intensity of several Auger transitions are followed. In this way an intensity profile as a function of time is obtained. With the knowledge of the sputtering rate, and the elemental sensitivities, this can be converted into concentrations with depth.

Normally, an Ar ion beam with energy between 0.5-5 keV (3 keV in the present work) is used for sputtering. The energy is chosen either to increase the sputtering rate, by choosing a high energy, or to reduce the effects of ion beam mixing on the depth resolution by using a lower energy. A Scanning Auger electron spectrometer Microlab 310F (Fisons) with field-emission cathode and hemispherical sector analyser [Fig. 2.14(a)] was used for the determination of depth profiles. The minimal lateral resolution with this instrument is 15 nm and the analysed area may be varied between 1.5 and some 100 μm^2. For the sputter depth profiles (with sample rotation) an electron beam of about 1 µm diameter was used.

Figure 2.14(b) shows the typical aspect of the Ni-Ti samples (indicated by the arrow) after the AES measurements.

Important information about the in-depth chemical composition profile for the different chemical elements in the film could be obtained. This technique provided also information linked to the interfacial reaction products (at the substrate/film interface) such as excess/depletion on some specific chemical element(s).

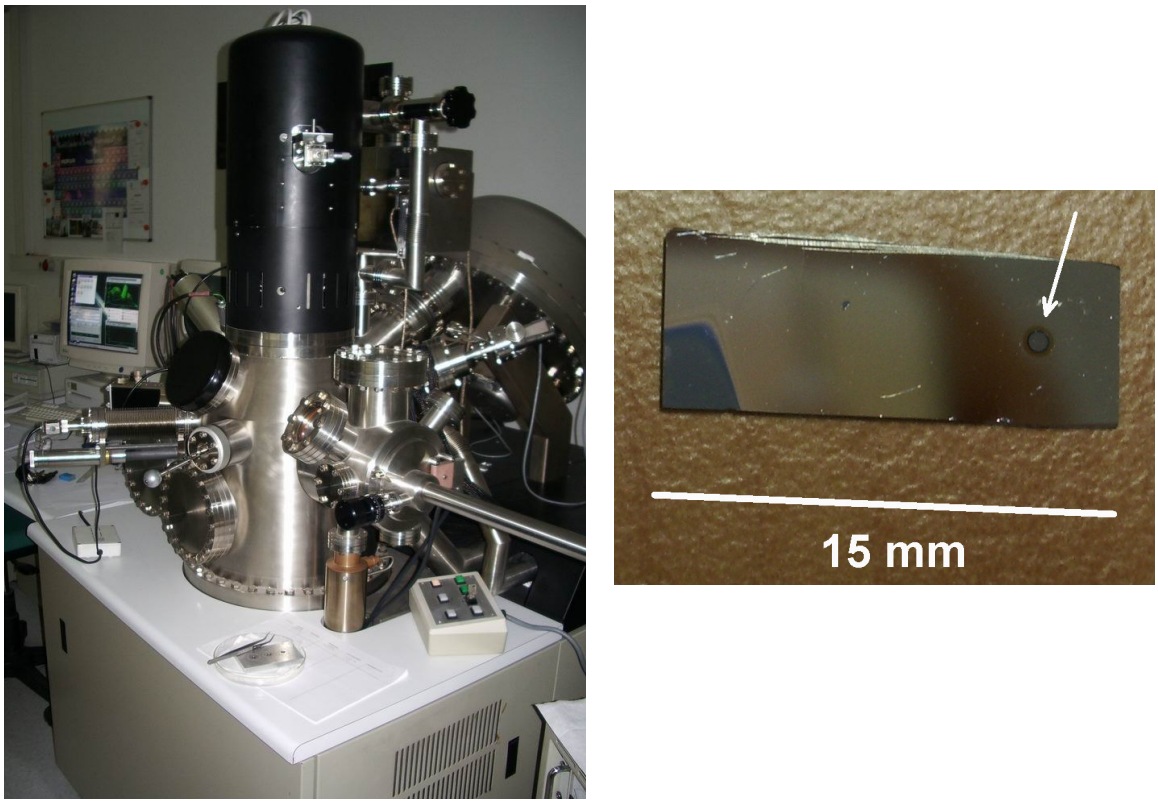

(a) (b)

Fig. 2.14: (a) AES spectrometer Microlab 310F (Fisons), (b) Aspect of a Ni-Ti sample after the AES measurement (investigated spot indicated by the arrow).

2.5. CROSS-SECTIONAL TRANSMISSION ELECTRON MICROSCOPY (X-TEM)

The conventional TEM involves the illumination of a transparent object by a beam of electrons, and the formation of a magnified image of the electron waves emerging from the object using an objective lens and two or more projector lenses. TEM is a versatile technique capable of characterizing the internal structure of a large variety of materials. This characterization includes not only the imaging of the microstructure directly but, at the same time, the identification of the phases present in the specimen by either electron diffraction or spectroscopic chemical analysis. The results obtained from a typical TEM characterization of

materials allow a better understanding of the relation between microstructure and properties. There are a rich variety of operation modes of the electron microscope. The bright field (BF) mode is commonly used to image grain and defect structures within materials. It can also reveal second phases such as precipitates and inclusions. The dark field (DF) imaging mode makes use of the specific Bragg diffracted electrons to image the region from which they originate. The DF mode enables the link between the crystallographic information and specific regions or phases in the sample. The primary purpose of the electron diffraction technique is to identify the crystal structure of the materials under investigation. By placing an aperture in the image plane, then projecting the diffraction pattern of that image onto the recording plate, one obtains the selected area electron diffraction (SAED) technique.

X-TEM observations were carried out on a Philips CM300 microscope (Fig. 2.15) with a LaB_6 filament at 300 keV (without intentional heating of the sample). For this purpose, the samples were prepared by gluing two pieces film to film and then cutting a perpendicular section, which was thinned by mechanical grinding. Final thinning to electron transparency was accomplished using 5 keV Ar^+ ion milling. The sample ready for microscopy is a disc of 3 mm in diameter thinned and having a small hole in the centre. Further information concerning the preparation of the samples for X-TEM is presented in Appendix C.

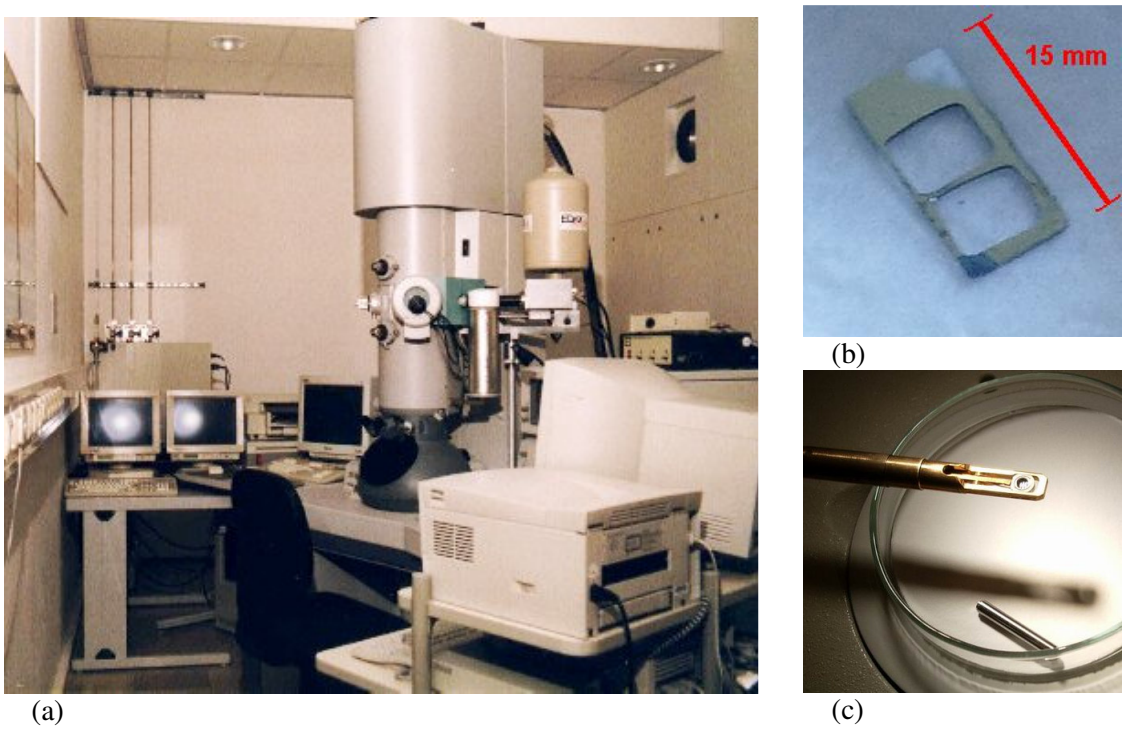

Fig. 2.15: (a) Transmission electron microscope CM300 SuperTWIN (Philips), (b) NiTi/SiO_2/Si(100) sample after removing the 2 pieces of 5×4 mm^2 each for TEM preparation, (c) sample holder *(double tilt).*

Characteristics of the equipment:

- TEM CM300 (300 kV) with LaB_6 - cathode and SuperTWIN-α lens (line resolution 0.14 nm);
- CCD Multi Scan Camera (GATAN) for digital imaging (including image processing);
- EDX unit (EDAX), S-UTW-window and Si-detector suitable down to Z = 5.

The TEM equipment is appropriate for high-resolution (HR) thus offering the possibility for lattice-fringe imaging of single-crystalline regions. For phase identification, electron diffraction, lattice imaging and imaging processing by FFT are used. The identification of elements in selected small regions as well as the element mapping of extended regions can be done using the supplementary analytical EDX-device. In this work, TEM observations were especially relevant for the study of the interface morphology, allowing the identification of the phases present resultant of interfacial reactions.

2.6. SCANNING ELECTRON MICROSCOPY (SEM)

Scanning Electron Microscopy (SEM) has been used in some cases to characterize the surface morphology of the films. It is known that when a Ni-Ti film undergoes a phase transformation, both its surface roughness and its refractive index change. A different surface morphology is thus expected for the B2, R and B19' phases. Energy dispersive X-ray spectroscopy (EDX) was also useful in some cases for a fast rough control of the film composition as well as to analyse the target's material composition and to detect possible impurities.

Fig. 2.16: Scanning electron microscope Hitachi S-4800 II.

Characteristics of the equipment (Fig. 2.16):

- Hitachi S-4800 with cold field emission cathode;
- 0.1 – 30 kV;
- Lateral resolution 1.0 nm at 15 kV, 2.0 nm at 1 kV;
- Sample move 0 – 110 mm in x- and y-direction, 1.5 – 40 mm in z-direction;
- Rotation 360°;
- Tilt –5 to +70°;
- Maximum sample size 150 mm in diameter, 23 mm height;
- IR-camera;
- Sample heating and cooling (–185 to 200°C);
- Electrostatic beam-blanking-unit;
- YAG backscattered electron detector;
- Analytic EDX accessory (Energy Dispersive X-ray Analysis) with digital pulse processor: INCA (Oxford Instruments) Si-detector with S-UTW-window, down to Z = 5 usable, 133 eV resolution.

2.7. ELECTRICAL RESISTIVITY (ER) MEASUREMENTS

In order to investigate the phase transformations, the temperature dependence of the electrical resistivity of the samples was measured using the four-probe van der Pauw geometry (BIO-RAD HL 5550, Fig. 2.17). Although the equipment at FZD has been used for this type of measurements, several experiments were also carried out at CENIMAT (both equipments have the same characteristics). A schematic of the van der Pauw configuration used in this work is shown in Fig. 2.17. As originally devised by van der Pauw [120], [121], one uses a "thin-plate" sample (simply connected, i.e., no holes or nonconducting islands or inclusions) containing four very small ohmic contacts placed on the periphery (preferably in the corners) of the "plate".

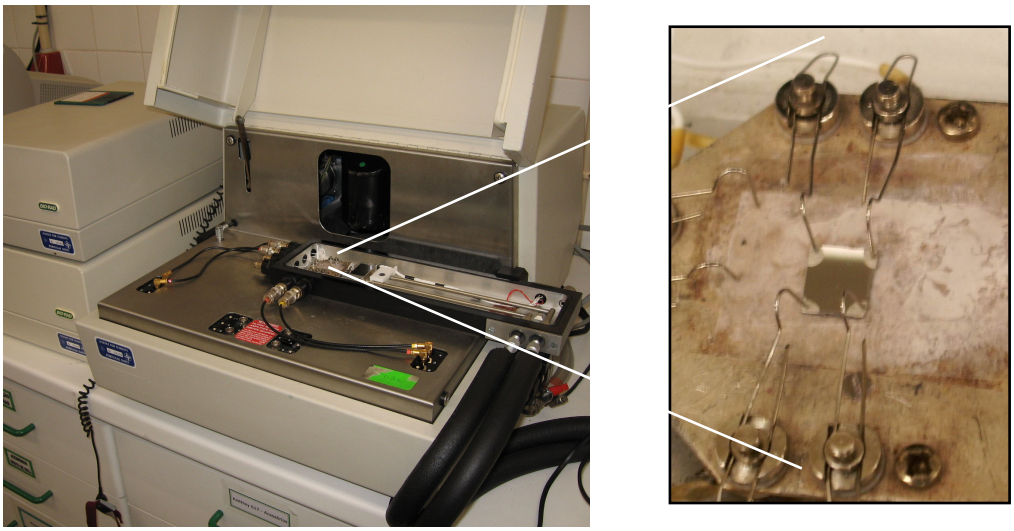

Fig. 2.17: Four-probe experimental apparatus (van der Pauw geometry) used to measure the electrical resistivity (ER) of the films (BIO-RAD HL 5550).

With this type of resistivity measurements it is possible to determine the sheet resistance R_S. Van der Pauw demonstrated that there are actually two characteristic resistances R_A and R_B, associated with the corresponding terminals shown in Fig. 2.18. R_A and R_B are related to the sheet resistance R_S through the following equation:

$$\exp(-\pi R_A/R_S) + \exp(-\pi R_B/R_S) = 1 \tag{2.1}$$

which can be solved numerically for R_S.

The bulk electrical resistivity ρ can be calculated using

$$\rho = R_S.d \tag{2.2}$$

where d is the thickness. To obtain the two characteristic resistances, a DC current I is injected between contact 1 and contact 2 and measures the voltage V_{43} from contact 4 to contact 3 as shown in Fig. 2.18. Next, the current I is injected between contact 2 and contact 3 while measuring the voltage V_{14} from contact 1 to contact 4. R_A and R_B are calculated by means of the following expressions:

$$R_A = V_{43}/I_{12} \text{ and } R_B = V_{14}/I_{23}. \tag{2.3}$$

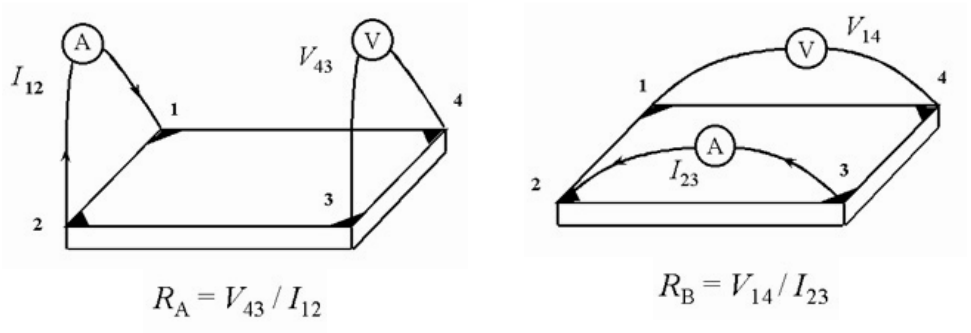

Fig. 2.18: Schematic of a rectangular van der Pauw configuration.

There are practical aspects that must be considered when carrying out resistivity measurements. Primary concerns are: (1) ohmic contact quality and size, (2) sample uniformity and accurate thickness determination, (3) the sample lateral dimensions must be large compared to the size of the contacts and (4) the sample thickness. Finally, one must accurately measure sample temperature, electrical current, and voltage.

The thermal cycles comprised (i) heating from RT up to 110ºC, followed by (ii) cooling down to –110ºC, and finishing by (iii) heating up to 110ºC. The analysis of the transformation characteristics was based on the cycles (ii) and (iii). The measurements were performed with the Ni-Ti films attached to the substrate.

Chapter 3

Results

3. RESULTS

This chapter includes the *in-situ* X-ray studies performed during the deposition (and subsequent annealing) of Ni-Ti SMA films, and their complementary *ex-situ* studies. The role of the substrate type and the influence of the deposition parameters (the substrate bias voltage, V_b, as well as the variation of the power applied to the magnetron with the Ti target during growth) on the preferential crystallographic orientation of the Ni-Ti B2 phase were investigated.

The results are presented in the following sequence:

Near equiatomic Ni-Ti films grown on:

- naturally oxidized Si substrates,
- thermally oxidized Si(100) substrates,
- TiN buffer layers,
- MgO single crystals.

Controlled change of the Ti:Ni ratio during the deposition of Ni-Ti on:

- naturally oxidized Si(100) substrates,
- a TiN buffer layer.

The results, for each substrate type, are divided into two subsections:

1) the information obtained from the *in-situ* XRD measurements at ROBL,
2) results of the measurements performed with the complementary *ex-situ* techniques.

The tests concerning the deposition of NiTiHf SMA films showing prospective results for future deposition of this type of ternary alloys are reported in the last section of the chapter.

3.1. NEAR EQUIATOMIC Ni-Ti FILMS GROWN ON NATURALLY OXIDIZED Si SUBSTRATES

The processing conditions of the samples deposited on naturally oxidized Si substrate (2-3 nm native oxide) are presented in Tab. 3.1.

Substrate type	V_b (V)	Deposition time (min.)	Annealing time (min.)	Deposition and annealing temperature (°C)
Si(100)	0	143	0	≈ 470
Si(100)	-25	121	136	≈ 470
Si(100)	-45	122	60	≈ 470
Si(111)	0	123	146	≈ 470

Tab. 3.1: Process conditions of near equiatomic Ni-Ti films deposited on naturally oxidized Si substrate in the sputtering chamber of the beamline ROBL at ESRF.

3.1.1. *In-situ* experiments

Figure 3.1 shows examples of *in-situ* XRD spectra of a homogeneously growing film of B2 phase obtained at ROBL. The film was deposited on naturally oxidized Si(100) substrate and no substrate bias voltage (V_b) was applied during the processing of the sample.

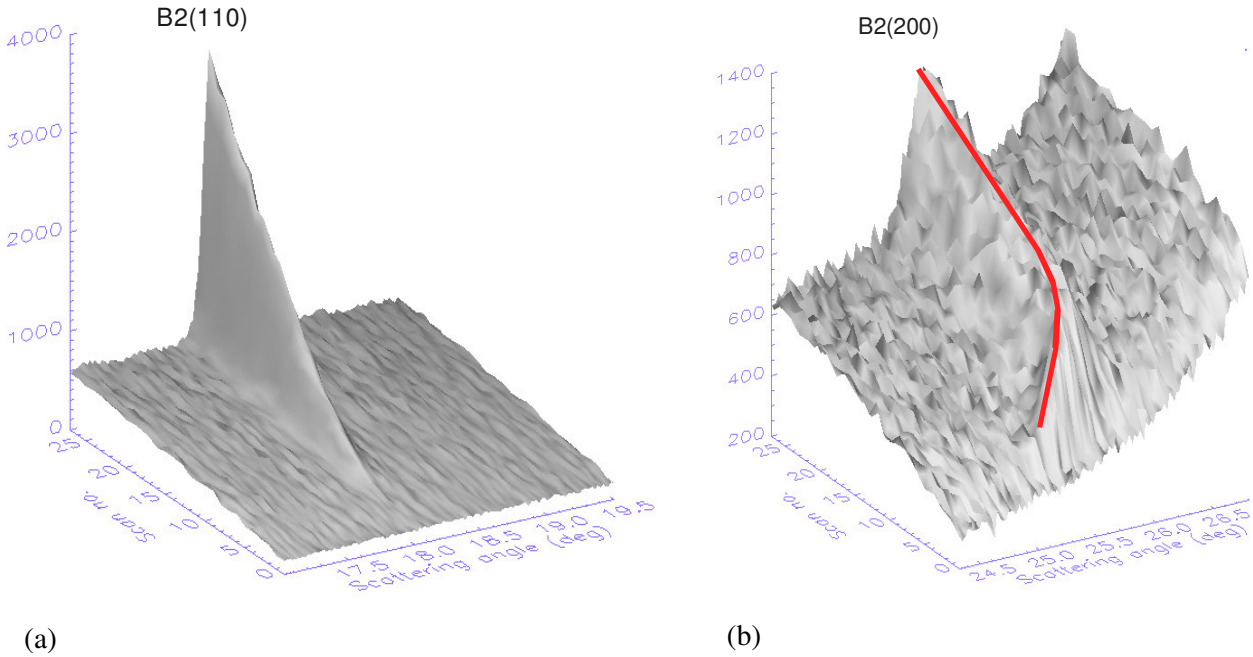

(a) (b)

Fig. 3.1: XRD peak intensities during continuous co-sputtering of Ni-Ti for 143 min without V_b on a naturally oxidized Si(100) substrate. Each scan corresponds to ≈ 2 min deposition; (a) in the diffraction range $17.0^o<2\theta<19.5^o$ and (b) in the range $24.3^o<2\theta<26.8^o$ (the z-axis scale represents the detector intensity in cps).

Figure 3.2(a) shows the variation of the net areas of the (110) and (200) peaks of the Ni-Ti B2 phase as well as that of the lattice parameter, a_0 (as calculated from $d_{(110)}$ and $d_{(200)}$ according to the corresponding XRD peak positions), as a function of deposition time for the Ni-Ti film from Fig. 3.1. After the growth of an initial layer with the {200} planes parallel to the surface during the first 30 min (≈ 180 nm thick, taking into account that the growth rate was estimated as ≈ 0.1 nm/s), the B2(200) peak intensity saturates and stays constant. The

B2(110) peak intensity was linearly growing, starting from the B2(200) peak intensity stabilization, until the end of the deposition. An initial significant change of a_0 as calculated from $d_{(200)}$ is observed and its tendency for stabilization is coincident with the deposition time where the preferential stacking of B2 phase on (110) planes is starting (after ≈ 30 min deposition). The evolution with time of the calculated a_0 suggests that at the beginning of the deposition, the film experiences compressive stresses, which are significantly relaxed as the film grows.

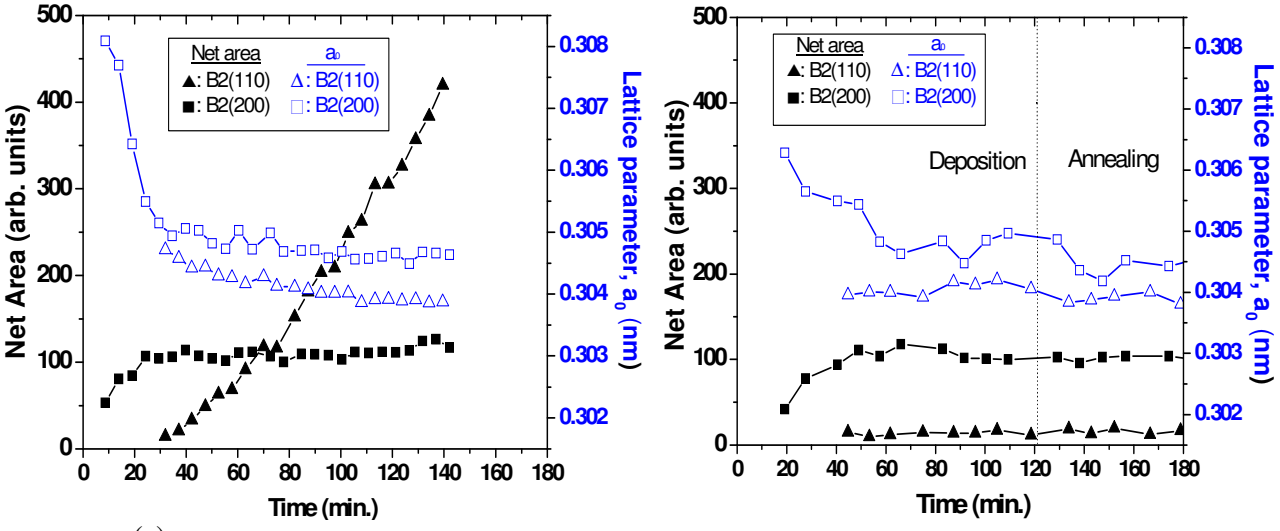

Fig. 3.2: The net areas of the Bragg-Brentano B2(110) and B2(200) diffraction peaks and the lattice parameter a_o, as obtained from the positions of the respective peaks, recorded as a function of time after start of Ni-Ti film growth on naturally oxidized Si(100); (a) deposited without applying V_b, (b) deposited with a V_b of −25 V.

Figure 3.2(b) represents the variation of the net areas of the B2(110) and B2(200) peaks, and the variation of a_0 as a function of time, again for a sample deposited on a naturally oxidized Si(100) substrate, with a V_b of −25 V. When a V_b is applied during the deposition of Ni-Ti on naturally oxidized Si(100), the net area of B2(110) shows a different trend, as compared to the sample deposited without V_b. A first layer with the {h00} planes parallel to the substrate surface was again observed. After approximately 40 min of deposition, B2(200) diffraction peak gets saturated and the B2(110) peak was detected. Both peak intensities stayed almost constant until the end of the deposition and on further annealing (at the same temperature of deposition ≈ 470°C). The variation of a_0 approached the values of the sample deposited without V_b. In order to detect other possible Bragg-Brentano XRD peaks of the B2 phase, an XRD scan, in a larger range, was performed during the annealing period. At $2\theta \approx 41.12°$, a high intensity of the B2(310) diffraction peak could be observed showing that a significant number of grains exhibit (310) parallel to the film surface (result not shown here).

Further, an experiment was performed by applying a V_b of −45 V. This time the B2(310) diffraction peak was monitored *in situ*. Similar to the previous experiment (with −25 V), after the stabilization of the B2(200) peak intensity, the intensity of B2(110) gradually increase. Furthermore, once the B2(200) peak intensity saturates the B2(310) diffraction peak was observed – Fig. 3.3(a). However, its intensity was not comparable to that of the B2(110) peak in the case of the deposition performed without V_b. The values obtained for a_0 show a convergence to a common value [Fig. 3.3(b)], which was not observed in the previous two experiments (without applying V_b and deposition with V_b = −25 V).

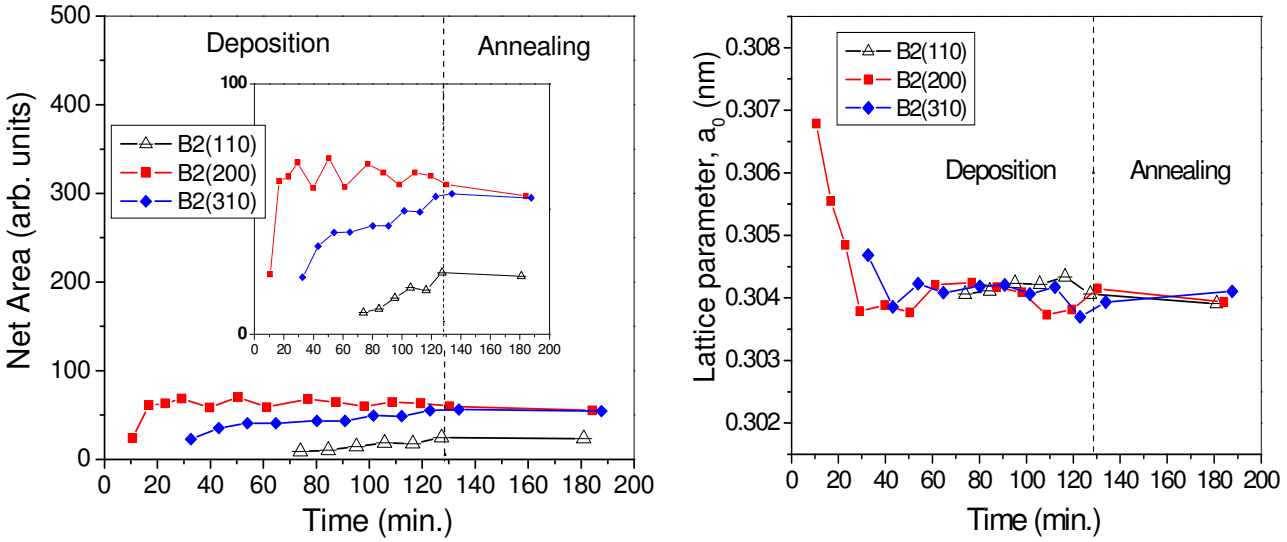

Fig. 3.3: Results obtained for the Ni-Ti sample deposited on naturally oxidized Si(100), with V_b = −45 V, recorded as a function of time after start of film growth; (a) the net areas of the Bragg-Brentano B2(110), B2(200) and B2(310) diffraction peaks, (b) a_o as obtained from the positions of the respective peaks.

Figure 3.4 shows the respective XRD spectra (with V_b = −45 V) obtained during annealing after deposition at ≈ 470°C and after subsequent cooling, at RT. Grains of the B2 phase showing the (310) orientation parallel to the film surface presented a considerable scattering fraction when compared to the other diffraction peaks of the B2 phase (see diffractogram obtained at ≈ 470°C). Furthermore, the B2(310) peak was no longer visible after cooling to RT since the B2 ⇒ R-phase transformation has occurred.

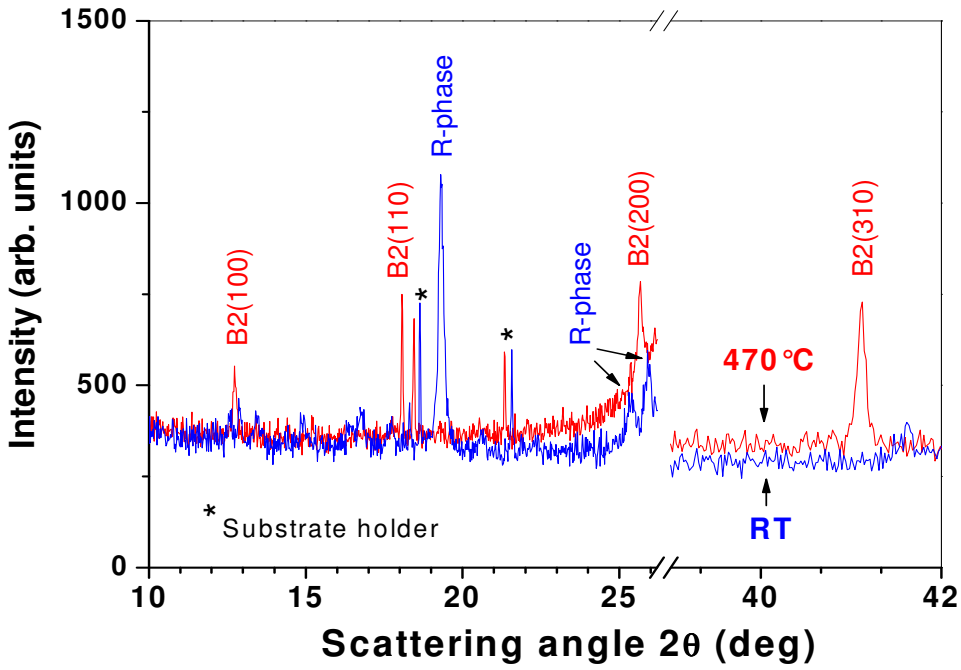

Fig. 3.4: XRD spectra from a Ni-Ti sample deposited with a V_b of –45 V on naturally oxidized Si(100), during annealing after deposition stop at 470°C and at RT.

The deposition of Ni-Ti on naturally oxidized Si(111) substrates without applying a substrate bias voltage was also studied. The net areas calculated from the B2(110) and B2(200) diffraction peaks recorded as a function of time during the film growth, as well as the values calculated for a_o, are shown in Fig. 3.5. There was a preferential development of the B2(200) peak intensity when compared with the B2(110) peak. The presence of faint intensities of the B2(310) were detected by performing a measurement in a higher 2θ range during annealing after the deposition is stopped (results not shown here). The values obtained for a_o as calculated from B2(110) and B2(200) show a convergence to a common value (≈ 0.303 nm), which is lower than the values observed in the experiments using naturally oxidized Si(100) substrates with and without V_b.

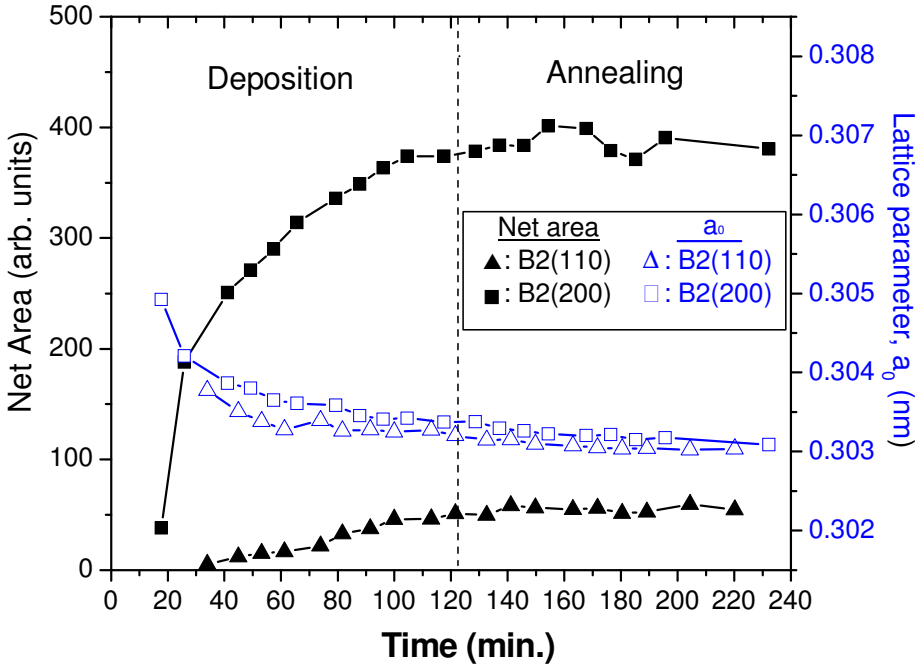

Fig. 3.5: The net areas of the B2(110) and B2(200) diffraction peaks recorded as a function of time after start of Ni-Ti film growth, as well as the values obtained for a_o, on naturally oxidized Si(111) without V_b.

3.1.2. *Ex-situ* characterization

The composition control of the films is a fundamental aspect to achieve the desired shape memory properties in the Ni-Ti films (see 1.3.1. Composition control). Although the deposition parameters for the production of near equiatomic Ni-Ti films have been optimised during preliminary *ex-situ* depositions, the composition of several samples obtained during the present *in-situ* studies was also investigated. An example of depth profiles of the atomic concentrations in the Ni-Ti films deposited on naturally oxidized Si(100) without V_b is shown in Fig. 3.6. The results prove a near equiatomic composition and it is also perceptible an interfacial diffusion as demonstrated by the presence of Ni inside the Si(100) substrate.

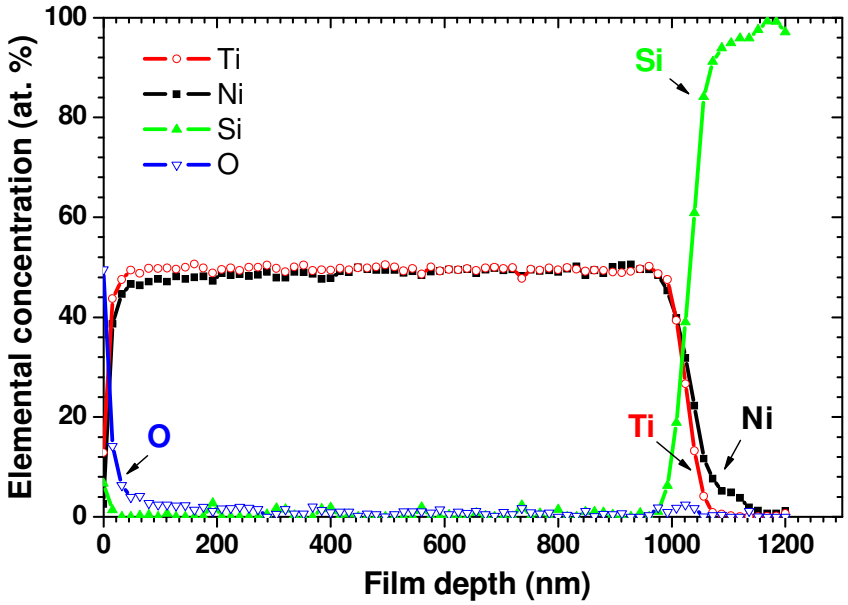

Fig. 3.6: AES elemental concentration profiles for a Ni-Ti sample on naturally oxidized substrate deposited without V_b.

The interface structure of several samples was also investigated by X-TEM in order to put in evidence the relationship between the substrate type and the interface morphology. It is known that the reaction layer can affect film properties considerably when its thickness is comparable to film thickness, as it has been already described (1.3.4. Interfacial film/substrate reactions).

A detailed analysis of the morphology of the interface Ni-Ti/naturally oxidized Si(100) was performed resulting in the identification of several phases. The experimental results obtained by X-TEM show that for the deposition temperature used, Ni atoms are the main species diffusing at the Ni-Ti/Si interface resulting in the growth of $NiSi_2$ growing towards the Si substrate (Fig. 3.7). The formation of A-$NiSi_2$ and B-$NiSi_2$ precipitates in the Si substrate was detected [Fig. 3.7(a)]. A-precipitates grow epitaxially to the Si host lattice with growth fronts {111} resulting in a semi-octahedron shape. $NiSi_2$ precipitates with a twin orientation (rotation by 180º around the [111]) were as well found in the Si(100) substrate. These silicides are reported as B-$NiSi_2$ and they exhibit a rod shape with a facetted growth front (see inset of Fig. 3.7(b) – dark field micrograph). B-$NiSi_2$ could be observed deeper inside the Si(100) substrate when compared with the A-$NiSi_2$.

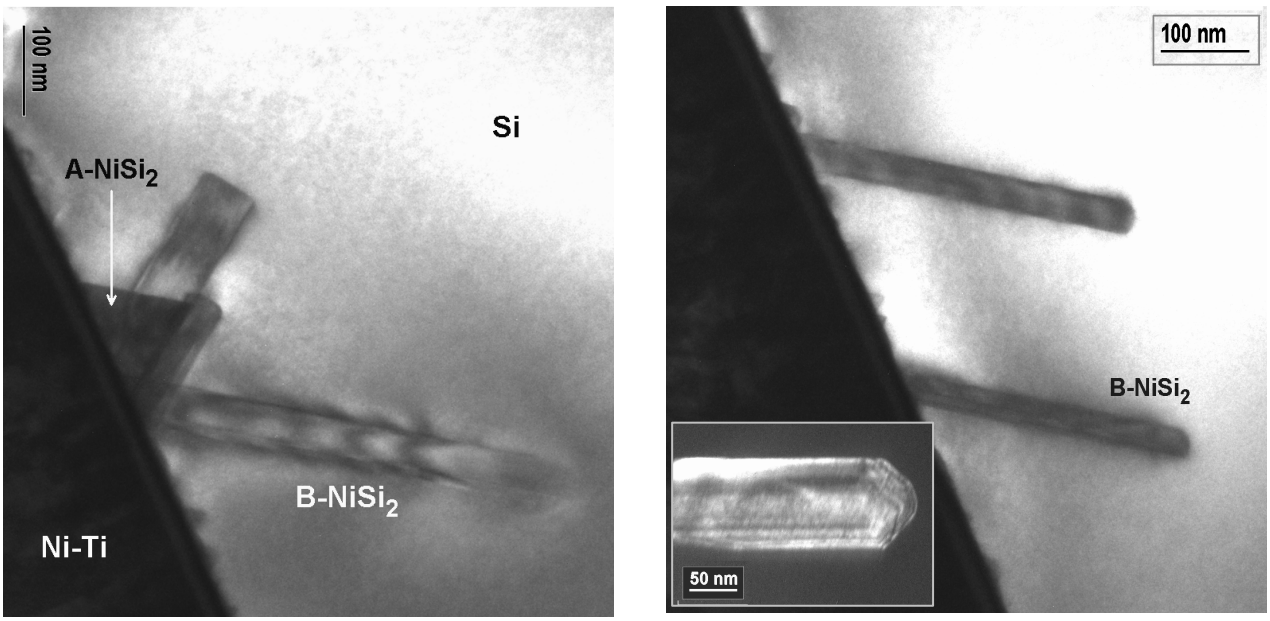

(a) (b)

Fig. 3.7: X-TEM micrographs of the Ni-Ti film grown on naturally oxidized Si(100) without V_b; (a) two types of interfacial reaction products are perceptible in the image (A-$NiSi_2$ and B-$NiSi_2$), (b) X-TEM micrographs focusing the presence of the B-$NiSi_2$ in the Si(100) substrate.

The main micrograph in Fig. 3.8 shows that A-$NiSi_2$ silicides grow epitaxially towards the Si substrate with growth fronts {111} resulting in a semi-octahedron shape. A deeper insight into the circled area can be found in the inset of the figure. In the substrate Si oxide layer, it is possible to distinguish the presence of disruptions. The $Ti_4Ni_4Si_7$ compound (identified by cross-section HR-TEM) nucleated between the oxide layer and the A-$NiSi_2$. It can be expected that at higher temperatures the tendency would be to grow into the A-$NiSi_2$ and the Si substrate (as observed by Wu *et al.* [130]). Between the Ni-Ti film and the oxide layer [the (Si, O)-rich layer, i.e. the native silicon oxide of the Si substrate], another layer can be distinguished (lighter grey in the micrograph). It was possible to conclude, by electron dispersive X-ray spectroscopy (EDX) performed in a sample with analogous interface morphology (3.5.1.2. *Ex-situ* characterization), that this layer contains not only Ni and Ti but also Si (identified as Ti, Ni, Si in Fig. 3.8). However, the structural analysis by cross-section HR-TEM did not detect the presence of crystalline order.

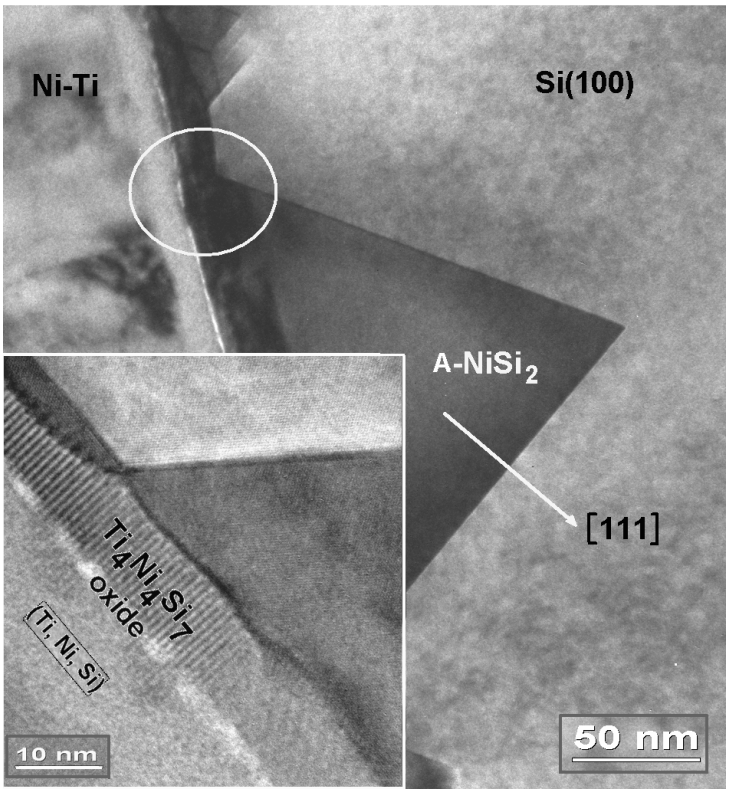

Fig. 3.8: X-TEM micrographs of the interface's morphology obtained on a sample grown on naturally oxidized Si(100) without V_b. The main micrograph shows that A-$NiSi_2$ grows epitaxially towards the Si substrate with growth fronts {111} resulting in a semi-octahedron shape. The inset represents the circled region in HR-TEM.

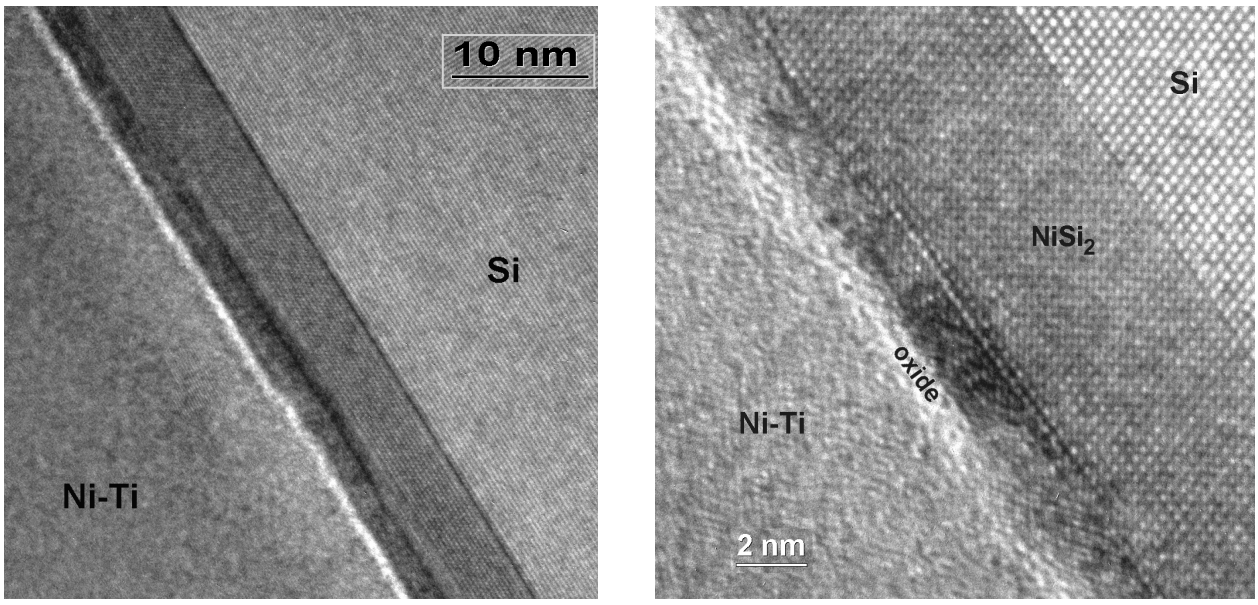

(a) (b)

Fig. 3.9: X-TEM micrographs of a sample obtained on naturally oxidized Si(111) substrate (without V_b); (a) overview of the Ni-Ti/Si(111) region, (b) HR-TEM enlargement of the interfacial diffusion zone.

Results obtained on Ni-Ti samples on naturally oxidized Si(111) substrates (deposited without V_b) confirmed that $NiSi_2$ grows epitaxially on silicon. The micrographs from Fig. 3.9 show that the $NiSi_2$ grows along Si<111>. In this case, instead of the semi-octahedron shape observed for the deposition on Si(100), a uniform thickness plate appeared due to the alignment between substrate orientation and the (111) growth front. Ni diffuses preferentially along <111> as it can be observed by comparing the deposition on Si(100) and Si(111) substrates.

It is important to point out that the micrographs presented in Fig. 3.10 were recorded along the Si[110] zone axis. In Fig. 3.10(a) $NiSi_2$ precipitates showed up as bright regions due to their particular alignment with the Si substrate. Theoretically, it is estimated that the angle between the (111) planes of Si is 70.53°. A white line was inserted in Fig. 3.10(b) to emphasize the orientation relationship between the $NiSi_2$ precipitate and the Si substrate since it shows an angle of ≈ 70° with the substrate surface.

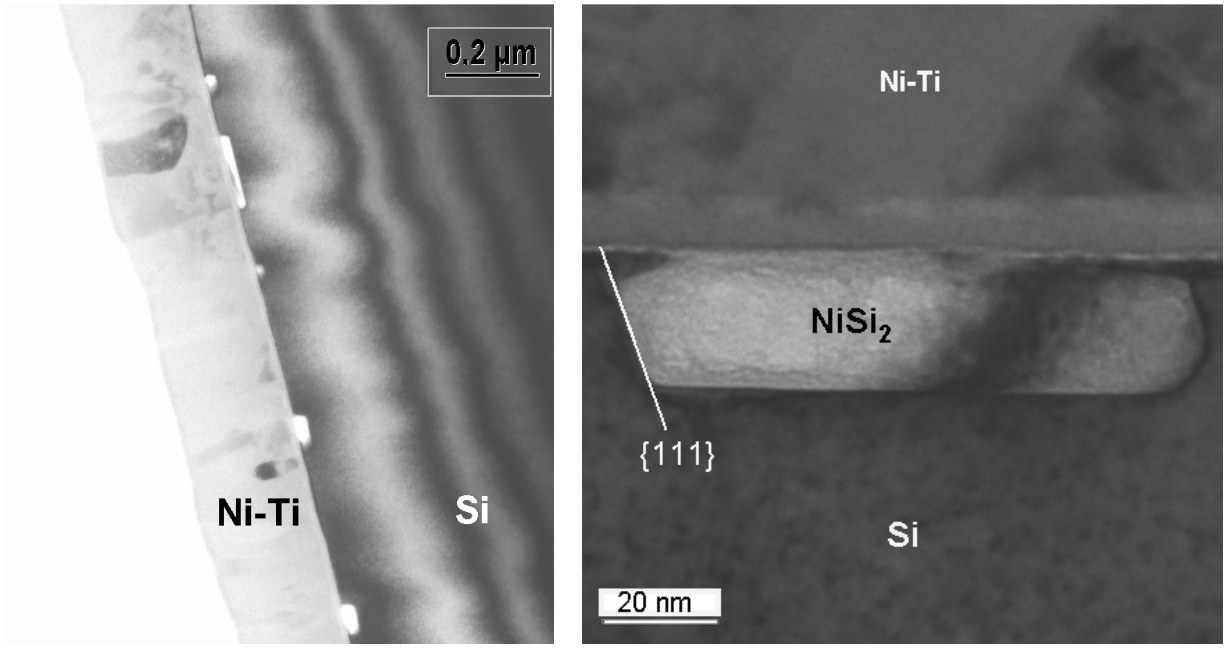

(a) (b)

Fig. 3.10: X-TEM micrographs of a Ni-Ti/Si(111) sample deposited without V_b (recorded along the Si[110] zone axis); (a) overview over the sample cross-section, (b) micrograph focusing the presence of the $NiSi_2$ in the substrate (the angle between the line and the substrate surface is roughly 70°).

When comparing the results obtained with Si(100) and Si(111) substrates (i.e., the epitaxial growth of $NiSi_2$), a complementary Ni-Ti sample was produced (*ex-situ*, without V_b) using a poly-Si intermediate layer with a thickness of ≈ 500 nm (Si without a defined orientation). The production of the poly-Si layer previously obtained at 675°C on naturally

oxidized Si(100) by LPCVD is described in the literature [160]. X-TEM observations (Fig. 3.11) revealed that the diffusion of Ni into the poly-Si is inhomogeneous. Preferential diffusion was found along the columnar grains of poly-Si, which were favourably aligned for Ni diffusion. In Fig. 3.11(c) it is possible to observe that the diffusion process stops at the next grain.

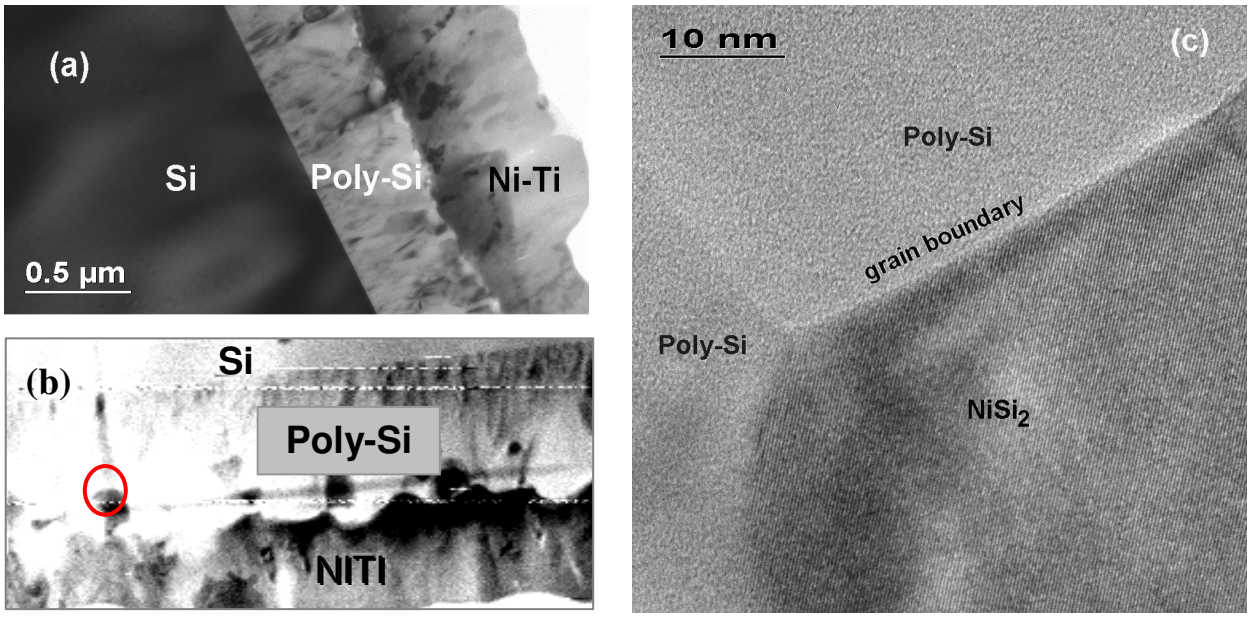

Fig. 3.11: X-TEM micrographs of the Ni-Ti film grown without V_b on an intermediate layer of poly-Si; (a) overall morphology, (b) micrograph with indication of the area (circle) studied in (c), (c) cross-section HR-TEM image showing Ni diffusion into the poly-Si layer.

The results presented in this section have shown that on naturally oxidized Si(100) substrates, without V_b, the Ni-Ti B2 phase starts by stacking onto (h00) planes, and as the thickness increases, evolves into a (110) fibre texture. When a V_b is applied during the growth of the Ni-Ti film, a first layer with the (h00) planes parallel to the surface is as well observed. Nevertheless, after the intensity stabilization of the B2(200) diffraction peak, the development of the B2(110) peak is not observed. In this case, as suggested by the intensity of the B2(310) diffraction peak, grains of the Ni-Ti B2 phase grow with a tilting (relative to the substrate) that favours (310) scattering.

The *ex-situ* AES and TEM observations allowed the identification of a significant interfacial diffusion and chemical interactions at the interface Ni-Ti/naturally oxidized Si substrates. The study of the interfacial zone of Ni-Ti films deposited on Si substrates with different types of orientation put in evidence the relationship between the Si orientation and the interface morphology.

3.2. NEAR EQUIATOMIC Ni-Ti FILMS GROWN ON THERMALLY OXIDIZED Si(100) SUBSTRATES

The processing conditions of the samples deposited on thermally oxidized Si(100) substrate (≈ 140 nm amorphous SiO_2 capping layer) are presented in Tab. 3.2.

V_b (V)	Deposition time (min.)	Annealing time (min.)	Deposition and annealing temperature (°C)
0	136	32	≈ 470
–45	128	83	≈ 470
0	119	78	≈ 520

Tab. 3.2: Process conditions of near equiatomic Ni-Ti films deposited on thermally oxidized Si(100) substrate in the sputtering chamber of the beamline ROBL at ESRF.

3.2.1. *In-situ* experiments

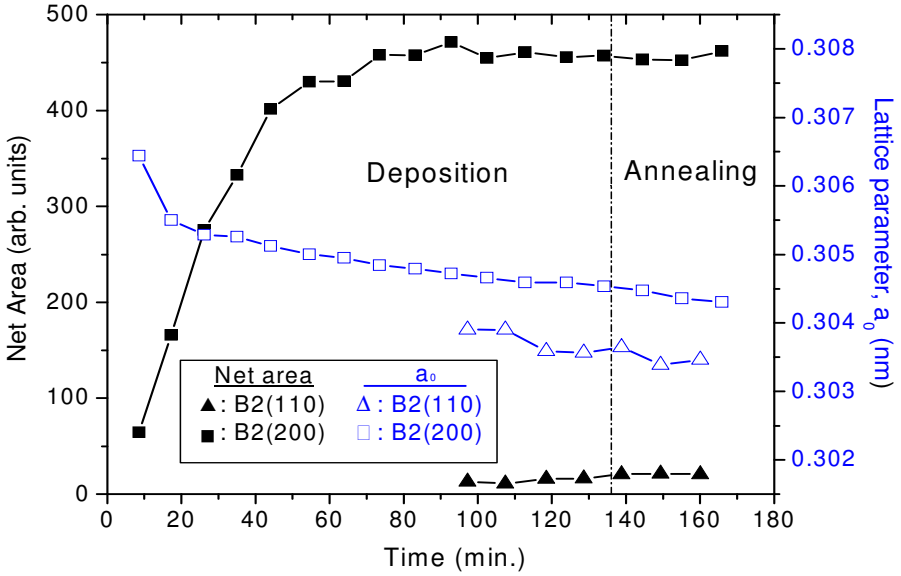

Fig. 3.12: The net areas of the B2(110) and B2(200) diffraction peaks and the values obtained for a_o, represented as a function of time after start of Ni-Ti film growth on thermally oxidized Si(100) without V_b.

In the case of the Ni-Ti film grown on thermally oxidized Si(100) without V_b (Fig. 3.12), there was a strong preferential stacking on (h00) planes of B2 phase leading to a <100> fibre texture. However, after approximately 70 min of deposition (≈ 540 nm film thickness), a stabilization of the intensity of the B2(200) diffraction peak was observed. The B2(110) peak was detected but, in contrast to the deposition on naturally oxidized substrate without V_b, it is then increasing very gradually. This phenomenon will be analysed in the subsection 3.2.2. Considering the evolution of a_o of the B2 phase for the Ni-Ti film deposited

on a thermally oxidized Si(100) substrate without V_b (Fig. 3.12), the initial decrease of the a_o value was not as pronounced as for the film deposited on naturally Si(100) without V_b. Here, during the whole film processing, a continuous slight decrease of a_o, as calculated from $d_{(200)}$, was perceptible.

An experiment was also performed in order to analyse the effect of ion bombardment (using a V_b of –45 V) during Ni-Ti film growth on thermally oxidized Si(100) substrate. The results are shown in Fig. 3.13. In this case, the (100) peak intensity starts growing and stabilizes at a relatively lower value. Then, (110) peak intensity starts growing, after ≈ 70 min of deposition. However, the intensity of the B2(110) peak, when compared with the Ni-Ti film deposited on naturally oxidized Si(100) without V_b, is much lower. The results obtained for the samples deposited on naturally and thermally oxidized Si(100) substrates [Fig. 3.3(a) and Fig. 3.13(a)] show that for this type of substrates a V_b of –45 V has led to a considerable reduction of the net areas of the B2(110) and B2(200) Bragg-Brentano diffraction peaks. The values of a_o of B2 phase showed two very different features [Fig. 3.13(b)], as compared to the previous sample:

(i) the relative magnitude of the a_o values is reversed [a_o calculated from $d_{(200)}$ is smaller than the one calculated from $d_{(110)}$] and,

(ii) instead of a continuous decrease of both values of a_o as a function of time, a convergence to an intermediate value of a_o was observed.

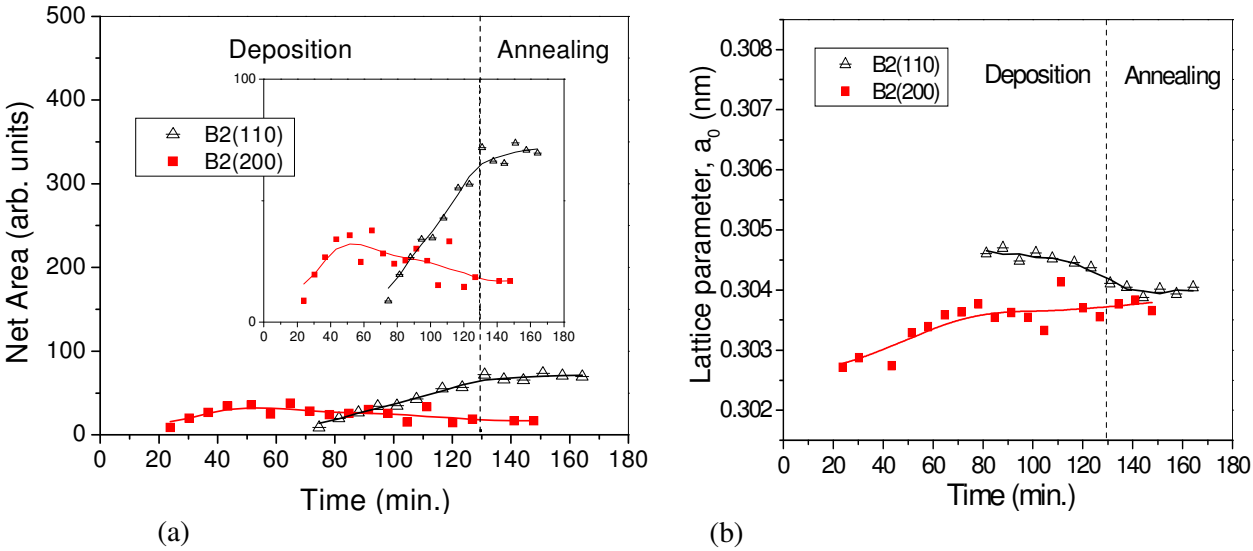

Fig. 3.13: *In-situ* XRD results for a Ni-Ti film deposited on thermally oxidized Si(100) with a V_b of –45 V; (a) net areas of the B2(110) and B2(200) diffraction peaks recorded as a function of time, (b) a_o values as obtained from the positions of B2(110) and B2(200) peaks as a function of time.

During the growth of the Ni-Ti film deposited on thermally oxidized Si(100) substrate with and without V_b, besides the peaks related to the B2 phase, another one, most likely associated with the presence of TiO_2 at the interface, was detected (Fig. 3.14). This is in agreement with results obtained by Fu *et al.* [132], who claim the formation of a TiO_2 interfacial layer for depositions on SiO_2 substrates.

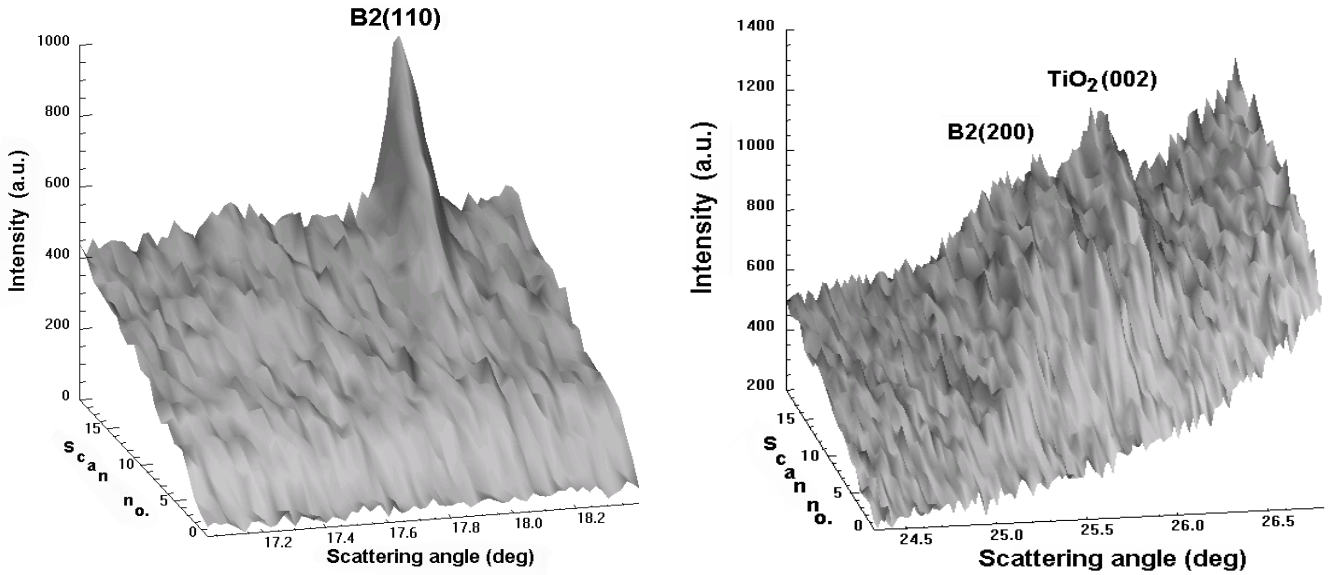

Fig. 3.14: XRD peak intensities during continuous co-sputtering of Ni-Ti for 128 min with a V_b of –45 V on a thermally oxidized Si(100) substrate. Each scan corresponds to ≈ 3 min deposition: (a) in the diffraction range $17.0^o<2\theta<18.4^o$ and (b) in the range $24.3^o<2\theta<26.8^o$.

As mentioned above, for the Ni-Ti film deposited on thermally oxidized Si(100) without V_b, after ≈ 540 nm film thickness there is a stabilization of the intensity of the B2(200) diffraction peak. This was attributed to a gradual tilting (relative to the substrate normal) of the growing direction of the columnar crystals. In order to explore this phenomenon, a complementary experiment was performed. A near equiatomic Ni-Ti film was deposited on thermally oxidized Si(100) without applying V_b at a deposition temperature of ≈ 520°C (instead of ≈ 470°C). Figure 3.15 shows the variation of the net areas of the B2 diffraction peaks and the respective values obtained for a_o as a function of time (for both deposition temperatures). With an increase of the deposition temperature, the intensity of the B2(200) peak increases continuously along the deposition process. No stabilization of the peak intensity is observed, as it was in the case of the deposition at ≈ 470°C [Fig. 3.15(a)]. The variation of the value of a_o as obtained from the positions of the B2(200) peak did not exhibit such a continuous decrease during the deposition [Fig. 3.15(b)]. There is a convergence to an intermediate value of a_o [values calculated using the B2(200), B2(211) and B2(110) diffraction peaks].

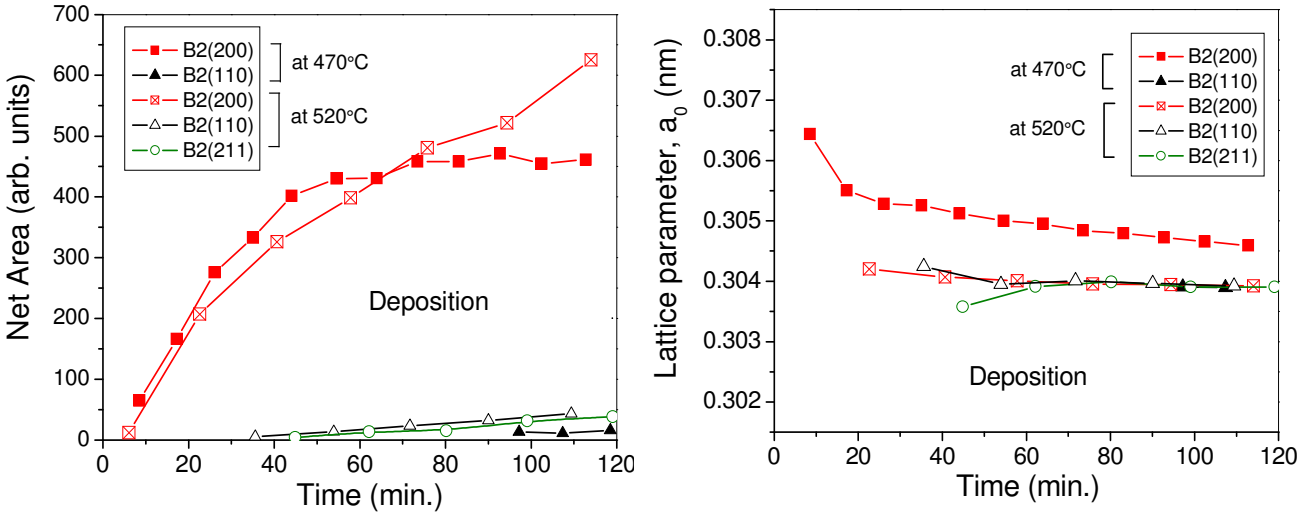

Fig. 3.15: *In-situ* XRD results for Ni-Ti films deposited on thermally oxidized Si(100), without V_b, deposited at ≈ 470°C and at ≈ 520°C; (a) net areas of the B2 diffraction peaks recorded as a function of time, (b) a_o values as obtained from the positions of the B2 diffraction peaks as a function of time.

The diffractograms presented in Fig. 3.16 show that there was a strong preferential stacking on (h00) planes of B2 phase leading to a <100> fibre texture, and the B2(310) peak was not detected for a higher deposition temperature (≈ 520°C), on thermally oxidized Si(100) without V_b. Cooling the film from deposition temperature to RT has led to the B2 ⇒ R-phase transformation.

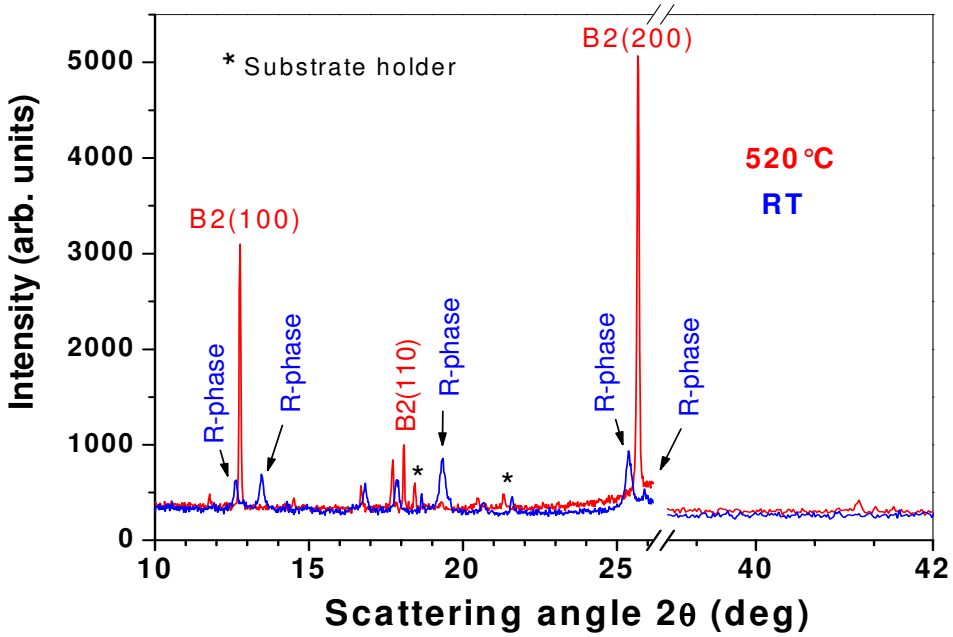

Fig. 3.16: XRD spectra obtained at the deposition temperature (≈ 520°C) and at RT for a Ni-Ti sample deposited without V_b on thermally oxidized Si(100).

3.2.2. *Ex-situ* characterization

Depth profiles of the atomic concentrations in the Ni-Ti film deposited on thermally oxidized Si(100) substrate without V_b are shown in Fig. 3.17. The results confirm a near equiatomic composition. The thermally grown SiO_2 layer acts as a diffusion barrier.

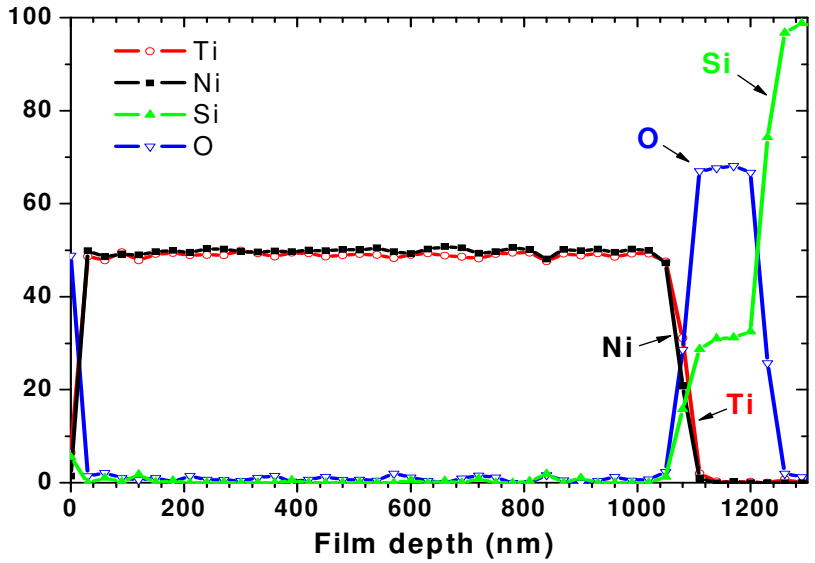

Fig. 3.17: AES elemental concentration profiles for the Ni-Ti sample on thermally oxidized Si(100) substrate deposited without V_b.

In Fig. 3.18 are presented X-TEM micrographs (obtained at the interface film/substrate) for the Ni-Ti films grown on thermally oxidized Si(100) substrates at ≈ 470°C: (a) without V_b, (b) with a V_b of –45 V. In both cases, it is distinguishable a very thin layer between the Ni-Ti film and the SiO_2 layer of the Si(100) substrate. However, the information obtainable by the X-TEM observations does not allow a complete characterization of this reaction product. Nevertheless, during the *in-situ* XRD measurements, the presence of TiO_2 was detected (Fig. 3.14), which can be related with interfacial reactions [132], [133].

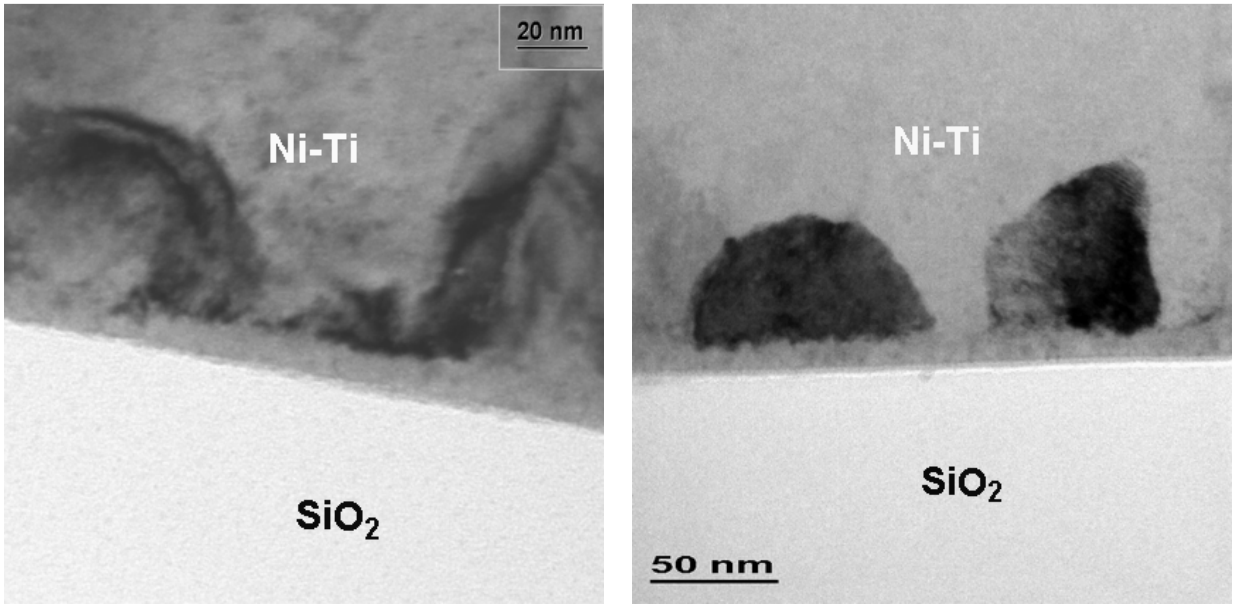

(a) (b)

Fig. 3.18: X-TEM micrographs of the Ni-Ti films grown on thermally oxidized Si(100) at ≈ 470°C; (a) without V_b, (b) with a V_b of –45 V. A thin interfacial reaction layer is perceptible in both cases.

Figure 3.19 shows X-TEM micrographs of the same Ni-Ti samples grown at ≈ 470°C but, this time, illustrating the overall film morphology: (a) without V_b, (b) with a V_b of –45 V. For the deposition parameters used, a columnar structure is observed in both cases. Furthermore, it is perceptible an inclination of the film columns. In the micrograph showing the structure of the Ni-Ti film grown on thermally oxidized without V_b, a dashed line was inserted indicating the thickness related with the deposition time corresponding to the stabilization of the intensity of the B2(200) peak [detected during the *in-situ* XRD studies (Fig. 3.12)]. In the micrograph exhibiting the structure of the Ni-Ti film grown with V_b, a dashed line was inserted indicating the thickness associated with the deposition time corresponding to the detection of the B2(110) peak [detected during the *in-situ* XRD studies (Fig. 3.13(a)]. As it can be observed, in particular, when examining the columns indicated by the arrows, a gradual change of the growing direction of the columnar crystals occurred.

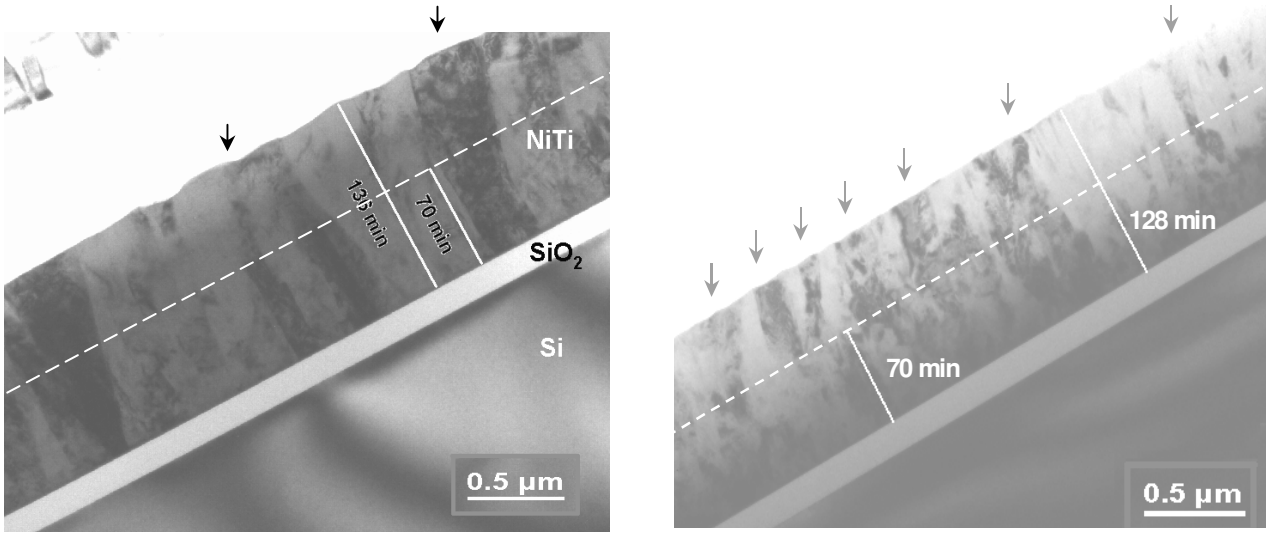

(a) (b)

Fig. 3.19: Bright field X-TEM micrographs of the films deposited on thermally oxidized Si substrates at ≈ 470°C; (a) without V_b, (b) with a V_b of –45 V.

It should be remembered that the chamber is equipped with two magnetrons positioned at a distance of 100 mm from the substrate and tilted 30° away from the substrate normal (see Fig. 2.6). To avoid cross contamination of the two targets cylindrical chimneys are mounted on the magnetrons. During the deposition, the magnetron with the Ni-Ti alloy target was running at a power of 40W and the one with the pure Ti target was running at a power of 20W. The results presented in Fig. 3.19 suggest that the geometry of the deposition process has an important role on the development of tilted columns. They are inclined towards the Ni-Ti magnetron (higher power applied – higher incident flux).

Additional X-TEM observations were performed along the film thickness to study this effect (Ni-Ti film deposited at ≈ 470°C on thermally oxidized Si(100) without V_b). By choosing a spot from a SAED pattern, associated with (100) of the B2 phase, the respective grains showed up as bright regions in the corresponding X-TEM dark field image of Fig. 3.20.

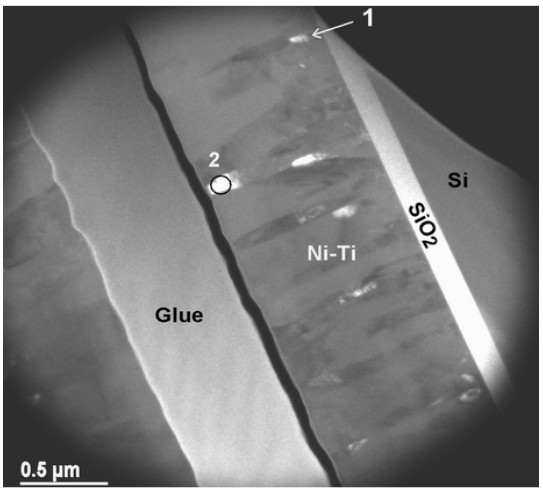

Fig. 3.20: X-TEM dark field image [Ni-Ti film deposited at ≈ 470°C on thermally oxidized Si(100) without V_b] resulting from the selection of a spot associated with B2(100). The respective grains show up as bright regions in the X-TEM micrograph.

B2(100) planes parallel to the interface were identified by cross-section HR-TEM (Fast Fourier Transformation procedure) nearby the interface (*area 1* of Fig. 3.20). The cross-section HR-TEM results are shown in Fig. 3.21 with the respective indication of the interface orientation. By *in-situ* XRD (Fig. 3.12), it was observed that the B2 phase started by stacking onto (h00) planes, which is in conformity with TEM observations. It should be mentioned that the film is in the austenitic state during the TEM measurements (it was not cooled below RT until this step).

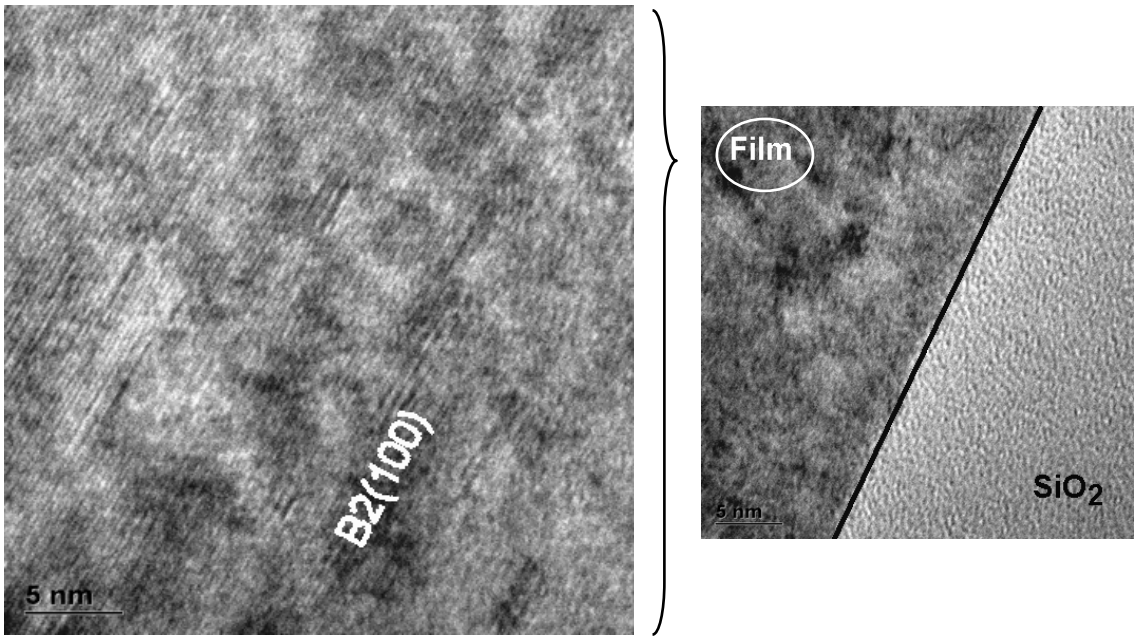

Fig. 3.21: X-TEM micrograph showing the structure of the film from Fig. 3.20; (a) image obtained in *area 1* showing the B2(100) planes parallel to the interface, (b) indication of the interface location.

For *area 2* (surface region in Fig. 3.20) the angle between the (100) planes of the B2 phase and the surface is about 19° (SAED – Fig. 3.22). This is in agreement with the *in-situ* XRD results where the stabilization of the intensity of the B2(200) peak was observed after ≈ 70 min deposition (≈ 540 nm) meaning that close to the surface region, the B2(200) planes could not be found parallel to the film surface.

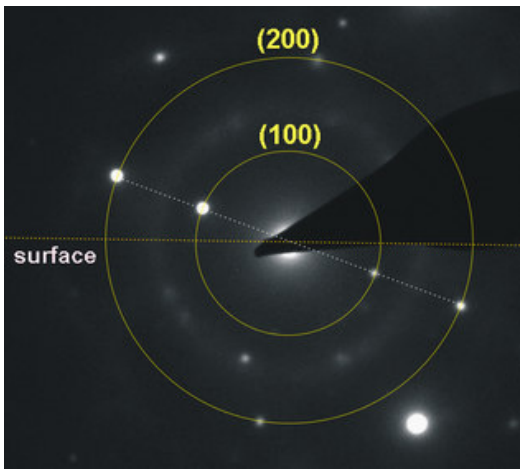

Fig. 3.22: SAED pattern of the Ni-Ti film from Fig. 3.20 obtained in *area 2* (surface region).

The previous X-TEM micrographs have shown that, close to the interface region, the B2(100) planes are parallel to the interface, while close to the surface region they make an angle of ≈ 19°. TEM observations have also been performed nearby the region where the gradual change of the growing direction of the columnar crystals is supposed to occur *(area 3)*. The SAED pattern obtained in *area 3* of the micrograph from Fig. 3.23(a) is presented in Fig. 3.23(b). The SAED pattern revealed the presence of B2(100) planes parallel to the interface and B2(100) planes making roughly 18° with the film surface (this also means that the information in the SAED pattern is obtained from more than one grain). This information suggests that *area 3* is located in a transition zone.

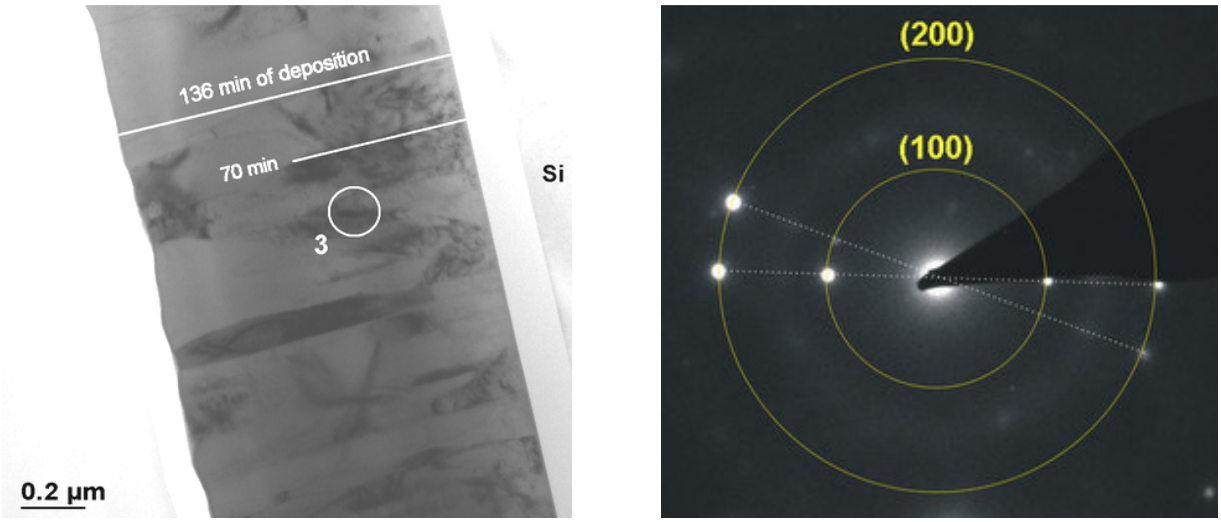

(a) (b)

Fig. 3.23: TEM observations of the Ni-Ti film deposited at ≈ 470°C on thermally oxidized Si(100) without V_b; (a) X-TEM micrograph, (b) SAED pattern obtained in *area 3*. B2(100) planes parallel to the interface and B2(100) planes inclined by roughly 18° to the film surface are detected.

The TEM results presented above, obtained for the Ni-Ti film deposited at ≈ 470°C on thermally oxidized Si(100) without V_b, have confirmed a gradual change of the growing direction of the columnar crystals. The sample was complementary studied by *ex-situ* XRD experiments at RT and 100°C using Cu-K_α radiation in off-plane Bragg-Brentano geometry. The (310) peak of the B2 phase, which could not be detected *in-situ* due to the chamber windows size limitation of the set-up used for the deposition of this sample, was found *ex-situ* as it can be seen in Fig. 3.24. The inclination of the columnar crystals favoured the diffraction (in Bragg-Brentano geometry) of the (310) peak of the B2 phase and the stabilization of the intensity of the B2(200) peak, which was observed *in-situ* during the deposition process.

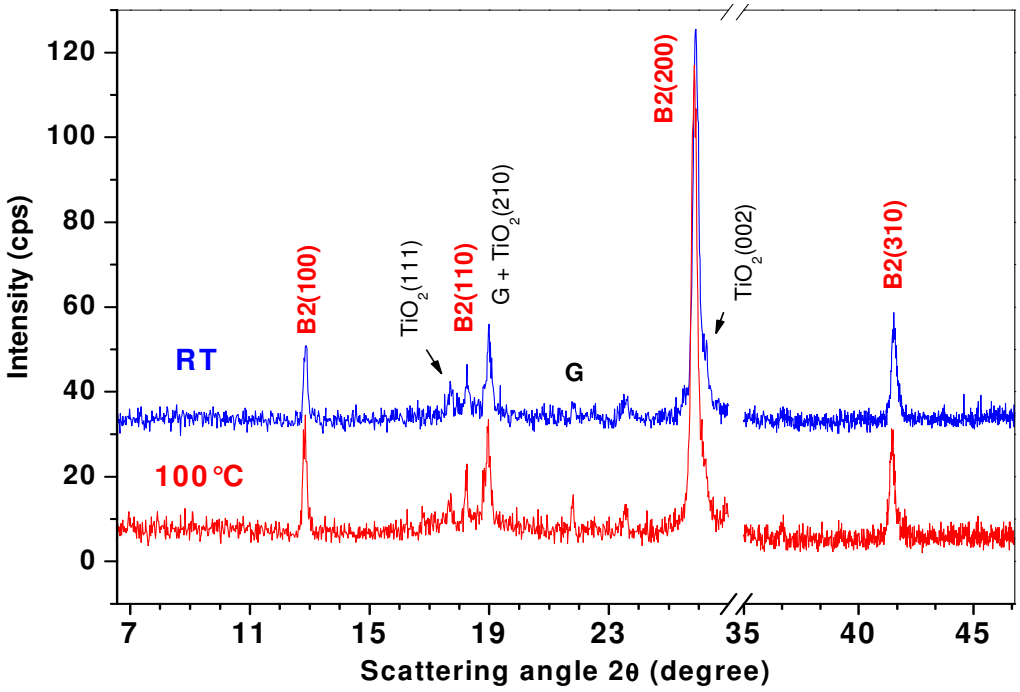

Fig. 3.24: *Ex-situ* XRD spectra with change of temperature (at RT and 100°C) using Cu-K_α radiation. The Bragg-Brentano peaks associated with the clamps of the sample holder are indicated with a "G".

Complementary measurements were performed to investigate the texture through the realization of pole figures B2(110) and B2(200). The measurements were carried out at RT, in the austenitic state (the sample had not been cooled below RT). The results have shown the existence of (h00) planes as well as (310) planes of the B2 phase, parallel to the film surface (Fig. 3.25). The initial preferential stacking on (h00) planes (observed *in-situ*) leading to a <100> fibre texture is the reason for the detection of (h00) planes parallel to the film surface. After ≈ 540 nm film thickness, as observed by XRD and complementary TEM studies, the stabilization of the intensity of the B2(200) diffraction peak occurred due to the gradual change of the growing direction of the columnar crystals favouring the (310) orientation of the B2 phase parallel to the film surface.

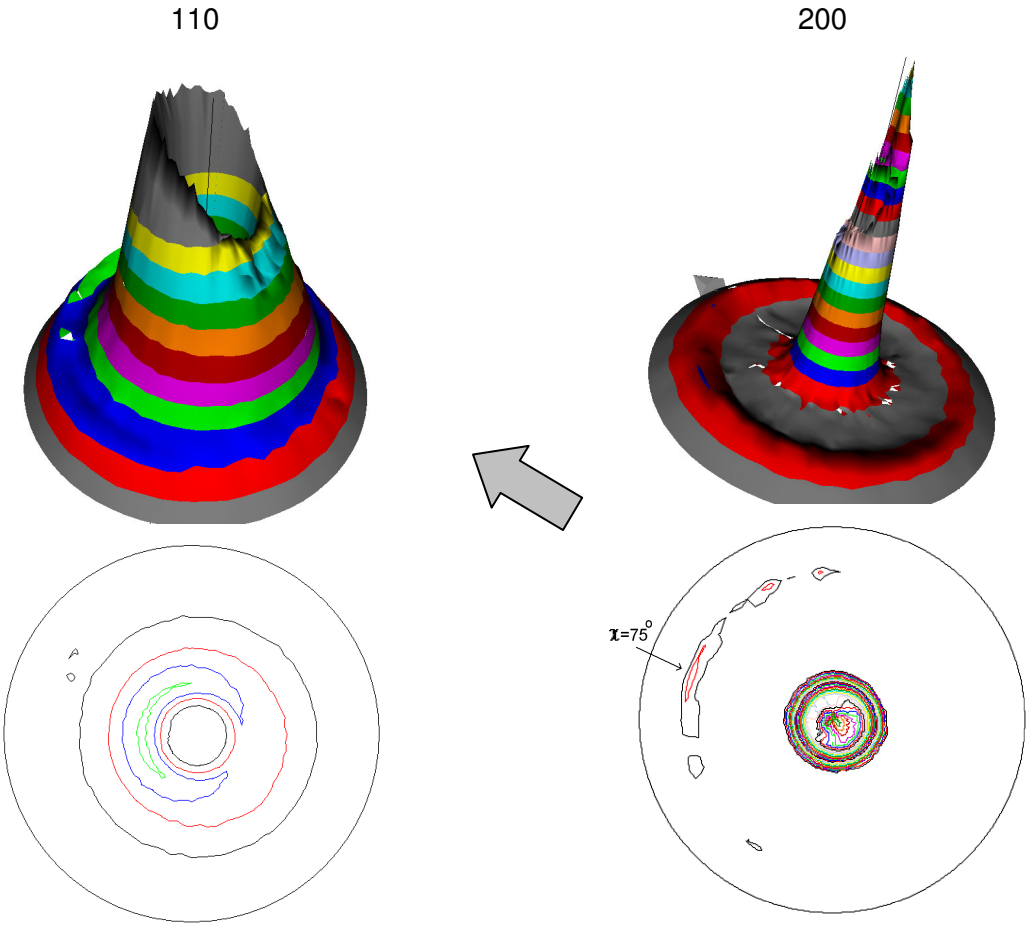

Fig. 3.25: Pole figures of Ni-Ti B2 phase grown on thermally oxidized Si(100) substrate at ≈ 470°C, nominally measured in the Bragg peaks B2(110) and B2(200). The grey arrow indicates the direction of the vapour flux coming from the magnetron with the Ni-Ti target.

In order to observe the corresponding reflexions with more detail, sections at $\varphi = 0°$ and $\varphi = 90°$ from the pole figure measured in the Bragg peak B2(110) are shown in Fig. 3.26.

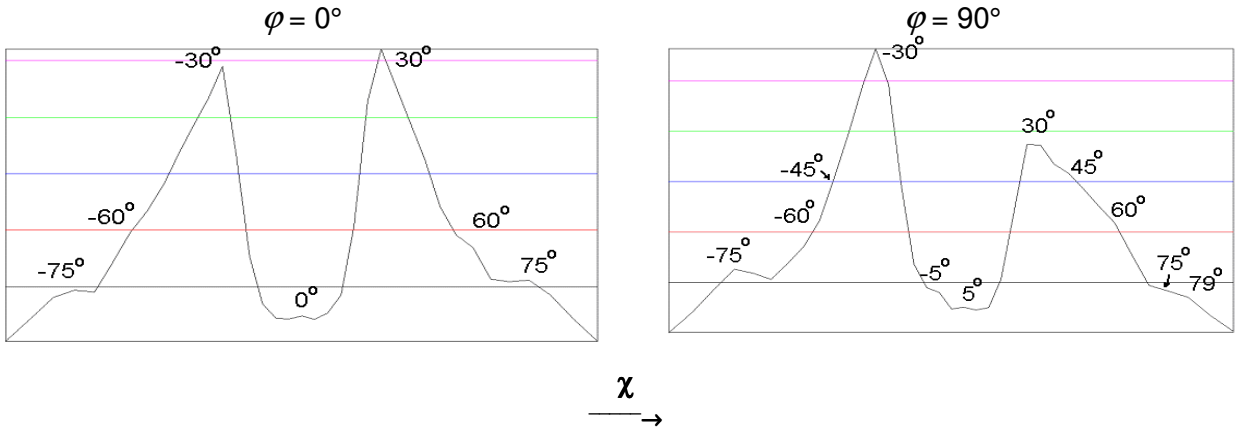

Fig. 3.26: Sections at $\varphi = 0°$ and $\varphi = 90°$ from the measured austenite pole figure of the 110 diffraction plane of the previous figure.

The results, when compared with schematic theoretical pole figures derived from the stereographic projection of the B2 phase using the CARINE 3.1 software (calculated for 100 and 310 planes, parallel to the film surface) [161], confirm what has been described above. There are different grains with (h00) and (310) planes parallel to the substrate surface.

In this section it has been shown that for the Ni-Ti film deposited on thermally oxidized Si(100) substrates, without applying V_b, there is a strong preferential stacking on (h00) planes of B2 phase leading to a <100> fibre texture. Nevertheless, after ≈ 540 nm film thickness, a stabilization of the intensity of the B2(200) diffraction peak was observed. This was the result of a gradual change of the growing direction of the columnar crystals; in the present experiments, this inclination favoured the diffraction (in Bragg–Brentano geometry) of the B2(310) peak. This trend was confirmed by *ex-situ* pole figures measurements and X-TEM observations.

The results obtained *in situ* for the Ni-Ti sample deposited on thermally oxidized Si(100), have shown a considerable reduction of the net area of the B2(110) and B2(200) Bragg-Brentano diffraction peaks, when going from $V_b = 0$ to $V_b = -45$ V. *Ex-situ* XRD experiments in off-plane Bragg-Brentano geometry detected the presence of the B2(310) diffraction peak, which could not be detected *in-situ* due to the chamber windows size limitation of the set-up used for the deposition of this sample. The inclination of the columnar crystals favoured the diffraction (in Bragg-Brentano geometry) of the (310) peak of the B2 phase and the stabilization of the intensity of the B2(200) peak, which was observed *in-situ* during the deposition process. Although this behaviour has also been observed for the Ni-Ti deposition without V_b, it is much more pronounced when a V_b (–45V) is applied during Ni-Ti film growth.

The growth of Ni-Ti at a temperature of ≈ 520°C has shown that, increasing the deposition temperature, the intensity of the B2(200) diffraction peak increased along the deposition process and, therefore, a stabilization of the peak intensity was not observed as it has been for the depositions at ≈ 470°C (without and with a V_b of –45V).

Ex-situ AES and TEM studies performed on samples obtained without and with V_b revealed that the thermally grown SiO_2 layer acts as a diffusion barrier. However, the XRD and X-TEM results suggest the presence of TiO_2 at the interface Ni-Ti/SiO_2.

The temperature dependence of the ER of the sample obtained on naturally oxidized Si(100) substrate without V_b and the samples on thermally oxidized Si(100) substrate, without and with a V_b of −45 V (all deposited at ≈ 470°C), are shown in Fig. 3.27 for cooling and heating. It is possible to observe that the films on naturally oxidized Si(100) without V_b and on thermally oxidized Si(100) with V_b exhibit a very similar trend during temperature cycling (bottom and top curves in Fig. 3.27), while the film deposited on thermally oxidized Si without V_b (centre curve in Fig. 3.27) shows a completely different tendency. The curves of the two samples with similar trend showed a rough increase of the ER related with the B2 ⇒ R-phase transformation during cooling (and a corresponding decrease during heating). The temperature range where the R-phase is stable during cooling is larger for the samples deposited on the naturally oxidized Si(100), without V_b, and on the thermally oxidized Si(100) with V_b. Thus, the transformation is occurring in two steps, B2 ⇔ R-phase ⇔ B19'. In contrast, during heating, a corresponding decrease of ER associated with the R-phase transformation was not visible for the sample on thermally oxidized Si(100) substrate (without V_b).

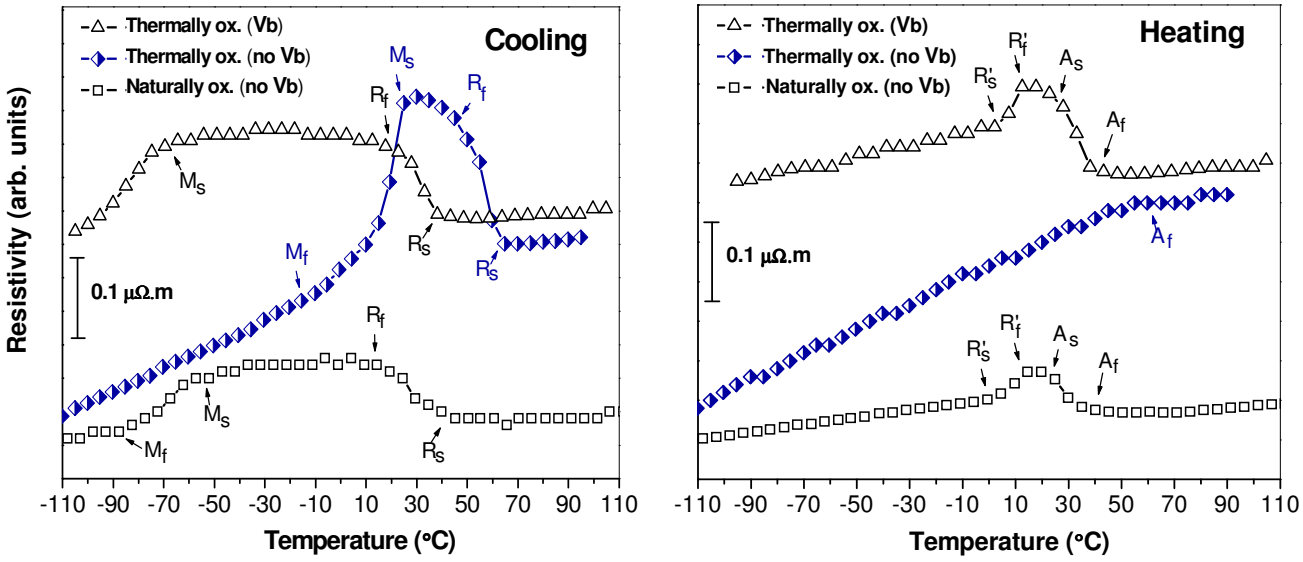

(a) (b)

Fig. 3.27: Dependence of ER with temperature for three sample types (deposited at ≈ 470°C), during (a) cooling and (b) heating.

During the ER measurements the samples were subjected to thermal cycles (for the first time after deposition) in order to induce the phase transformation. Due to this fact, the samples were checked again at RT by XRD, this time using the BRUKER AXS D5000 diffractometer in GIXD (Fig. 3.28). The sample on thermally oxidized Si(100) without V_b had

a big fraction of the Ni-Ti film already transformed to B19', which corroborates the ER results. For the other samples, R-phase was still clearly present at RT.

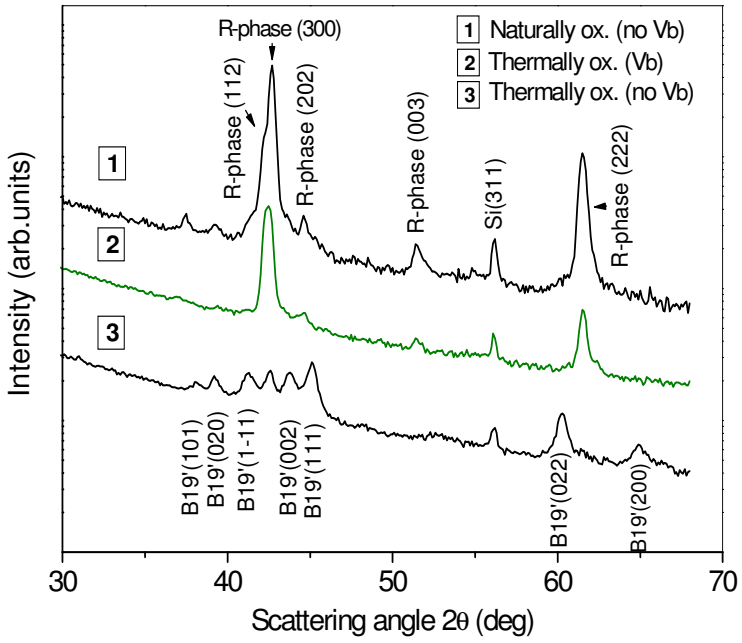

Fig. 3.28: GIXD diffractograms (Cu-K_α radiation) at RT. The films had already been subjected to a complete thermal cycle.

The temperature dependence of the ER of the Ni-Ti samples allowed us to detect different types of behaviour during phase transformation. Ni-Ti samples possessing different crystallographic orientations [Fig. 3.2(a), Fig. 3.12 and Fig. 3.13] exhibit different phase transformation characteristics (Fig. 3.27).

3.3. NEAR EQUIATOMIC Ni-Ti FILMS GROWN ON A TiN BUFFER LAYER

The effect of a TiN layer deposited on top of the thermally oxidized Si(100) substrate, prior to the deposition of the Ni-Ti films, was analysed. TiN films grown by vapour phase deposition techniques usually have a preferred growth orientation that varies according to the growth conditions. The orientations most often observed are <100> and <111>. Primarily <100> and <111> oriented grains nucleate during the initial stages of growth but, with increasing film thickness, the development of a preferred layer orientation either <100> or <111> is observed, depending on the deposition conditions. Frequently, the so-called "orientational cross-over" is clearly detected, i.e. a change in the preferential orientation of

the growing grains. In the present study, the effect of the TiN crystallographic orientation on the texture of Ni-Ti B2 phase was investigated.

3.3.1. *In-situ* experiments

The net areas of the Bragg-Brentano diffraction peaks TiN(111) and TiN(200) recorded during deposition and annealing of a TiN buffer layer are presented in Fig. 3.29(a). This sample was prepared in order to analyse the evolution of the TiN structure under the previously selected deposition parameters. During the initial stages of growth, primarily <100> and <111> oriented grains nucleate and grow. The results show that <111> grains take over at larger thickness values. No changes were detected during the annealing period.

3.3.1.1. Effect of the TiN crystallographic orientation on the development of Ni-Ti B2 phase

The growth of near equiatomic Ni-Ti films was studied. The varying deposition parameter for the set of samples presented in this subsection was the thickness of the TiN buffer layer (see Tab. 3.3.).

TiN deposition time (min.)	**TiN thickness (nm)**	**Annealing time** at ≈ 470°C **(min)**	
		TiN (on top of SiO_2)	**After deposition of Ni-Ti**
40	215	27	57
15	80	28	60
3	15	27	60

Tab. 3.3: Process conditions of near equiatomic Ni-Ti films deposited on TiN buffer layers in the sputtering chamber of the beamline ROBL at ESRF. The thickness of the Ni-Ti films was ≈ 800 nm (≈ 120 min of deposition).

TiN buffer layers of thickness of approximately 15, 80 and 215 nm were chosen (corresponding to 3, 15 and 40 min deposition). In all cases a V_b of −30V was applied during TiN growth and no V_b was applied during the deposition of the Ni-Ti films. The respective X-ray diffractograms obtained *in situ* with Bragg-Brentano scattering geometry, immediately after the deposition of the TiN buffer layers, are shown in Fig. 3.29(b). TiN(111) and TiN(200) diffraction peaks can be observed for a thickness of ≈ 80 and ≈ 215 nm. However, only for a ≈ 215 nm TiN layer it is possible to conclude that <111> grains dominate.

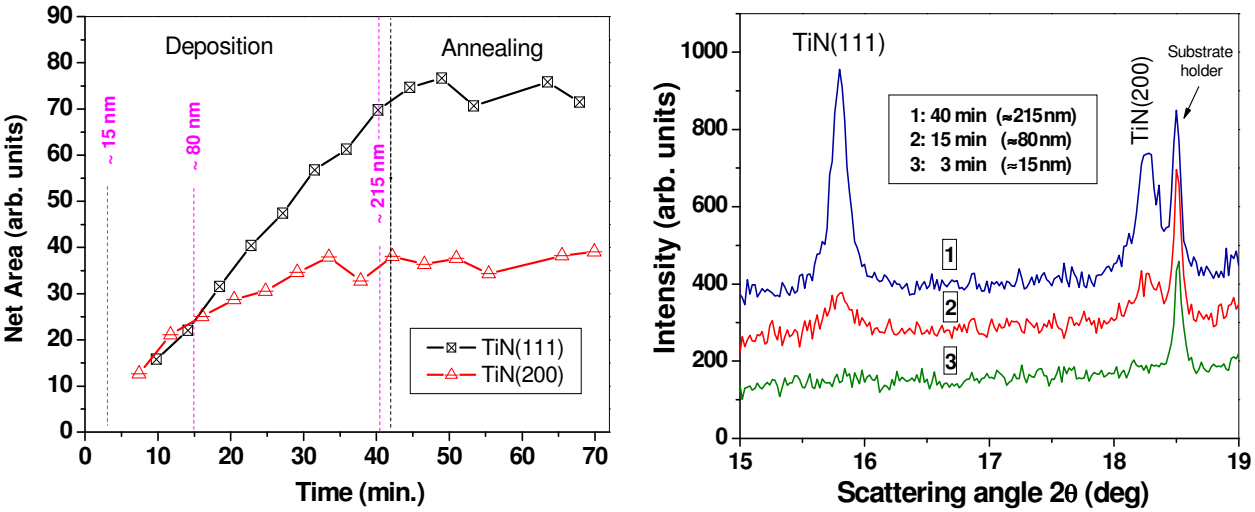

Fig. 3.29: (a) Net areas of the TiN(111) and TiN(200) diffraction peaks recorded during the processing of a TiN buffer layer. (b) X-ray diffractograms from three TiN buffer layers ≈ 15, ≈ 80 and ≈ 215 nm thick. They were obtained *in situ* in vertical, i.e. off-plane Bragg–Brentano scattering geometry immediately after the TiN deposition and before the deposition of Ni-Ti. In all cases a V_b of –30V was applied during TiN deposition.

A typical XRR result is shown in Fig. 3.30(a) which has been obtained *in situ* for a TiN layer after 3 min deposition (the red curve is the result of the fitting procedure). The thickness data was obtained from the Bede Mercury REFS code [157]. This technique allowed to calculate the growth rate for the TiN buffer layers (≈ 0.088 nm/s). However, XRR is in general useful only for lower film thicknesses. Thickness values larger than ≈ 100 nm could hardly be resolved by the reflectivity experiments because of interference with the SiO_2 buffer layer.

XRR has been also employed to analyse the effect of the annealing time on the TiN buffer layer [Fig. 3.30(b)]. The results did not show evidence of structural changes due to the annealing step. The XRR curves, obtained immediately after deposition and 90 min later, are superposed.

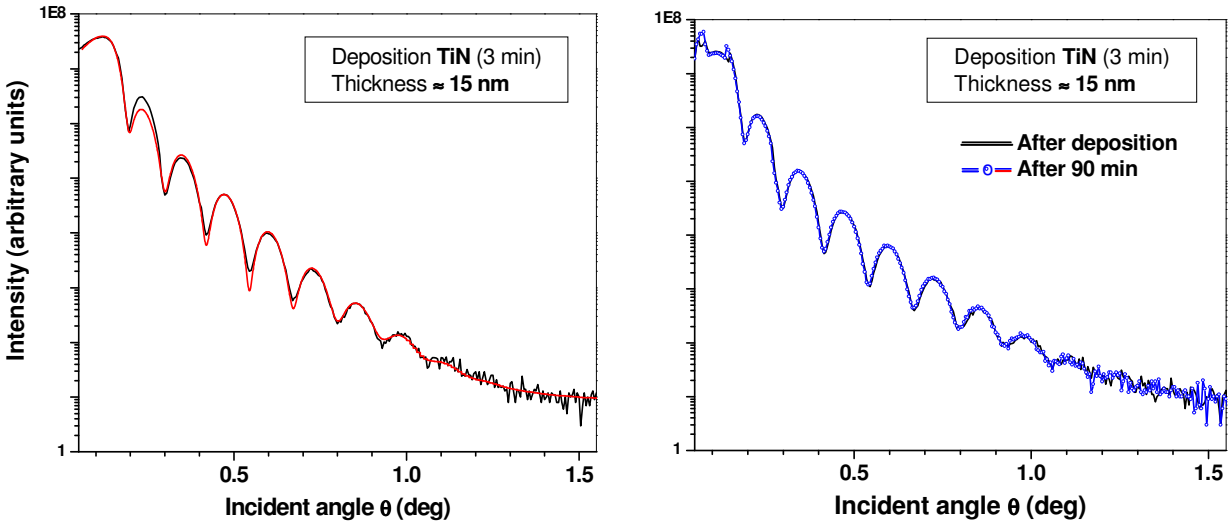

Fig. 3.30: Typical XRR spectra; (a) for a 3 min deposition of a TiN buffer layer (black line) with the fitting curve (red line), (b) obtained immediately after deposition (black line) and obtained 90 min after deposition of TiN (blue curve). A V_b of −30V was applied during the growth of the TiN layers.

Figure 3.31 shows results obtained from the *in-situ* XRD data for the Ni-Ti depositions on top of the three different TiN buffer layers (three different TiN thickness values: ≈ 15, ≈ 80 and ≈ 215 nm). Represented are: (a) the variation of the net area of the B2(110) peak for all samples and additionally the variation of the net area of the B2(211) peak for the sample with a TiN layer of thickness ≈ 15 nm, (b) the variation of the a_0 values (as calculated from the lattice constant, *d*, according to the B2(110) and B2(211) peak positions), *versus* time. The Ni-Ti film deposited on the TiN layer with thickness ≈ 215 nm shows a preferential growth of <110> oriented grains of the Ni-Ti B2 phase from the beginning of the deposition, with a constant growth rate during the whole deposition. For the Ni-Ti film deposited on a TiN layer of thickness ≈ 15 nm, the B2(110) diffraction peak also appeared from the beginning of the deposition, but much less intense. In this latter case, the B2(211) peak was also detected with a crossover from <110> oriented grains dominating at small thicknesses to <211> oriented grains taking over at larger thicknesses. Despite an initial stronger increase, the net area of the B2(110) peak, for the Ni-Ti film deposited on a TiN buffer layer with ≈ 80 nm thickness, approached the one of the B2(110) peak of the previous sample (with a TiN layer of thickness ≈ 15 nm) after ≈ 85 min [in the case of the sample with a TiN layer of ≈ 80 nm, the B2(211) peak was not monitored *in situ*]. These experiments have also shown that the B2(200) diffraction peak did not assume an important relevance (in contrast to the depositions on oxidized Si substrates) and, thus, not considered for this representation.

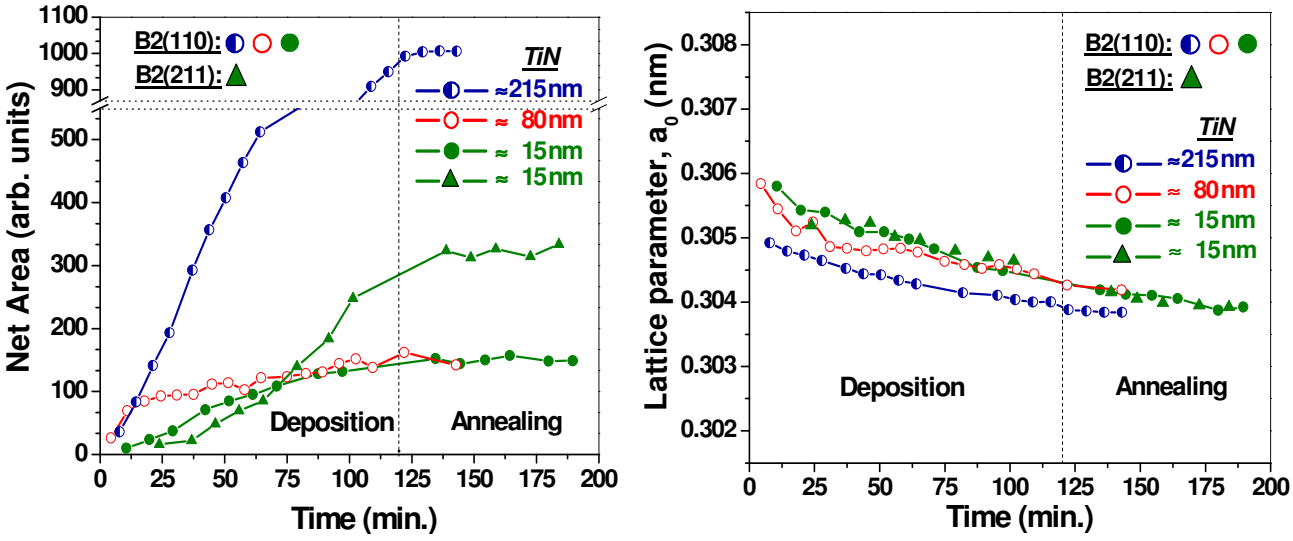

Fig. 3.31: *In-situ* XRD results for Ni-Ti films deposited without V_b on three different TiN buffer layers; (a) net areas of the diffraction peaks of the B2 phase recorded as a function of time, (b) a_0 values as obtained from the positions of the diffraction peaks as a function of time.

Figure 3.31(b) shows the variation of the a_0 values of the Ni-Ti films during the deposition and annealing steps. A continuous decrease was perceptible during the whole film deposition. In the case of the film with a TiN buffer layer of thickness ≈ 80 nm, when the propensity for the development of the diffraction peak B2(110) is noticeable, a_0 of B2 phase, as calculated from $d_{(110)}$, shows lower values, when compared with the film deposited on the TiN buffer layer with ≈ 15 nm. Nevertheless, when the net areas of the B2(110) diffraction peak of both samples approached the same value (approximately after 85 min), also the calculated a_0 values approached each other.

3.3.1.2. Effect of the substrate bias voltage on the structure of Ni-Ti films deposited on TiN

The effect of a V_b of –45 V during the deposition of a Ni-Ti film on a TiN buffer layer with a thickness of ≈ 15 nm (a dominating orientation could not be identified for this TiN layer, i.e. primarily <100> and <111> oriented grains nucleate and grow) was tested [Fig. 3.32(b)]. The development of the <211> oriented grains of the Ni-Ti B2 was suppressed when compared with the sample deposited without bias [Fig. 3.32(a)]. In the case of the Ni-Ti film deposited with an ion bombardment promoted by the applied V_b, the <110> oriented grains dominated since the beginning. This extra parameter favoured the stacking of (110) planes of the B2 phase parallel to the substrate surface.

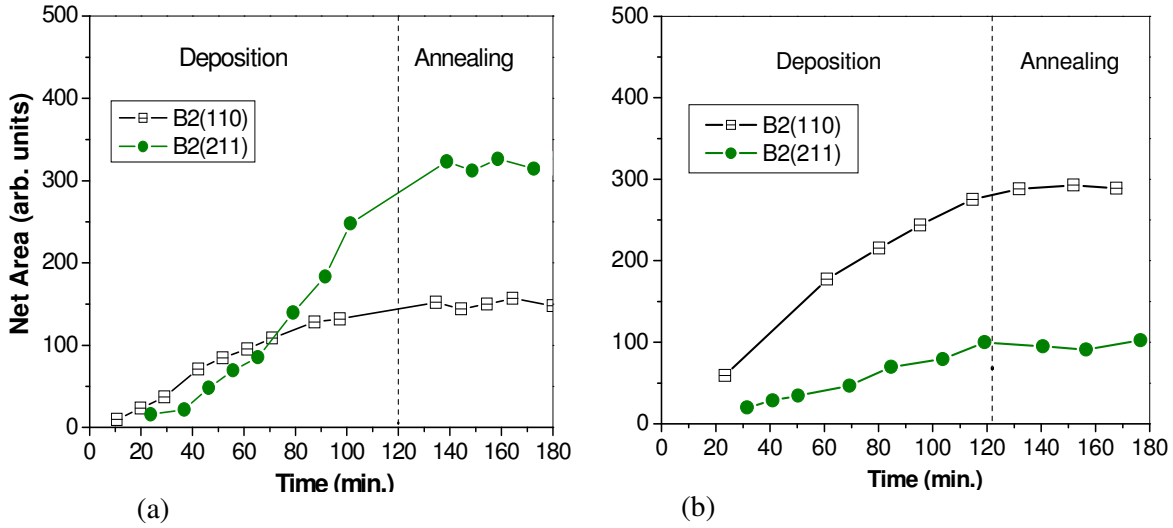

Fig. 3.32: The net areas of the B2(110) and B2(211) diffraction peaks, recorded as a function of time after start of Ni-Ti deposition. The Ni-Ti film was deposited on a TiN layer (≈ 15 nm) previously deposited on top of a thermally oxidized Si(100) substrate; (a) without V_b, (b) with V_b = –45V.

The variation of the a_0 of B2 phase [calculated from $d_{(110)}$ and $d_{(211)}$] as a function of deposition time for the Ni-Ti films deposited without and with V_b of –45 V is represented in Fig. 3.33. A continuous decrease is perceptible, during deposition and annealing, for the Ni-Ti film deposited without V_b. The decrease of the a_0 value suggested that the film experience compressive stress, which was significantly relaxed with increasing film thickness. In the case of the film deposited with V_b, the a_0 values obtained *in-situ* are relatively stable exhibiting an average value of ≈ 0.303 nm.

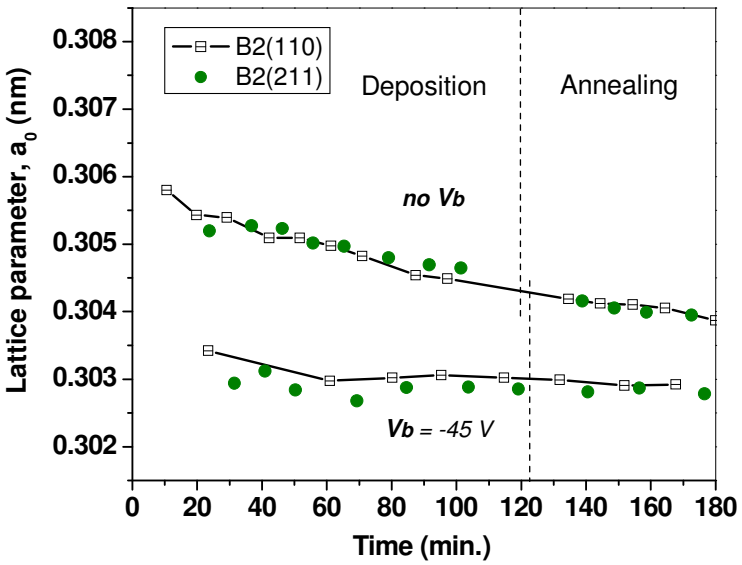

Fig. 3.33: Lattice parameter a_o, recorded as a function of time after start of Ni-Ti film growth on a TiN layer (≈ 15 nm) previously deposited on top of a SiO_2/Si(100) substrate. Results obtained for a Ni-Ti film deposited without V_b and results obtained for a film deposited with V_b = –45 V are represented.

The effect of V_b on the growth of near equiatomic Ni-Ti films on a TiN buffer layer of thickness ≈ 215 nm (topmost layer formed mainly by <111> oriented grains) was also investigated. The applied V_b values are 0 V, –45 V and –90 V. The net areas of the B2(110) diffraction peak recorded during the processing of the samples are presented in Fig. 3.34(a). There was a preferential growth of <110> oriented grains of the Ni-Ti B2 phase from the beginning of the deposition, with a constant rate up to the end of the deposition. Nevertheless, the increase in V_b to –90 V led to a decrease of the intensity of the B2(110) peak.

A continuous decrease of the a_0 value of B2 phase during the deposition of the Ni-Ti film without V_b has been observed in Fig. 3.34(b), as already shown in Fig. 3.31(b). The deposition with –45 V led to a slight decrease of a_o at the beginning of the deposition, followed by a stabilisation. Increasing the V_b further to –90 V, showed a practically constant value of a_o during all the deposition time. It can be observed that as V_b was increased, a_o value decreased, approaching the equilibrium value of 0.303 nm for applied –90 V.

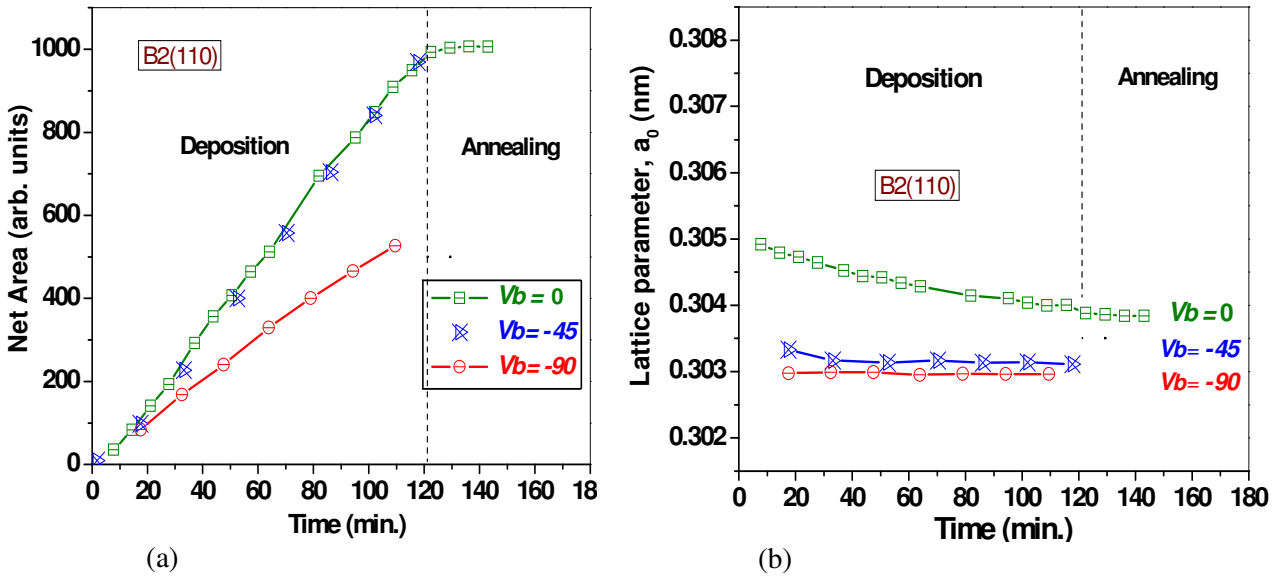

Fig. 3.34: Effect of V_b applied during Ni-Ti deposition on TiN buffer layers of thickness ≈ 215 nm; (a) the B2(110) net areas, (b) a_o as calculated from the lattice constant, *d*, according to the B2(110) peak position.

The XRD spectra for this set of samples obtained after deposition at ≈ 470°C and at RT, are presented in Fig. 3.35. The results recorded at high temperature (austenitic state) show a higher intensity and a lower FWHM value for the Ni-Ti films deposited with V_b. The film deposited without V_b exhibits the presence of the R-phase at RT and at high temperatures shows mainly the austenitic structure.

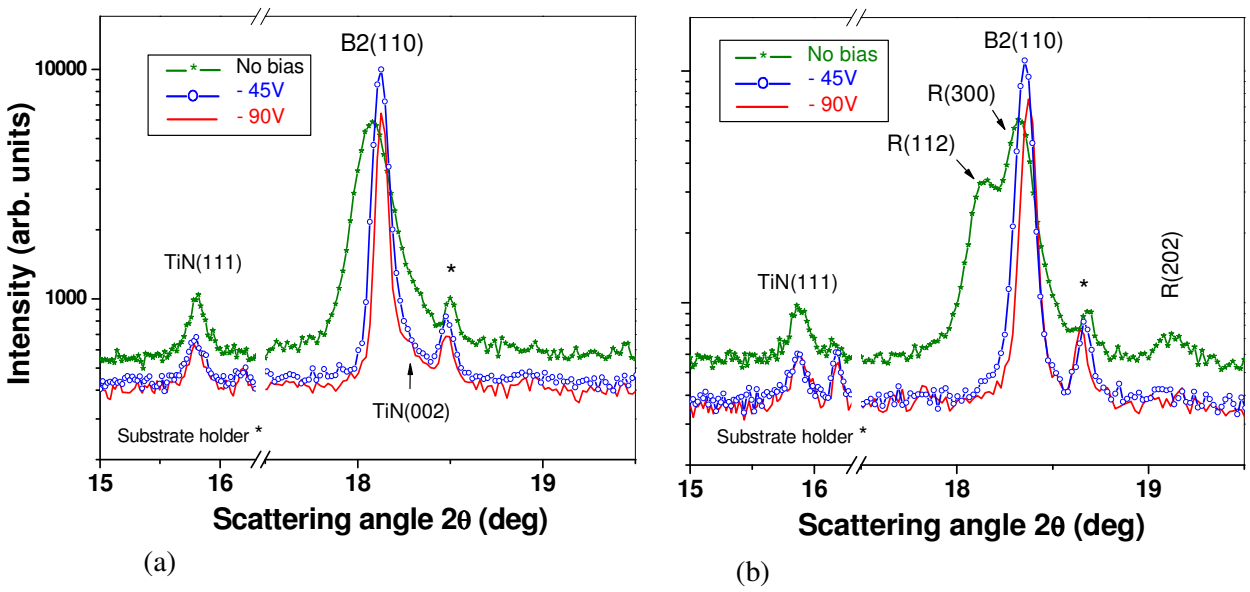

Fig. 3.35: XRD spectra obtained for the Ni-Ti films deposited without V_b, with –45 V and –90 V on TiN buffer layers of thickness ≈ 215 nm; (a) after deposition at ≈ 470°C, (b) at RT.

A decrease of the full width at half maximum (FWHM) value with the increasing V_b is seen in Fig. 3.35(a). This suggests an overall trend of increasing coherence domain length with increasing V_b for the deposition of the Ni-Ti films on a TiN buffer layer of thickness ≈ 215 nm.

3.3.2. *Ex-situ* characterization

Typical bright field X-TEM micrographs for the Ni-Ti samples deposited without V_b on a TiN layer of thickness values of ≈ 15 and ≈ 215 nm are shown in Fig. 3.36. A columnar structure was identified for the Ni-Ti films. In accordance with the Thornton structure model, the TiN layers also show a columnar structure due to the substrate temperature of ≈ 470°C when compared with the T_m of ≈ 3000°C.

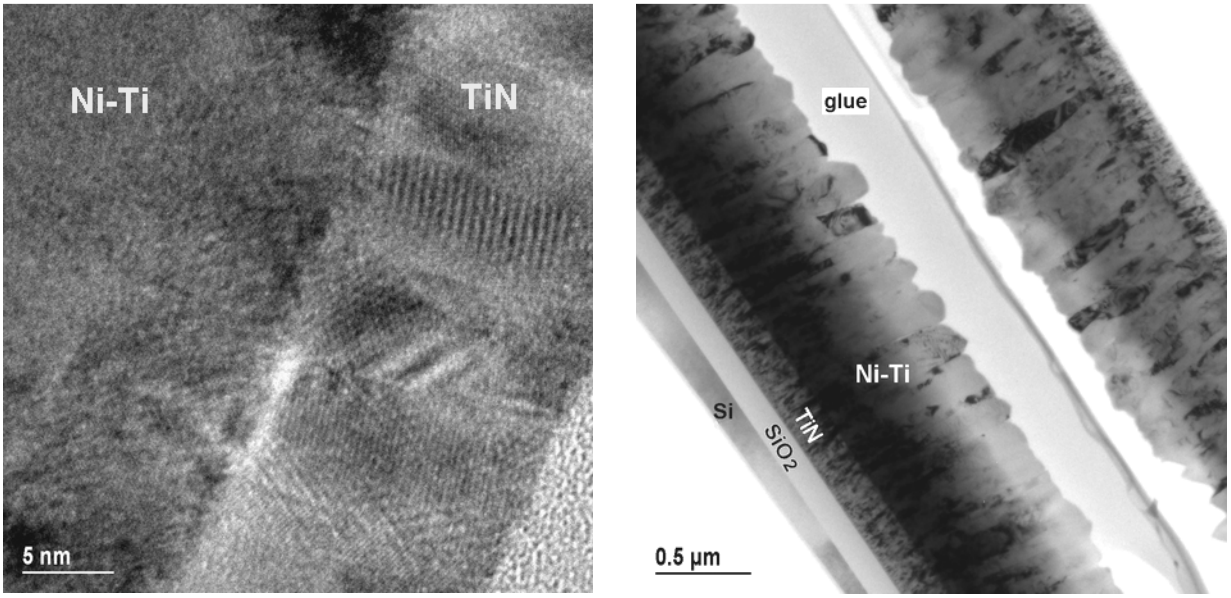

(a) (b)

Fig. 3.36: X-TEM micrographs from Ni-Ti samples deposited without V_b; (a) on a TiN layer of thickness ≈ 15 nm, (b) on a TiN layer of thickness ≈ 215 nm.

3.3.2.1. Effect of the TiN crystallographic orientation on the development of Ni-Ti B2 phase

Ex-situ XRD analyses results obtained at RT and 100°C for the Ni-Ti samples deposited without V_b on TiN are shown in Fig. 3.37. At RT the film structure was mainly rhombohedral (R-phase) as shown in Fig. 3.37 (a, b). With the increase of temperature to 100°C it transformed to B2 phase [Fig. 3.37 (c, d)]. During the transformation from the high temperature phase (B2) to the rhombohedral R-phase while cooling, the height of the B2(110) diffraction peak decreased, splitting into two resolvable R(112) and R(300) peaks. This was especially visible in the case of the Ni-Ti film deposited on top of a TiN layer with thickness ≈ 215 nm. Furthermore, it was perceptible a splitting of the B2(211) peak into the (033) and (141) peaks of the R-phase structure for the samples with TiN layers of ≈ 15 and ≈ 80 nm.

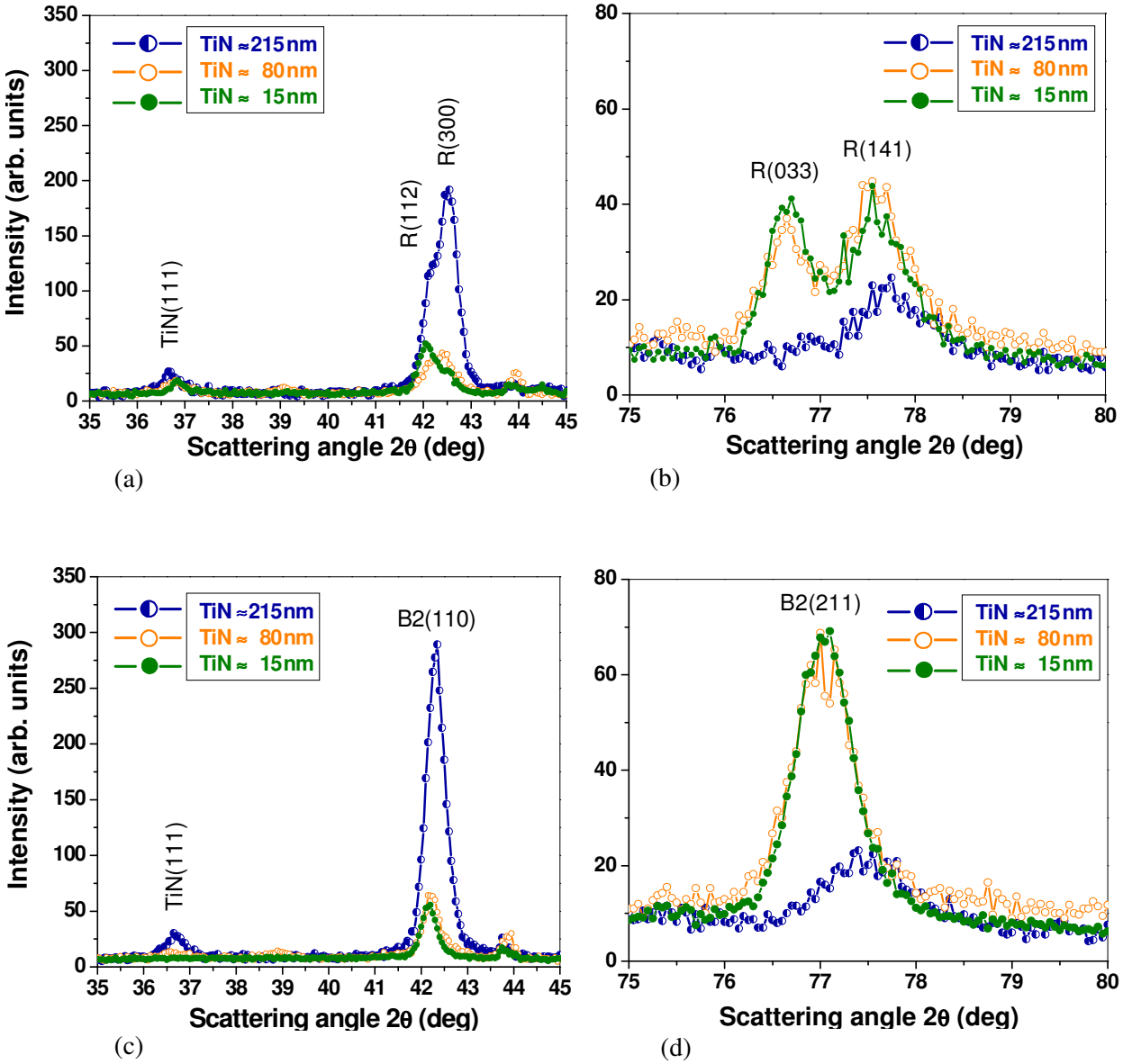

Fig. 3.37: *Ex-situ* XRD spectra with change of temperature for the Ni-Ti samples obtained without applying a V_b; (a), (b) at RT and (c), (d) at 100°C.

The temperature dependence results of the ER of the Ni-Ti samples with TiN buffer layers of thickness ≈ 15, ≈ 80 and ≈ 215 nm are shown in Fig. 3.38 for cooling and heating. The measurements were performed with the Ni-Ti films attached to the substrate.

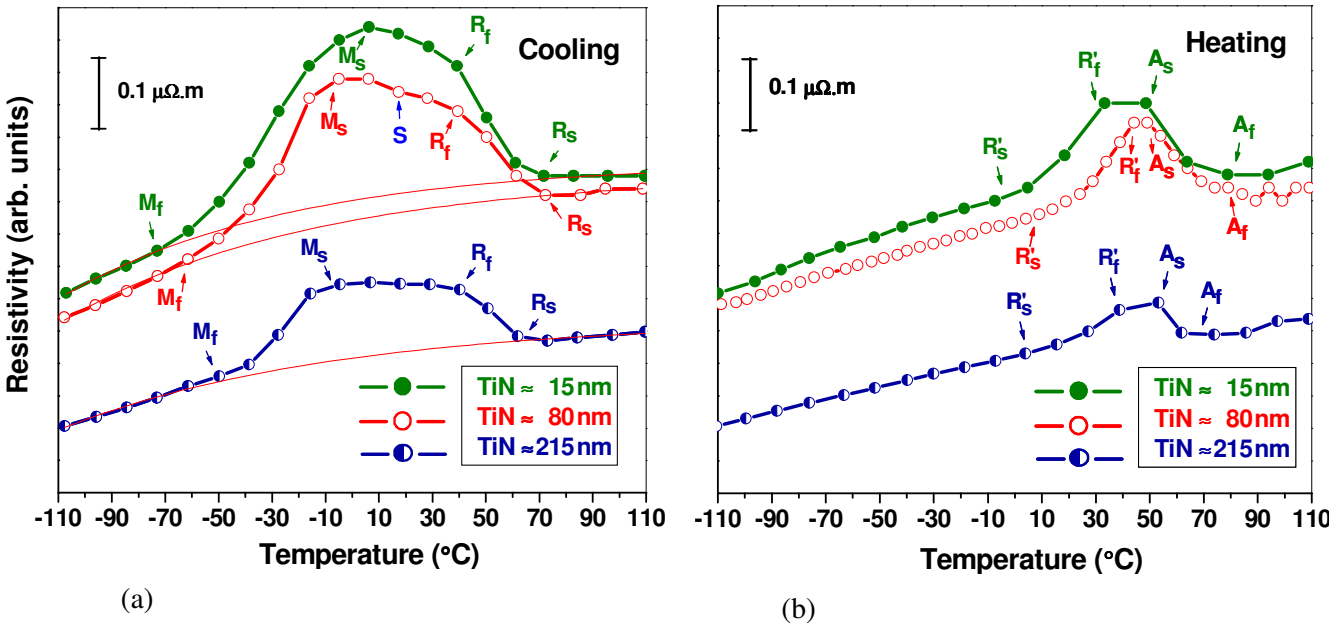

Fig. 3.38: Dependence of ER with temperature for the Ni-Ti samples (deposited without V_b) with TiN buffers layers of thickness approximately 15, 80 and 215 nm during (a) cooling and (b) heating.

For all the samples, as the temperature decreases, a clear increase in the resistivity was observed (B2 ⇒ R−phase transformation), followed by a decrease associated with the R−phase ⇒ B19' transformation [Fig. 3.38(a)]. The increase of the ER during R-phase formation is much higher for the Ni-Ti sample with a TiN buffer layer of ≈ 15 nm. During heating the transformation was also occurring in two steps, B19' ⇒ R−phase ⇒ B2 as observed by the increase in resistivity [Fig. 3.38(b)]. However, during heating the increase in resistivity was much smaller than the one observed on cooling.

3.3.2.2. Effect of the substrate bias voltage on the structure of Ni-Ti films deposited on TiN

The effect of the structural changes in the Ni-Ti films, promoted by the V_b applied to the substrate during the film growth, on their transformation characteristics during thermal cycling in the temperature range between –110 and 110°C was examined in the context with the ER measurements. The temperature dependence results of the ER of the Ni-Ti samples with TiN buffer layers of thickness ≈ 15 nm, deposited without and with V_b of –45 V, are shown in Fig. 3.39.

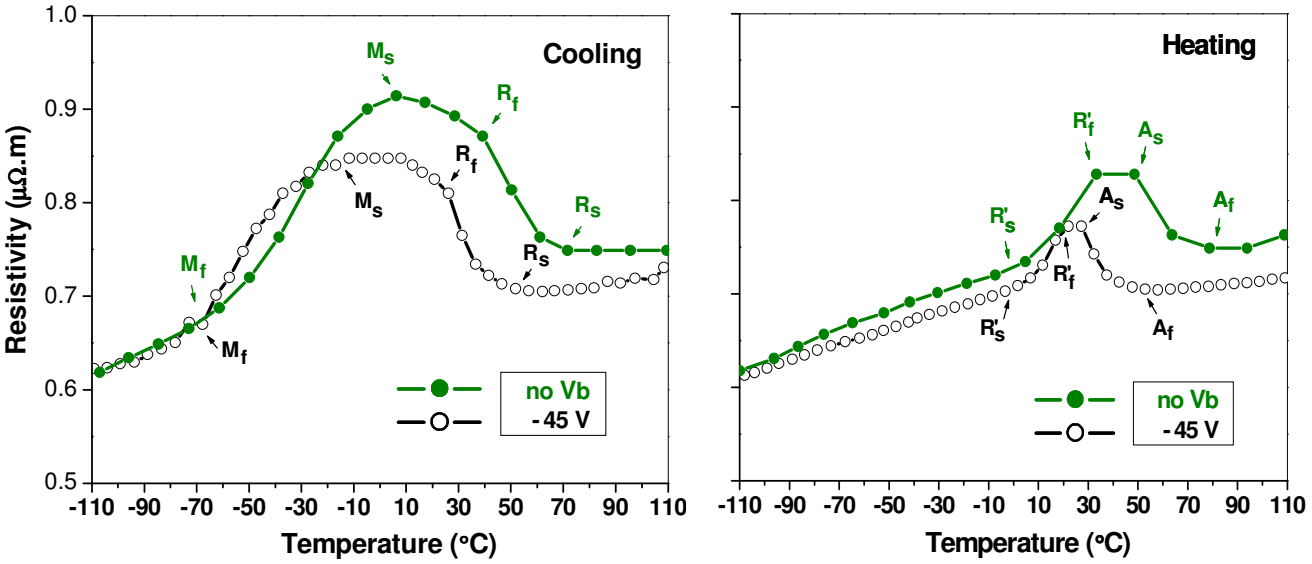

(a) (b)

Fig. 3.39: Dependence of the ER with temperature for the Ni-Ti samples, deposited without and with a V_b of –45 V on a TiN buffer layer of thickness ≈ 15 nm; (a) during cooling and (b) heating. The result from Fig. 3.38 has been inserted for comparison.

For the Ni-Ti sample deposited without V_b, the ER values of R-phase and B2 phase are higher than for deposition with V_b = –45 V. Additionally, it has been observed that for the samples deposited with V_b = –45 V, the transformations temperatures are lower when compared with the Ni-Ti sample deposited without V_b.

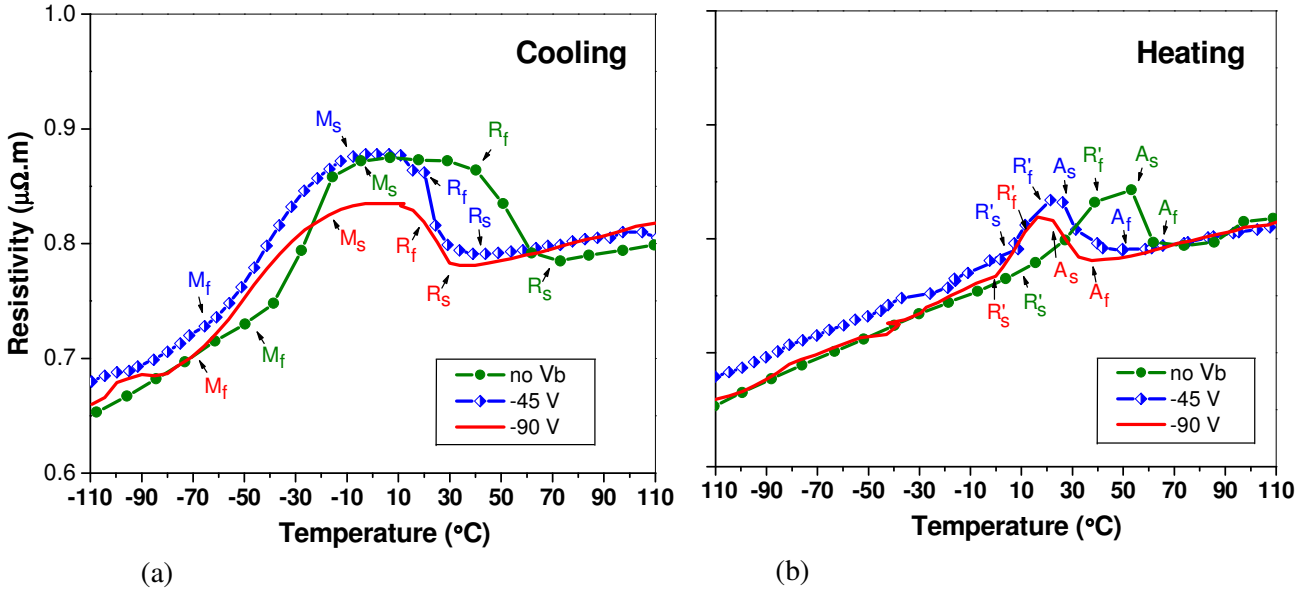

(a) (b)

Fig. 3.40: Dependence of the ER with temperature for the Ni-Ti samples deposited without V_b, with –45 and –90 V on a TiN buffer layer of thickness ≈ 215 nm; (a) during cooling and (b) during heating.

The ER results obtained for the set of samples with a TiN buffer layer of thickness ≈215 nm are shown in Fig. 3.40. The anomalous behaviour of the ER response has been attributed to lattice distortion and twinning, which are dominant mechanisms in self-accommodation R-phase transformation (both forward and reverse). The Ni-Ti film deposited without applying V_b exhibited higher phase transformation temperatures. The increase of the resistivity during R-phase formation for the Ni-Ti sample deposited with a V_b of –90 V was not as high as for the other samples.

The transformation temperatures also depend on composition. Increasing Ni content causes a decrease in the transformation temperatures. In order to detect a possible compositional effect on the transformation characteristics of this set of samples, AES was used to obtain depth profiles of elemental distribution in the films. In Fig. 3.41 results are presented concerning the Ni-Ti films deposited on a TiN buffer layer of thickness ≈215 nm without V_b and using a V_b of –90 V.

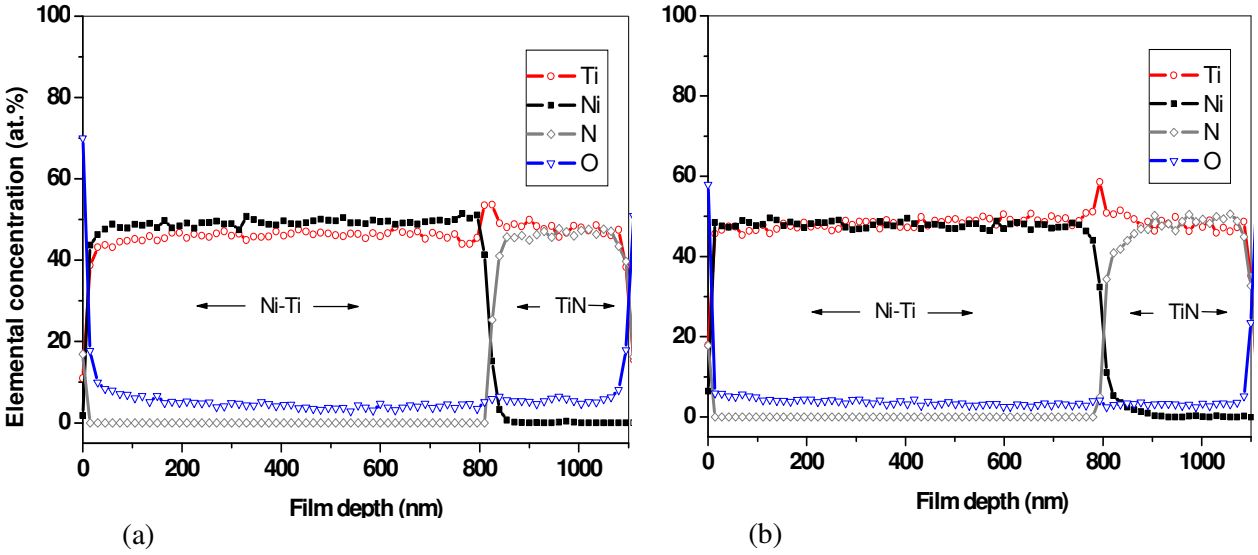

Fig. 3.41: AES elemental concentration profiles for the Ni-Ti samples on TiN buffer layers of thickness ≈ 215 nm; (a) Ni-Ti deposited without V_b, (b) deposition using a V_b of –90 V.

These results show that the higher transformation temperatures observed for the Ni-Ti film deposited without applying V_b cannot be explained by a compositional effect. The composition of both films is near equiatomic with only a slight Ni enrichment for the film deposited without V_b. For a possible role of the composition on the increase of transformation temperatures, a higher Ti content would be expected. It should be mentioned that the XRD data did not show the presence of precipitates.

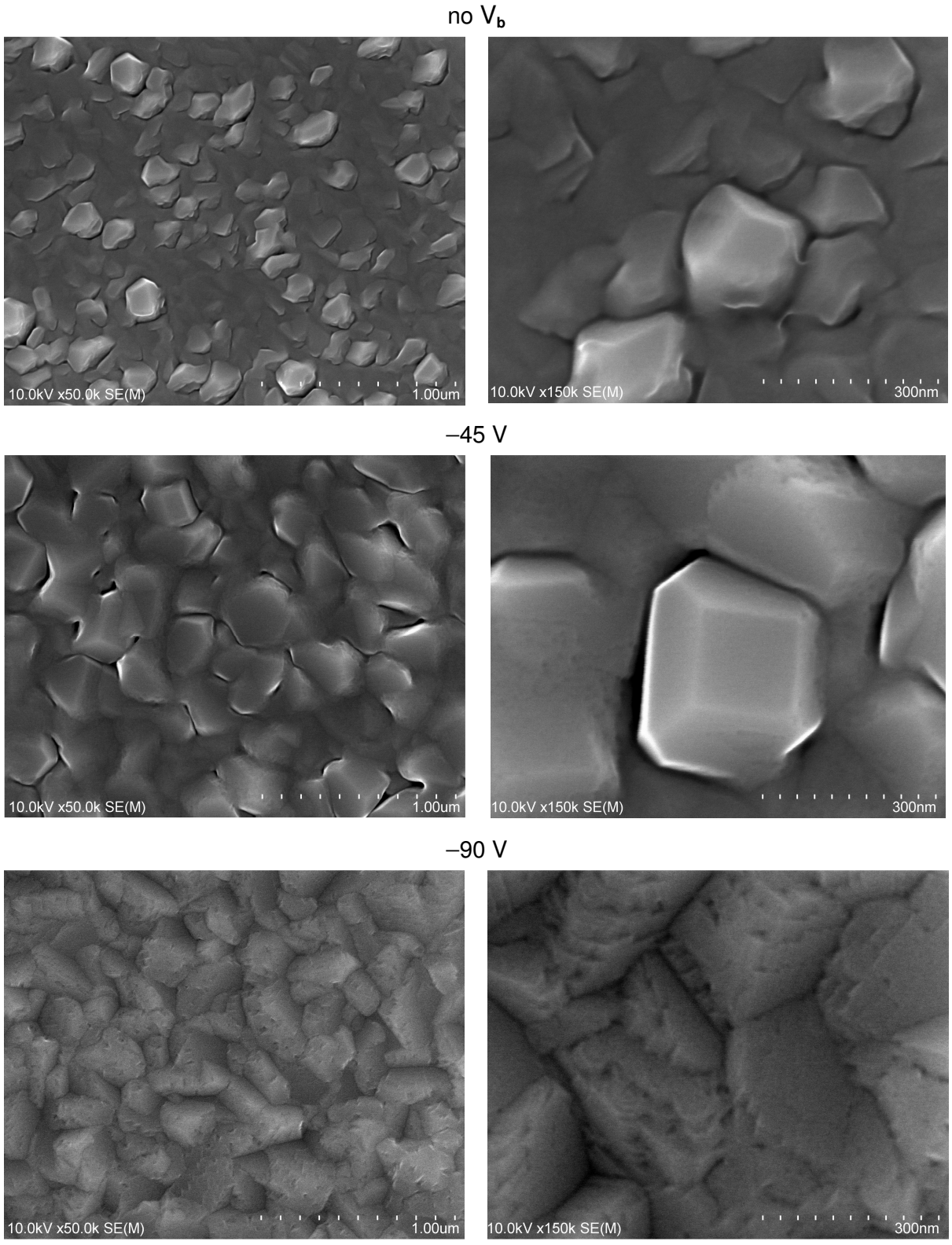

Fig. 3.42: SEM micrographs showing the effect of the V_b on the surface morphology of Ni-Ti films deposited on TiN buffer layers of thickness ≈ 215 nm.

Figure 3.42 shows SEM micrographs of the surface morphology of the Ni-Ti film, deposited without V_b and of the Ni-Ti films subjected to an additional ion bombardment during growth (–45 and –90 V), on TiN buffer layers of thickness ≈ 215 nm. It is important to stress that unbalanced magnetron sputtering sources exhibit a higher deposition rate and

concomitant high ion flux. A characteristic of this source discharge is a column of plasma, which leaves the magnetic tunnel region and projects normal to the target surface towards the substrate position. In consequence, a large flux of charged particles (electrons and ions) reaches the substrate and, by suitable biasing, the energy of ions impinging on the growing film can be varied. The micrographs have shown that the microstructure of the films was influenced by the degree of ion bombardment (V_b). The increase in ion energy by applying a V_b of −45 V led to apparently larger crystals in the form of regular polyhedron visible on the surface of the film. A further increase of V_b to −90 V led to the appearance of surface steps on the crystals morphology.

The results presented in this section have shown that a TiN buffer layer acts not only as a diffusion barrier, but there is also a relationship between the TiN substrates and Ni-Ti texture development (B2 phase):

1) there was a preferential growth of <110> oriented grains of the Ni-Ti B2 phase from the beginning of the deposition, with a constant growth rate during the whole deposition, for a Ni-Ti film deposited (without and with V_b of −45 and −90V) on TiN with a topmost layer formed mainly by <111> oriented grains;

2) in the case of Ni-Ti films deposited on top of a TiN layer where a dominating orientation could not be identified (primarily, <100> and <111> oriented grains of TiN nucleate and grow), a different behaviour was observed;
   - without V_b applied, <110> oriented grains of the Ni-Ti B2 phase dominated at lower thickness values, while, <211> oriented grains took over at higher thickness values.
   - with V_b of −45V, the development of the <211> oriented grains of the Ni-Ti B2 was reduced and the <110> oriented grains dominated since the beginning.

According to the ER results obtained during temperature cycling, the distinct crystallographic orientations of the Ni-Ti films influence their phase transformation characteristics. The resistivity increase during R-phase transformation, on cooling and heating, was higher for Ni-Ti films with a higher fraction of grains of the B2 phase with (211) parallel to the film surface. The ER measurements have also shown that for the deposition of Ni-Ti films with V_b (−45 and −90 V), the transformation temperatures of the various phases were shifted to lower values, when compared with the depositions performed without applying V_b.

3.4. NEAR EQUIATOMIC Ni-Ti FILMS GROWN ON MgO SINGLE CRYSTAL SUBSTRATE

The cleavage surfaces of alkali halides, i.e. NaCl and KCl, have been extensively used for studies of film formation and mechanism of epitaxial growth of different type of materials. Nevertheless, they do not exhibit such a high resistance to radiation damage by electron, thermal decomposition and low sensitivity to contamination as compared to MgO substrates [162].

In order to gain better understanding of the growth mechanism of epitaxial Ni-Ti films, real-time *in-situ* X-ray scattering measurements were conducted during Ni-Ti deposition on: MgO(100), MgO(111) and TiN(100)/MgO(100), without V_b. The processing conditions of these samples are presented in Tab. 3.4. Additional *ex-situ* techniques allowed a fine-structural characterization for the detection of possible interfacial reaction products.

Substrate type	Buffer layer	V_b (V)	Ni-Ti deposition time (min.)	Annealing time after Ni-Ti dep. (min.)
MgO(100)	-	-	129	
MgO(111)	-	-	69	
MgO(100)	TiN (15 nm thick)	−30 for TiN dep.	120	54

The deposition and annealing temperature of the layers was ≈ 470°C.

Tab. 3.4: Process conditions of near equiatomic Ni-Ti films samples, on MgO single crystal substrates, produced in the sputtering chamber of the beamline ROBL at ESRF.

3.4.1. *In-situ* experiments

3.4.1.1. Ni-Ti deposited directly on MgO single crystals

Figure 3.43 shows the time-dependent X-ray specular reflectivity (θ = 1°) of the Ni-Ti deposition on an MgO(100) substrate (without V_b). The intensity was recorded at intervals of 1 s, starting 60 s before the shutter was opened and the deposition began. The deposition was performed for 163 s. The arrow indicates the moment when the shutter was closed again. Intensity oscillations are depicted showing heteroepitaxial layer-by-layer growth, with increased surface roughening. This technique has also been employed for the first minutes of deposition of a Ni-Ti film on MgO(111) substrate (also in Fig. 3.43). A quick damping of

intensity is observed implying that the Ni-Ti film surface becomes fast rougher for such depositions conditions (the Ni-Ti film was also deposited without applying V_b).

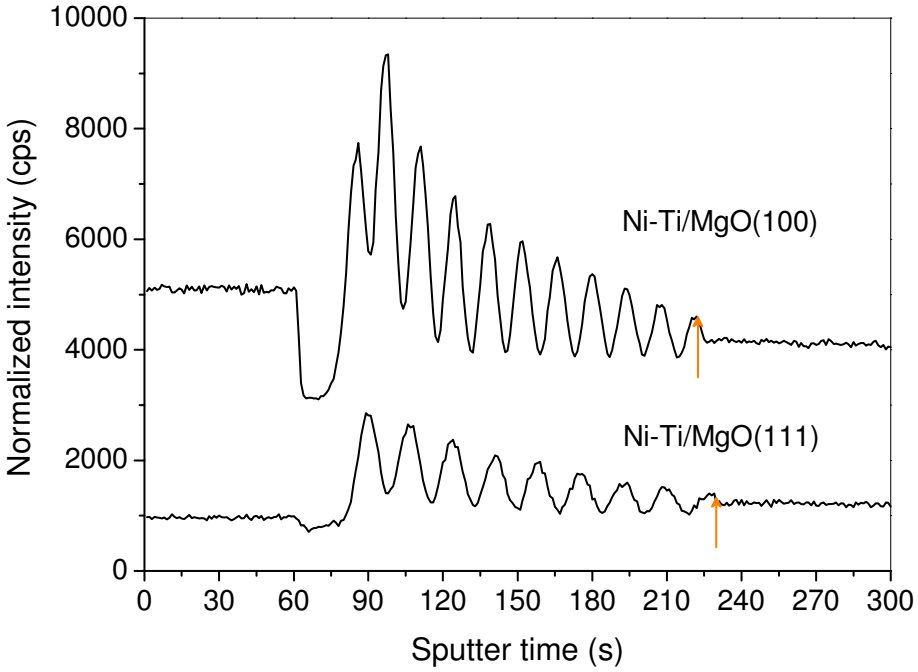

Fig. 3.43: Time-dependent *in-situ* specular X-ray reflectivity for the first minutes of deposition of the Ni-Ti films on MgO(100) and MgO(111) substrates (the arrow indicates the moment when the shutter was closed again).

The *in-situ* XRD measurements have shown a preferential stacking of (100) planes of the B2 phase parallel to the substrate surface for the Ni-Ti film deposited on MgO(100) substrate. The preferential orientation of B2(100) // MgO(100) was very strong and was maintained as such until the end of the deposition, which lasted for 2 h (≈ 900 nm), as shown in Fig. 3.44. However, additionally two diffraction peaks located near the B2(200) diffraction peak were detected suggesting the presence of interfacial reaction products. The peak at $2\theta \approx 25.98°$ (position at the end of the deposition) reveals the presence of TiO_2. A clear identification of the diffraction peak located at $2\theta \approx 24.65°$ could not be achieved (i.e., Ni_3Ti or Ni_3Ti_2 phase). The peak has then been identified as Ni-rich phase.

In the case of the Ni-Ti film grown on MgO(111) substrate, the *in-situ* XRD measurements have shown a preferential stacking of (110) planes of the B2 phase parallel to the film surface (Fig. 3.45) but, due to the fast increase of the intensity of the diffraction peaks of the interfacial reaction products (Ni-rich phase and TiO_2), it was decided to stop the deposition 60 min earlier (i.e., with only 69 min deposition time).

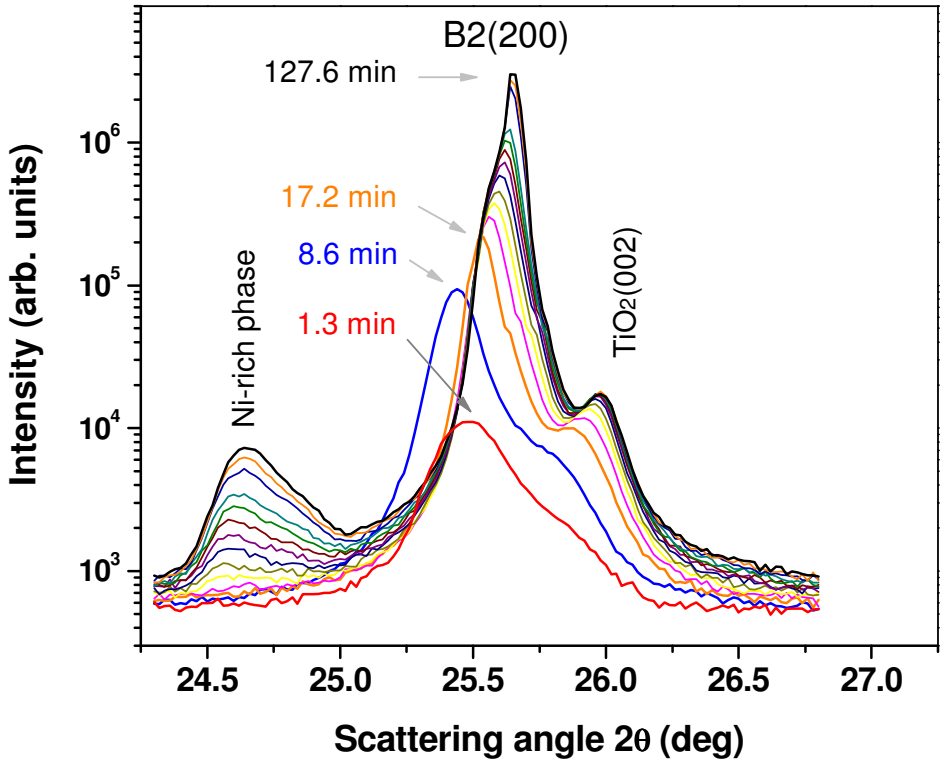

Fig. 3.44: Bragg-Brentano X-ray diffractograms obtained *in situ* during the deposition of a Ni-Ti film at ≈ 470°C on MgO(100) substrate (without V_b).

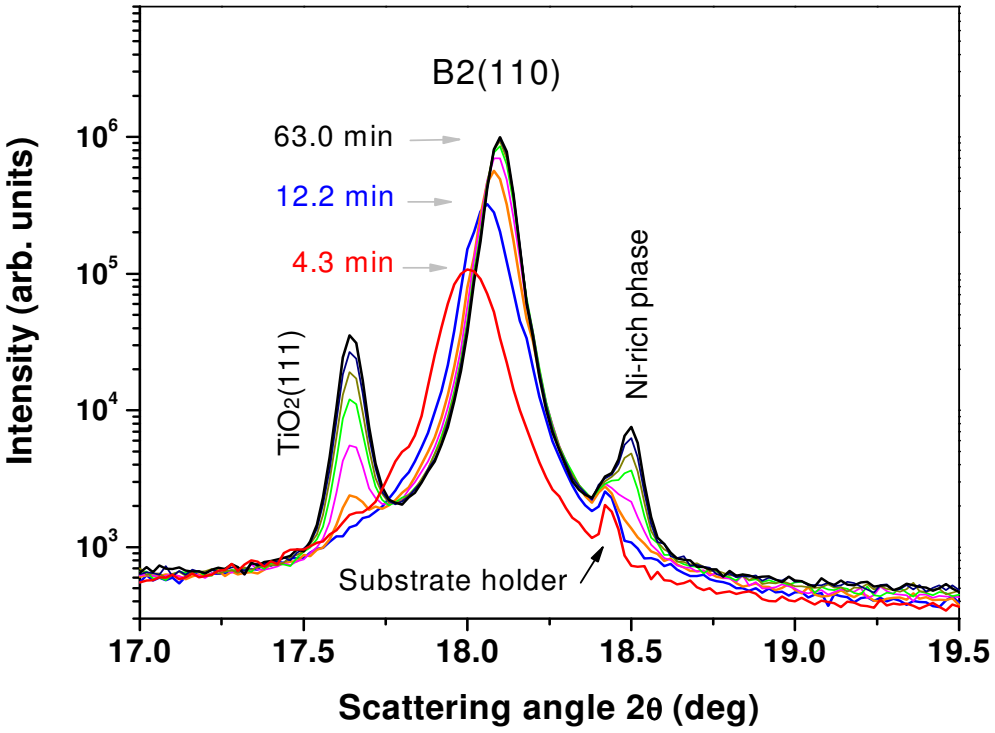

Fig. 3.45: Bragg-Brentano X-ray diffractograms obtained *in situ* during the deposition of a Ni-Ti film at ≈ 470°C on MgO(111) substrate (without V_b).

3.4.1.2. Ni-Ti deposited on TiN(100)/MgO(100)

As mentioned earlier, TiN films are an example of barrier-layers and they have been used in microelectronics industry. Typically, the deposition conditions chosen to obtain a preferred (111) grain orientation lead to a higher volume of voids between grains, whereas the (200) textured film is denser.

The heteroepitaxial growth of TiN on MgO(100), deposited by reactive magnetron sputtering, has been studied *in situ* by Bøttiger *et al.* [92]. Using real-time specular X-ray reflectivity, layer-by-layer growth was observed, with the surface roughening decreasing with an increase in the deposition temperature. TEM observations revealed atomic planes passing through the MgO/TiN boundary. The TiN(100) films are pseudomorphic to the underlying MgO(100) substrate. The tabulated lattice parameter for bulk TiN is 0.424 nm and the corresponding one for MgO is 0.420 nm.

In the present work, a further experiment was carried out using a TiN buffer layer (≈ 15 nm thick) to act as a diffusion barrier and also because it was believed to be useful as a buffer for epitaxial growth of the Ni-Ti film on the MgO(100) substrate. The respective *in-situ* characterization results are presented below.

Low angle specular reflectivity time resolved at a fixed incidence angle ($\theta = 1°$) was useful to determine the growth mode of the TiN buffer layer and of the Ni-Ti film (first 9min 30s) for the deposition on MgO(100) substrate (Fig. 3.46), revealing a layer-by-layer growth mode (with the decrease in oscillation amplitude, indicating that the surface becomes rougher during sputtering). The intensity oscillations were observed for a longer time comparing the deposition with a TiN buffer layer and the deposition of Ni-Ti directly on MgO(100). In both cases no V_b was applied.

A single orientation of the Ni-Ti B2 phase grew during the 129 min of deposition, with (100) planes stacking parallel to the substrate (Fig. 3.47). The first layers deposited on the TiN(100) were constrained (compressive planar stress state) and this deformation remained until the end of the deposition; later layers had a gradually relaxed interplanar distance (smaller $d_{(200)}$ in the direction of the surface normal), indicating a gradual relaxation of the compressive stress constraint imposed at the interface Ni-Ti/TiN (Fig. 3.48).

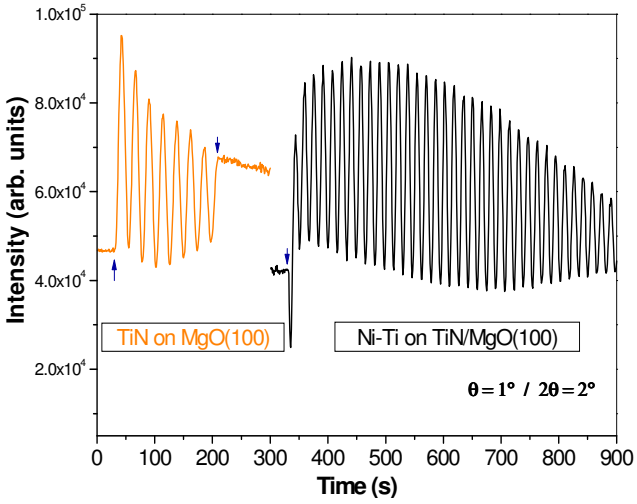

Fig. 3.46: Time-dependent *in-situ* XRR for the TiN buffer layer and the first minutes of deposition of the Ni-Ti film on MgO(100) substrate at ≈ 470°C.

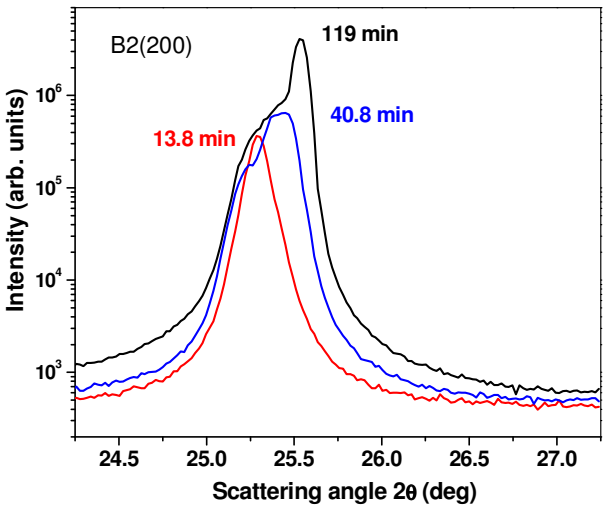

Fig. 3.47: XRD results, for the Ni-Ti film deposited on TiN(100)/MgO(100), obtained during deposition (without V_b).

The experiments have also shown that the TiN layer acts as a diffusion barrier. In contrast to the Ni-Ti film deposited directly onto MgO(100), in this case, no diffraction peaks from interfacial reaction products were detected.

Figure 3.49 shows the diffractograms obtained after deposition (at ≈ 470°C) and at RT (after naturally cooling). The results recorded at RT revealed the presence of the R-phase structure in the Ni-Ti film.

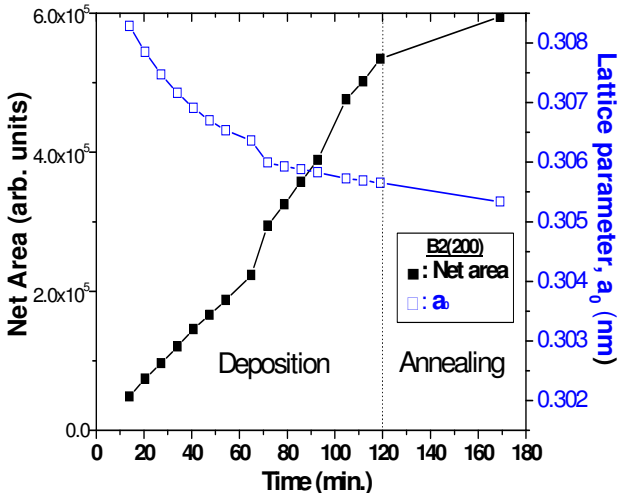

Fig. 3.48: The net areas of the Bragg-Brentano B2(200) diffraction peak and the a_o values as obtained from the position of the peak, recorded as a function of time after start of Ni-Ti film growth on TiN(100)/MgO(100).

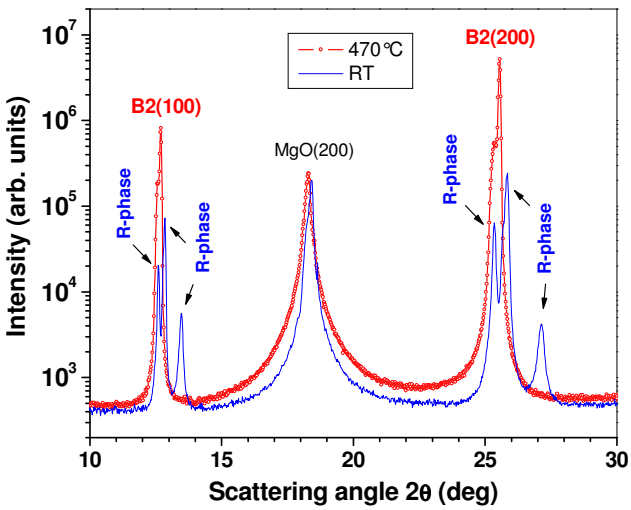

Fig. 3.49: XRD results, for Ni-Ti film deposited on TiN(100)/MgO(100), obtained at ≈ 470°C and RT.

3.4.2. *Ex-situ* characterization

3.4.2.1. Ni-Ti deposited directly onto MgO single crystals

The pole figures measurements performed for the Ni-Ti film on MgO(100), in the austenitic state, i.e. at RT, have confirmed the presence of a strong texture (Fig. 3.50). They have shown a stacking of the B2(100) parallel to the MgO(100) substrate, with B2[100]//MgO[110], suggesting that the Ti-O adsorption sites between the Ni-Ti and oxide substrate are essential to improve the (100) orientation of the B2 phase.

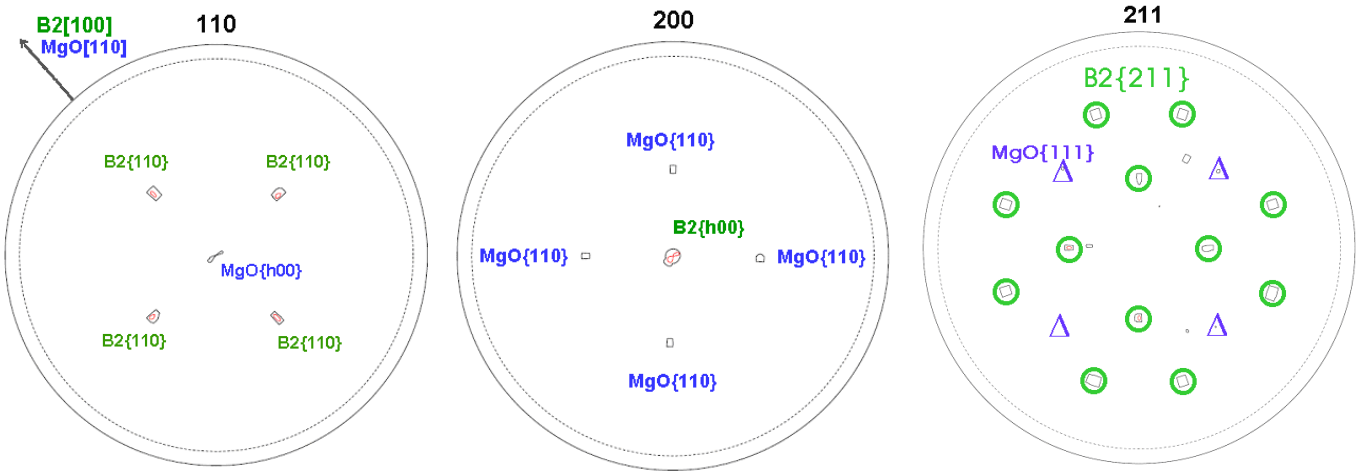

Fig. 3.50: Pole figures of Ni-Ti B2 phase grown on MgO(100) substrate, nominally measured in the diffraction peaks B2(110), B2(200) and B2(211).

The crystal structure of MgO is NaCl type with the lattice constant of 0.421 nm. If one considers that the interatomic distance of O is 0.297 nm for the (100) plane of MgO, and the interatomic distance of Ti is 0.302 nm for the (100) plane of the B2 phase, their misfit is only approximately 1.3 % (Fig. 3.51). This is in agreement with the behaviour observed by low angle specular reflectivity time resolved for the growth mode of the first few monolayers (Fig. 3.43), which has shown a good matching of the Ni-Ti B2 phase structure to the MgO(100) substrate.

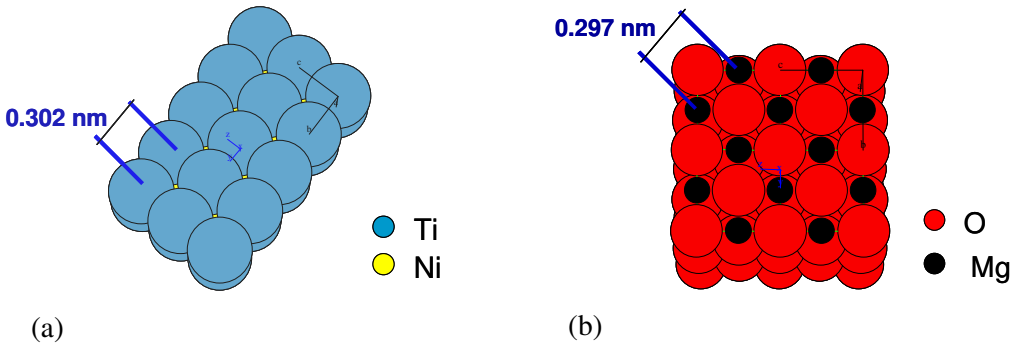

(a) (b)

Fig. 3.51: Atomic model illustration of the (100) crystallographic planes of; (a) Ni-Ti B2 phase, (b) MgO.

X-TEM observations were later performed in order to get additional information to correlate with the XRD data. At this point it is important to remember that for TEM studies the samples were cut perpendicular to the surface of the film. This should be taken into consideration for the interpretation of the results obtained by those two techniques, since the atomic planes arrangements are visualized using different approaches. Vertical Bragg-Brentano large angle XRD probes planes parallel with the film surface.

Figure 3.52(a) depicts a SAED pattern taken with the specimen aligned along the MgO[100] zone axis. Spots associated with the MgO substrate and the Ni-Ti film (B2 phase) were selected resulting in the images presented in Fig. 3.52(b) and (c), respectively. Using dark field imaging in the B2 phase spot, the internal structure of the Ni-Ti film was perceptible. It should be noted that the stacking of the (100) planes of the B2 phase on the MgO(100) substrate occurred with B2[100]//MgO[110].

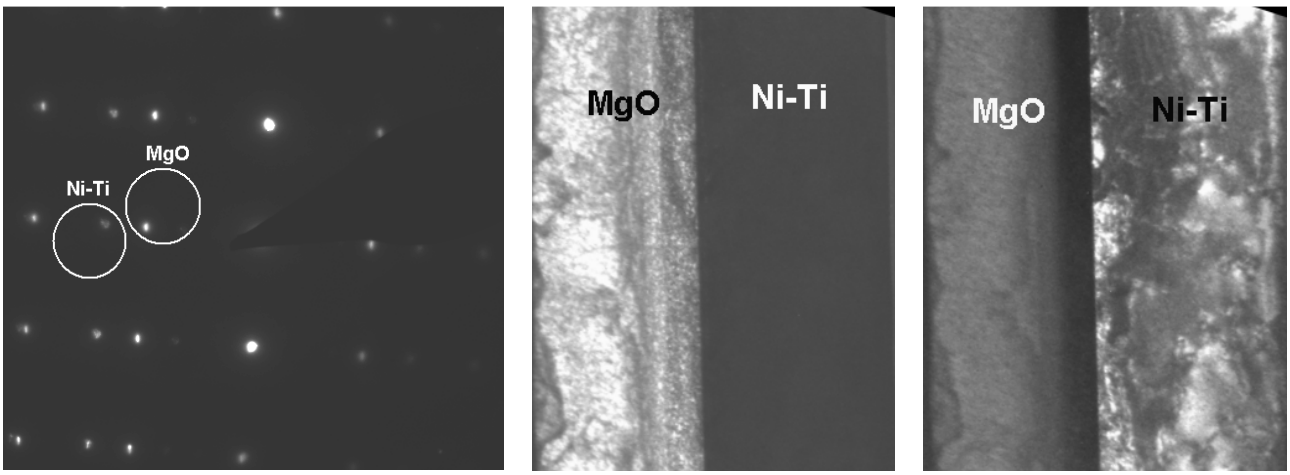

(a) (b) (c)

Fig. 3.52: TEM observations of the Ni-Ti film attached to the MgO(100) substrate; (a) SAED pattern, (b) dark field image taken in the reflection of MgO and (c) in the reflection of Ni-Ti, respectively.

The cross-section HR-TEM micrograph in Fig. 3.53 exhibits an area located at the interface substrate/film. In the micrograph, it has been inserted a reference to the lattice spacings of MgO(200) and Ni-Ti B2(110), which were obtained using the FFT procedure. As observed by the *in-situ* XRR measurements presented earlier (Fig. 3.43), the Ni-Ti film is pseudomorphic to the underlying MgO(100) substrate. The stacking of the Ni-Ti film (B2 phase) on the MgO(100), due to the different lattice parameters of the two materials (Fig. 3.51), leads to the development of compressive stress in the film. This stress results in an increase in the out-of-plane Ni-Ti planar distance to compensate for the smaller in-plane planar distance.

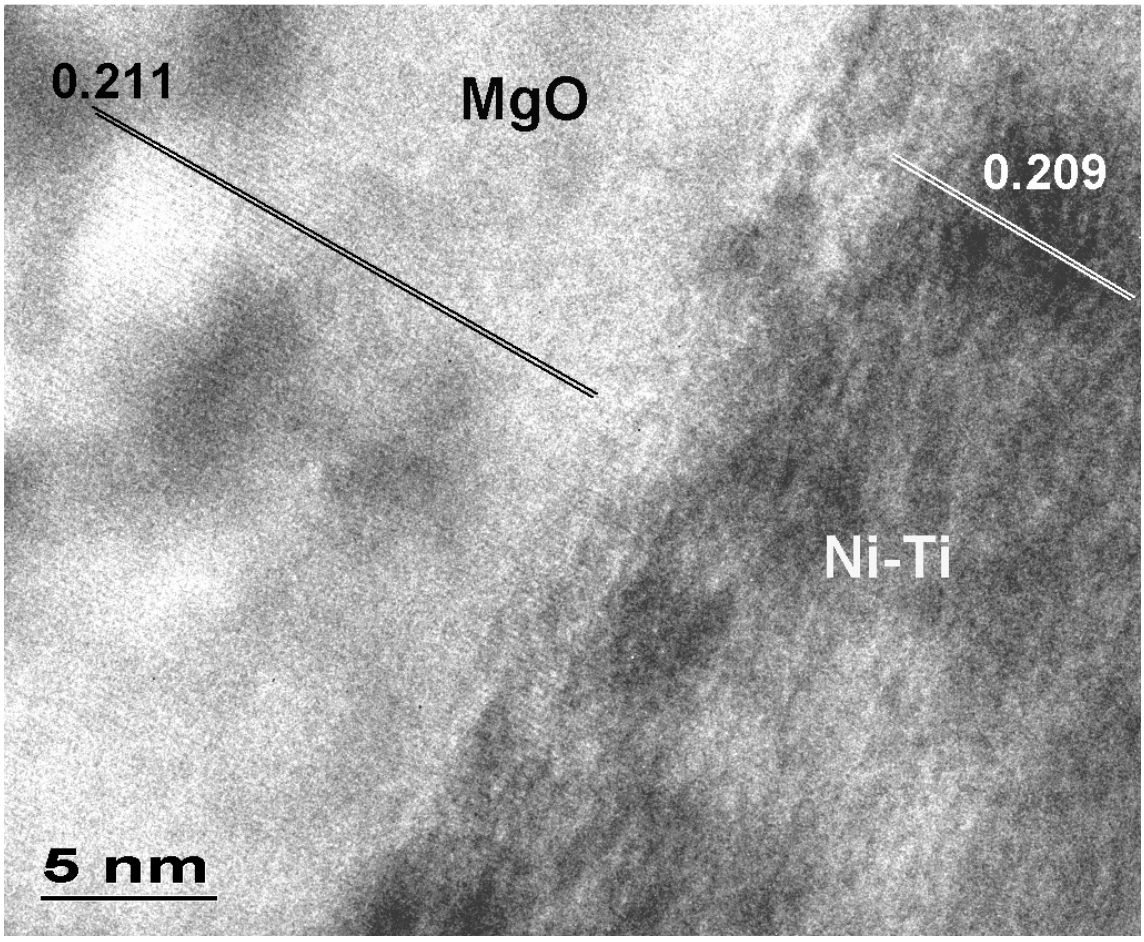

Fig. 3.53: Cross-section HR-TEM micrograph of the interfacial zone of the sample shown in Fig. 3.52. The lattice spacings of MgO(200) and Ni-Ti B2(110) planes are inserted in the micrograph.

Further observations were carried out in order to confirm the indication of compound formation at the MgO/Ni-Ti interface as anticipated by XRD measurements. In SAED patterns obtained for the overall specimen, reflections of low intensity were detected that could not be linked to the MgO or B2 phase structures [Fig. 3.54(a)]. The dark-field micrograph shown in Fig. 3.54(b) was taken in the reflection selected in the previous image.

This micrograph corroborates what has been said before, i.e., the formation of reaction products at the interface occurred as the bright regions show up at the interface. The compound indicated by the black arrow in Fig. 3.54(b) is shown in more detail in Fig. 3.54(c) and the corresponding bright-field image is presented in Fig. 3.54(d). Although it is suggested that these compounds are Ni-rich, these techniques did not provide enough information for their identification.

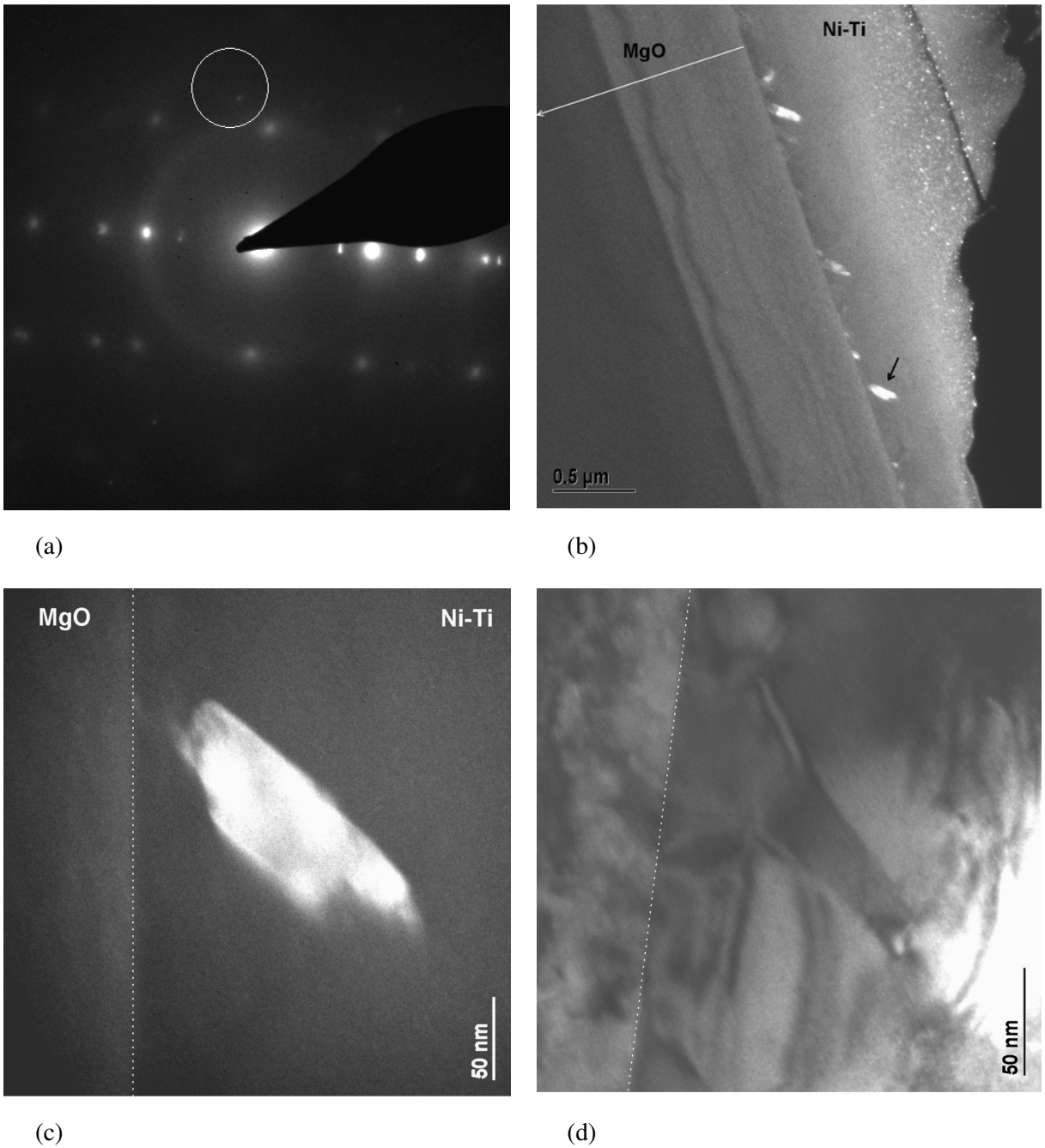

Fig. 3.54: TEM observations of the Ni-Ti film attached to the MgO(100) substrate; (a) SAED pattern of the overall sample, (b) dark-field image taken in the reflection selected in (a), (c) detail of an interfacial compound (dark-field) and (d) corresponding bright-field image.

The temperature dependence results of the ER of the samples obtained directly on MgO(100) and MgO(111) are shown in Fig. 3.55, for heating and cooling. An increase of the ER related with the R-phase transformation was detected for both specimens during heating and cooling. The results have revealed a big fraction of the Ni-Ti films transformed to B2 phase at RT. It has been observed before by XRD, for the sample with a TiN buffer (Fig. 3.49), that the Ni-Ti film structure at RT is mainly rhombohedral (R-phase).

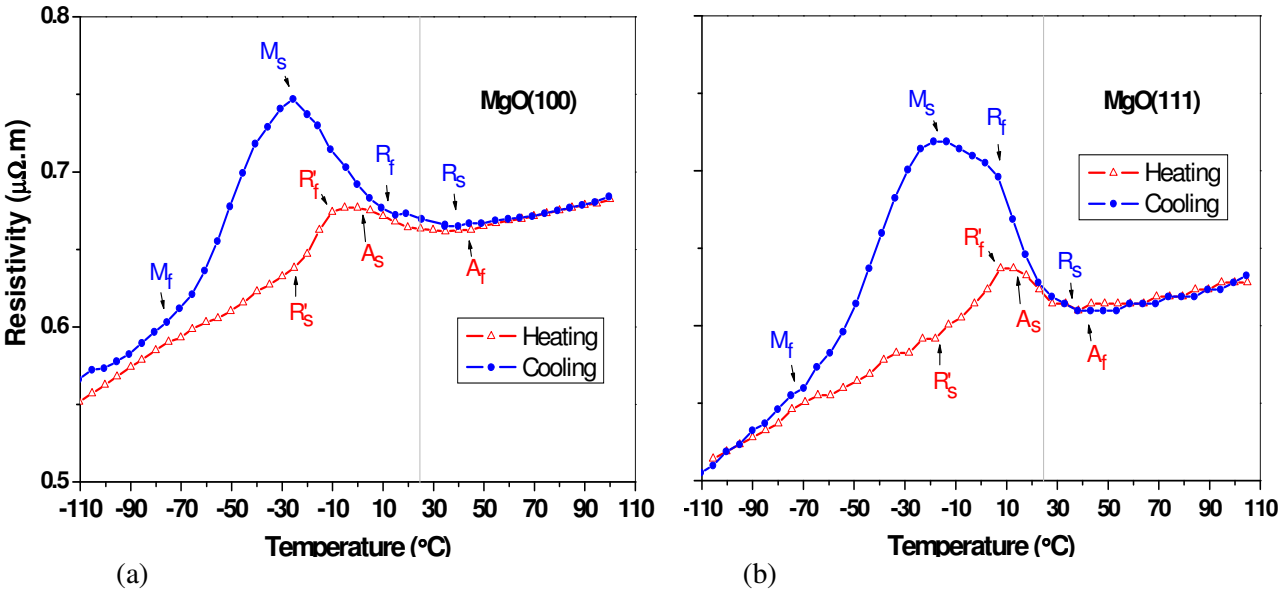

Fig. 3.55: Dependence of the ER with temperature for the Ni-Ti sample on; (a) MgO(100) and (b) MgO(111), during cooling and heating.

3.4.3. Deposition of a TiN film with a topmost layer formed mainly by <100> oriented grains

The deposition of Ni-Ti on TiN(100)/MgO(100) has shown that the (100) orientation of TiN clearly induces the (100) orientation of the B2 phase. For practical applications, the use of an MgO single substrate is not, in most of the cases, the desired solution. Experiments at ROBL have shown that a TiN layer with a topmost layer formed mainly by <100> oriented grains can be obtained on thermally oxidized Si(100) substrates (Fig. 3.56), using the following deposition parameters: Ti = 80 W, Flux ratio Ar/N = 4/2, P_{Ar} = 0.35 Pa, T_S = 300°C and V_b = −30V. In this case the TiN film has been deposited stepwise.

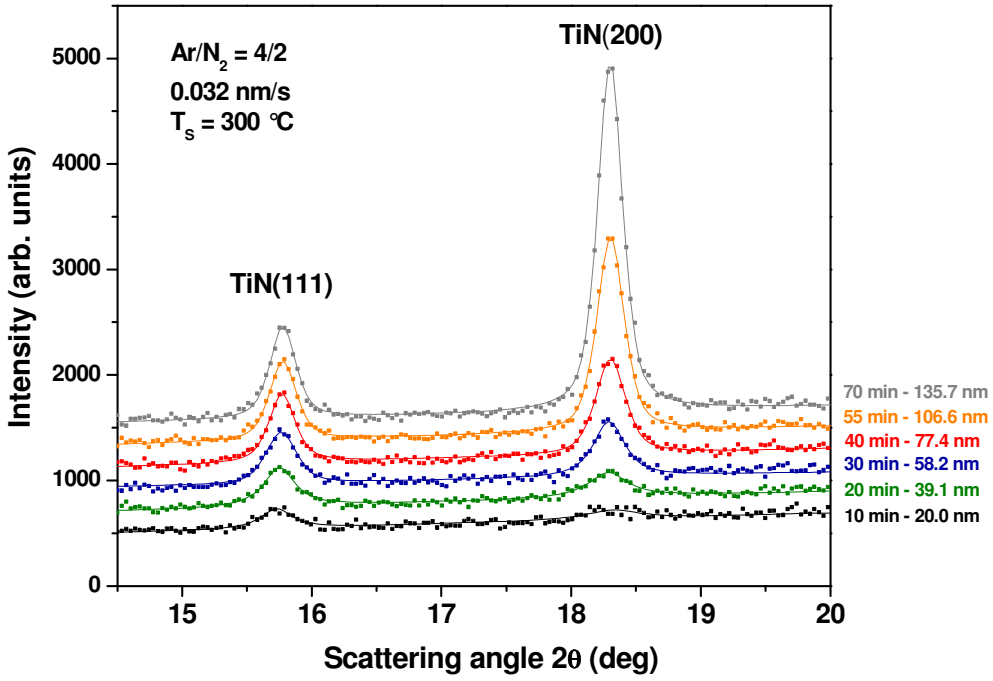

Fig. 3.56: *In-situ* XRD spectra of pure TiN film sputtered at low growth rate at 300°C. Ion irradiation at a bias of –30 V leads to (100) preferred orientation in pure TiN.

Figure 3.57(a) exhibits the development of the net areas of the TiN(111) and TiN(200) diffraction peaks as a function of time. During the initial stages of growth, primarily <100> and <111> oriented grains nucleated and grew. The results show that <100> grains took over at higher thickness values.

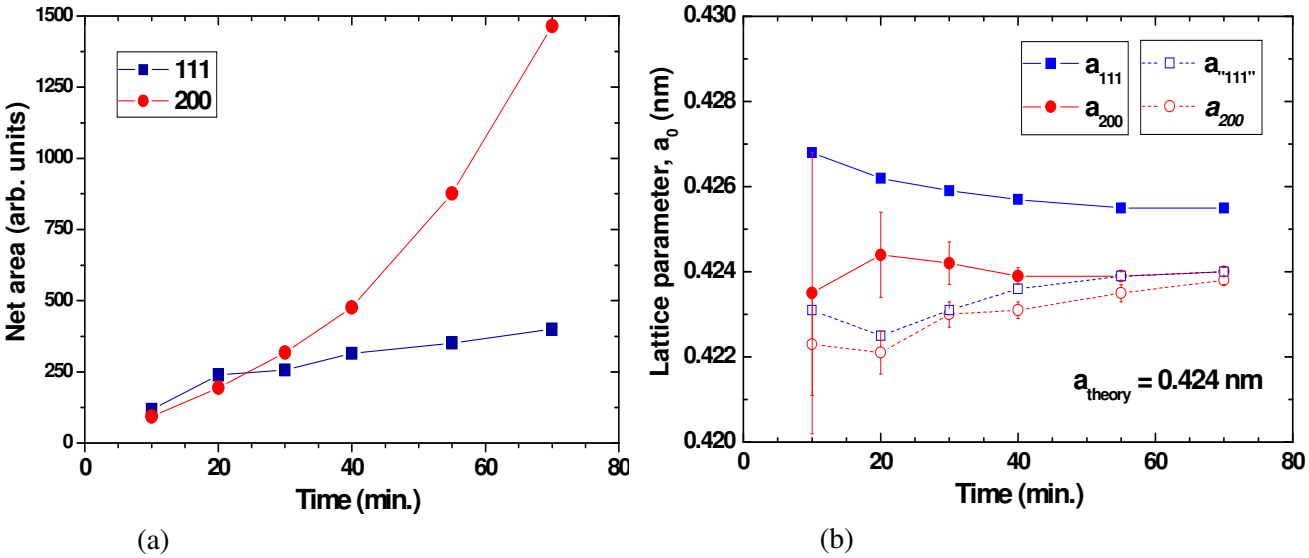

Fig. 3.57: *In-situ* XRD results recorded as a function of time after start of TiN film growth on thermally oxidized Si(100); (a) The net areas of the Bragg-Brentano 111 and 200 diffraction peaks of TiN, (b) comparison of in-plane lattice constants ($a_{\text{“111”}}$ and a_{200}).and off-plane lattice constants (a_{111} and a_{200}).

For a qualitative evaluation of the internal film stress, the off-plane and in-plane lattice parameters of the growing film were determined from the peak positions in Bragg-Brentano, and grazing exit in-plane large angle scattering (GIXS) geometry with an incident angle of 0.2° (where planes perpendicular to the film surface are probed). Figure 3.57(b) shows the comparison of these lattice parameters as a function of deposition time. The film exhibits in-plane a_0 values that are slightly smaller than the off-plane ones. This implies a compressive stress that diminishes the in-plane interplanar distance, while because of the Poisson's effect the interplanar distance expands out of plane. It further shows that for higher thickness values the compressive stress is generally reduced, suggesting that during the 70 min deposition time the film relaxes into a lower stress state.

XRR spectra have been taken after each deposition step and later fitted with the Bede Mercury REFS code [157]. The results are shown in Fig. 3.58. From the fitting an average roughness of 1-2 nm is derived. The film exhibits a density of approximately 91% of the bulk density (TiN = 5.43 g/cm^3), thus a porosity less than 9%, which is a typical value for physical vapour deposition TiN films. The fitted average deposition rate was 0.032±0.003 nm/s.

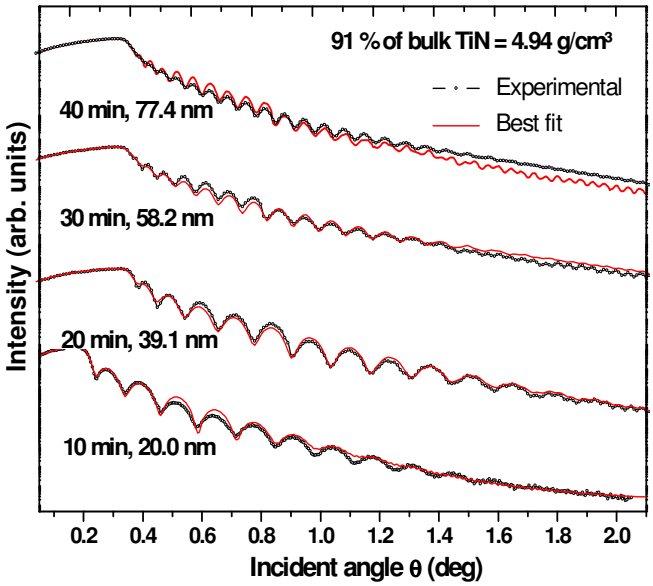

(a)

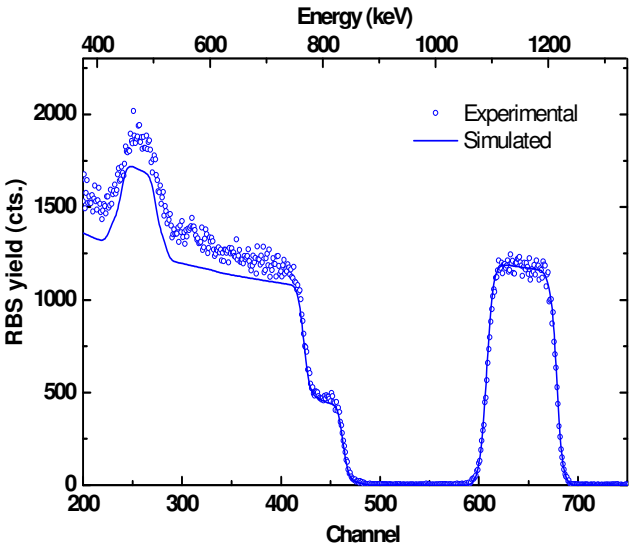

(b)

Fig. 3.58: XRR spectra with respective fits for the TiN film deposited on SiO_2/Si(100) substrate.

Fig. 3.59: RBS analysis of pure TiN deposited on SiO_2/Si(100) substrate showing data from experiment and simulation.

The film composition was measured *ex situ* by RBS confirming the desired stoichiometry (Fig. 3.59). From previous experiments, the total oxygen content of the films should not change when the growth is stopped at regular intervals although, during the stops,

the exposure of oxygen to the surface is increased. Since a low oxygen concentration from the surface is detected (oxygen contamination of less than 3 %), it is suggested that oxygen is incorporated during the transfer to the RBS facility rather than during the actual growth. Most likely, the oxygen entered the film after deposition via grain boundaries migration when they were exposed to the atmosphere.

The film was also characterized by electron microscopy. A typical micrograph obtained in cross-section by SEM is shown in Fig. 3.60 where a columnar structure is discerned.

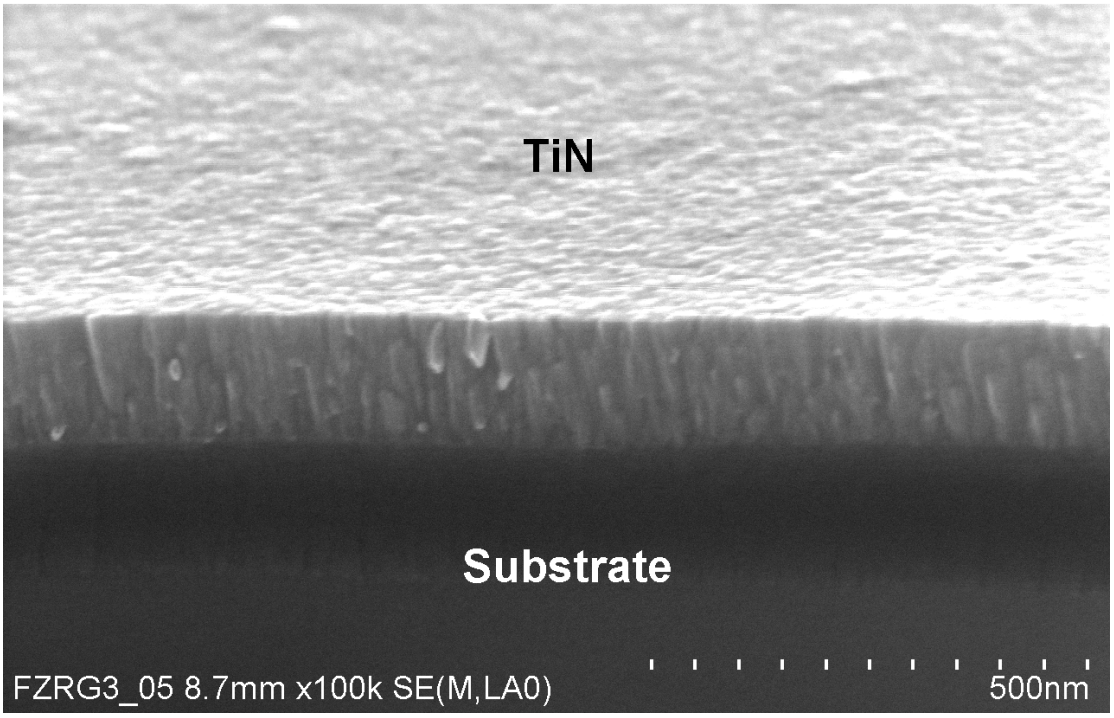

Fig. 3.60: SEM micrograph of pure TiN deposited on SiO_2/Si(100) substrate.

Figure 3.61 shows a typical bright field X-TEM micrograph for the same sample. In accordance with the Thornton structure zone model the deposited TiN film show zone-T columnar structure due to the low substrate temperature of ≈ 300°C compared with the T_m of ≈ 3000°C. There is a random nucleation at the interface developing into *v*-shaped columns, i.e., a competitive growth between different crystal orientations with the faster growing orientation gradually overgrowing the slower one. A closer look into the topmost region of the film (indicated with the white arrow) by cross-section HR-TEM reveals the presence of (100) planes parallel to the surface, which corroborates the *in-situ* XRD results.

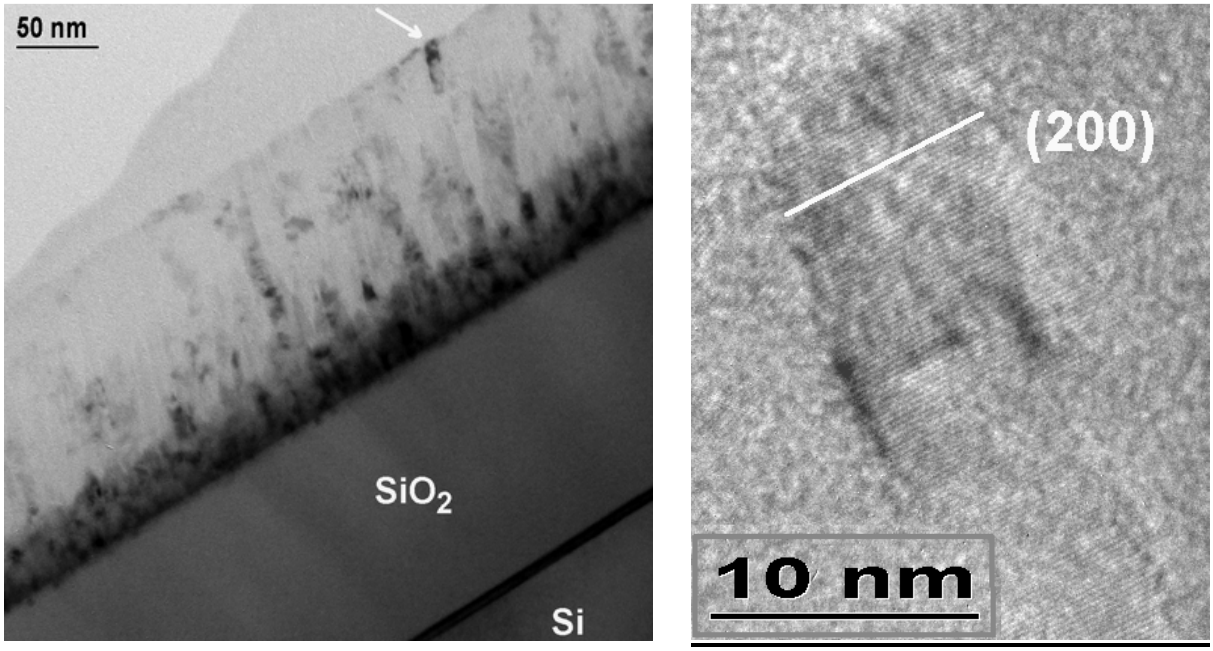

Fig. 3.61: Bright field X-TEM micrograph of the TiN film deposited on SiO_2/Si(100) substrate at ≈ 300°C, with an enlargement of the topmost film's region.

In this section, it has been observed by *in-situ* XRD a preferential stacking of (100) planes of the B2 phase parallel to the film surface for Ni-Ti depositions directly onto MgO(100) substrates. The XRD data and complementary *ex-situ* TEM observations led to the identification of reaction products between the Ni-Ti film and the MgO substrate. The XRD results obtained during the deposition of Ni-Ti directly onto MgO(111) also suggest the presence of interfacial reaction products. In this later case, the development of the (110) orientation of the B2 phase was observed.

The effect of the introduction of a TiN layer, with a (100) orientation, on the structural development of the Ni-Ti film (deposited on top) was as well tested. A single orientation of the B2 Ni-Ti phase with (100) stacking parallel to the substrate could be once more produced. Using this procedure, a highly ordered epitaxial growth was obtained with the crystallographic relationship of Ni-Ti(100) // TiN(100) // MgO(100). Furthermore, it has been recognized that the TiN buffer layer acted as a diffusion barrier.

In this section it was also shown that it is possible to produce TiN films with the topmost layer mainly constituted by <100> oriented grains for depositions on thermally oxidized Si(100) substrates. These are promising results concerning future development of practical applications seeking the production of Ni-Ti films with the (100) orientation for the B2 phase.

3.5. CONTROLLED CHANGE OF THE Ti:Ni RATIO DURING THE DEPOSITION OF Ni-Ti FILMS

The effect of the deliberate change of the Ti:Ni ratio during the deposition of Ni-Ti films was tested and, thus, graded films were deposited exhibiting distinctive composition and microsctructure along the growth direction. The structural characterization of this type of films (graded films) by *ex-situ* techniques was also performed and selected results are also shown in this chapter.

3.5.1. Deposition on naturally oxidized Si(100) substrates

The *in-situ* study of the sputter deposition of Ni-Ti films using two targets Ni-Ti and Ti puts in evidence the possibilities of the real-time structural design during magnetron deposition by co-sputtering excess Ti. The magnetron with the Ni-Ti alloy target was run at a power of 40 W while the magnetron with the pure Ti target was run at varying power levels of 0-30 W. In this series of experiments, the near equiatomic composition could be obtained with the Ti target running at 8 W. This is the only case presented where the power applied to the Ti magnetron had to be lower than 20 W due to the different shutters configuration used for the processing of the sample. Si(100) wafers (15×15 mm^2) with a natural oxide layer on top served as substrates. No V_b was applied during the growth of the Ni-Ti graded film.

3.5.1.1. *In-situ* experiments

Figure 3.62 demonstrates the benefit of following *in situ* the evolution of the structure of the film during growth, revealing intermediate conditions, which cannot be observed by *ex-situ* techniques. In this experiment the magnetron with the Ni-Ti alloy target was run at a constant power of 40 W during the 4 steps of the deposition while the magnetron with the pure Ti target was run at 8, 20 and 30 W on the 1st, 2nd and 3rd deposition steps, respectively. The chosen sequence and amount of co-sputtering led to different peak intensities of the various phases.

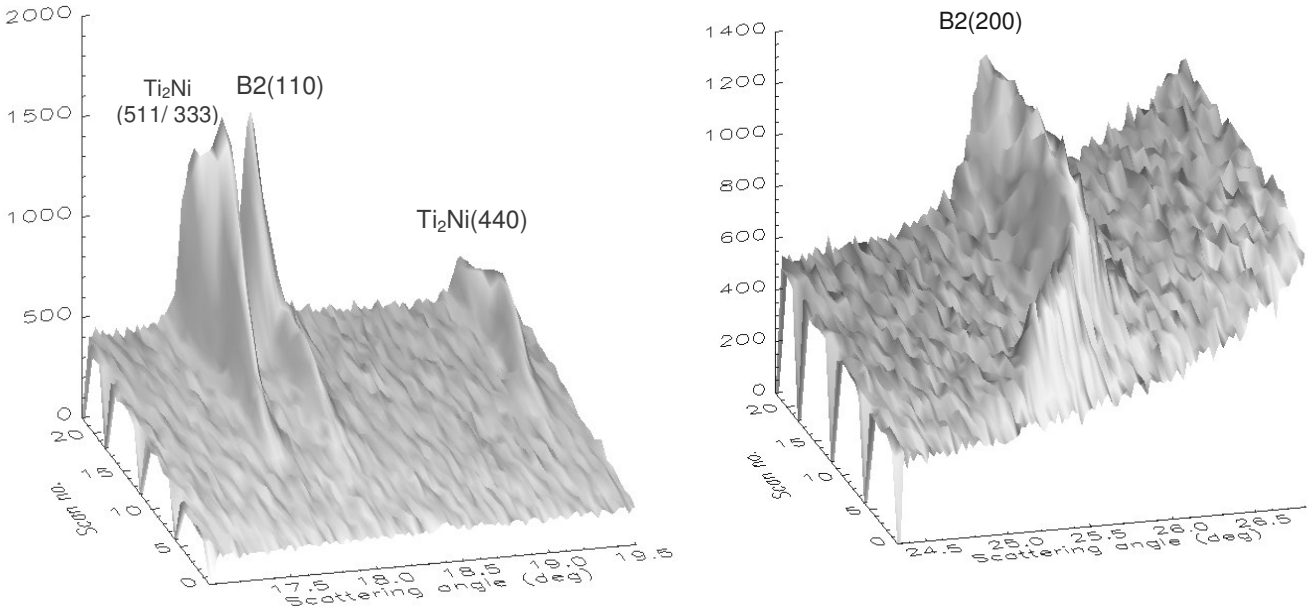

Fig. 3.62: XRD data of a growing film where for each 30 min the co-sputtering with Ti changed from 8 W to 20 W to 30 W to finally 0 W (deposition without V_b). 23 scans are added representing the microstructural development of the Ni-Ti film (the zero intensities are manually inserted into the graphs to mark the various changes in the sputtering conditions; the z-axis scale represents the detector intensity in cps).

In Fig. 3.63 are represented the variation of the integrated intensities of B2 and Ti_2Ni diffraction peaks [B2(110), B2(200) and Ti_2Ni(333/511), respectively] and the variation of the a_0 values (as calculated from d according to the corresponding Bragg-Brentano peak position), as a function of time after start of deposition. Using the chosen deposition parameters the B2 phase started by stacking onto (h00) planes. During this initial period of the deposition, a significant change of the a_0 value of B2 phase as calculated from $d_{(200)}$ was observed. This is a typical behaviour already observed during the deposition of near equiatomic films on naturally oxidized Si(100) substrates (section 3.1.1.). In that previous case, after the formation of a strained layer with the B2 phase with (h00) planes parallel to the substrate during the first 30 min, it relaxed, and then the diffracted intensity of B2(200) stayed constant while the B2(110) intensity was linearly growing. Here, after this initial period (≈ 30 min), the Ti co-sputtering power was increased to 20 W and, consequently, the Ti_2Ni(333/511) peak together with the B2(110) peak were detected. A further increase of co-sputtered Ti in the film (increasing the Ti magnetron power to 30 W) enhanced the development of the Ti-rich phase. During co-sputtering with a Ti power of 30 W the a_0 values of B2 phase, as calculated from $d_{(200)}$ and $d_{(110)}$, were already quite stable, while for Ti_2Ni, as calculated from $d_{(333/511)}$, a continuous slight decrease of this value was perceptible.

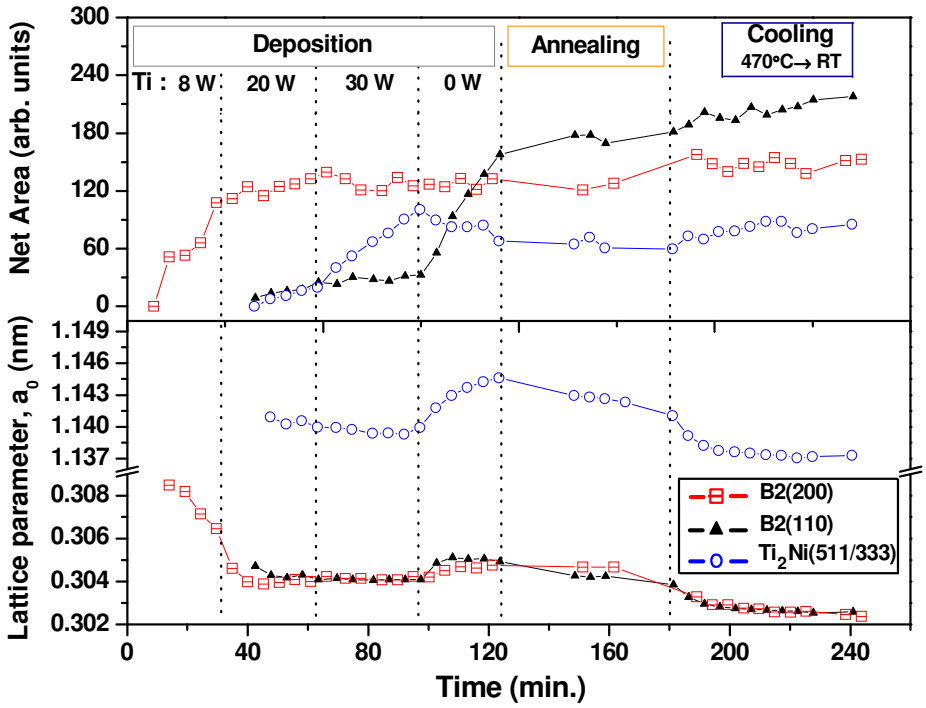

Fig. 3.63: *In-situ* XRD results for a Ni-Ti graded film deposited on naturally oxidized Si(100) substrate during continuous co-sputtering of Ni-Ti (40 W) and Ti (8/20/30/0 W), during annealing and natural cooling. Represented are the net areas of the Bragg-Brentano B2(110), B2(200) and Ti_2Ni(333/511) diffraction peaks as well as the a_0 values as obtained from the positions of the respective Bragg-Brentano peaks, as a function of time.

After approximately 97 min by stopping the Ti co-sputtering (i.e., decreasing the Ti:Ni ratio of the atoms deposited at the growing film), Ti_2Ni dissolved and, thus, played the role of a Ti reservoir for the formation of B2 phase now preferentially stacking onto (110). A significant increase of the a_0 value of the Ti_2Ni as calculated from $d_{(333/511)}$ was observed. For the B2 phase the increase is slightly higher for the value calculated from $d_{(110)}$. During the annealing step no relevant peak intensity changes, i.e. no structural or phase changes, could be discerned. However, just the a_0 value of B2 phase as calculated from $d_{(200)}$ stayed stable. The a_0 value of B2 phase as calculated from $d_{(110)}$ and the one calculated for Ti_2Ni decreased. The cooling stage from deposition temperature to RT results in an overall decrease of a_0 for both phases and for the B2 phase the values calculated from $d_{(110)}$ and $d_{(200)}$ were comparable.

3.5.1.2. *Ex-situ* characterization

The depth profile of the atomic concentrations in the Ni-Ti film from Fig. 3.63 is shown in Fig. 3.64. For the AES and X-TEM results presented, the substrate can be found on the right hand side. In Fig. 3.64 the different steps of co-sputtering deposition are marked with dashed lines and identified by Roman numerals. The control of the Ti power resulted in a non-

homogeneous composition along the film's cross-section, and the first fraction of the film (I), supposed to exhibit a near equiatomic composition, shows evidence of an interfacial reaction between the film and the substrate as deduced from the altered composition nearby the substrate. Starting the evaluation from the interface to the surface of the film, Ni and Ti are detected in the Si substrate. Ni atoms appear to be the primary diffusing species into the substrate. There is also considerable inter-diffusion of Si atoms into the Ni-Ti film, therefore, a near equiatomic composition in fraction I is only obtained at a distance from the interface where diffusion is no longer relevant. Fraction II is richer in Ti and proportionally poorer in Ni due to the increase of the Ti power to 20 W. The consequence of the additional increase to 30 W is also clearly perceptible in fraction III but the most interesting is the tendency of the system to achieve the near equiatomic composition during the last deposition step (fraction IV). Most likely, the observed composition variation in fraction IV was mainly the result of stopping the Ti co-sputtering and consequently a Ti_2Ni dissolution.

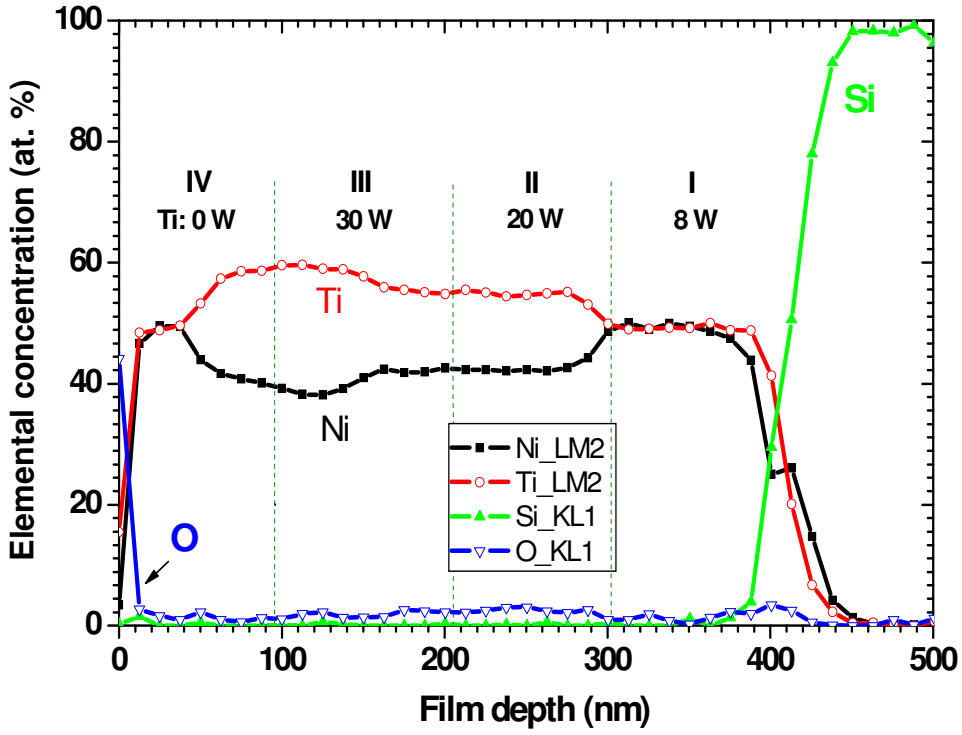

Fig. 3.64: AES elemental concentration profiles for the graded Ni-Ti film deposited on naturally oxidized Si(100).

Figure 3.65 shows a X-TEM micrograph from the Ni-Ti film on the naturally oxidized Si(100) substrate recorded along the Si[110] zone axis, with an enlargement of the topmost region of the film (indicated with the arrow). Apart from the columnar structure, a topmost layer with different contrast (apparently showing also different morphology) is visible. This altered fraction of the film was a result of the last deposition step, i.e. only with the Ni-Ti

target running there was a dissolution of the Ti_2Ni rich precipitates formed in the preceding two steps (see fraction IV of Fig. 3.64).

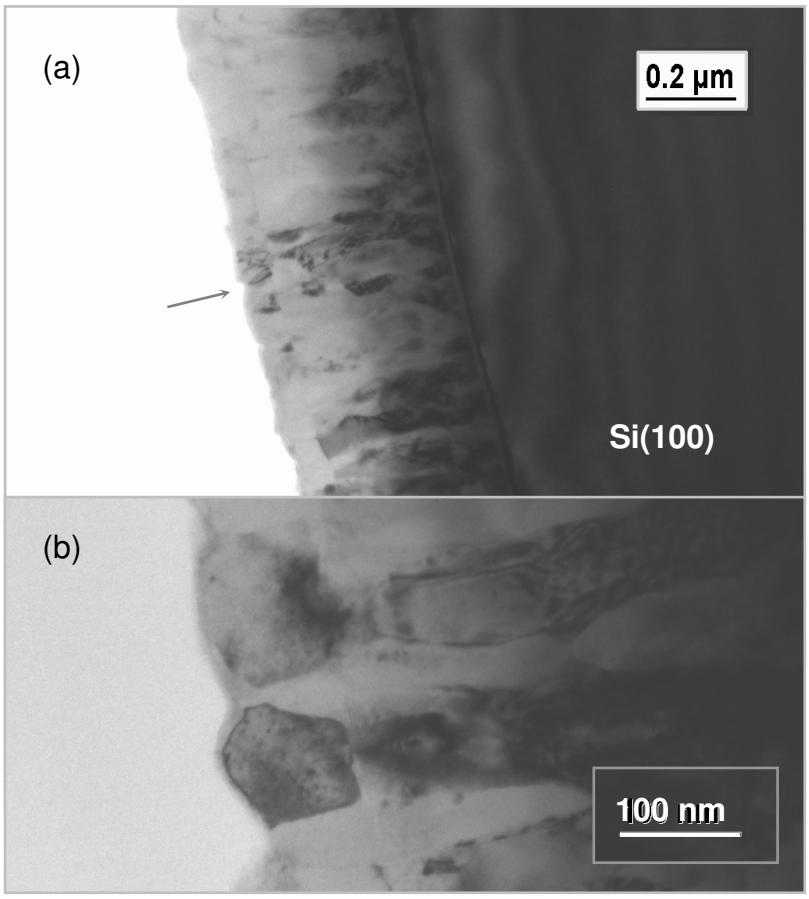

Fig. 3.65: X-TEM micrograph from the Ni-Ti graded film on the naturally oxidized Si substrate recorded along the Si[110] zone axis (a), with an enlargement of the topmost film's region (b).

A SAED pattern obtained on the overall cross-section of the Ni-Ti film is presented in the inset of Fig. 3.66. By choosing the spot delimited in the SAED pattern, which is associated with $Ti_2Ni(220)$, the respective precipitates showed up as bright regions in the corresponding X-TEM dark field image of Fig. 3.66. They were generally detected in the central zone being in agreement with the depth profile of Fig. 3.64. The Ti content exceeds largely the one of Ni in this zone (fractions II and III).

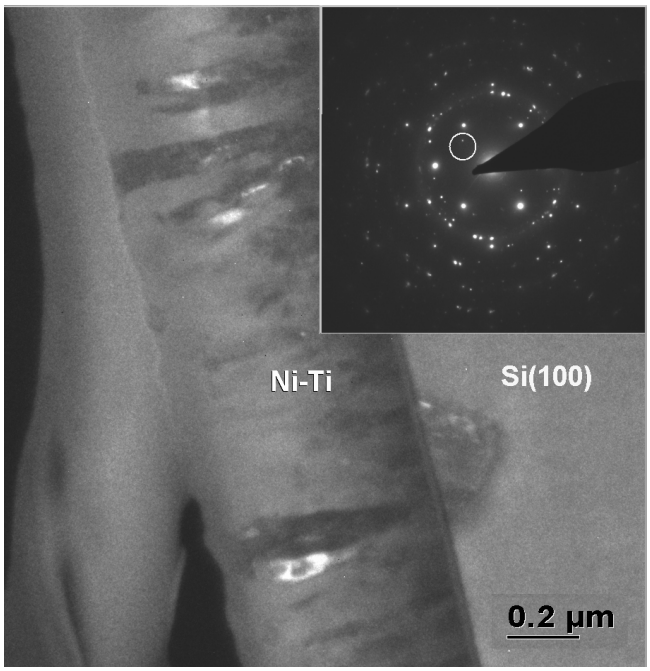

Fig. 3.66: SAED pattern obtained on the overall cross-section of the Ni-Ti graded film, with a delimitation of the spot associated with $Ti_2Ni(220)$, and the X-TEM dark field image resulting from the selection of this spot. The respective Ti_2Ni precipitates show up as bright regions in the X-TEM micrograph.

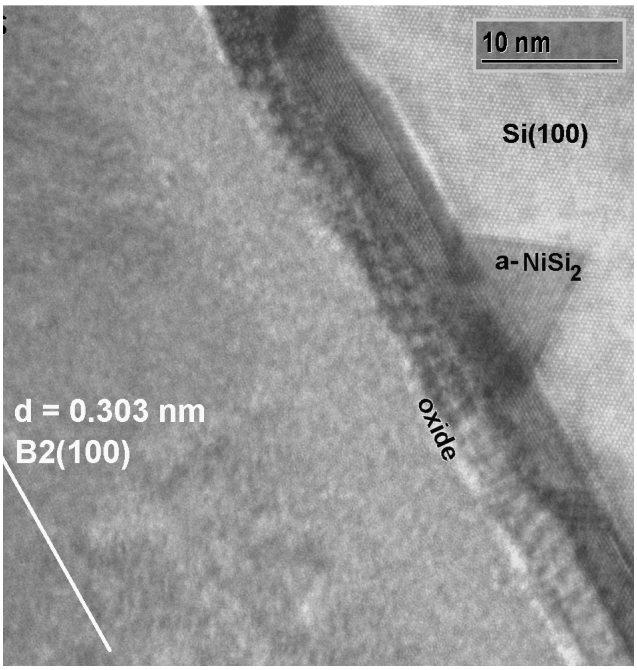

Fig. 3.67: X-TEM micrograph showing the structure of the graded film near the interface film/substrate. The B2(100) planes parallel to the interface were identified as well as the presence of distinct phases at the interface.

The X-TEM micrograph of Fig. 3.67 shows the structure of the film nearby the interface film/substrate. The B2(100) planes parallel to the interface were identified by cross-section HR-TEM (FFT procedure). By *in-situ* XRD (Fig. 3.63) it was observed that the B2 phase started by stacking onto (h00) planes, which is in conformity with X-TEM observations (Fig. 3.67). It also suggests that the Ni-Ti film near the interface (fraction I in Fig. 3.64) is austenitic at RT. Figure 3.67 also puts in evidence the presence of distinct phases in the reaction product at the interface. Between the Ni-Ti B2 structure [with the (100) planes parallel to the interface] and the oxide layer [most probably a (Si, O)-rich layer, i.e. the native silicon oxide of the Si substrate], a lighter grey layer could be distinguished. However, this phase could not be identified by cross-section HR-TEM, suggesting that no crystalline order is present. The same was observed for other samples with this type of interfacial morphology [near equiatomic Ni-Ti films on naturally oxidized Si(100) substrates (Fig. 3.8)]. On the substrate side, $NiSi_2$ was formed epitaxially towards the Si substrate, which agrees with the finding of Ni deeper inside the substrate in Fig. 3.64. A detailed analysis of the interfacial structure can be found below.

The EDS system of the transmission electron microscope (electron dispersive X-ray spectroscopy technique) was used in order to identify the elements present in the different reaction layers. Figure 3.68 shows the results obtained using the line scan mode along a distance of 430 nm, probing information from the substrate, interface and Ni-Ti film. With this complementary information provided by the EDS measurement it was possible to conclude that the lighter grey layer located between the Ni-Ti B2 structure and the Si oxide native layer has in its composition not only Ni and Ti but also Si (see zone C in Fig. 3.68). This confirmed the diffusion of Si into the alloy and has suggested the presence of ternary silicides. An expected increase of the Ni content in the interface substrate's side (zone B) was discernible mainly as a result of the formation of $NiSi_2$ compounds (detected in Fig. 3.67).

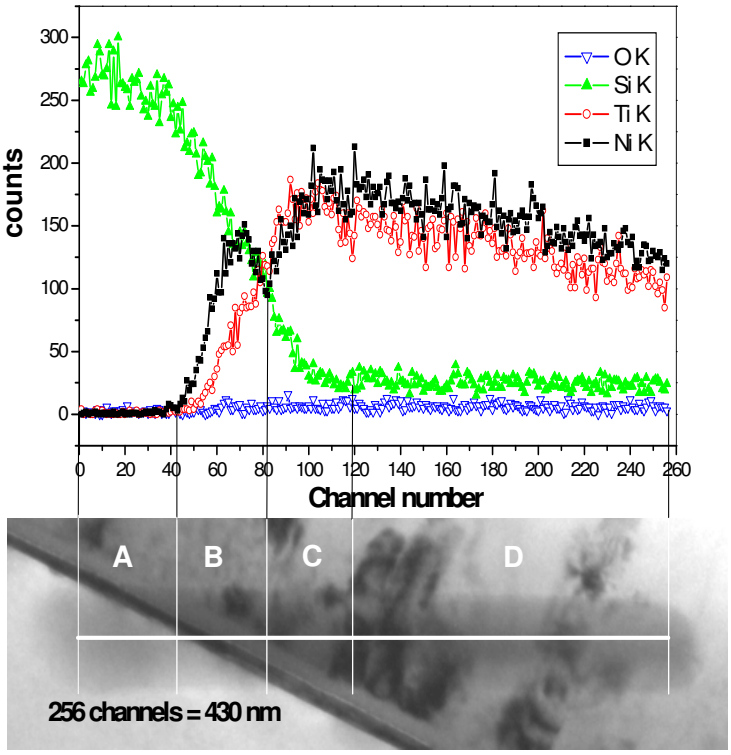

Fig. 3.68: EDS results obtained using the line scan mode of the transmission electron microscope along a distance of 430 nm, probing information from the substrate, interface and the Ni-Ti graded film.

In Fig. 3.69 the interfacial reaction products of the graded film are not all visible because the focus was in the area on the left hand side of the lighter grey layer (film's region). A dashed line was inserted on top of the thin Si oxide layer as a reference. The goal has been the detection of possible Ti_2Ni phase. Stemmer *et al.* [129] mention the formation of a Ti-rich layer with no significant amount of Si that was associated with the Ti_2Ni compound. This layer adjacent to the Ni-Ti near equiatomic film could be the result of the migration of the Ni

atoms, which are the main species diffusing to the Si substrate below 600ºC [130]. In the present study, in some areas along the interface, lattice spacings agreeing well with those of Ti_2Ni were observed between the Ni-Ti film and the lighter grey layer (ternary compound: Ti, Ni, Si). The (111) planes of Ti_2Ni could be identified by cross-section HR-TEM. They make an angle of ≈ 54.74° with the interface (Fig. 3.69). This observation suggests that the (400) planes are approximately parallel to the interface. A white line on the figure indicates the expected arrangement of the (400) planes.

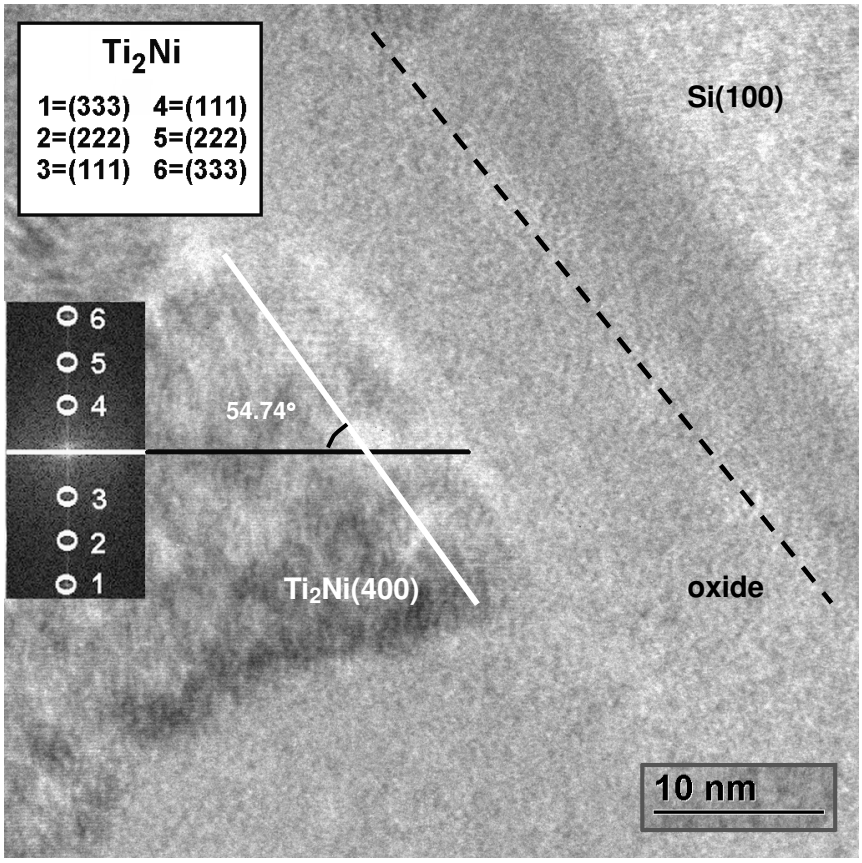

Fig. 3.69: X-TEM micrograph of the interfacial zone of the Ni-Ti graded film with a black line inserted on top of the thin Si oxide layer as a reference. Lattice spacings agreeing well with those of Ti_2Ni were observed suggesting that the (111) planes of Ti_2Ni make with the interface an angle that leads the (400) planes approximately parallel to the interface.

As it was mentioned earlier, there are two possible $NiSi_2$ families (A-precipitates and B-precipitates). In this sample, the formation of B-$NiSi_2$ precipitates in the Si substrate was also detected (Fig. 3.70).

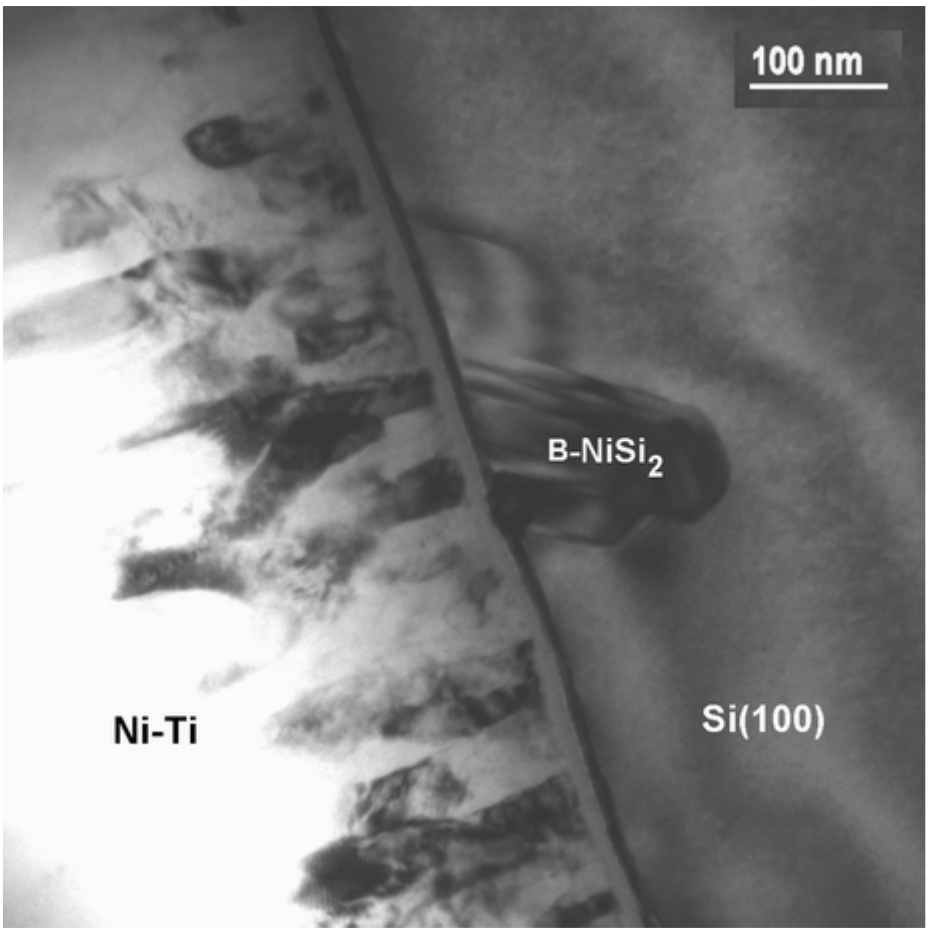

Fig. 3.70: X-TEM micrograph (Ni-Ti graded film) focusing the presence of the B-$NiSi_2$ in the Si(100) substrate.

The ER *versus* temperature response of the Ni-Ti graded film during thermal cycling is shown in Fig. 3.71. The resistivity value decreased linearly with the temperature during cooling from 110°C down to R_s and then started the B2 $\Rightarrow$ R-phase transformation. The transformation to R-phase is finished once the temperature decreased to R_f and an additional cooling promoted the R-phase distortion (R⇑). At M_s the R-phase started transforming to B19'.

On heating, the B19' $\Rightarrow$ R-phase led to a rapid increase in the ER and it is suggested that the film completely transforms to R-phase before transforming to B2. Two processes overlap upon heating: (i) B19' $\Rightarrow$ R-phase and (ii) decreasing distortion. The R−phase $\Rightarrow$ B2 led to de-twinning and rapid decrease in the ER.

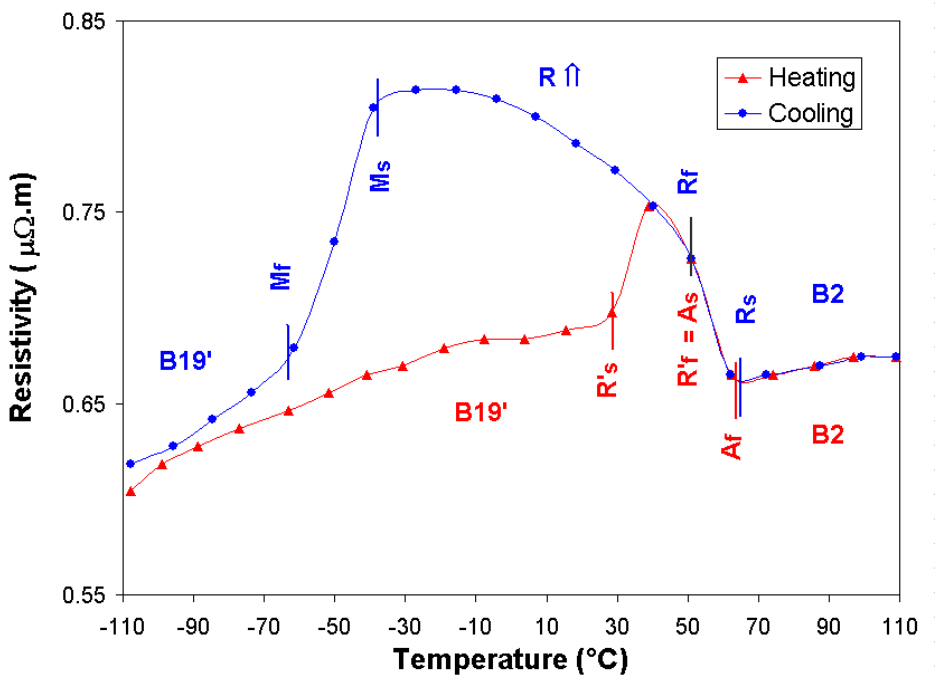

Fig. 3.71: Dependence of the ER in the Ni-Ti graded film with temperature during cooling and heating.

The ER measurements do not suggest the presence of the B2 phase at RT. Nevertheless, B2(100) planes parallel to the substrate surface were identified close to the interface film/substrate by cross-section HR-TEM (see Fig. 3.67).

3.5.2. Deposition on TiN/SiO_2/Si(100) substrates

Previously, the *in-situ* study of the sputter deposition of Ni-Ti film on naturally oxidized Si(100) substrate was reported, whereby the possibilities of the real-time structural design during deposition were stressed. The effect of a TiN layer deposited on top of thermally oxidized Si(100) substrates prior to the deposition of the near equiatomic Ni-Ti has also been analysed (section 3.3). These experiments have shown that TiN acts not only as a diffusion barrier but also induces different crystallographic orientations. The *in-situ* XRD results have shown a preferential growth of <110> oriented grains of the Ni-Ti B2 phase from the beginning of the deposition, with a constant growth rate during the whole deposition, for a Ni-Ti film deposited on TiN with a topmost layer formed mainly by <111> oriented grains. Here, the effect of the controlled change of the Ti:Ni ratio during the deposition of Ni-Ti films on a TiN buffer layer (topmost layer formed mainly by <111> oriented grains) was tested.

The substrate mounted on the resistive heater was a 15×15 mm^2 Si(100) wafer with a 140 nm thick amorphous SiO_2 capping layer on top. For the deposition of the TiN buffer layer

the Ti target was run at a constant power of 80 W (during 40 min) resulting in a final thickness of ≈ 215 nm. The Ni-Ti and Ti magnetrons were then driven during 60 min at a power of 40 and 20 W, and additionally 69 min at a power of 40 and 25 W, respectively (total thickness ≈ 710 nm). A V_b of −45 V was applied to the substrate during the Ni-Ti deposition. In these series of experiments, the near equiatomic composition could be obtained with the Ti target running at 20 W.

X-ray diffractograms obtained *in situ* during the deposition of the TiN buffer layer are shown in Fig. 3.72. During the initial stages of growth <100> and <111> oriented grains nucleated and grew. The results also show that <111> grains took over at larger thickness. No changes were detected during the annealing period of 27 min.

Figure 3.73 shows the variation of the net areas of the B2(110), B2(200), B2(211) and Ti_2Ni(333/511) peaks, obtained from the *in-situ* XRD data, for the Ni-Ti deposition on top of the TiN buffer layer *versus* time. A preferential growth of <110> oriented grains of the Ni-Ti B2 phase from the beginning of the deposition, with a constant growth rate during the whole deposition was observed. The precipitation of the Ti_2Ni phase was detected in the second step of the deposition (Ti power = 25 W) by the presence of the Ti_2Ni(333/511) diffraction peak (with low intensity), which did not affect the preferential growth of <110> oriented grains of the Ni-Ti B2 phase. However, a slight increase of the a_0 values of B2 phase as calculated from $d_{(110)}$ and $d_{(211)}$ was observed during this second deposition period (Fig. 3.74). They were calculated as a function of time and according to the deposition rate, are represented as a function of thickness.

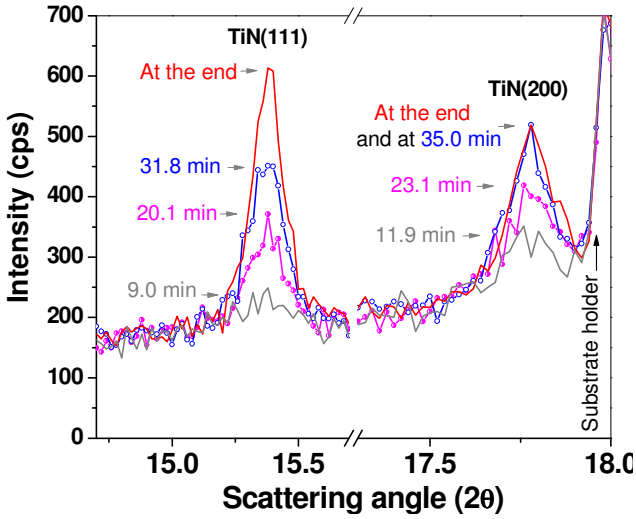

Fig. 3.72: X-ray diffractograms obtained *in situ* during the deposition (V_b = −30V) of the TiN buffer layer (deposition time = 40 min).

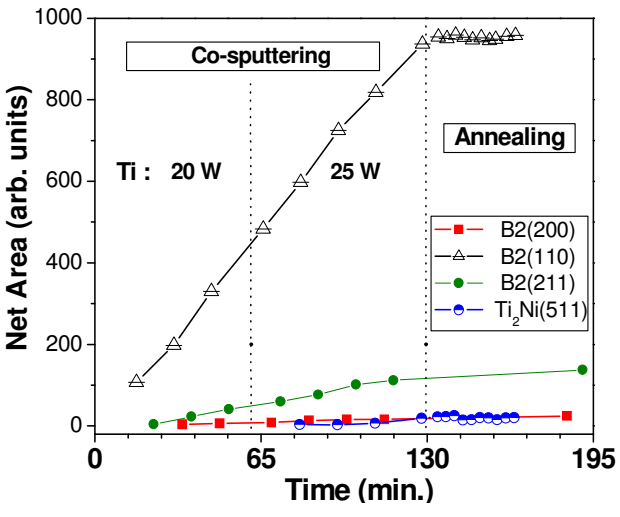

Fig. 3.73: Net areas of the B2(110), B2(200), B2(211) and Ti_2Ni(333/511) diffraction peaks recorded during the processing of the Ni-Ti graded film (V_b = −45V).

At the initial deposition stage (Ti power = 20 W), considering the evolution of the a_0 values of B2 phase, a stress relaxation took place suggesting that the film exhibited compressive stresses, which were relaxed with increasing thickness. Nevertheless, with the increase of the Ti content (Ti power = 25 W) and, thus, Ti_2Ni precipitation, the a_0 values started rising again. The depth profile of the atomic concentrations obtained *ex situ*, shown also in Fig. 3.74, confirmed a near equiatomic composition for the first part of the deposition, and a Ti-rich composition, result of the increase of the power applied to the magnetron with the Ti target.

XRD patterns obtained at ≈ 470°C, after the deposition process (during the annealing period), and at RT, are presented in Fig. 3.75. In the austenitic state, the Ni-Ti film is highly oriented with the (110) planes of the B2 phase parallel to the substrate surface. At RT, the diffraction peaks from the B19' phase were detected, which means that for this type of Ni-Ti films the transformation to B2 phase occurs above RT.

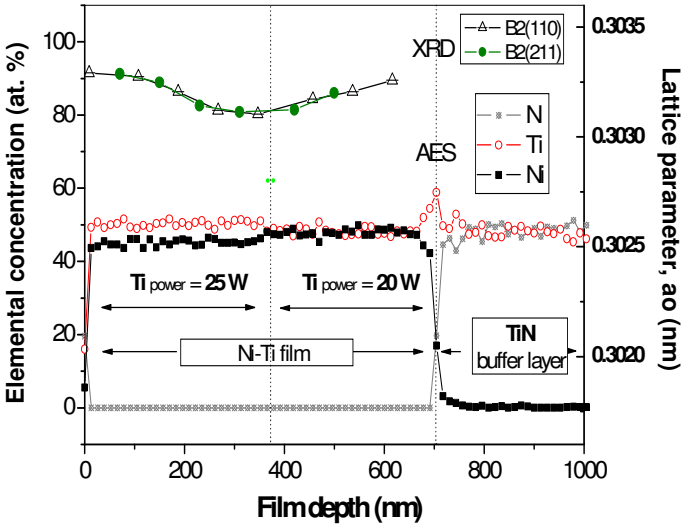

Fig. 3.74: Variation of the a_0 values (as calculated from *d* according to the corresponding XRD peak positions) during deposition, combined with the depth profile of the atomic concentrations in the Ni-Ti film (obtained *ex situ*).

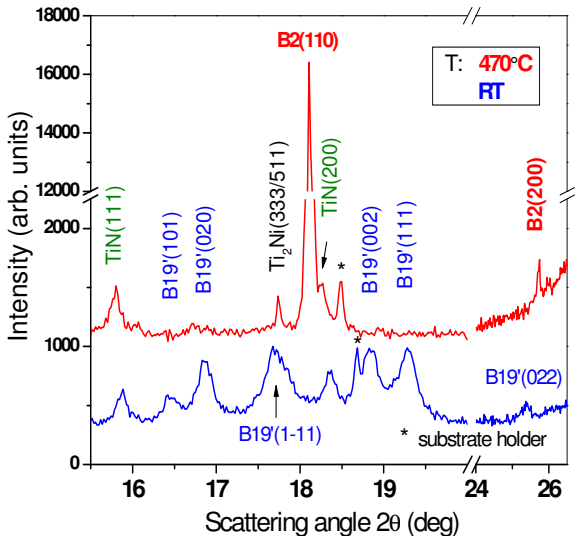

Fig. 3.75: XRD spectra obtained at 470°C after the deposition process (top), and at RT (bottom).

The temperature dependence results of the ER of the sample are shown in Fig. 3.76 for cooling and heating. On cooling, there was a resistivity increase associated with the B2 ⇒ R-phase transformation, followed by a resistivity decrease due to the R-phase ⇒ B19' transformation. During heating, a similar increase of the ER was not detected. The resistivity results have also shown that a big fraction of the Ni-Ti film was already transformed to B19'at RT, which corroborates the XRD results from Fig. 3.75.

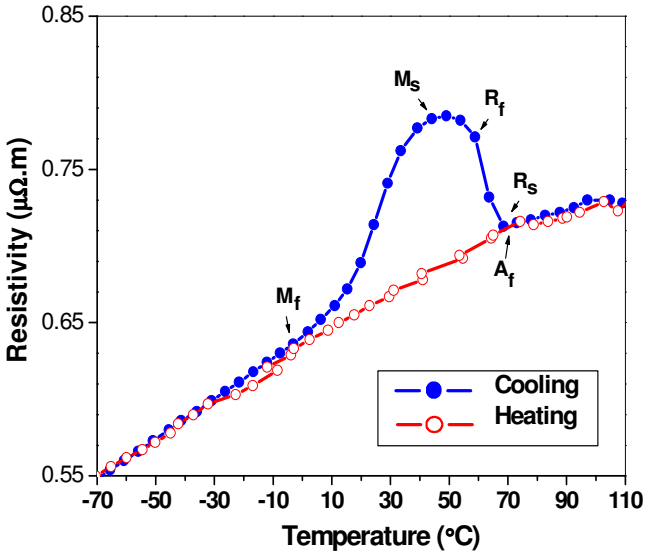

Fig. 3.76: Dependence of ER with temperature during cooling and heating.

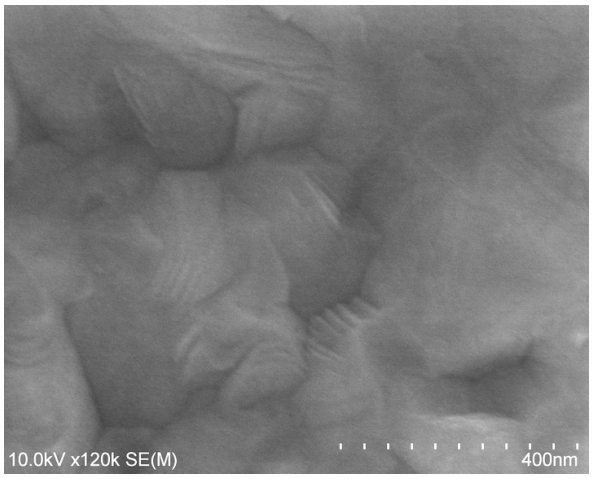

Fig. 3.77: SEM micrograph of the surface of the Ni-Ti film grown on the TiN buffer layer.

A typical SEM micrograph of the Ni-Ti film surface grown on the TiN buffer layer is shown in Fig. 3.77. These micrographs show surface steps presumably due to twinning associated with the martensitic structure present at RT. A fine-grained structure is also perceptible, which is in agreement with results obtained by Liu *et al.* [109] for a Ti-rich Ni-Ti film deposited at ≈ 500°C on a Si(100) substrate.

In this section it was shown that the equipment used in this work allowed the *in-situ* study of the structural evolution of the growing Ni-Ti films as a consequence of changing the Ti:Ni ratio. With these experiments the knowledge of the structural development is improved (phase formation or strain evolution) during Ni-Ti film growth by magnetron co-sputtering (Ni-Ti + Ti) and its correlation with the deposition parameters.

When comparing the experiments concerning the deposition of the near equiatomic films, presented in the previous sections, and the growth of the near equiatomic fraction, on the initial deposition period on the study of graded Ni-Ti films, the behaviour observed for texture development is reproducible, i.e.:

- grains exhibiting the B2 phase with (h00) planes parallel to the film surface dominate at the initial growth stage for the deposition of Ni-Ti films at ≈ 470°C on naturally oxidized Si(100) substrates (depositions performed without applying V_b);

- the results obtained during the deposition of the Ni-Ti films on TiN with a topmost layer formed mainly by <111> oriented grains have shown a preferential growth of <110> oriented grains of the B2 phase since the beginning of the deposition, with a constant growth rate (for depositions without and with a V_b of −45 V).

3.6. DEPOSITION OF HIGH-TEMPERATURE NiTiHf SMA FILMS

A preliminary study was performed concerning the introduction of Hf on the Ni-Ti system in order to analyse the influence of Ti replacement by Hf. First, *ex-situ* depositions were carried out to test the effect of different powers applied to the magnetrons on the film composition, which was obtained by RBS. Later, *in-situ* experiments were conducted focusing on the specific parameters selected on the basis of the RBS results.

3.6.1. Study of the power applied to the magnetrons on the film composition

The RBS data obtained for the NiTiHf samples deposited *ex situ* are shown in Fig. 3.78. Two different powers were applied to the magnetron with the Ni-Ti target and, for each of them, 3 different powers were tested for the Hf magnetron. Thus, a total of 6 samples were produced. The temperature during deposition of the NiTiHf films (on graphite substrates) was ≈ 70°C (no further annealing).

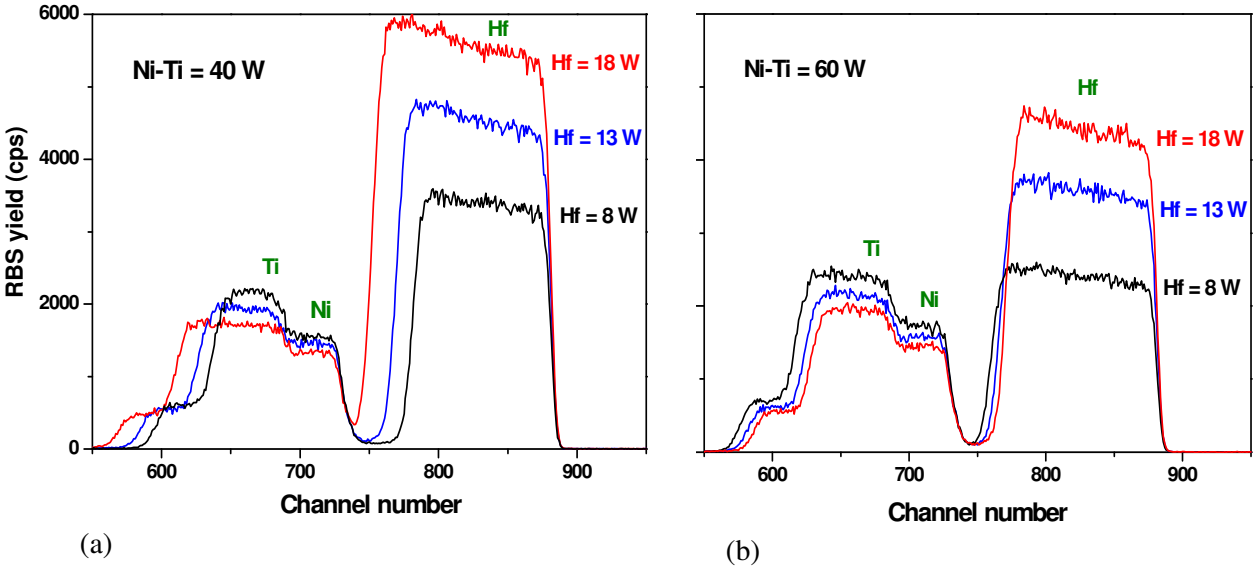

Fig. 3.78: RBS spectra of the NiTiHf films deposited *ex situ* on graphite substrates; (a) power applied to the Ni-Ti magnetron: 40 W, (b) power applied to the Ni-Ti magnetron: 60 W.

The Hf content in the films increased with increasing power on the Hf magnetron. For a higher power applied to the Ni-Ti target the overall Hf concentration decreased, and the Ni and Ti amounts increased. An overview of the composition results is given in Fig. 3.79.

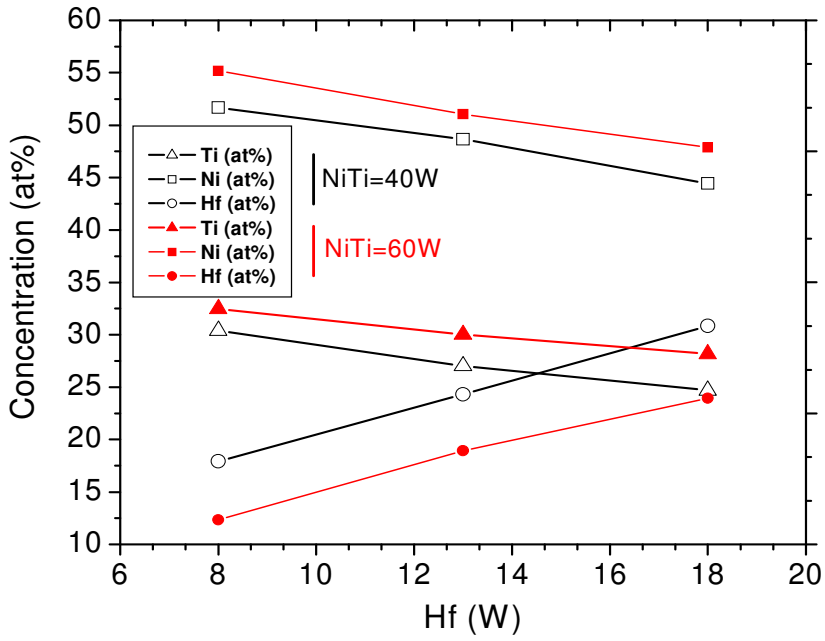

Fig. 3.79: Overview of the composition results obtained for the NiTiHf films deposited *ex situ* after the simulation of the data from Fig. 3.78 with the RUMP code.

3.6.2. *In-situ* XRD results

The *in-situ* experiments at ROBL were carried out according to parameters selected on the basis of the RBS results. The NiTiHf films were deposited on a HfN(111) layer previously deposited on top of a SiO_2/Si(100) substrate. The magnetron with the Hf target was running at 80 W and a V_b of −30 V was applied during the growth of the HfN buffer layer. Further information concerning the processing conditions of the samples, which their characterization is presented here, can be found in Tab. 3.5.

Power Ni-Ti (W)	Power Hf (W)	Deposition rate (nm/s)
60	18	0.185
60	13	0.180
40	8	0.120

The films were deposited with a V_b of –45 V at a temperature of ≈470 °C (deposition time ≈120 min).

Tab. 3.5: Process conditions of NiTiHf films produced in the sputtering chamber of the beamline ROBL at ESRF during *in-situ* tests.

X-ray diffractograms obtained *in situ* during the deposition of a NiTiHf film (Ni-Ti = 60W and Hf = 13W) are shown in Fig. 3.80. The results show a preferential growth of grains with <110> of the B2 phase from the beginning of the deposition.

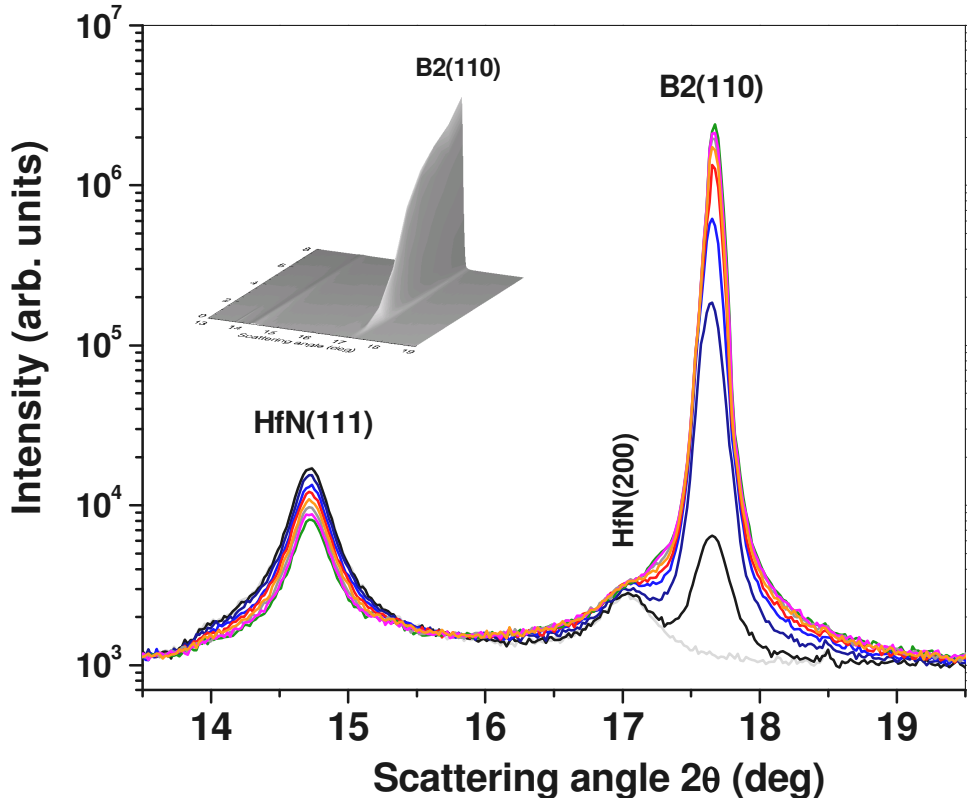

Fig. 3.80: X-ray diffractograms obtained *in situ* during the deposition of a NiTiHf film at ≈ 470°C (Ni-Ti = 60W and Hf = 13W) with $V_b = -45$ V.

In Fig. 3.81 are shown XRD results of NiTiHf samples deposited at ROBL, obtained *in situ* after deposition, during the annealing period at ≈ 470°C and RT, respectively. For a higher power applied to the Hf magnetron (18 W) it has been detected two extra diffraction peaks at 2θ ≈ 16.10° and 2θ ≈ 17.20° (angular positions at ≈ 470°C). The detection of these peaks suggest the presence of precipitates, most likely $(Ti,Hf)_3Ni_4$.

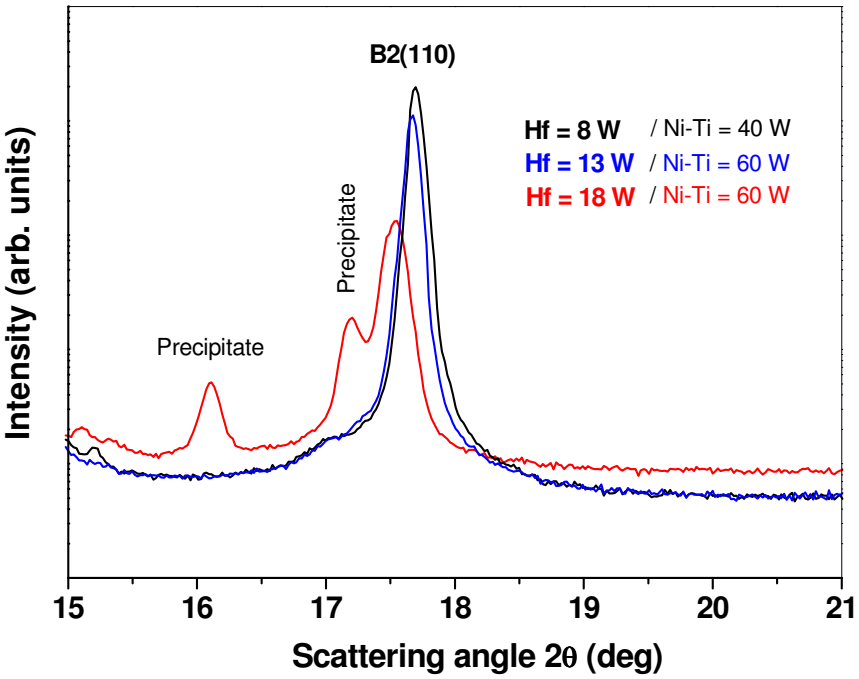

(a)

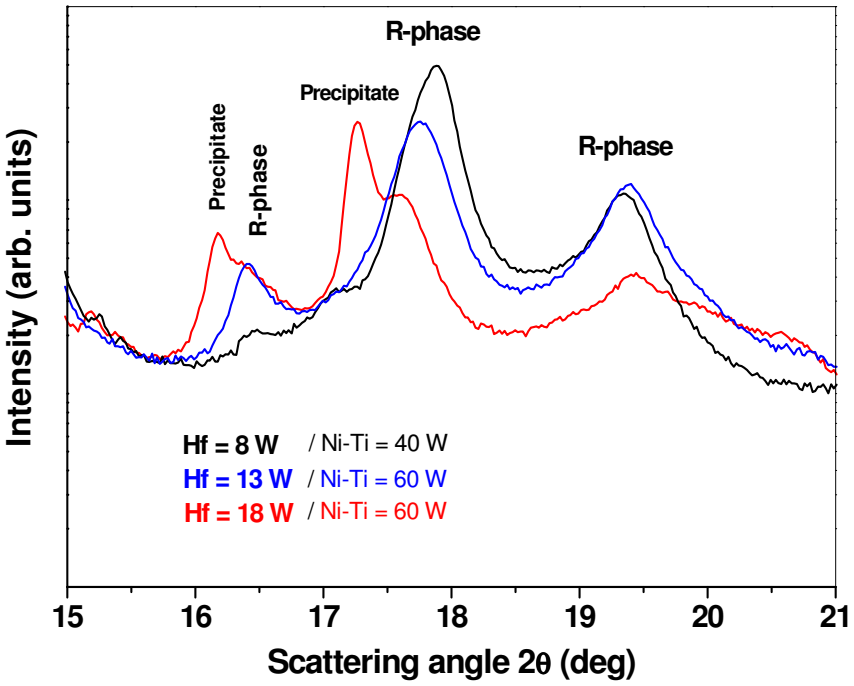

(b)

Fig. 3.81: XRD spectra of the NiTiHf samples deposited at ROBL (V_b = −45 V); (a) obtained *in-situ* after deposition, during the annealing period at ≈ 470°C, (b) at RT.

The XRD evaluation of phase transformation during cooling for the NiTiHf film from Fig. 3.80 is given in Fig. 3.82. The higher transformation temperatures of the NiTiHf SMA, when compared to what was previously observed for Ni-Ti films, have been confirmed by XRD.

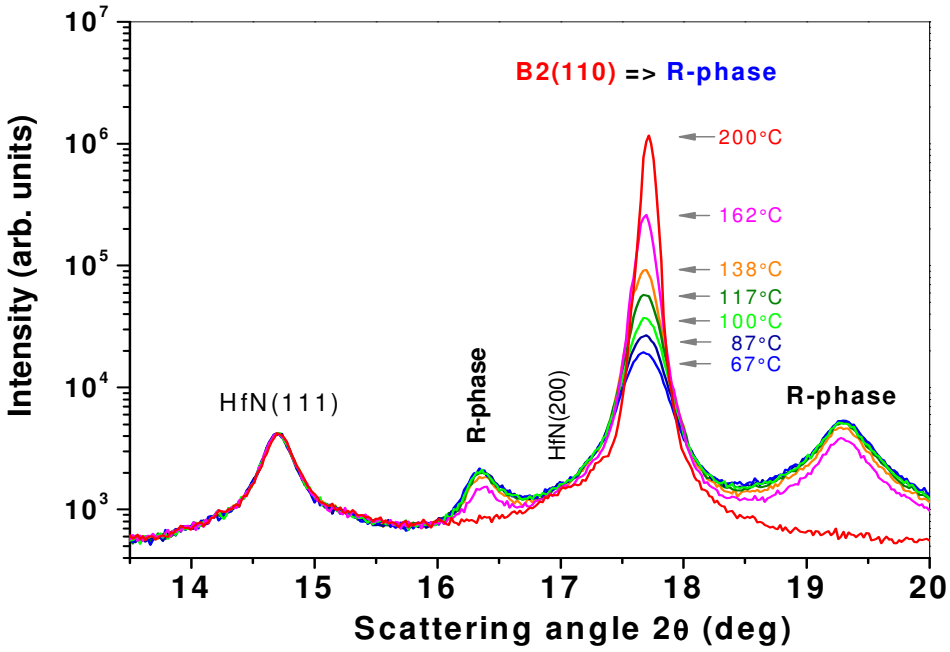

Fig. 3.82: XRD evaluation of phase transformation during cooling for the NiTiHf film from Fig. 3.80.

These results have confirmed the advantage of the dual magnetron-sputtering-chamber installed at ROBL for future fabrication and characterization of ternary SMAs.

Chapter 4

Discussion

4. DISCUSSION

The use of the magnetron-sputtering-chamber installed at the six-circle diffractometer of ROBL has allowed to follow *in-situ* by XRD the structural evolution of the films during growth. Together with the results obtained from the complementary *ex-situ* characterization techniques, this has led to the optimisation of the deposition conditions of Ni-Ti films for possible use in microdevices. After an initial period dedicated to the optimisation of the deposition parameters controlling the composition of the films, fully crystallized material was produced (the crystallization process is taking place during the film growth). In this study, major parameters involved are the use of different type of substrates and the effect of applied bias voltage (V_b) to the substrate during film deposition. The configuration of the unbalanced magnetrons permits the plasma to extend to the region of the substrate and, thus, a greater number of ions are directed towards the growing film. When a negative V_b is applied, it causes a higher energetic ion bombardment of the growing film, resulting in enhanced surface-atom mobility. Therefore, it has been concluded that the control of the ion bombardment energy would be one of the key factors in determining the microstructure and properties of the Ni-Ti films. During this work, a new sputtering chamber was successfully commissioned at ROBL. The *in-situ* XRD results were reproducible with both the chambers and the main advantage of the new chamber came from the enlarged windows (Be foils) allowing the study of a higher number of Bragg peaks of the phases present in the sample.

In this chapter, the experimental results are discussed. The combination of results from different experiments yields valuable explanations for the observed behaviour. The results are interpreted in a way that is beneficial for the development of shape memory Ni-Ti films with distinct crystallographic orientations and transformation characteristics. Therefore, the effects on the preferential orientation of the SMA films resulting from the use of different types of substrates and in some cases, the combination with V_b are the first topic of discussion. The second section of this chapter deals with the interface structure resulting from depositions on different substrates, as well as the link between the distinct crystallographic orientations of the Ni-Ti films together with the interface morphology on their phase transformation characteristics.

4.1. PREFERENTIAL ORIENTATION

The texture evolution during the deposition of Ni-Ti film is clearly affected by the substrate type and the ion bombardment (using V_b).

4.1.1. Effect of a SiO_2 buffer layer

For Ni-Ti depositions (without V_b) on naturally oxidized Si(100) substrates, grains exhibiting the B2 phase with (h00) planes parallel to the film surface, dominate at the initial growth stage, while the (110) orientation takes over at a later stage of the growth. A key role is attributed to the amorphous Si oxide layer on this initial preferential stacking as demonstrated by the use of thermally oxidized Si(100) substrates.

Kim *et al.* [108] proposed that a strong interfacial adsorption on the heated substrate promotes the preferential coverage by a first layer of Ti on top of thermally oxidized Si substrates. This leads to the preferential formation of the (h00) oriented Ni-Ti film since, in the B2 cubic structure, the (h00) planes are alternately occupied by Ti and Ni atoms. Gisser *et al.* [96] reported that Ni-Ti films crystallized during the deposition process on Si(100) are highly oriented, with the B2(110) parallel to the (100) of the Si wafer. Peak intensity ratios for the B2 phase diffraction peaks, (110), (200) and (211) are 50000:1:<0.01 in their study. The B2(200) diffraction peak was too small to be seen without rescaling the data. In contrast, in the present work, for near equiatomic films deposited on naturally Si(100) substrates, the B2(200) diffraction peak, which appears at the beginning of the deposition, could be detected without rescaling the data as can be observed in Fig. 3.1. Although it should be taken into consideration that the films produced by Gisser *et al.* [96] exhibit thickness values between 2 and 10 μm (thicker than the films obtained in this work, < 1 μm), the reason for this difference is most likely the fact that they have used Si wafers etched with aqueous HF and rinsed with methanol and, here, the native Si oxide layer (2-3 nm) was not removed before Ni-Ti deposition. Liu *et al.* [109] also observed a strong <110> fibre texture, with good axis symmetry, for a film deposited at ≈ 500°C. In this case, they have used a Si(100) wafer as substrate, which was cleaned by "inverse" sputtering.

In the present work, again, the deposition on thermally oxidized substrate has been done with $V_b = -45$ V, to show the effect of the oxide layer on the development of B2 phase with (100) orientation during deposition on heated substrates (≈ 470ºC). As it can be observed

in Fig. 3.13, by applying V_b to the thermally oxidized substrate, the influence of the SiO_2 layer on the development of a strong <100> fibre texture is considerably reduced due to the more energetic ion bombardment on the growing film when compared with the results of deposition without V_b shown in Fig. 3.12. Further, it is observed that for depositions performed without applying V_b, if the oxide layer is not thick enough (i.e. on naturally oxidized Si substrates), the tendency for the formation of a preferential stacking on the packed crystallographic plane leads to a <110> fibre texture.

4.1.2. Deposition on MgO single crystal

In order to gain better understanding of the growth mechanism of Ni-Ti films, real-time *in-situ* X-ray scattering measurements were conducted during Ni-Ti deposition on MgO(100). The time-dependent XRR results obtained during the deposition of Ni-Ti directly onto the MgO(100) substrate (Fig. 3.43) have revealed intensity oscillations attributing to heteroepitaxial layer-by-layer growth, with increased surface roughening. The *in-situ* XRD measurements have shown a preferential stacking of (100) planes of the B2 phase parallel to the film surface (Fig. 3.44). The preferential orientation of B2(100)//MgO(100) was very strong and was kept as such until the end of the deposition, which lasted for 129 min (≈ 900 nm).

As in the case of deposition on thermally oxidized Si(100) substrates, Kim *et al.* [108] proposed that a stronger interfacial adsorption on the heated substrate promotes the preferential coverage by a first layer of Ti on top of the MgO(100) substrates. This leads to the preferential formation of the (h00) oriented Ni-Ti film as, in the B2 cubic structure, the (h00) planes are alternately occupied by Ti and Ni atoms. The crystal structure of MgO is NaCl type with the lattice parameter of 0.421 nm. If one considers that the interatomic distance of oxygen is 0.297 nm for the MgO(100) plane, and the interatomic distance of titanium is 0.301 nm for the Ni-Ti B2(100) plane, the misfit between their interatomic distances is only roughly 1.3 %. This is in agreement with the behaviour observed by low angle specular reflectivity time resolved for the growth mode of the first few monolayers, which shows a good matching of Ni-Ti structure with MgO(100) substrate. The pole figures also show that the stacking of the Ni-Ti B2 phase on the MgO(100) substrate occurs with B2[100]//MgO[110] (Fig. 3.50), suggesting that the Ti-O adsorption sites between the Ni-Ti and oxide substrate are essential to improve the (100) orientation of the B2 phase (see Fig. 3.51).

The experiment carried out using a TiN buffer layer [≈ 15 nm thick, with a (100) texture induced by the (100) orientation of the MgO single crystal substrate] has shown that the TiN layer acts as a diffusion barrier. In contrast to the Ni-Ti film deposited directly onto MgO(100), no diffractions peaks from interfacial reaction products were detected (Fig. 3.47). A single orientation of Ni-Ti B2 (thickness ≈900 nm) with (100) stacking parallel to the substrate could again be produced. A highly ordered epitaxial growth was obtained with the crystallographic relationship of Ni-Ti(100)// TiN(100) // MgO(100).

Based on previous experience of the deposition of TiN films the choice to use a TiN buffer layer with thickness ≈ 15 nm has been taken [60]. It could be expected that the epitaxial growth of the Ni-Ti film would be more readily promoted on an even thinner TiN film. However, on a 3 nm TiN film, for example, the TiN buffer layer may have a granular uneven surface giving a suppressive effect on the Ni-Ti epitaxial growth. A film with thickness of the order of a few nm should have a rough or granular surface with different crystal facets because it is considered to still stand near the coalescence growth stage from the island to continuous structure. The surface roughening of a very thin TiN film may be enhanced by residual species on the MgO(100) substrate surface. In order to minimize this problem, in the present work, the MgO substrates have been reconstructed and thermally degassed by heating to 690°C for 60 min before the deposition of the TiN layer.

Low angle time resolved specular reflectivity at a fixed incidence angle has been as well very useful to determine the growth mode of the TiN buffer layer (3 min deposition) and the Ni-Ti film (first 9 min 30 s of deposition), revealing a layer-by-layer growth mode (Fig. 3.46). The decrease in oscillation amplitude with time indicates that the surface becomes rougher during sputtering. Nevertheless, the intensity oscillations during Ni-Ti film growth are observed for a longer time when comparing the deposition with a TiN buffer layer and the deposition of Ni-Ti directly onto MgO(100). It is suggested that the interfacial reactions taking place during the Ni-Ti film deposition directly onto MgO(100) have an important role on the faster decrease of the intensity of the oscillations.

4.1.3. Effect of a TiN buffer layer

Although the use of MgO single crystal as the substrate leads to an interesting control of the B2 phase crystallographic orientations, it is not the desired solution in some of the practical applications. Since the deposition of Ni-Ti on TiN(100)/MgO(100) substrate has

shown that the (100) orientation of TiN induces the (100) orientation of the B2 phase, additional experiments were carried out seeking the optimal parameters for the deposition of a TiN film, with a topmost layer formed mainly by <100> oriented grains, on thermally oxidized Si(100). This goal was achieved by reducing the deposition rate, by increasing the N_2 partial pressure, leading to a more dense TiN film with a strong (100) preferential orientation. The results are interpreted by a competitive growth process in which the (100) orientation of TiN is promoted by atomic nitrogen that is delivered mainly by molecular nitrogen ions from the plasma. A complementary experiment using a positive V_b (+10 V) has shown a (111) preferred orientation [60]. It is known the possibility to change the preferred orientation of the TiN films using sufficiently high substrate temperatures (approaching thermodynamic equilibrium). The same should happen when using low energy ion-irradiation during magnetron sputtering (increasing adatom mobility).

In the present work, further experiments were performed in order to obtain TiN films [deposited on thermally oxidized Si(100) substrates] with their topmost layer exhibiting other distinct crystallographic orientations. The aim was to test their effect on the development of the texture of B2 phase of the Ni-Ti films (by *in-situ* XRD), deposited on top (in the same chamber without breaking the vacuum).

TiN films grown by vapour phase deposition techniques usually have a preferred growth orientation that varies according to the growth conditions. They exhibit competitive growth of <100> and <111> polycrystalline grains. In the present work, apart from the TiN film deposited on thermally oxidized Si(100), with the optimised parameters to obtain a topmost layer dominated mainly by <100> oriented grains, all the other TiN films were deposited with the same deposition parameters. TiN(111) and TiN(200) Bragg peaks were observed for thickness values of ≈ 80 nm and ≈ 215 nm but, only for the latter, it was possible to conclude that <111> grains dominate. The *in-situ* X-ray diffractograms obtained during the annealing period did not show additional structural changes [Fig. 3.29(a)].

The *in-situ* XRD results obtained during the deposition of the Ni-Ti films on TiN with a topmost layer (of thickness ≈ 215 nm) formed mainly by <111> oriented grains have shown a preferential growth of <110> oriented grains of the B2 phase from the beginning of the deposition, with a constant growth rate during the whole deposition. It is generally assumed that for most bcc metals the lowest surface energies correspond to the (110) surface, as predicted from calculations [68]. Due to surface energy minimization, (110) texture is favoured in bcc films. This is most likely the reason for the preferential growth of <110>

oriented grains of the Ni-Ti B2 phase. This experiment has also shown that the B2(200) diffraction peak did not assume an important relevance as in the case of the Ni-Ti deposition on naturally oxidized Si(100) substrates. For depositions on TiN buffer layers (topmost layer formed mainly by <111> oriented grains), there is no Ni-Ti/SiO_2 interface and, thus, the development of the (100) orientation parallel to the substrate surface is not observed. Therefore, a preferential growth of <110> oriented grains of the B2 phase is observed since the beginning of Ni-Ti film deposition.

The Ni-Ti films deposited on top of TiN buffer layers, with thickness values ≈ 15 nm and ≈ 80 nm, where a dominating orientation could not be identified (i.e., primarily <100> and <111> oriented grains nucleate and grow) exhibit a different behaviour. In this case, <110> oriented grains of the Ni-Ti B2 phase dominate at the beginning of the deposition, while <211> oriented grains take over at a later stage of the deposition. In the case of these two samples, their TiN buffer layer has a considerable role in the appearance of the <211> oriented grains of the Ni-Ti B2 phase. There is an initial competitive growth between the <211> and <110> crystal orientations – competition between an orientation promoted by the TiN layer (due to its surface morphology) and, the (110) orientation, which is the more densely packed crystallographic plane. Most likely, for the thinner TiN film (≈ 15 nm) on the thermally oxidized substrate, a rough or granular surface with different crystal facets plays an important role on the initial competitive growth between the <211> and <110> crystal orientations of the Ni-Ti B2 phase. The XRD results performed on TiN layers with such thickness did not detect any family of atomic planes of the TiN structure parallel to the TiN surface [see Fig. 3.29(b)].

The effect of V_b applied during the deposition of Ni-Ti films on TiN buffer layers with ≈ 15 nm and ≈ 215 nm, previously deposited on thermally oxidized Si(100) substrates, was as well analysed. The Ni-Ti deposition with a substrate bias of −45 V on a TiN film with ≈ 15 nm has shown more pronounced development of the (110) orientation of the B2 phase when compared with the sample deposited without V_b. The more energetic ion bombardment during the film growth and consequential increase in adatom mobility, which opposes shadowing – due to the V_b – favoured the stacking of (110) planes of the B2 phase parallel to the substrate since the beginning of the deposition.

As described before, the Ni-Ti deposition on a topmost layer of TiN mainly formed by <111> oriented grains (TiN film with thickness ≈ 215 nm) leads to the preferential growth of (110) planes of the Ni-Ti B2 phase parallel to the substrate from the beginning of the

deposition with a constant growth rate during the whole deposition. This trend is also observed for depositions with applied V_b (−45 V and −90 V). However, a slight decrease of the B2(110) peak intensity has been observed for the higher applied V_b (−90 V). SEM observations, performed *ex-situ*, have shown that the microstructure of the Ni-Ti films was influenced by the degree of ion bombardment (Fig. 3.42). The SEM micrographs suggest that the increase in ion energy by using V_b (−45 and −90 V) led to apparently larger crystals in the form of regular polyhedron (visible on the films surface). This observation is consistent with the trend observed *in situ* by XRD, i.e., a decrease in the FWHM value with increasing applied V_b. An overall trend of increasing coherence domain length with increasing V_b is thus observed when Ni-Ti films are deposited on the TiN films with the topmost layers mainly formed by <111> oriented grains. In general, in literature, it is mentioned that an increase in negative V_b leads to a higher energy of the incident ions leading to an increase in the grain size because of the increase in adatom mobility. Nevertheless, it should be taken in consideration that a sufficiently high voltage can lead to increased defect formation. As the ion energy is increased, the film volume affected by the ions becomes larger giving rise to defect generation at increasingly larger distances below the growth surface, thus reducing the probability of the point defects becoming annihilated.

4.1.4. Shadowing effects

It was observed during the deposition on oxidized Si(100) substrates (either naturally or thermally oxidized) at ≈ 470°C that a gradual change of the growing direction of the columnar crystals with increasing thickness favoured the diffraction (in Bragg-Brentano geometry) of the (310) peak of the B2 phase. This effect has been analysed in more detail for the deposition on thermally oxidized substrates without V_b. As shown in Fig. 3.12, for a Ni-Ti film deposited on thermally oxidized Si(100) without applying V_b, after ≈ 70 min deposition (≈ 540 nm film thickness), there is a stabilization of the intensity of the B2(200) peak due to the gradual change of the crystallographic direction of the growing columnar crystals. X-TEM observations are consistent with the results obtained by *in-situ* XRD (see Fig. 3.19, Fig. 3.21, Fig. 3.22 and Fig. 3.23). The grains near the substrate are aligned to the normal direction and those near the top surface, grown later, are tilted towards the direction of the incident flux (preferentially towards the magnetron with the Ni-Ti target running at 40 W). As mentioned before, this orientation favoured the diffraction peak of (310) of the B2 phase. This gradual change of the preferential crystallographic direction along which the columnar crystals

growth, after an initial stacking of the B2 phase onto (h00) planes, is attributed to the combined effects of low surface mobility and shadowing (regions with a relatively greater initial height or growth rate can obstruct the flow of incident flux to other areas – due to tilting of the magnetrons). It is suggested that as the film thickness increases and the grains grow, the depositing particles cannot migrate around them and augment the effect of shadowing. Shadowing becomes more effective as the film thickness increases.

In the case of the Ni-Ti deposition without V_b on TiN buffer layers of thickness values ≈ 15 nm and ≈ 80 nm, it is also similarly suggested that the fact that the targets are tilted 30° away from the substrate normal has a considerable role on the later development of the <211> orientation (after the initial competitive growth between the <211> and <110> crystal orientations, detected *in situ* for the deposition on TiN buffer layers of thickness ≈ 15 nm). During the initial Ni-Ti deposition period, the growing direction of the columnar crystals have a tendency to lie along the substrate normal. However, due to the surface morphology of the TiN layer (without a dominating crystallographic orientation – most likely a granular uneven surface) and the geometrical shadowing effects, as growth proceeds the growth direction is more influenced by the direction of incident particles. This favoured the diffraction peak (in Bragg–Brentano geometry) of (211) of the B2 phase. In conclusion, it is suggested that this crystallographic preferential orientation development is associated to the combined effects of low surface mobility and shadowing. The Ni-Ti film depositions on TiN buffer layers with different thickness values have shown an initial stronger increase of the B2(110) diffraction peak intensity on the thicker TiN layers. However, only for the TiN layer mainly formed by <111> oriented grains (thickness ≈ 215 nm) was observed a continuously increase of the B2(110) peak intensity during the film growth.

The surface mobility of the deposited atoms under a relatively high growth temperature (as commonly mentioned in the literature [163]) allows them to migrate efficiently and form relatively large columnar grains. These grains would initially grow along the substrate normal direction. When increasing the film thickness, however, the mounds of columns become sufficiently large, and the nucleation of new grains on their sides becomes possible. In this case, the initial tilt direction of the new grains is set by the average slope of the mounds, which is distinctly separated from the substrate normal. The nucleation and growth of the tilted grains will also alter the surface morphology, which will, in turn, change the shadowing configuration. Therefore, the quantitative tilt angle of these new grains will depend on the film thickness as well as on growth conditions such as the substrate temperature and the off-axis angle of the magnetrons.

The competition between shadowing and atomic migration is, thus, supposed to determine the crystallographic orientation during growth when the depositing particles are incident to the substrate obliquely. In order to explore this phenomenon, a near equiatomic Ni-Ti film was deposited on thermally oxidized Si(100) without applying V_b but this time at a deposition temperature of ≈ 520°C. With an increase of the deposition temperature, the intensity of the B2(200) diffraction peak increased during the whole deposition process (≈ 800 nm film thickness), as observed in Fig. 3.15(a).

Jang *et al.* [163] have also found that the crystallographic orientation of AlN/Si(100) thin films crosses over from the substrate normal towards the direction of incident flux during off-axis RF magnetron sputter growth. At high growth temperatures (500°C), the crystalline *c*-axis orientation is initially maintained along the substrate normal direction, but jumps discontinuously towards the direction of incident flux for higher thicknesses. In contrast, at low growth temperatures (≤ 280°C), the *c*-axis direction shifts continuously towards the incident flux direction and saturates in the middle agreeing with the tangential rule of oblique deposition, i.e., $\tan\beta = ½ \tan\alpha$, where α and β denote the angles of incident flux and column inclination, respectively. However, in a rigorous sense, the crystallographic orientation can be different from the grain growth direction. The shadowing effect is more relevant to the grain shape or the grain growth direction than to the crystallographic axis orientation. Nevertheless, since the growth front is usually the surface of lowest energy, the low index (0001) plane of the AlN film is likely to be parallel to the growth front. They consider that the grain growth direction might exhibit similar features as the crystallographic axis direction.

4.1.5. Study of Ni-Ti graded films

The experiments analysed above concern the deposition of near equiatomic Ni-Ti films but they were also extremely useful for the preparation of experiments investigating the deposition of graded Ni-Ti films as in the controlled change of the Ti:Ni ratio during the deposition. Ni-Ti films were deposited exhibiting distinct composition and microstructure (absence/presence of precipitates) along the growth direction. This type of studies allows the identification of intermediate states during deposition and annealing, and the correlation with the final structure of the film, being useful for the optimisation of the deposition parameters in order to fabricate films with a two-way reversible actuation (a combination of superelasticity and shape memory characteristics).

Different experiments were performed on naturally oxidized Si(100) substrates and on TiN buffer layers with thickness ≈ 215 nm. An example of a Ni-Ti graded film deposited on a naturally oxidized Si(100) substrate without applying V_b is given in section 3.5.1. It concerns a film (total thickness of ≈ 420 nm) with a Ti-rich composition in the central part (ranging from 50 to ≈ 60 at%) and a near equiatomic composition in the extremities, following four distinct deposition periods (different Ti magnetron powers). During the initial deposition step (near equiatomic composition), the Ni-Ti B2 phase starts by stacking onto (h00) planes on the naturally oxidized Si(100) substrate due to the presence of the native silicon oxide (2-3 nm). The *in-situ* XRD studies [evolution of the a_o values of B2 phase as calculated from $d_{(200)}$] have shown also a considerable reduction of compressive stresses with increasing thickness. These observations are in agreement with the previous study of the growth of near equiatomic Ni-Ti films (143 min deposition - see Fig. 3.1). In that experiment, with increasing film thickness a crossover of the crystallographic orientation into a (110) preferred orientation is observed (≈ 30 min after deposition start), which is the more densely packed crystallographic plane. The preferential stacking of B2 phase on (110) planes starts at the moment the stabilization of a_0 of B2 phase as calculated from $d_{(200)}$ is detected (significant decrease of compressive stress). However, for the present sample, after this initial deposition period of ≈ 30 min, the Ti co-sputtering power was increased, first to 20 W and later to 30 W, leading to a gradual increase of the Ti content and the precipitation of the Ti-rich phase Ti_2Ni. During the precipitation process the a_0 value of Ti_2Ni, as calculated from $d_{(333/511)}$, slightly decreases in a continuous way.

Ishida *et al.* [164] observed that when an amorphous Ti-rich Ni-Ti film is crystallized (Ti-48.2 at. % Ni in the study), the microstructure changes in the sequence of (1) Guinier-Preston (GP) zones, (2) GP zones and Ti_2Ni precipitates within Ni-Ti grains, (3) Ti_2Ni precipitates within Ni-Ti grains and (4) Ti_2Ni precipitates along grain boundaries. The microstructure of a sample annealed at 500°C for 60 min was reported to have a dispersion of Ti_2Ni inside the Ni-Ti grains, as well as GP zones. The Ti_2Ni has partial coherency with the matrix and the misfit is considerably relaxed. They found the close relationship between the Ti_2Ni precipitates and the Ni-Ti matrix, and observed some similarity between the units cells of both phases. A high magnification image of the interface in their study revealed that some of the {110} planes are continuous through the precipitate and the matrix. Since the d-spacing of $Ti_2Ni(400)$ is 0.283 nm and that of B2(100) is 0.301 nm, if the Ti_2Ni precipitate is coherent with the matrix at the beginning of the precipitation process, a tensile stress field is formed around the precipitate. In the present study, it is not possible to compare directly the results

with what has been obtained by Ishida *et al.* [164] because here the Ni-Ti film is crystallized during the deposition process. Nevertheless, it should be considered that the continuous slight decrease of the a_0 value of Ti_2Ni, as calculated from $d_{(333/511)}$, could also be associated with the formation of a stress field around the precipitate.

During the last deposition period (without Ti co-sputtering), Ti_2Ni dissolves and, thus, plays the role of a reservoir for the formation of the B2 phase now preferentially stacking onto (110). As suggested by the depth profile results of the atomic concentrations (Fig. 3.64) this dissolution process is a consequence of the shift of the global composition towards Ni-richer, ending up at the near equiatomic composition. Since no relevant peak intensity changes could be discerned by *in-situ* XRD during the annealing period, the main progress to reach the near equiatomic composition occurs certainly during this last deposition step. During this step, a significant increase of the a_0 value of the Ti_2Ni is observed and for the B2 phase the increase is slightly higher for the value calculated from $d_{(110)}$. The variation observed for the a_0 value of the B2 phase could be related with the incorporation of Ti in the matrix. It should be also considered that if this dissolution process leads to the formation of GP zones, compressive stress fields in the matrix around them are produced.

Following these studies [using a naturally oxidized Si(100) substrate], a TiN film with a topmost layer formed mainly by <111> oriented grains has been used as substrate. It has been shown before (during the deposition of near equiatomic Ni-Ti films) that TiN acts not only as a diffusion barrier, but also induces different crystallographic orientations on the B2 phase. The *in-situ* XRD results have shown a preferential growth of <110> oriented grains of the B2 phase from the beginning of the deposition, with a constant growth rate during the whole deposition for a Ni-Ti film deposited on this type of buffer layers [Fig. 3.31(a)]. However, it is also important to know what would be the trend of the B2 preferred orientation for an increase of the Ti content during the deposition of graded films (e.g. half near equiatomic and half Ti-rich), since the precipitation of Ti_2Ni would be expected in the Ti-rich film fraction. This is a typical question that can be answered taking profit of the unique equipment installed at ROBL. In section 3.5.2, the effect of the controlled change of the Ti:Ni ratio during the deposition of Ni-Ti films on the TiN buffer layer (with a V_b of −45 V) was tested. The precipitation of the Ti_2Ni phase in the second step of the deposition (due to the increase of the power of the Ti target) did not affect the preferential growth of <110> oriented grains of the Ni-Ti B2 phase (Fig. 3.73).

4.1.6. Deposition of NiTiHf films

The magnetron-sputtering chamber installed at ROBL proved also to be a very efficient instrument to deposit and follow *in situ* the evolution of the structure of ternary alloys like, NiTiHf growing films. Although the deposition chamber does not allow the use of three separate elemental targets, a direct control over the film composition is achievable by varying independently the power of each magnetron. Furthermore, the use of a Ni-Ti target and a Hf target avoids the complexity of alloy target preparation (i.e., a NiTiHf target). The *in-situ* experiments presented in section 3.6.2. have shown that a preferential growth of <110> oriented grains of the B2 phase from the beginning of the deposition could be obtained using a HfN film with the topmost layer constituted mainly by <111> grains. It has been observed that the increasing amount of Hf incorporated in NiTiHf films shifts the B2(110) peak towards lower 2θ (higher d-spacings) and decreases its intensity. This is most likely linked to the atomic size difference between Hf and Ti. In NiTiHf SMA, Ti is substituted by Hf, and since the atomic radius of Hf is 0.216 nm, which is slightly larger than Ti with a radius of 0.200 nm, there is an increased lattice distortion.

The presence of precipitates [identified as $(Ti,Hf)_3Ni_4$] was detected in the films deposited with a higher power applied to the magnetron with the Hf target. In earlier times, NiTiHf SMAs (Ti+Hf) richer used to be preferred since the transformation temperatures dramatically decrease with the increase of Ni concentration when the Ni is over 50 at.%. Nevertheless, several methods including aging, thermo-mechanical treatment, alloying *etc*, used to overcome the low strength of the matrix, did not show any obvious improvement of their properties. In the case of Ni-rich NiTiHf alloys, due to the severe decrease of the phase transformation temperatures, they cannot be used as high temperature SMAs. However, if they are subjected to a proper thermal annealing process, a fine precipitation of $(Ti,Hf)_3Ni_4$ particles can be induced, leading to higher phase transformation temperatures [165]. The use of these alloys having in their matrix these fine precipitates has several advantages:

(1) The amount of $(Ti,Hf)_2Ni$ precipitates decreases since the Ni content is higher for these alloys, which will benefit the improvement of workability and mechanical behaviour;

(2) The precipitation of $(Ti,Hf)_3Ni_4$ leads to relatively high phase transformation temperatures;

(3) The $(Ti,Hf)_3Ni_4$ precipitates strengthen the matrix of NiTiHf alloys, which would lead to the increase of both the stability of transformation temperatures and shape memory properties.

Nevertheless, it should be taken in consideration that if the precipitation process is not controlled, further precipitation of secondary phases could suppress the martensite transformation.

4.2. INTERFACE ANALYSIS AND PHASE TRANSFORMATION CHARACTERISTICS

4.2.1. Interface morphology

The depth profile of the atomic concentration in the Ni-Ti films deposited on naturally oxidized Si(100) substrates (Fig. 3.6) not only gives important information concerning the composition of the Ni-Ti films but also puts in evidence a strong interfacial diffusion (Ni into the Si substrate). A special analysis of this point is, thus, required since the Ni-Ti film thickness required for MEMS applications are frequently a few micrometers and a moderately thin reaction layer can have a major effect on shape memory properties.

A detailed analysis of the morphology of their interfaces by X-TEM was performed resulting in the identification of several phases. $NiSi_2$ silicides (A-$NiSi_2$ and B-$NiSi_2$; the type-A orientation represents coincidence of crystallographic axes in the $NiSi_2$ and Si lattices and type-B involves a 180° mutual rotation about the [111] growth direction) were detected on the substrate's side as well as $Ti_4Ni_4Si_7$. A different ternary silicide type (not identified) and Ti_2Ni are perceptible on the Ni-Ti film's side (Fig. 3.8 and Fig. 3.69). The native SiO_2 layer of the Si substrate is here used as a reference in this delimitation (substrate's side and film's side). For the deposition of near equiatomic Ni-Ti films on naturally oxidized Si(100) at high temperature (≈ 470°C) Ni atoms migrate from the Ni-Ti film to the Si substrate leading to di-silicide formation. Wu *et al.* [130] reported that the development of $NiSi_2$ instead of NiSi or Ni_2Si might be due to the (Si, O)-rich layer (native SiO_2 layer), which acts against the diffusion of Ni atoms, resulting in a lower Ni supply rate. Using a Ni/Ti bilayer system on Si(100) substrates, Falke *et al.* [166] also found a preferential growth of epitaxial $NiSi_2$ at reaction temperatures of about 475°C, i.e., the Ni di-silicide phase forms first. This was

associated to the relatively slow Ni transport rate through the Ti layer, which acts as a diffusion rate-limiting barrier.

The migration of Ni from the Ni-Ti film leaves the film adjacent to the interface depleted in Ni and the Ti-rich Ti_2Ni phase is formed, having been detected in some areas along the interface in the present study. For the Ni-Ti graded film presented in section 3.5.1, the appearance of Ti_2Ni phase close to the interface is not related with the increase of the power of the Ti target. The (111) planes of Ti_2Ni were identified making with the interface an angle that leads to the (400) planes approximately parallel to the interface. In the areas where the Ti_2Ni is present, the B2 phase was identified with the (100) planes parallel to the interface. Published studies concerning the crystallization of Ti-rich Ni-Ti films at temperatures above crystallization temperature report granular Ti_2Ni precipitates [16]. In this temperature range two situations with respect to the orientation relationship to the B2 matrix were identified. For a Ti content lower than 53 at%, Ti_2Ni precipitates have a specific orientation relationship with the matrix (B2 phase), because the precipitates are formed after the crystallization of the B2 matrix. In this case it is expected that the crystal axes of Ti_2Ni and those of B2 are parallel to each other. On the contrary, when Ti content is higher, the Ti_2Ni phase is formed first, and then crystallization occurs and no orientation relationship between the precipitate and matrix could be identified. Based on the information provided by these earlier studies, it is believed that it is not a coincidence to find Ti_2Ni with (400) planes approximately parallel to the interface, in the B2 matrix with the (100) planes parallel to the interface in the present study. It seems that, after the deposition and crystallization of a near equiatomic film fraction, the diffusion process led to the formation of Ti_2Ni precipitates apparently with an orientation relationship with the matrix.

The Si and Ti atoms also migrate probably at a lower rate than Ni since the formation of nickel silicide is less sensitive to the O-rich layer than the formation of titanium silicide in the Ti/Si-substrate system [131]. A near-$Ti_4Ni_4Si_7$ compound nucleates at the interface and, for higher temperatures, according to the results from Wu *et al.* [130] it would grow into the A-$NiSi_2$ and the Si substrate. A ternary compound (Ti, Ni, Si) of a different type also nucleates at the interface and grows into the Ni-Ti film. Wu *et al.* [130] observed a ternary silicide in this region and mentioned that it has a stoichiometry close to TiNiSi. However, in the present work this phase could not be identified. No crystalline order was detected by HR-TEM.

Experimental results obtained by X-TEM on the Ni-Ti/Si(111) interface confirmed that $NiSi_2$ grows epitaxially on Si. Figure 3.9 shows that A-$NiSi_2$ grows in an orientation that is identical to that of Si. In this case, instead of the semi-octahedron shape observed for the deposition on Si(100), a uniform thickness plate appears due to the alignment between substrate orientation and the [111]-growth front.

When analysing the depositions on Si(100) and Si(111) substrates the morphology of the films interface revealed the presence of $NiSi_2$ evidencing that Ni diffuses preferentially along Si<111>. In the case of the Ni-Ti deposition on poly-Si the diffusion is inhomogeneous. Diffusion of Ni occurs preferentially along the columnar grains of poly-Si, which are favourably aligned for the diffusion process.

These results show that for the Ni-Ti/Si system, the morphology of the diffusion interface is strongly dependent on the orientation of the Si substrate.

The depth profiles results of the atomic concentrations in the Ni-Ti films deposited on thermally oxidized Si(100) substrates (Fig. 3.17) suggest that the thermally grown SiO_2 layer acts as a diffusion barrier. This has already been reported by Fu *et al.* [132], but they also have mentioned that it serves as an effective diffusion barrier - yet at the expense of film adhesion. The existence of oxygen on the SiO_2 layer promotes the oxidization of the Ti atoms during the Ni-Ti film processing, forming a fragile and brittle layer of TiO_2. In the present study, during the deposition of Ni-Ti on thermally oxidized substrates (with and without V_b) as well as on MgO(100) substrates (without a TiN buffer layer), diffraction peaks associated with the presence of TiO_2 in the interface were identified. Although the X-TEM micrographs obtained for the Ni-Ti films grown on this type of substrates did not allow a complete characterization of the reaction products (by HR-TEM), by combining the results obtained using the different characterization techniques, it is suggested that TiO_2 is present in their interface film/substrate. The experiments carried out using a TiN buffer layer have shown that the TiN layer acts as a diffusion barrier. This is more notable when comparing the depositions of Ni-Ti films on MgO(100) substrates with and without a TiN buffer layer.

In the case of the deposition on MgO(100) substrates, two diffraction peaks located near the B2(200) peak were detected, suggesting the presence of interfacial reaction products (Fig. 3.44). Additional *ex-situ* TEM observations allowed a fine-structural characterization confirming the existence of reaction products between the Ni-Ti deposited material and the MgO substrate (Fig. 3.54). In the deposition performed directly onto MgO(111) the two

diffraction peaks from the same phases were as well detected. Nevertheless, the peaks were indexed to different planes, which suggests a relationship between the diffusion process and the orientation of the MgO single crystal substrates.

4.2.2. Variation of the Ni-Ti lattice parameter values

It is known that various sources of stress may be discerned when a film is deposited on a substrate, such as, intrinsic stress or growth stress, thermal stress and epitaxial stress. The deposition technique used in this work is typically associated to the growth of films far from the thermodynamic equilibrium, with the consequence that highly non-equilibrium microstructures are created. These microstructures lead to additional stress caused by the tendency of the film to shrink or expand once it has been deposited onto the substrate. A film attached to the substrate is subjected to biaxial strains. The volume changes involved during the growth process (crystallization, reactions *etc*) are in general accompanied by a change in microstructure, grain size, impurity incorporation, *etc*. The study of the evolution of the variation of the lattice parameter, a_0, values obtained from the different diffraction peaks (Bragg-Brentano geometry) recorded during the growth and annealing processes gave an important indication of the intermediate biaxial stress state of the Ni-Ti films. Therefore, a correlation could be made with the film processing parameters.

Considering the evolution of a_o, as calculated from $d_{(200)}$ of B2 phase, during the initial deposition stage on naturally oxidized Si(100) substrates without V_b [Fig. 3.2(a)], a considerable reduction of compressive stresses with increasing thickness is observed. Its tendency for stabilization is coincident with the deposition time (≈ 30 min deposition) where the preferential stacking of B2 phase on (110) planes is starting. Gisser *et al.* [96] also observed in their samples that the film stress parallel to the substrate is compressive (by *ex-situ* measurements). Having the Si substrate peak as an internal standard, they obtained larger d-spacings for the B2(110) when compared with the same plane in bulk Ni-Ti. Furthermore, Grummon and Zhang [167] have observed a variation of the intrinsic stress with film thickness. A decrease of the compressive stress from −430 MPa for 1.3 μm thick films to −250 MPa for 4.2 μm thick material was reported. It was suggested that a dependence between the intrinsic stress developed and the effective shear compliance of the substrate exists, such that, for the initial deposited layers, the Ni-Ti film experiences a substrate compliance identical to that of pure Si(100), developing large compressive stresses. Additionally, here it is suggested that the higher variation of the biaxial stress state at the

beginning of the deposition, i.e. next to the film/substrate interface, is also related to the interfacial reactions processes [168], [169].

For the Ni-Ti film deposited on a thermally oxidized substrate without bias (Fig. 3.12), such a strong initial decrease of the a_0 value of B2 phase is not observed. In contrast, a continuous slight decrease of this value is perceptible, as calculated from $d_{(200)}$ of B2 phase, during the whole film processing. It has been shown in section 3.2.2 that the thick Si oxide acts as a diffusion barrier.

When V_b (−45 V) is applied during the deposition of the Ni-Ti film on Si(100) naturally oxidized, again an initial significant change of a_0 of B2 phase, as calculated from $d_{(200)}$, is observed [Fig. 3.3(b)]. Nevertheless, the values of a_o of B2 phase obtained from $d_{(200)}$ and $d_{(110)}$ are in close proximity. For the deposition on thermally oxidized Si(100) substrate with −45V [Fig. 3.13(b)] the relative magnitude of the a_o values of B2 phase is reversed [a_o calculated from $d_{(200)}$ is smaller than the one calculated from $d_{(110)}$] when compared with the deposition without V_b. Additionally, instead of a continuous decrease of both values of a_o of B2 phase as a function of time, there is a convergence to a common value of a_o. However, in both cases [depositions with V_b of −45 V on naturally and thermally oxidized Si(100) substrates], the values obtained for a_o of B2 phase converge to ≈ 0.304 nm.

The results obtained for the Ni-Ti film deposited on thermally oxidized Si(100), without applying V_b at ≈ 520°C (Fig. 3.15), has shown that with an increase of the deposition temperature, the variation of the value of a_o of B2 phase, as obtained from the positions of the Bragg-Brentano B2(200) peak, does not exhibit a continuous decrease during the deposition like in the case of the deposition at ≈ 470°C. There is a strong convergence to a common value of a_o, i.e. 0.304 nm [values calculated using the B2(200), B2(211) and B2(110) diffraction peaks]. As it can be observed, an increase of the deposition temperature from ≈ 470°C to ≈ 520°C led to a convergence of a_o of B2 phase to ≈ 0.304 nm like in the case of the application of V_b of −45 V. It appears that, in these cases, V_b increases the energy of the ions bombarding the film surface during growth, which results in enhanced mobility of the adatoms in the near-surface region, corresponding to a higher temperature close to the surface. Thermodynamics drives the system towards the minimum possible sum of surface and strain energies under the restrictions imposed by kinetics. The increase in the energy of the adatoms allows them to diffuse on the substrate surface. Thus, the adatoms are no longer kinetically constrained to metastable high-energy configurations. Also, the defect-annealing rate will eventually become higher than the defect generation rate as the substrate temperature is

increased and films with lower growth stresses will result. The temperature at which this occurs depends on several factors such as film material, energy of the impinging particles, contamination level, growth rate *etc*. For example, a high growth rate requires a higher temperature before obtaining films free of growth stresses. However, as the temperature is increased the thermal stress will increase.

The deposition of near equiatomic Ni-Ti films on naturally oxidized Si(111) substrates (without V_b) has shown a convergence of the a_0 value of B2 phase to ≈ 0.303 nm. This is even a lower value when compared to the cases mentioned above [depositions on naturally and thermally oxidized Si(100) substrates with and without V_b]. It is suggested that the different crystal orientation of the substrate and consequential distinct migration path/direction of front growth (section 3.1.2) plays an important role on this respect.

For epitaxial films on thick substrates, the accommodation strain is given by the ratio between the difference of the lattice parameters of the film and the substrate, and the lattice parameter of the film. In this case, the elastic accommodation is assumed to take place in the film because the substrate, being so much thicker than the film, is essentially rigid. The evolution of a_o of B2 phase, as calculated from $d_{(200)}$, for the Ni-Ti deposition on TiN(100)/MgO(100) substrate has shown that the first layers of Ni-Ti deposited on the TiN(100) are constrained (compressive planar stress state) and this deformation remains until the end of the deposition (Fig. 3.48). Later layers are having a gradually relaxed interplanar distance (smaller $d_{(200)}$ in the direction of the surface normal), indicating a gradual relaxation of the compressive stress constraint imposed at the interface Ni-Ti/TiN (Fig. 3.47).

In the case of the Ni-Ti film deposition directly onto MgO(100), when considering the evolution of the position of B2(200) diffraction peak (Fig. 3.44), a significant stress relaxation takes place at the initial deposition stage. This is consistent with the results obtained for the deposition on naturally oxidized Si(100) substrates [Fig. 3.1(b)]. Most likely, this typical behaviour at the beginning of the deposition, i.e. next to the interface film/substrate, is also linked to the interfacial reactions processes.

For the Ni-Ti depositions on the TiN buffer layers with thickness values of approximately 15, 80 and 215 nm, previously deposited on thermally oxidized Si(100) substrates, the decrease of the a_o value of B2 phase as shown in Fig. 3.31(b) suggests, once more, that the Ni-Ti films experience compressive biaxial stress, which is relaxed with increasing film thickness. It is also detectable that, when the (110) planes of the Ni-Ti B2 phase parallel to the substrate assume higher relevance, a_o, as calculated from $d_{(110)}$, exhibits

lower values. If one considers that a lower a_o value corresponds to a lower compressive biaxial stress, a film exhibiting the (110) planes of the Ni-Ti B2 phase parallel to the substrate should possess a lower compressive biaxial stress. It has been suggested that for the deposition of Ni-Ti on TiN layers without applying V_b, the development of the B2(211) diffraction peak in Bragg-Brentano geometry, for TiN thickness values of ≈ 15 nm and ≈ 80 nm, is the result of a gradual change of the growing direction of the columnar crystals with increasing thickness. Therefore, for a higher inclination of the (110) planes of the B2 phase, higher residual compressive biaxial stresses are observed (according to the a_o values). Nevertheless, in the different samples, the a_o value approaches ≈ 0.304 nm during the annealing step.

Falub *et al.* [63] have deposited TiAlN films with the preferred orientation of the crystallites tilted with respect to the surface of the samples. The observed preferred orientation was explained by the oblique paths between the substrate and the Ti/Al targets. They have stated that the inclination of the (200) diffracting planes increased with increasing residual compressive stress in the coating suggesting that there is interdependence between intrinsic stress and fibre texture (it should be mentioned that Falub *et al.* have used a rotating sample holder). Nevertheless, they concluded that it is still unresolved, whether it is the stress that influences the texture or inversely the texture developing the stress.

The analysis of the variation of the a_0 values, as calculated from $d_{(110)}$ and $d_{(211)}$, as a function of deposition time, for the Ni-Ti B2 phase of the film deposited with a V_b of −45 V (on a TiN buffer layer of thickness ≈ 15 nm) has shown a reasonable stability along the processing steps (Fig. 3.33). Furthermore, there is an overall decrease of this value (being ≈ 0.303 nm) when compared with the deposition without V_b (which has approached a value of 0.304 nm at the end of the annealing step). This indicates that an increase of energy of the incident ions resulted in enhanced mobility of the adatoms allowing them to diffuse on the substrate surface and, as a result, the adatoms are no longer kinetically constrained. Most likely this contributes significantly to the lower biaxial compressive stress state when using V_b (−45 V) during the Ni-Ti deposition on the TiN buffer layer of thickness ≈15 nm.

For the Ni-Ti deposition with V_b of −45 V on TiN buffer layers with a thickness of ≈ 215 nm, a continuous decrease of the a_0 value of B2 phase and its approach to ≈ 0.304 nm at the end of the annealing step, like in the case of the deposition without applying V_b was not observed. In this case, a very small decrease of a_0 at the beginning of the deposition, followed by a stabilisation near the value of 0.303 nm [Fig. 3.34(b)] was visible. A further increase to

−90 V showed a practically constant value of a_0 during the whole deposition process. It is then possible to conclude that as V_b is increased (in the range of the values used in this work), a_0 value of B2 phase decreases, approaching the equilibrium value of 0.303 nm for −90 V applied. This variation of the a_0 values suggests a relaxation of the compressive biaxial state resulting from the higher energetic ion bombarding.

4.2.3. Phase transformation characteristics

In-situ and *ex-situ* characterizations of Ni-Ti films have allowed not only to obtain essential information concerning the structural development of Ni-Ti films on the different types of substrates that have been used, but also to determine the phase transformations characteristics of Ni-Ti films. A link has been identified between the different transformation characteristics of the Ni-Ti films observed in ER measurements during the thermal cycles and their different preferred orientations. There is also a stress effect resultant from the film/substrate system. Substrate-attached Ni-Ti films are subject to stresses related with differential thermal expansion, whose relaxation might take place at low temperature by shear-variant boundary motion and stress-induced transformation of lower-symmetry phases (R-phase and B19'). The interfacial reaction products also play a key role on the phase transformation characteristics. Furthermore, an extra effect induced by V_b led to a very interesting finding, i.e., the control of the energy of the bombarding ions can be used to control the transformation temperatures of the Ni-Ti films. These effects on the transformation characteristics of the Ni-Ti films are discussed below.

The temperature dependence of ER results combined with X-TEM observations on films deposited on naturally oxidized Si(100) substrates put forward some important observations. From the transformation temperatures obtained from ER measurements, the existence of B2 phase at RT is not expected, but cross-section HR-TEM images have shown lattice spacing agreeing well with those of B2 phase close to the interface film/substrate (see Fig. 3.67). These images were obtained without intentional heating of the TEM sample holder, but it is necessary to note that the *e*-beam from the electron microscope can provide energy and as a consequence, slightly heating of the film. If the phase transformation temperature of this area of the film is only a few degrees above RT, the *e*-beam can possibly provide enough energy to cause the phase transformation. Johnson *et al.* [170] demonstrated the actuation of a micro-scale device by using *e*-beam (ISI60 scanning electron microscope) heating. Nevertheless, it is believed that this is not the reason for the detection of the B2 phase

near the interface in the present measurements. Fu *et al.* [128] studied the effects of film thickness on phase transformation of constrained $Ni_{49.8}Ti_{50.2}$ films deposited onto Si(100) substrates. They have found a minimum thickness (about 100 nm, for the Ni-Ti film) necessary to guarantee apparent phase transformation behaviour in the Ni-Ti films. For very thin films the surface oxide and interfacial diffusion layers exert a dominant constrained effect that renders high residual stress and low recovery stress in the film. The detection of the B2 phase near the interface film/substrate is in agreement with the study performed by Fu *et al.* [128], since in both studies the interfacial reaction products are present. Additionally, Su *et al.* [137] observed (by X-TEM) for Ni-Ti films deposited on thermally oxidized Si substrates (200 nm SiO_2 thick layer) an interlayer adjacent to the substrate which never transforms to martensite even though the above layer shows a clear transformation microstructure, presumably due to the mechanical constraints imposed by the substrate. In their work, the untransformed interlayer, consisting of parent phase (about 50-100 nm thick), has been found in films of various thicknesses.

The martensitic transformation in Ni-Ti alloys involves strains up to 8-10 %. In the bulk material this large strain is largely accommodated through twinning. Concerning martensitic transformations occurring in Ni-Ti films attached to substrates, the transforming film has to accomplish the strain accommodation at the interface by itself, since the rigid substrates cannot respond to accommodate the potential discontinuity at the interface. On one hand, the untransformed interlayer observed by X-TEM [137] is playing this role since it accommodates the strain through a gradient, eliminating the potential discontinuity at the interface. However, as the film thickness is reduced to a few hundred nanometers and the thickness becomes comparable with the thickness of the interlayer, the transformation will not occur in the film. Thus, it is necessary to understand the mechanism behind this phenomenon.

Su *et al.* in the same work [137], suggested that the mechanism of interface stabilization of the parent B2 structure may be understood in view of the strong (110) orientation of the B2 phase observed in their films attached to the substrate. In Fig. 4.1 it is presented a schematic representation of the B2 and B19' structures of Ni-Ti alloy. Their parameters are quoted in the parent phase coordinate system and indexed as "p" for parent and "m" for martensite for an easier comparison. Su *et al.* state that the transformation in the Ni-Ti films requires a_p and b_p to shrink from the parent phase parameters $a_p = 0.2998$ nm, $b_p = 0.4240$ nm and $c_p = 0.4239$ nm to the parameters of the martensitic phase, $a_m = 0.2889$ nm, $b_m = 0.4120$ nm and $c_m = 0.4622$ nm.

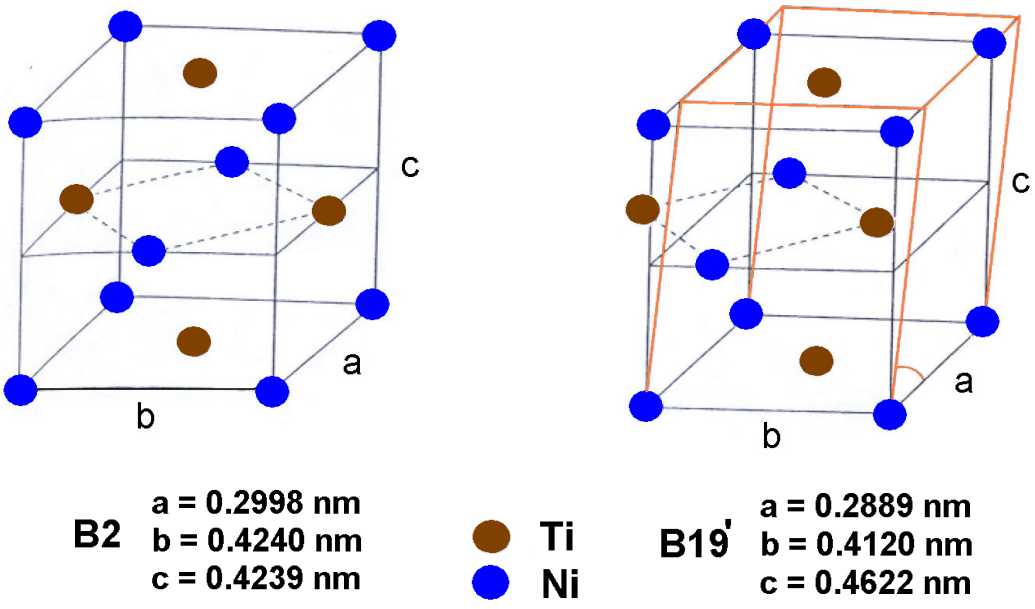

Fig. 4.1: Schematic unit cells of the B2 and B19' phases of Ni-Ti alloy with the *c* axis chosen along (110) in B2 and along (001) in B19' (figure adapted from [137]).

It can be observed that an expansion occurs in the *c* direction perpendicular to the (110) plane. For a perfectly (110) oriented Ni-Ti film, the *c* direction is "free" of constraints so the martensitic expansion need not be accommodated in the film/substrate composite reed. Nevertheless, the shrinkage of (110) planes is blocked at the film/substrate interface. Strong interfacial adhesion will thus stabilize the B2 structure. As the film thickness increases, a larger volume fraction of the film is sufficiently distant from the interface, so that its constraining effect is reduced and, consequently, the martensitic transformation will approach its behaviour for thicker Ni-Ti films.

The ER results obtained, in the present work, for the samples deposited on naturally oxidized Si(100) and thermally oxidized Si(100) without V_b (Fig. 3.27) have shown completely different trends. During cooling, a clear increase in the ER is observed, followed by a decrease associated with B2 $\Rightarrow$ R-phase $\Rightarrow$ B19' transformation, for both samples. However, the increase of the resistivity during R-phase formation is considerably higher for the Ni-Ti sample deposited on thermally oxidized Si(100) when compared to the sample on naturally oxidized Si(100) substrate. A further disparity concerns the temperature range where the R-phase is stable during cooling since it is larger for the sample deposited on the naturally oxidized Si(100). The sample deposited on naturally oxidized Si(100) also shows a greater stability of the B2 phase, which is inferred from the lower transformation temperatures. It

should be remembered that both samples have nearly the same composition (near equiatomic films – see Fig. 3.6 and Fig. 3.17). After an analysis of the overall results obtained for these two samples, it is concluded that the different trends observed in the ER measurements during the thermal cycles (phase transformation) are related to the different preferred orientations of the Ni-Ti films together with the stress effect resultant from the film/substrate system.

The results obtained by Su *et al.* [137] are for films presenting good film-substrate adhesion, where a greater stability of B2 phase is reported close to the substrate interface when the Ni-Ti film is strongly (110) oriented (B2 phase). In the present work, the Ni-Ti films deposited on oxidized Si(100) that exhibits mainly grains with the (110) planes of the B2 parallel to the substrate surface exhibit also the presence of (100) planes parallel in the region close to the film/substrate interface. Although, due to this divergence, it is not possible to compare directly the present results with what has been observed by Su *et al.*, it is suggested a combined effect of the substrate and the crystallographic orientations of the Ni-Ti films on their transformation characteristics.

The temperature dependence of ER results of the near equiatomic Ni-Ti samples (deposited without V_b) with TiN buffer layers, of thickness values of ≈ 15, ≈ 80 and ≈ 215 nm presented in Fig. 3.38 highlight this preliminary conclusion (i.e. an effect of the crystallographic orientation on the transformation characteristics of the Ni-Ti films). The XRD measurements have essentially shown the existence of grains with (110) planes parallel to the film surface (for the B2 phase) for the deposition on the TiN layer of thickness ≈ 215 nm. The resistivity curves obtained during phase transformation showed a similar trend to the curves recorded for the Ni-Ti sample deposited on naturally oxidized Si(100), also deposited without V_b (Fig. 3.27). In both cases, the Ni-Ti films exhibit mainly grains with (110) planes parallel to the film surface.

For the deposition on a TiN layer of thickness ≈ 15 nm, the B2(110) diffraction peak also appears from the beginning of the deposition but much less intense. In this case, the B2(211) peak was also detected with a crossover from <110> oriented grains dominating at small thicknesses to <211> grains taking over at larger thicknesses. The increase of the ER during R-phase formation (on cooling) is much higher for this later Ni–Ti sample with a TiN buffer layer of thickness ≈ 15 nm (Fig. 3.38). During heating, the transformation is also occurring in two steps, B19' ⇒ R-phase ⇒ B2. It is possible to distinguish a greater increase in the ER values for the Ni-Ti sample deposited on a TiN layer of thickness ≈15 nm.

In the case of the sample with an intermediate TiN layer of thickness ≈ 80 nm, the *in-situ* XRD measurements have shown an initial stronger increase of the B2(110) peak, when compared with the deposition on a TiN layer of thickness ≈ 15 nm. Nevertheless, the diffraction peak B2(110) approaches the intensity of the previous sample approximately after 85 min [Fig. 3.31(a)]. The ER results (Fig. 3.38) show an "intermediate" behaviour for this sample when compared to the other two analysed above (with TiN layers of thickness ≈ 15 and ≈ 215 nm, respectively). During cooling, self-accommodation R-phase transformation commenced at temperature R_s and the austenite phase began to transform to the twinned R-phase with the decrease of the temperature below R_s. Nevertheless, R-phase transformation (R-phase distortion) exhibits a tendency to end prematurely due to the resistance force (i.e., energy barrier) introduced probably by spatial constraints generated by the film/substrate interface, as indicated by the ER plateau tendency produced in the temperature range of R_f to S (see Fig. 3.38). When the driving force for phase transformation increased because of the decrease of the temperature, the resistance force was overcome and B2 ⇒ R-phase transformation (R-phase distortion) resumed again. This is demonstrated by the increase of the ER with the decrease of the temperature from S. Cooling below (M_s) promoted transformation from R−phase to the martensite phase. Since this phase change occurred with the simultaneous decrease of the lattice distortion, the ER exhibited significant decay.

Wang *et al.* [171], based in a previous work [172] reported that the greater the extent of sub micro twinning, the higher the increase in the resistivity. They also mentioned the finding of Cross *et al.* [173], i.e., there is a one-to-one correspondence between the mechanical "memory" effect and the ER curve; the larger the electrical resistivity "peak" (between A_s-M_s) the more pronounced is the "memory" effect (i.e., the shape recovery performance). These authors [171], by combining these two hypotheses, suggest the following: *it can be reasoned that if there is more sub micro twinning (which brings about a higher resistivity) there would be less strain energy involved in returning to the B2 structure and thus the "memory" effect would be more pronounced.* It seems, the use of a TiN buffer layer is an important finding for the present work to manipulate the crystallographic orientations of the Ni-Ti films and consequently influence their phase transformation characteristics.

All the ER results discussed up to now resulted from the deposition of near equiatomic Ni-Ti films with comparable composition for all the cases. This is emphasized here since the transformation temperatures are greatly dependent on composition (Fig. 1.6). The main

factors considered on the phase transformation characteristics of the Ni-Ti films have been: (i) the different preferred orientations of the Ni-Ti films, (ii) the stress effect resulting from the film/substrate system. The high level of stress presented in films, due to substrate effects, suggests that they can compete with internal stresses in the martensite or martensite-austenite microstructure and considerably change the self-accommodation of the martensitic transformation in SMAs. As a result, the transformation characteristics in constrained films should be investigated using a different approach when compared to bulk materials. A phase transformation in a constrained film is a "closed-loop" interaction. The transformation changes the state of stress of the film and the changing stress, in turn, affects the transformation.

When combining the results obtained by *in-situ* XRD and the ER results, although further studies are required in the future, it seems realistic to state that there is a link between the stress induced by the film/substrate system and the phase transformation temperature values, which can be separated from the effect of the distinct fibre textures. In the case of the deposition of Ni-Ti film on naturally oxidized Si(100), without applying V_b, it has been shown that a significant stress relaxation takes place at the initial deposition stage. It was suggested that the interfacial reaction processes could play a role in this observed trend. It is known that a thermally grown oxide layer (≈ 140 nm) acts as a diffusion barrier. A comparison between the ER results recorded for the Ni-Ti films deposited on naturally and thermally oxidized Si(100), without applying V_b, could suggest that the substrate-induced stress shifts the M_s to higher temperatures values. Nevertheless, in this case it is not possible to separate stress and texture effects since the Ni-Ti films exhibit different crystallographic orientations. For the Ni-Ti films deposited on MgO(100), with and without TiN intermediate layer, a strong (100) texture was identified. The TiN film acted as an efficient diffusion barrier and, in contrast with the deposition of Ni-Ti directly onto MgO, no extra phases were detected by XRD. This diffusion barrier did not allow a considerable relaxation of the biaxial stress state associated with the (100) of the B2 phase through the mechanism of interfacial diffusion (contrary to the case of the Ni-Ti film deposited directly on MgO – Fig. 3.44). In Fig. 3.47, it can be observed that the first layers deposited on the TiN(100) are constrained (compressive planar stress state) and this deformation remains until the end of the deposition. The XRD results performed at RT and the ER results (Fig. 3.55) have shown that B2 is the predominant phase at RT for the film deposited directly onto MgO (interfacial reactions products have been detected). In contrast, the higher constrained film (with the TiN buffer layer) exhibits mainly the R-phase at RT. For this observation, it was taken into consideration

that no significant change in composition is detected in the overall thickness of the Ni-Ti film (with exception of the nearest fraction close to the film/substrate interface due to diffusion effects).

The depositions of Ni-Ti films on a TiN buffer layer of thickness ≈ 215 nm (without V_b, with −45 and −90 V) have, furthermore, put in evidence the effect of different biaxial stress states on the phase transformation temperatures. For these three samples there is a preferential growth of <110> grains of the austenitic phase from the beginning of the deposition, with a constant growth rate up to the end of the deposition [Fig. 3.34 (a)]. The variation of a_0 (as calculated from the lattice constant, *d*, according to the B2(110) peak position) as a function of time [Fig. 3.34 (b)] have shown a continuous decrease during the whole film processing (without V_b), suggesting that the films experience compressive stress, which is appreciably relaxed for higher thickness values. In the case of the Ni-Ti films grown with V_b, the higher energetic ion bombardment increases the energy of the adatoms to diffuse on the substrate surface and a lower biaxial stress state was observed (having in consideration the variation of the a_0 values of B2 phase for the three samples). The ER curves obtained for these three samples (Fig. 3.40) show higher phase transformation temperatures for the sample deposited without V_b. This is attributed to the higher biaxial stress state. An effect of compositional difference is not expected as confirmed by the AES results presented in Fig. 3.41. The lower increase of the resistivity during R-phase (prominent on cooling) for the Ni-Ti film grown with V_b of −90 V is the result of the higher energetic ion bombardment. An increase of V_b from −45 V to −90 V led to the appearance of surface steps on the crystals (Fig. 3.42). The ER results are consistent with the assumption that spatial constraints introduced by the higher energetic bombardment (−90 V) in the microstructure of the film could generate a resistance force for lattice distortion and twinning. It is then revealed in the present work that the control of the energy of the bombarding ions is a promising tool for the manipulation of the transformation temperatures.

Roytburd *et al.* [174] have presented a first attempt (a thermodynamic analysis) to understand the martensitic transformation in constrained films upon cooling and heating. Their analysis describes the onset of transformation in polycrystalline films. The theory predicts a considerable shift of the temperature interval of transformation and its broadening due to the constraint. Experimental studies of the stress evolution with changing temperature in Ni-Ti polycrystalline films on Si substrates supported the principal thermodynamic conclusions. The film used in their studies was highly textured, i.e., each grain had (110)

planes parallel to the surface of the film. In fact, during the present thesis work, a typical broadening of the transformation temperature interval during cooling has been observed for films possessing mainly grains with (110) planes parallel to the film surface (Fig. 3.27 and Fig. 3.38). This is particularly visible while comparing the results obtained for the different samples in Fig. 3.27 [Ni-Ti films deposited on naturally oxidized Si(100) without V_b, on thermally oxidized Si(100) with V_b and without V_b]. Additionally, it has been shown that the stress relaxation promoted by the higher energetic ion bombarding during Ni-Ti film growth shifted the transformation temperature interval towards lower temperatures (Fig. 3.40 – Ni-Ti films deposited on TiN layers of ≈ 215 nm).

The ER results presented in Fig. 3.39, for Ni-Ti films deposited with and without V_b on TiN layers of thickness ≈ 15 nm, also show the effect of the biaxial stress on the shift of the transformation temperature interval. The results also show a variation of the transformation temperature interval amplitude due to the changing of the crystallographic orientation. The sample deposited with V_b [mainly grains with (110) parallel to the film surface and lower biaxial stress] exhibits lower transformation temperatures. The Ni-Ti film deposited without V_b [mainly grains with (211) parallel to the film surface and higher biaxial stress] exhibits higher resistivity values for R-phase.

Future directions for Ni-Ti films include the production of functionally graded films. The deposition of graded films by changing deliberately the Ti:Ni ratio, thereby changing microstructure and transformation temperature across the film thickness, can be very useful to produce films with a bimorph structure exhibiting "*two-way*" SME. It is desirable to control the gradual change of the properties across the film thickness during the processing of Ni-Ti films in order to exhibit the *"two-way"* SME. In the present work, parameters were tested to produce, in the future, optimised systems with a combination of superelasticity and shape memory properties (Fig. 4.2).

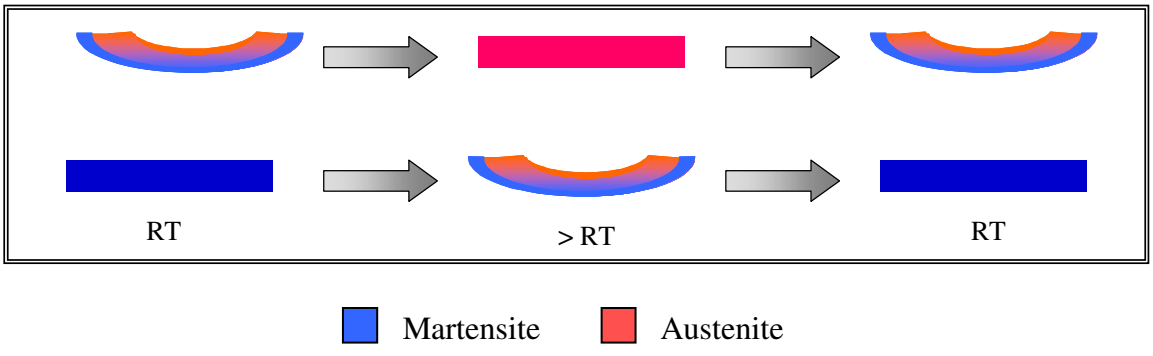

Fig. 4.2: Model for the gradual change of the properties and possible precise tailoring, for a two-dimensional bimorph Ni-Ti structure, resulting in a defined layering of austenite and martensite.

Two different possible situations are shown in Fig. 4.2:

1) deposition of a film with half of its thickness with a near equiatomic composition and the other half Ni-rich. At RT, half of its thickness will exhibit the martensite phase and the other half the austenite phase (Fig. 4.2 – top situation);

2) deposition of a film with half of its thickness with a Ti-rich composition and the other half near equiatomic. At RT, the film will be martensitic and a little above RT, the Ti-rich fraction will be still martensitic (Fig. 4.2 – bottom situation).

Due to the different mechanical properties of martensite and austenite phases a curvature should thus be observed (due to a constraint). This would simplify the fabrication of microactuation devices using SMA films, maximizing actuation strain and enhancing reliability. However, for the successful development of this type of films, it is important to characterize, model and control the variations in composition, crystalline structure and transformation temperatures.

The deposition of Ni-Ti graded films and respective *in-situ* and *ex-situ* characterization performed in this work allowed not only to obtain essential information concerning the structural development of the films but also the production of Ni-Ti films exhibiting phase transformations was achieved. The temperature dependence results of the ER for cooling and heating have detected variations of the resistivity values associated with the B2, R-phase and B19' phases transformations. It is usually mentioned that the intermediate transformation to the R-phase can be observed if the Ni-Ti alloy is subject to specific processing conditions like: variation of Ni content, introduction of a third element, thermal annealing, thermal cycling or cold working. However, the R-phase transformation has been already observed in Ti-rich Ni-Ti films fabricated by sputtering, possessing Ti_2Ni precipitates with a specific orientation relationship with the Ni-Ti matrix and strong strain fields around them [164]. Nam *et al.* [32] also reported for Ti-rich Ni-Ti alloy ribbons, made by melt spinning, the presence of Ti_2Ni particles with an orientation relationship to the B2 phase and coherency strains around them, which was thought to play an important role to induce the R-phase transformation. In view of these results, for the present samples a correlation is predicted between the Ti_2Ni precipitates and the R-phase transformation.

The ER results obtained for the graded film deposited on naturally oxidized Si(100) substrate presented in Fig. 3.71 also shows the very low hysteresis associated with the R-phase transformation. This is an advantage for microactuators applications. XRD, SEM

observations and temperature dependence results of the ER proved the presence of martensite at RT for the Ni-Ti graded film grown on a TiN buffer layer with thickness ≈ 215 nm. For several applications (like in microsystems), it is desirable to have the transformations temperatures above RT, as observed in this case.

For the NiTiHf films grown on a HfN buffer layer, the higher transformation temperatures of the NiTiHf SMAs, when compared to what was previously observed for Ni-Ti films, have been confirmed by XRD (Fig. 3.82). It has been successfully obtained films with R_s above 162°C. Nevertheless, it should be taken in consideration that there is an increased lattice distortion with the addition of Hf. This is related to the atomic size difference between Hf and Ti. In NiTiHf SMA, Ti is substituted by Hf. The atomic radius of Hf is 0.216 nm, which is slightly larger than that of Ti with 0.200 nm. This might lead to larger internal stresses being built up during the transformation. However, the preliminary results obtained in the present study on the deposition of NiTiHf films have shown good perspectives for future investigation of new SMAs ternary systems.

Chapter 5

Conclusions and Future Works

5. CONCLUSIONS AND FUTURE WORKS

5.1. CONCLUSIONS

The technological importance of films has led to an unabated interest in the detailed characterization of their structure, morphology and their interfaces. A better understanding of the underlying growth mechanisms and their microstructural development requires sophisticated *in-situ* techniques. XRD is such a well-established and powerful technique as demonstrated in this thesis work for the study of Ni-Ti SMA films. Numerous examples of investigations on Ni-Ti films can be found in the literature but it has been also reported that the deposition of Ni-Ti films with definite stoichiometry and high purity remains a challenge, and important issues like formation of film texture and its control are still unresolved.

The first experiments performed worldwide concerning *in-situ* X-ray investigations of the microstructural development during Ni-Ti film growth have been presented. The magnetron-sputtering chamber installed at ROBL proves to be a very efficient instrument to follow *in situ*, the evolution of the structure of the Ni-Ti growing film. The experimental procedure adopted leads to a controlled manipulation of the composition and preferential orientation of the film. It has been found that the type of substrate plays an important role for the preferential orientation of sputtered Ni-Ti films:

- an amorphous SiO_2 buffer layer induces the development of the (100) orientation of the B2 phase during deposition on heated substrates ($\approx$ 470ºC);

- a TiN buffer layer allows a control of the crystallographic orientations of Ni-Ti films and acts as an efficient diffusion barrier. Ni-Ti films mainly containing grains with (100), or (110), or (211) planes of the B2 phase parallel to the film surface could be produced using TiN buffer layers.

The preferential orientation of the sputtered Ni-Ti films is also influenced by the application of a substrate bias voltage. In this work, it has been revealed that the control of the energy of the bombarding ions could be used as a tool for the manipulation of the transformation temperatures. Furthermore, films exhibiting SME above RT have been produced.

The present thesis work as well allowed the identification of different phenomena on the growth of graded Ni-Ti films leading to the optimisation of the deposition parameters for

future fabrication of films with a combination of superelasticity and shape memory characteristics.

The sputtering equipment installed at ROBL is also a very efficient instrument to deposit, and simultaneously follow *in situ* the evolution of the structure of ternary alloys like, NiTiHf films:

- a preferential growth of <110> oriented grains of the B2 phase from the beginning of the deposition could be obtained using a HfN buffer layer;
- the increasing amount of Hf incorporated in NiTiHf films shifts the B2(110) peak towards lower 2θ (higher d-spacings) and decreases its intensity;
- the higher transformation temperatures of the NiTiHf SMA, when compared to what was previously observed for Ni-Ti films, have been confirmed by XRD.

5.2. FUTURE WORKS

Based on our experiences with the successful versatility of sputter deposition chambers with two magnetrons and in view of the potential of combining the deposition with energetic ion bombardment for growth assistance or amorphization, an additional ion gun (IQ 100 [175]) has been commissioned (during the final period of this PhD thesis work) to allow post-deposition ion irradiation or ion bombardment during sputter deposition (Fig. 5.1). The ion gun operating under a fixed incidence angle of 20° to the substrate normal can deliver energetic ions of ≤ 6 keV and up to 10 μA current. It has a sub-mm focus and a maximum scanning field of $10 \times 10\ \text{mm}^2$. Separate differential pumping allows its operation independent from the working pressure for magnetron sputtering, characteristically in the range from 0.1 to 1 Pa. The first experiments with *in-situ* XRD observation of film growth and post-deposition surface modification have been performed for the study of a Ni-Ti sample.

Following the first experiments described in this thesis on the *in-situ* analysis of the sputtering of Ni-Ti films and the preliminary results obtained on the *in-situ* study of the energetic ion bombardment of this type of SMA films, it is suggested that future experiments should be dedicated to study changes of film properties by energetic ion irradiation *during* deposition. Energy and flux of the ions delivered by the gun can be varied independently of the ions and atoms from the magnetron targets.

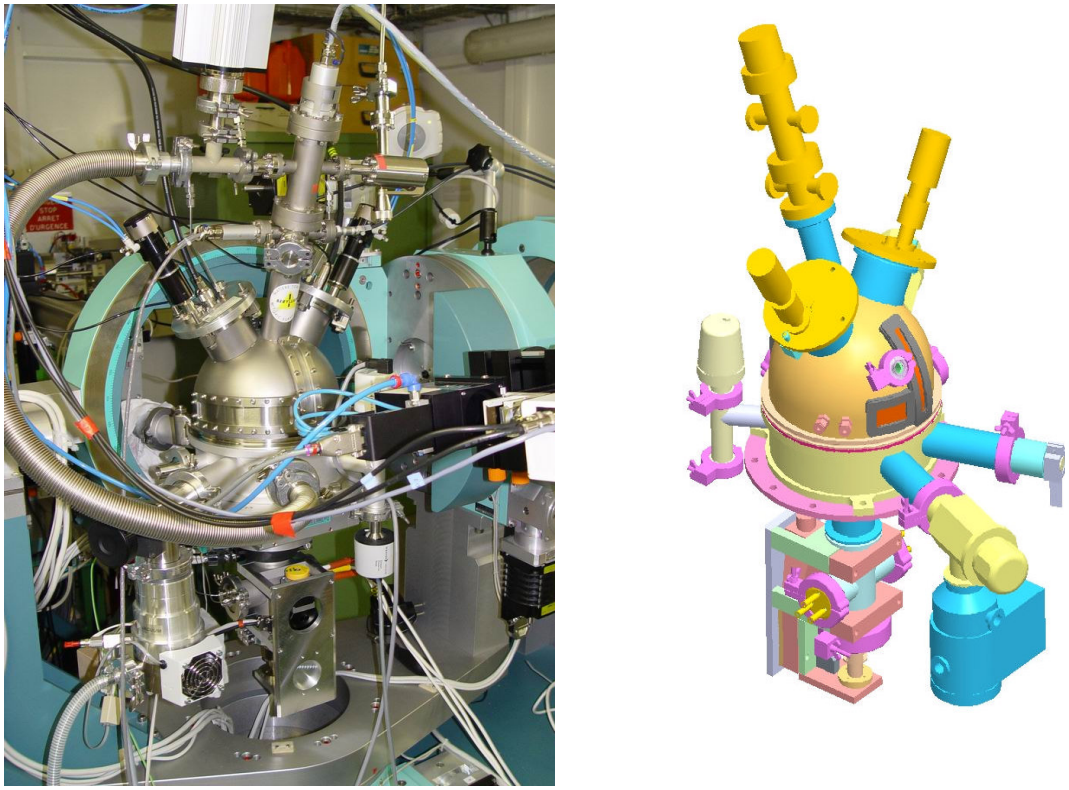

Fig. 5.1: Sputter deposition chamber inserted into the six-circles HUBER goniometer of ROBL viewed from the detector side with the ion gun (gas supply connected) and the two magnetrons on top (left); design study from the beam entrance side (right) with symmetric magnetrons, ion gun, viewport between Be entrance windows, one turbo pump (70 l/s) at a corner valve which can be used for throttling and substrate alignment [156].

Bellow first results obtained for the study of a Ni-Ti sample using the processing parameters given in Tab. 5.1 give an idea of the potential of this equipment.

Ions →	He
Energy →	5 keV
Incident angle →	20°
Scanning field →	6 x 6 mm^2
Ion current →	6 µA
Current density →	≈ 20 µA/cm^2
Ion flux →	≈ 1.2×10^{14} He/cm^2s

Tab. 5.1: Process conditions for the *in-situ* ion bombardment (using an ion gun) of a near equiatomic Ni-Ti film deposited on a TiN buffer layer in the new sputtering chamber at ROBL.

A Ni-Ti film with a preferential growth of <110> oriented grains of the Ni-Ti B2 phase from the beginning of the deposition was deposited (at ≈ 470°C) on a TiN film with a topmost layer formed mainly by <111> oriented grains (Fig. 5.2). The Ni-Ti film was then

irradiated (at ≈ 180°C) with He ions (*without exposing the film to the atmosphere*, i.e. reduced surface oxide formation) thus modifying deliberately the film's microstructure locally. The integrated B2(110) Bragg peak area decreases during He ion irradiation due to the film thickness reduction by material ablation (Fig. 5.3). By Bragg-Brentano geometry no other peaks of the B2 phases were detected after the ion bombarding. The increase in temperature from 180°C to 470°C did not result in detectable changes in the B2 peak intensities (Fig. 5.4). The *ex-situ* characterization techniques confirmed the reduction of the film thickness on the irradiated area. From RBS simulations a reduction of approximately 50% is calculated (Fig. 5.5).

In the future it is aimed to achieve a *two-way* SME without the need of a complex device design. A localized amorphization by ion irradiation presents some advantages in this respect. With this method certain areas of the film could be modified (in order not to exhibit the SME). Its elastic response acts as a pullback spring during cooling process, when easily deformable martensite forms.

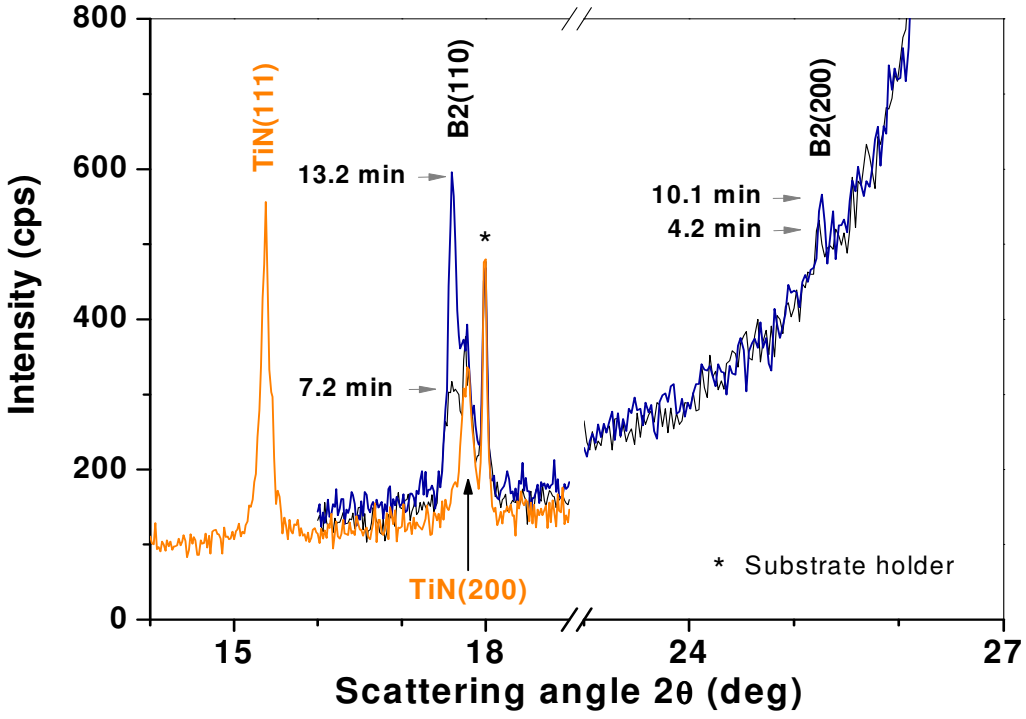

Fig. 5.2: Bragg-Brentano X-ray diffractograms obtained *in situ* during the deposition of the Ni-Ti film on a TiN buffer layer (total deposition time = 17.5 min) at ≈ 470°C.

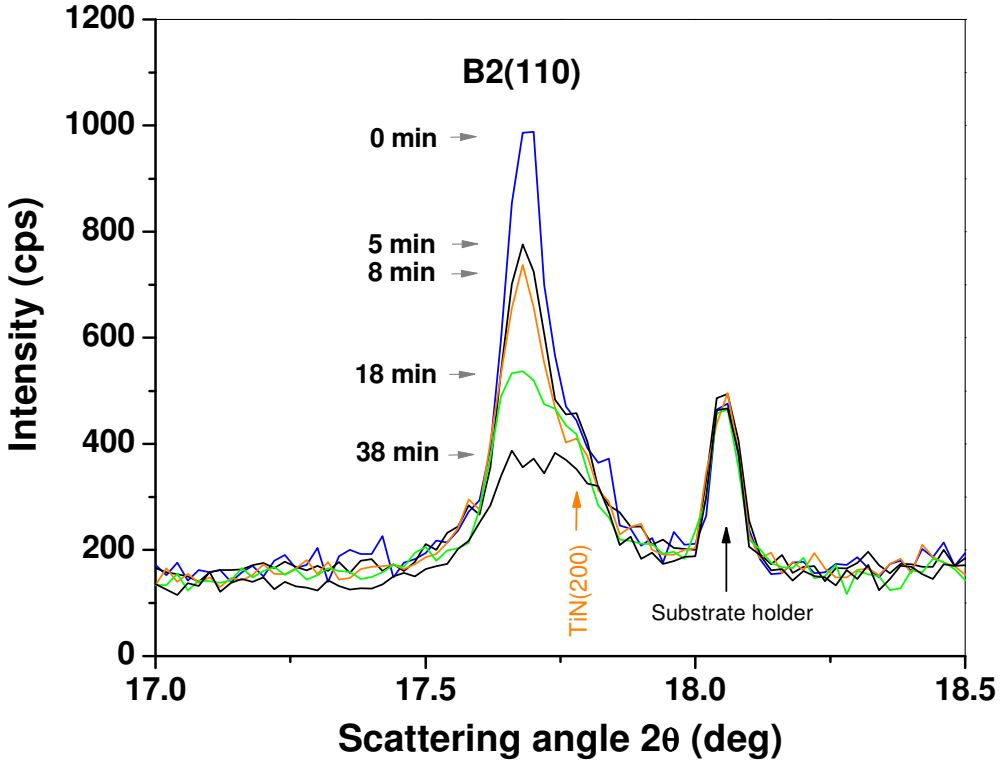

Fig. 5.3: XRD scans in Bragg-Brentano geometry around the dominating B2(110) peak after the consecutive bombardment with He ions (substrate T ≈ 180°C).

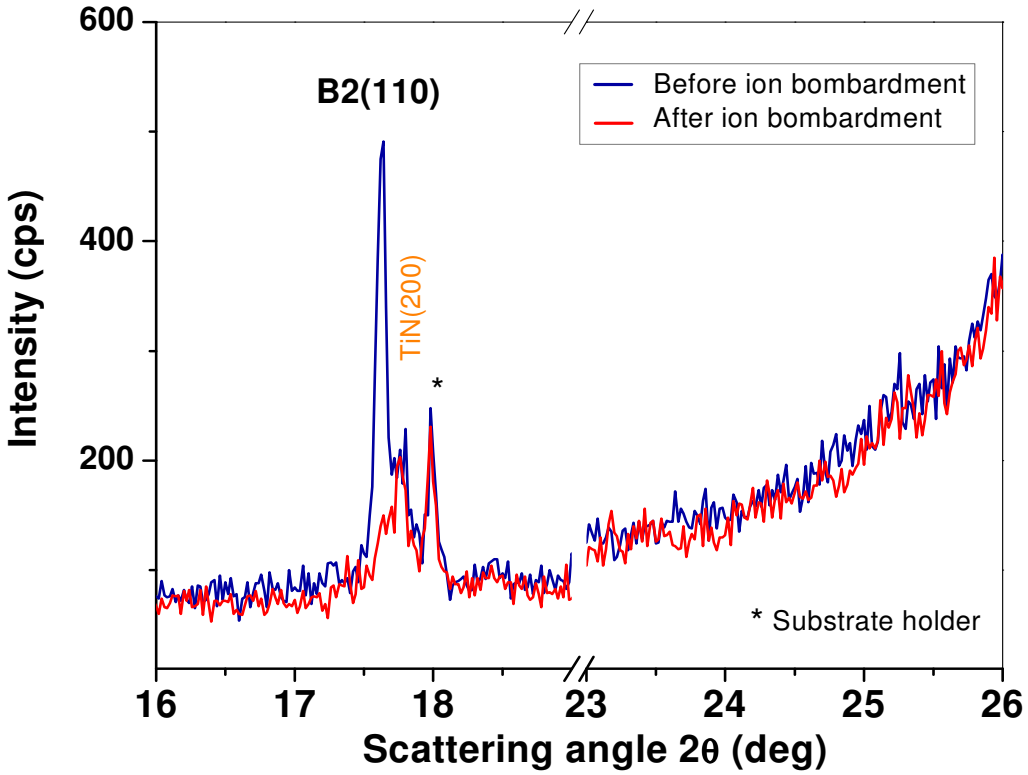

Fig. 5.4: XRD spectra obtained *in situ* at ≈ 470°C before and after the energetic ion bombardment of the Ni-Ti sample.

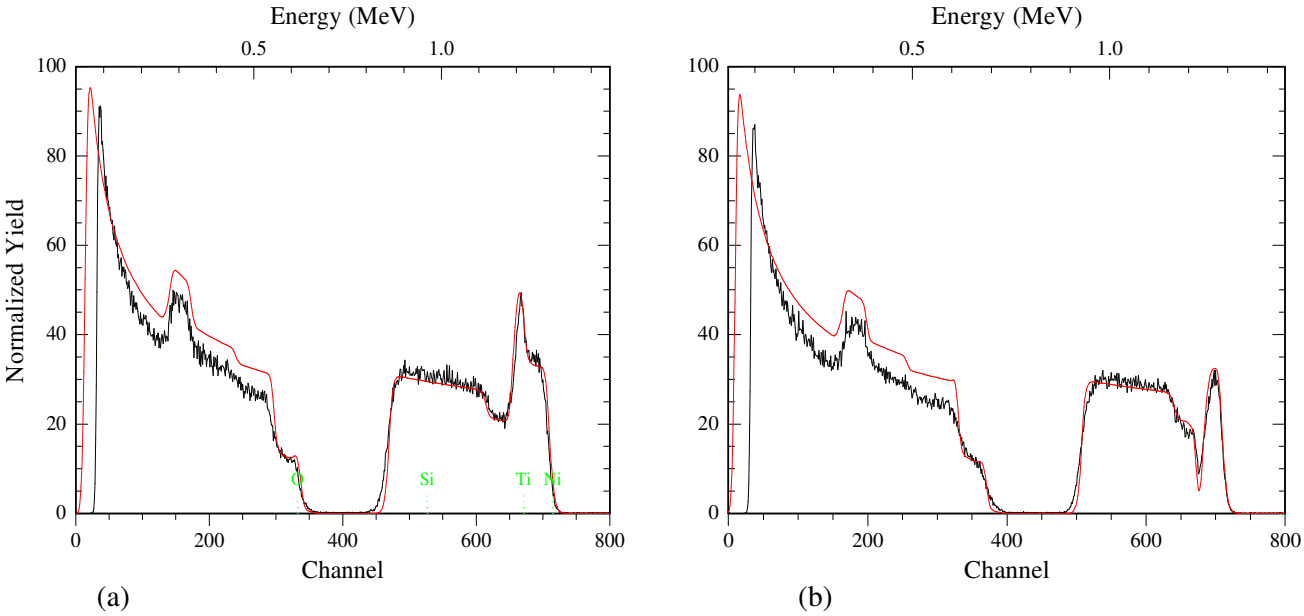

RUMP-Simulation:

Layer	Film	Composition		Thickness (in at/cm^2 or nm)	
1	TiO_2	Ti 0.33	O 0.67	0.50×10^{16} at/cm^2	5.2 nm
2	NiTi	Ni 0.5	Ti 0.5		**100 nm**
3	TiN	Ti 0.5	N 0.5	242×10^{16} at/cm^2	**240** nm

RUMP-Simulation:

Layer	Film	Composition		Thickness (in at/cm^2 or A)	
1	TiO_2	Ti 0.33	O 0.67	0.70×10^{16} at/cm^2	7.3 nm
2	NiTi	Ni 0.5	Ti 0.5		**50** nm
3	TiN	Ti 0.5	N 0.5	220×10^{16} at/cm^2	**218** nm

The RUMP-Simulation includes also the SiO_2 (140 nm) / Si substrate.

Fig. 5.5: RBS analysis; (a) before ion bombardment, (b) after 38 min ion bombardment.

References

REFERENCES

[1] K. Otsuka, T. Kakeshita, *Science and Technology of Shape-Memory Alloys: New Developments*, MRS Bull. **27** (2002) 91-100.

[2] S. Miyazaki, S. Kimura, K. Otsuka, *Shape Memory Effect and Pseudoelasticity associated with the R-phase transition in Ti-50.5 at-percent-Ni single crystals*, Phil. Mag. A **57** (1988) 467-478.

[3] T. Goryczka, H. Morawiec, *Structure studies of the R-phase using X-ray diffraction methods*, J. Alloys Compd. **367** (2004) 137-141.

[4] D. Shindo, Y. Murakami, T. Ohba, *Understanding precursor phenomena for the R-phase transformation in Ti-Ni-based alloys*, MRS Bull. **27** (2002) 121-127.

[5] J. Khalil-Allafi, W.W. Schmahl, D.M. Toebbens, *Space group and crystal structure of the R-phase in binary NiTi shape memory alloys*, Acta Mater. **54** (2006) 3171-3175.

[6] H. Sitepu, W.W. Schmahl, D.M. Toebbens, *Use of synchrotron diffraction data for describing crystal structure and crystallographic phase analysis of R-phase NiTi shape memory alloy*, Textures and Microstructures **35** (2003) 185-195.

[7] C. Gong, Y. Li, Y. Wang, D. Yang, *Ab initio study for electronic and crystal structure of NiTi R-phase*, Modelling Simul. Mater. Sci. Eng. **14** (2006) 33-39.

[8] P. Šittner, M. Landa, P. Lukáš, V. Novák, *R-phase transformation phenomena in thermomechanically loaded NiTi polycrystals*, Mech. Mater. **38** (2006) 475-492.

[9] A. Ishida, V. Martynov, *Sputter-deposited Shape-Memory Alloy thin films: properties and applications*, MRS Bull. **27** (2002) 111-114.

[10] Y. Fu, H. Du, W. Huang, S. Zhang, M. Hu, *TiNi-based thin films in MEMS applications: a review*, Sens. Actuators A **112** (2004) 395-408.

[11] M. Nishida, C.M. Wayman, T. Honma, *Precipitation processes in near-equiatomic TiNi Shape Memory Alloys*, Metall. Trans. **17A** (1986) 1505-1515.

[12] M. Nishida, C.M. Wayman, *Phase transformations in Ti_2Ni_3 precipitates formed in aged Ti-52 at. pct Ni*, Metall. Trans. **18A** (1987) 785-799.

[13] T. Hara, T. Ohba, K. Otsuka, M. Nishida, *Phase transformation and crystal structures of Ti_2Ni_3 precipitates in Ti-Ni alloys*, Mater. Trans. **38** (1997) 277-284.

[14] K. Otsuka, X. Ren, *Martensitic transformations in nonferrous shape memory alloys*, Mater. Sci. Eng. A **273-275** (1999) 89-105.

[15] Y. Kudoh, M. Tokonami, S. Miyazaki, K. Otsuka, *Crystal-structure of the martensite in Ti-49.2 at-Percent-Ni alloy analyzed by single-crystal X-ray diffraction method*, Acta Metall. **33** (1985) 2049-2056.

[16] K. Otsuka, X. Ren, *Physical metallurgy of Ti-Ni-based shape memory alloys*, Prog. Mater. Sci. **50** (2005) 511-678.

[17] D. Wan, K. Komvopoulos, *Thickness effect on thermally induced phase transformations in sputtered titanium-nickel shape-memory films*, J. Mater. Res. **20** (2005) 1606-1612.

[18] W. Tang, *Thermodynamic study of the low-temperature phase B19' and the martensitic transformation in near-equiatomic Ti-Ni Shape Memory Alloys*, Metall. Mater. Trans. **28A** (1997) 537-544.

[19] J. Uchil, K.P. Mohanchandra, K.K. Mahesh, K. Ganesh Kumara, *Thermal and electrical characterization of R-phase dependence on heat-treat temperature in Nitinol*, Physica B **253** (1998) 83-89.

[20] W.J. Buehler, J.V. Gilfrich, R.C. Wiley, *Effect of low-temperature phase changes on the mechanical properties of alloys near composition TiNi*, J. Appl. Phys. **34** (1963) 1475-1477.

[21] Y.Q. Fu, H.J. Du, *Effects of film composition and annealing on residual stress evolution for shape memory TiNi film*, Mater. Sci. Eng. A **342** (2003) 236-244.

[22] J.J. Gill, D.T. Chang, L.A. Momoda, G.P. Carman, *Manufacturing issues of thin film NiTi microwrapper*, Sens. Actuators **93** (2001) 148-156.

[23] S. Miyazaki, A. Ishida, *Martensitic transformation and shape memory behavior in sputter-deposited TiNi-base thin films*, Mater. Sci. Eng. A **273-275** (1999) 106-133.

[24] A. Gyobu, Y. Kawamura, T. Saburi, M. Asai, *Two-way shape memory effect of sputter-deposited Ti-rich Ti-Ni alloy films*, Mater. Sci. Eng. A **312** (2001) 227-231.

[25] R.M.S. Martins, *Produção e caracterização de películas finas de Ni-Ti*, Master Thesis, New University of Lisbon (2004).

[26] R.M.S. Martins, F.M.B. Fernandes, R.J.C. Silva, L. Pereira, P.R. Gordo, M.J.P. Maneira, M. Beckers, A. Mücklich, N. Schell, *The influence of a poly-Si intermediate layer on the crystallization behaviour of Ni-Ti SMA magnetron sputtered thin films*, Appl. Phys. A **83** (2006) 139-145.

[27] R.M.S. Martins, F.M.B. Fernandes, R.J.C. Silva, M. Beckers, N. Schell, *Structural in-situ studies of Ni-Ti thin films* in: Proceedings of Shape Memory and Superelastic Technologies 2004 - October 2004, Baden Baden, Germany, edited by T.W. Duerig and A.R. Pelton (ASM International, 2006), pp. 421-426.

[28] R.H. Wolf, A.H. Heuer, *TiNi (Shape Memory) films on silicon for MEMS applications*, J. Microelectromech. Syst. **4** (1995) 206-212.

[29] P. Krulevitch, A.P. Lee, P.B. Ramsey, J.C. Trevino, J. Hamilton, M.A. Northrup, *Thin film shape memory alloy microactuators*, J. Microelectromech. Syst. **5** (1996) 270-282.

[30] H. Kahn, M.A. Huff, A.H. Heuer, *The TiNi shape-memory alloy and its applications for MEMS*, J. Micromech. Microeng. **8** (1998) 213-221.

[31] M. Bendahan, K. Aguir, J.L. Seguin, H. Carchano, *NiTi thin films as a gate of MOS capacity sensors*, Sens. Actuators **74** (1999) 242-245.

[32] T.-H. Nam, J.-H. Kim, M.-S. Choi, H.-W. Lee, Y.-W. Kim, *Phase transformation behavior in Ti-Ni alloy ribbons fabricated by melt spinning*, J. Phys. IV **112** (2003) 893-896.

[33] H. Xing, H.Y. Kim, S. Miyazaki, *Microstructures of Ti-48%Ni shape memory melt-spun ribbons*, Trans. Nonferrous Met. Soc. China **16** (2006) s92-s95.

[34] A. Rockett, *Lecture notes; "Sputter deposition of thin films"*, University of Illinois, U.S.A., 1998.

[35] M.A. Lieberman and A.J. Lichtenberg, *Principles of Plasma Discharges and Materials Processing* (Wiley, New York, 1994), pp. 450-470.

[36] S.I. Shah in: *Handbook of Thin Film Process Technology*, edited by D.A. Glocker and S.I. Shah (IOP, Philadelphia, 1995) Chap. 3, pp. 3.0:1-3.0:18.

[37] AJA International, P.O. Box 246, 809 Country Way, North Scituate, MA 02060, http://ajaint.com

[38] J.H. Brophy in: *The Structure and Properties of Materials*, Vol. 2. *Thermodynamics of Structure*, edited by J.H. Brophy, R.M. Rose, and J. Wulff (Wiley, New York, 1964), pp. 82.

[39] B.A. Movchan, A.V. Demchishin, *Study of the structure and properties of thick vacuum consensates of nickel, titanium, tungsten, aluminium oxide and zirconium dioxide*, Phys. Met. Metallogr. **28** (1969) 83-90.

[40] J.A. Thornton, *Influence of apparatus geometry and deposition conditions on structure and topography of thick sputtered coatings,* J. Vac. Sci. Tecnol. **11** (1974) 666-670.

[41] P.B. Barna, and M. Adamik, *Fundamental structure forming phenomena of polycrystalline films and the structure zone models*, Thin Solid Films **317** (1998) 27-33.

[42] C.V. Thompson, *Structure Evolution During Processing of Polycrystalline Films*, Annu. Rev. Mater. Sci. **30** (2000) 159-190.

[43] Handbook of Hard Coatings: *Deposition Technologies, Properties and Applications*, edited by Rointan F. Bunshah, University of California Los Angeles UCLA, Los Angeles, California, Noyes Publications, Park Ridge, New Jersey, U.S.A., William Andrew Publishing, LLC, Norwich, New York, U.S.A.

[44] J.M. Nieuwenhuizen and H.B. Haanstra, *Microfractography of thin films*, Philips Tech. Rev. **27** (1966) 87-91.

[45] L. Dong, R.W. Smith, D.J. Srolovitz, *A two-dimensional molecular dynamics simulation of thin film growth by oblique deposition*, J. Appl. Phys. **80** (1996) 5682-5690.

[46] J.A. Thornton, *The microstructure of sputter-deposited coatings*, J. Vac. Sci. Technol. A **4** (1986) 3059-3065.

[47] A. Cavaleiro, M.T. Vieira, *Textos de apoio à disciplina de Engenharia de Superfícies* (1995), Universidade de Coimbra.

[48] K.P. Almtoft, J. Bøttiger, J. Chevallier, N. Schell, R.M.S. Martins, *Influence of the substrate bias on the size and thermal stability of grains in magnetron-sputtered nanocrystalline Ag films*, J. Mater. Res. **20** (2005) 1071-1080.

[49] http://en.wikipedia.org/wiki/Stress_(physics)

[50] M. Ohring, "Materials Science of Thin Films, *Deposition and Structure*, 2nd Edition" Academic Press San Diego (2002).

[51] K. Otsuka, C.M. Wayman, *Shape Memory Materials*, Cambridge University Press, (1998).

[52] Y. Okada, Y. Tokumaru, *Precise determination of lattice parameter and thermal expansion coefficient of silicon between 300 and 1500 K*, J. Appl. Phys. **56** (1984) 314-320.

[53] R.W. Hoffman in: *Phys. Thin Films*, edited by G. Hassand and R.E. Thun (Academic Press, New York, 1966), Vol. 3, pp. 211-273.

[54] C.A. Davis, *A simple model for the formation of compressive stress in thin films by ion bombardment*, Thin Solid Films **226** (1993) 30-34.

[55] A.K. Malhotra, J.F. Whitacre, Z.B. Zhao, J. Hershberger, S.M. Yalisove, J.C. Bilello, *An in situ/ex situ X-ray analysis system for thin sputtered films*, Surf. Coat. Technol. **110** (1998) 105-110.

[56] S.L. Lee, D. Windover, T.-M. Lu, M. Audino, *In situ phase evolution study in magnetron sputtered tantalum thin films*, Thin Solid Films **420-421** (2002) 287-294.

[57] J.H. Je, D.Y. Noh, H.K. Kim, K.S. Liang, *Preferred orientation of TiN films studied by a real time synchrotron x-ray scattering*, J. Appl. Phys. **81** (1997) 6126-6133.

[58] W. Matz, N. Schell, W. Neumann, J. Bøttiger, J. Chevallier, *A two magnetron sputter deposition chamber for in situ observation of thin film growth by synchrotron radiation scattering*, Rev. Sci. Instrum. **72** (2001) 3344-3348.

[59] M. Beckers, N. Schell, R.M.S. Martins, A. Mücklich, W. Möller, *In-situ x-ray diffraction studies concerning the influence of Al concentration on the texture development during sputter deposition of Ti-Al-N thin films*, J. Vac. Sci. Technol. A **23** (2005) 1384-1391.

[60] M. Beckers, N. Schell, R.M.S. Martins, A. Mücklich, W. Möller, *The influence of the growth rate on the preferred orientation of magnetron sputtered Ti-Al-N thin films studied by in-situ x-ray diffraction*, J. Appl. Phys. **98** (2005) 44901-1-44901-7.

[61] N. Schell, W. Matz, J. Bøttiger, J. Chevallier, P. Kringhøj, *Development of texture in TiN films by use of in situ synchrotron x-ray scattering*, J. Appl. Phys. **91** (2002) 2037-2044.

[62] K. Hasegawa, Y. Nakamura, T. Izumi, Y. Shiohara, *Comparative study on texture development of MgO and YSZ films grown by inclined substrate deposition technique*, Physica C **378-381** (2002) 955-959.

[63] C.V. Falub, A. Karimi, M. Ante, W. Kalss, *Interdependence between stress and texture in arc evaporated Ti-Al-N thin films*, Surf. Coat. Technol. **201** (2007) 5891-5898.

[64] H.-U. Krebs, M. Weisheit, J. Faupel, E. Süske, T. Scharf, C. Fuhse, M. Störmer, K. Sturm, M. Seibt, H. Kijewski, D. Nelke, E. Panchenko, M. Buback, *Pulsed laser deposition (PLD) – a versatile thin film technique*, Advances in Solid State Physics **43** (2003) 101-107.

[65] F. Ying, R.W. Smith, D.J. Srolovitz, *The mechanism of texture formation during film growth: The roles of preferential sputtering and shadowing*, Appl. Phys. Lett. **69** (1996) 3007-3009.

[66] A. van der Drift, *Evolutionary selection, a principle governing growth orientation in vapour-deposited layers*, Philips Res. Repts **22** (1967) 267-268.

[67] J.-M. Zhang, F. Ma, K.-W. Xu, *Calculation of the surface energy of FCC metals with modified embedded-atom method*, Appl. Surf. Sci. **229** (2004) 34-42.

[68] J.-M. Zhang, F. Ma, K.-W. Xu, *Calculation of the surface energy of bcc metals by using the modified embedded-atom method*, Surf. Interface Anal. **35** (2003) 662-666.

[69] J.-E. Sundgren, *Structure and properties of TiN coatings*, Thin Solid Films **128** (1985) 21-44.

[70] J. Pelleg, L.Z. Zevin, S. Lungo, N. Croitoru, *Reactive-sputter-deposited TiN films on glass substrates*, Thin Solid Films **197** (1991) 117-128.

[71] Y.M. Chen, G.P. Yu, J.H. Huang, *Characterizing the effects of multiprocess parameters on the preferred orientation of TiN coating using a combined index*, Vacuum **66**, (2002) 19-25.

[72] Y.H. Cheng, B.K. Tay, S.P. Lau, *Substrate bias dependence of the structure and internal stress of TiN films deposited by the filtered cathodic vacuum arc*, J. Vac. Sci. Technol. A **20** (2002) 1327-1331.

[73] J.S. Chun, I. Petrov, J.E. Greene, *Dense fully 111-textured TiN diffusion barriers: Enhanced lifetime through microstructure control during layer growth*, J. Appl. Phys. **86** (1999) 3633-3641.

[74] J.E. Greene, J.E. Sundgren, L. Hultman, I. Petrov, D.B. Bergstrom, *Development of preferred orientation in polycrystalline TiN layers grown by ultrahigh-vaccum reactive magnetron sputtering*, Appl. Phys. Lett. **67** (1995) 2928-2930.

[75] L. Hultman, J.E. Sundgren, J.E. Greene, D.B. Bergstrom, I. Petrov, *High-flux low-energy (≈20 eV) N_2^+ ion irradiation during TiN deposition by reactive magnetron sputtering: Effects on microstructure and preferred orientation*, J. Appl. Phys. **78** (1995) 5395-5403.

[76] U.C. Oh, J.H. Je, *Effects of strain energy on the preferred orientation of TiN thin films*, J. Appl. Phys. **74** (1993) 1692-1696.

[77] U.C. Oh, J.H. Je, J.Y. Lee, *Two critical thicknesses in the preferred orientation of TiN thin film*, J. Mater. Res. **13** (1998) 1225-1229.

[78] P. Patsalas, C. Charitidis, S. Logothetidis, *The effect of substrate temperature and biasing on the mechanical properties and structure of sputtered titanium nitride thin films*, Surf. Coat. Technol. **125** (2000) 335-340.

[79] T.Q. Li, S. Noda, Y. Tsuji, T. Ohsawa, H. Komiyama, *Initial growth and texture formation during reactive magnetron sputtering of TiN on Si(111)*, J. Vac. Sci. Technol. A **20** (2002) 583-588.

[80] J.H. Je, D.Y. Noh, H.K. Kim, K.S. Liang, *Preferred orientation of TiN films studied by a real time synchrotron x-ray scattering*, J. Appl. Phys. **81** (1997) 6126-6133.

[81] R. Banerjee, R. Chandra, P. Ayyub, *Influence of the sputtering gas on the preferred orientation of nanocrystalline titanium nitride thin films*, Thin Solid Films **405** (2002) 64-72.

[82] Y. Kajikawa, S. Noda, H. Komiyama, *Comprehensive perspective on the mechanism of preferred orientation in reactive-sputter-deposited nitrides*, J. Vac. Sci. Technol. A **21** (2003) 1943-1954.

[83] W.J. Meng, G.L. Eesley, *Growth and mechanical anisotropy of TiN thin films*, Thin Solid Films **271** (1995) 108-116.

[84] J.O. Kim, J.D. Achenbach, P.B. Mirkarimi, M. Shinn, S.A. Barnett, *Elastic constants of single-crystal transition-metal nitride films measured by line-focus acoustic microscopy*, J. Appl. Phys. **72** (1992) 1805-1811.

[85] N. Schell, W. Matz, J. Bøttiger, J. Chevallier, P. Kringhoj, *Development of texture in TiN films by use of in situ synchrotron x-ray scattering*, J. Appl. Phys**. 91** (2002) 2037-2044.

[86] D. Gall, S. Kodambaka, M.A. Wall, I. Petrov, J.E. Greene, *Pathways of atomistic processes on TiN(001) and (111) surfaces during film growth: an ab initio study*, J. Appl. Phys. **93** (2003) 9086-9094.

[87] C.-S. Shin, D. Gall, Y.-W. Kim, N. Hellgren, I. Petrov, J.E. Greene, *Development of preferred orientation in polycrystalline NaCl-structure δ-TaN layers grown by reactive magnetron sputtering: Role of low-energy ion surface interactions*, J. Appl. Phys. **92** (2002) 5084-5093.

[88] S. Kodambaka, V. Petrova, A. Vailionis, P. Desjardins, D.G. Cahill, I. Petrov, J.E. Greene, *TiN(001) and TiN(111) island coarsening kinetics: in-situ scanning tunneling microscopy studies*, Thin Solid Films **392** (2001) 164-168.

[89] U. Wahlström, L. Hultman, J.-E. Sundgren, F. Adibi, I. Petrov, J.E. Greene, *Crystal-growth and microstructure of polycrystalline $Ti_{1-x}Al_xN$ alloy-films deposited by ultra-high-vaccum dual-target magnetron sputtering*, Thin Solid Films **235** (1993) 62-70.

[90] N. Grandjean, J. Massies, P. Vennéguès, M. Leroux, F. Demangeot, M. Renucci, J. Frandon, *Molecular-beam epitaxy of gallium nitride on (0001) sapphire substrates using ammonia*, J. Appl. Phys. **83** (1998) 1379-1383.

[91] C.-H. Lee, S.-Y. Tseng, *In situ fixed-angle X-ray reflectivity measurement of thin film roughness and thickness during deposition*, J. Appl. Cryst. **31** (1998) 181-184.

[92] J. Bøttiger, J. Chevallier, J. H. Petersen, N. Schell, W. Matz, A. Mücklich, *Observation of the growth mode of TiN during magnetron sputtering using synchrotron radiation*, J. Appl. Phys. **91** (2002) 5429-5433.

[93] M. Beckers, N. Schell, R.M.S. Martins, A. Mücklich, W. Möller, L. Hultman, *Microstructure and nonbasal-plane growth of epitaxial Ti_2AlN thin films*, J. Appl. Phys. **99** (2006) 34902-1-34902-8.

[94] J.A. Walker, K.J. Gabriel, M. Mehregany, *Thin-film processing of TiNi shape memory alloy*, Sens. Actuators A**21**-A**23** (1990) 243-246.

[95] J.D. Busch, A.D. Johnson, C.H. Lee, D.A. Stevenson, *Shape-memory properties in Ni-Ti sputter-deposited film*, J. Appl. Phys. **68** (1990) 6224-6228.

[96] K.R.C. Gisser, J.D. Busch, A.D. Johnson, A.B. Ellis, *Oriented nickel-titanium shape memory alloy films prepared by annealing during deposition*, Appl. Phys. Lett. **61** (1992) 1632-1634.

[97] A.P. Jardine, H. Zhang, L.D. Wasielesky, *Investigation into the thin-film fabrication of intermetallic NiTi*, Mat. Res. Soc. Symp. Proc. **187** (1990) 181-186.

[98] A.P. Jardine, J.S. Madsen, P.G. Mercado, *Characterization of the deposition and materials parameters of thin-film TiNi for microactuators and smart materials*, Mater. Charact. **32** (1994) 169-178.

[99] J.S. Madsen, A.P. Jardine, *Lowering the crystallization temperature of thin-film shape memory effect TiNi by cold-working for smart materials fabrication*, Scripta. Metall. Mater. **30** (1994) 1189-1194.

[100] K.K. Ho, K.P. Mohanchandra, G.P. Carman, *Examination of the sputtering profile of NiTi under target heating conditions*, Thin Solid Films **413** (2002) 1-7.

[101] C.-L. Shih, B.-K. Lai, H. Kahn, S.M. Phillips, A.H. Heuer, *A robust co-sputtering fabrication procedure for TiNi shape memory alloys for MEMS*, J. MEMS **10** (2001) 69-79.

[102] A. Ohta, S. Bhansali, I. Kishimoto, A. Umeda, *Novel fabrication technique of TiNi shape memory alloy film using separate Ti and Ni targets*, Sens. Actuators A **86** (2000) 165-170.

[103] S. Sanjabi, Y.Z. Cao, S.K. Sadrnezhaad, Z.H. Barber, *Binary and ternary NiTi-based shape memory films deposited by simultaneous sputter deposition from elemental targets*, J. Vac. Sci. Technol. A **23** (2005) 1425-1429.

[104] K.K. Ho, G.P. Carman, *Sputter deposition of NiTi thin film shape-memory alloy using a heated target*, Thin Solid Films **370** (2000) 18-29.

[105] J.-M. Ting, P. Chen, *Dependence of compositions and crystallization behaviors of dc-sputtered TiNi thin films on the deposition conditions*, J. Vac. Sci. Technol. A **19** (2001) 2382-2387.

[106] H.-J. Lee, H. Ni, D.T. Wu, A.G. Ramirez, *Experimental determination of kinetic parameters for crystallizing amorphous NiTi thin films*, Appl. Phys. Lett. **87** (2005) 114102-1- 114102-3.

[107] H.-J. Lee, H. Ni, D.T. Wu, A.G. Ramirez, *Grain size estimations from the direct measurement of nucleation and growth*, Appl. Phys. Lett. **87** (2005) 124102-1- 124102-3.

[108] I.-J. Kim, H. Nanjo, T. Iijima, T. Abe, *Crystallization process of TiNi thin films sputtered at elevated temperatures on Pt/Si oxide/Si and Si oxide/Si substrates*, Jpn. J. Appl. Phys. **39** (2000) 568-571.

[109] Y.S. Liu, D. Xu, B.H. Jiang, Z.Y. Yuan, P. van Houtte, *The effect of crystallizing procedure on microstructure and characteristics of sputter-deposited TiNi shape memory thin films*, J. Micromech. Microeng. **15** (2005) 575-579.

[110] B. Winzek, S. Schmitz, H. Rumpf, T. Sterzl, R. Hassdorf, S. Thienhaus, J. Feydt, M. Moske, E. Quandt, *Recent developments in shape memory thin film technology*, Mater. Sci. Eng. A **378** (2004) 40-46.

[111] M. Bendahan, P. Canet, J.L. Seguin, H. Carchano, *Control composition study of sputtered Ni-Ti shape memory alloy film*, Mater. Sci. Eng. B **34** (1995) 112-115.

[112] M. Silva, P.R. Gordo, M. Maneira, F.M.B. Fernandes, *Optical emission spectroscopy study of magnetron assisted Ni-Ti dc sputtering*, Mat. Sci. Forum **514-516** (2006) 1274-1278.

[113] P. Surbled, C. Clerc, B.L. Pioufle, M. Ataka, H. Fujita, *Effect of the composition and thermal annealing on the transformation temperatures of sputtered TiNi shape memory alloy thin films*, Thin Solid Films **401** (2001) 52-59.

[114] S. Sanjabi, S.K. Sadrnezhaad, K.A. Yates, Z.H. Barber, *Growth and characterization of Ti_xNi_{1-x} shape memory thin films using simultaneous sputter deposition from separate elemental targets*, Thin Solid Films **491** (2005) 190-196.

[115] P. Chen, J.-M. Ting, *Characteristics of TiNi alloy thin films*, Thin Solid Films **398/399** (2001) 597-601.

[116] M.J. Vestel, D.S. Grummon, R. Gronsky, A.P. Pisano, *Effect of temperature devitrification kinetics of NiTi films*, Acta Mater. **51** (2003) 5309-5318.

[117] M.J. Vestel, D.S. Grummon, *Precipitates and lamellar microstructures in NiTi films*, Mater. Sci. Eng. A **378** (2004) 437-442.

[118] J.X. Zhang, M. Sato, A. Ishida, *On the Ti_2Ni precipitates and Guinier-Preston zones in Ti-rich Ti-Ni thin films*, Acta Mater. **51** (2003) 3121-3130.

[119] H. Ni, H.-J. Lee, A.G. Ramirez, *Compositional effects on the crystallization kinetics of nickel titanium thin films*, J. Mater. Res. 20 (2005) 1728-1734.

[120] L.J. van der Pauw, *A method of measuring the resistivity and Hall coefficient on lamellae of arbitrary shape*, Philips Technical Review **20** (1958) 220-224.

[121] L.J. van der Pauw, *A method of measuring specific resistivity and Hall effect of discs of arbitrary shape*, Philips Research Reports **13** (1958) 1-9.

[122] K.P. Mohanchandra, K.K. Ho, G.P. Carman, *Electrical Characterization of NiTi Film on Silicon Substrate*, J. Intell. Mater. Syst. Struct. **15** (2004) 387-392.

[123] X. Wang, Y. Bellouard, J.J. Vlassak, *Laser annealing of amorphous NiTi shape memory alloy thin films to locally induce shape memory properties*, Acta Mater. **53** (2005) 4955-4961.

[124] H. Rumpf, T. Walther, C. Zamponi, E. Quandt, *High ultimate tensile stress in nano-grained superelastic NiTi thin films*, Mater. Sci. Eng. A **415** (2006) 304-308.

[125] C.L. Chu, S.K. Wu, Y.C. Yen, *Oxidation behavior of equiatomic TiNi alloy in high temperature air environment*, Mater. Sci. Eng. A 216 (1996) 193-200.

[126] C.H. Xu, X.Q. Ma, S.Q. Shi, C.H. Woo, *Oxidation Behavior of TiNi Shape Memory Alloy at 450-750ºC*, Mater. Sci. Eng. A 371 (2004) 45-50.

[127] L. Zhang, C. Xie, J. Wu, *Oxidation behavior of sputter-deposited Ti-Ni thin films at elevated temperatures*, Mater. Charact. 58 (2007) 471-478.

[128] Y.Q. Fu, S. Zhang, M.J. Wu, W.M. Huang, H.J. Du, J.K. Luo, A.J. Flewitt, W.I. Milne, *On the lower thickness boundary of sputtered TiNi films for shape memory application*, Thin Solid Films **515** (2006) 80-86.

[129] S. Stemmer, G. Duscher, C. Scheu, A.H. Heuer, M. Rühle, *The reaction between a TiNi shape memory thin film and silicon*, J. Mater. Res. **12**, (1997) 1734-1740.

[130] S.K. Wu, J.Z. Chen, Y.J. Wu, J.Y. Wang, M.N. Yu, F.R. Chen, J.J. Kai, *Interfacial microstructures of rf-sputtered TiNi shape memory alloy thin films on (100) silicon*, Philos. Mag. A **81** (2001) 1939-1949.

[131] E. Horache, J. Van Der Spiegel, J.E. Fischer, *Ti/Ni bilayers on silicon – sputter-induced intermixing, rapid thermal annealing and ternary silicide formation*, Thin Solid Films **177** (1989) 263-270.

[132] Y. Fu, H. Du, S. Zhang, *Adhesion and interfacial structure of magnetron sputtered TiNi films on Si/SiO_2 substrate*, Thin Solid Films **444** (2003) 85-90.

[133] I. Jarrige, P. Jonnard, N. Frantz-Rodriguez, K. Danaie, A. Bosseboeuf, *Study of the NiTi/SiO_2 interface: analysis of the electronic distributions*, Surf. Interface Anal. **34** (2002) 694-697.

[134] I. Jarrige, P. Holliger, P. Jonnard, *Diffusion processes in NiTi/Si, NiTi/SiO_2 and NiTi/Si_3N_4 systems under annealing*, Thin Solid Films **458** (2004) 314-321.

[135] Y. Fu, H. Du, S. Zhang, S.E. Ong, *Effects of silicon nitride interlayer on phase transformation and adhesion of TiNi films*, Thin Solid Films **476** (2005) 352-357.

[136] A. Ishida, M. Sato, *Thickness effect on shape memory behavior of Ti-50.0at.%Ni thin film*, Acta Mater. **51** (2003) 5571-5578.

[137] Q. Su, S.Z. Hua, M. Wuttig, *Martensitic transformation in $Ni_{50}Ti_{50}$ films*, J. Alloys Compd. **211/212** (1994) 460-463.

[138] Y.C. Shu, K. Bhattacharya, *The influence of texture on the shape-memory effect in polycrystals*, Acta Mater. **46** (1998) 5457-5473.

[139] S.W. Robertson, X.Y. Gong, R.O. Ritchie, *Effect of product form and heat treatment on the crystallographic texture of austenitic Nitinol*, J. Mater. Sci. **41** (2006) 621-630.

[140] S. Miyazaki, K. Otsuka, C.M. Wayman, *The shape memory mechanism associated with martensitic-transformation in Ti-Ni alloys: self-accommodation*, Acta Metall. **37** (1989) 1873-1884.

[141] Y. Liu, *Detwinning process and its anisotropy in shape memory alloys*, Smart Materials - Proceedings of SPIE **4234** (2001) 82-93.

[142] D. Favier, Y. Liu, P.G. McCormick, *Three stage transformation behaviour in aged NiTi*, Scpt. Metall. Mat. **28** (1993) 669-672.

[143] J.K. Allafi, X. Ren, G. Eggeler, *The mechanism of multistage martensitic transformations in aged Ni-rich NiTi shape memory alloys*, Acta Mater. **50** (2002) 793-803.

[144] H. Inoue, N. Miwa, N. Inakazu, *Texture and shape memory strain in TiNi alloy sheets*, Acta Mater. **44** (1996), 4825-4834.

[145] L. Zhao, *Texture development and anisotropic behaviour in a Ti-45Ni-5Cu (at%) shape memory alloy*, Ph.D. thesis, University of Twente, Enschede, The Netherlands (1997).

[146] A.S. Paula, J.H.P.G. Canejo, K.K. Mahesh, R.J.C. Silva, F.M.B. Fernandes, R.M.S. Martins, A.M.A. Cardoso, N. Schell, *Study of the textural evolution in Ti-rich NiTi using synchrotron radiation*, Nucl. Instr. & Meth. B **246** (2006) 206-210.

[147] A.S. Paula, K.K. Mahesh, F.M.B. Fernandes, R.M.S. Martins, A.M.A. Cardoso, N. Schell, *In-situ high temperature texture characterisation in NiTi Shape Memory Alloy using synchrotron radiation*, Mat. Sci. Forum **495-497** (2005) 125-130.

[148] Y. Furuya, M. Matsumoto, H.S. Kimura, T. Masumoto, *Thermoelastic phase transformation of melt-spun $Ti_{50}Ni_{50-x}Cu$ (x = 0 - 20 at%) ribbons*, Mater. Sci. Eng. A **147** (1991) L7-L11.

[149] A.D. Johnson, V.V. Martynov, R.S. Minners, *Sputter deposition of high transition temperature Ti-Ni-Hf alloy thin films*, J. Phys. IV **5** (C8) (1995) 783-787.

[150] S. Sanjabi, Y.Z. Cao, Z.H. Barber, *Multi-target sputter deposition of $Ni_{50}Ti_{50-x}Hf_x$ shape memory thin films for high temperature microactuator application*, Sens. Actuators A **121** (2005) 543-548.

[151] C. Zhang, R.H. Zee, P.E. Thoma, *Surface evolution of NiTi and NiTiHf thin films*, Mat. Res. Soc. Symp. Proc. **648** (2001) P6.38.1-P6.38.6.

[152] W. Matz, N. Schell, G. Bernhard, F. Prokert, T. Reich, J. Claußner, W. Oehme, R. Schlenk, S. Dienel, H. Funke, F. Eichhorn, M. Betzl, D. Pröhl, U. Strauch, G. Hüttig, H. Krug, W. Neumann, V. Brendler, P. Reichel, M.A. Denecke, H. Nitsche, *ROBL – a CRG Beamline for Radiochemistry and Materials Research at the ESRF*, J. Synchroton Radiat. **6** (1999) 1076-1085.

[153] N. Schell, W. Matz, F. Eichhorn, F. Berberich, *Synchrotron radiation studies of thin films and implanted layers with the materials research endstation of ROBL*, J. Alloys Compd. **328** (2001) 105-111.

[154] G. Swislow, *SPEC X-ray diffraction software* (Certified scientific software), POB 390640, Cambridge, MA 01239, USA.

[155] HUBER X-ray Diffraction Equipment, 83253 Rimsting, Germany, http://www.xhuber.com

[156] N. Schell, J. von Borany, J. Hauser, *A two magnetron sputter deposition chamber equipped with an additional ion gun for in situ observation of thin film growth and surface modification by Synchrotron Radiation Scattering*, AIP conference proceedings **879** (2007) 1813-1816.

[157] http://www.bede.co.uk

[158] F. Golgberg, É.J. Knystautas, *NiTi thin film characterization by Rutherford backscattering spectrometry*, Mater. Sci. Eng. B **40** (1996) 185-189.

[159] L.R. Doolittle, *Algorithms for the rapid simulation of Rutherford Backscattering Spectra*, Nucl. Instr. and Meth. B **9** (1985) 344-351.

[160] L. Pereira, H. Águas, R. Miguel Martins, F. Braz Fernandes, E. Fortunato, R. Martins, *Role of process and annealing conditions on the electro-optical performances of undoped and n-doped polysilicon grown by LPCVD*, in Physics and Application of Disordered Materials, ed. by Popescu Mihai, 2002, 373-380.

[161] http://pro.wanadoo.fr/carine.crystallography/index.html

[162] T. Harada, H. Ohkoshi, *Influence of MgO(100) substrate surfaces on epitaxial growth of Ti films*, J. Cryst. Growth **173** (1997) 109-116.

[163] H.W. Jang, H.C. Kang, D.Y. Noh, M.S. Yi, *Crossover of the preferred growth orientation of AlN/Si(001) films during off-axis radio frequency sputter growth*, J. Appl. Phys. **94** (2003) 2957-2961.

[164] A. Ishida, K. Ogawa, M. Sato, S. Miyazaki, *Microstructure of Ti-48.2 at. pct Ni shape memory thin films*, Metall. Mater. Trans. A **28** (1997) 1985-1991.

[165] W. Cai, X.L. Meng, L.C. Zhao, *Recent development of TiNi-based shape memory alloys*, Curr. Opin. Solid State Mater. Sci. **9** (2005) 296-302.

[166] U. Falke, F. Fenske, S. Schulze, M. Hietschold, *XTEM studies of nickel silicide growth on Si(100) using a Ni/Ti bilayer system*, Phys. Stat. Sol. (a) **162** (1997) 615-621.

[167] D.S. Grummon, J. Zhang, *Stress in sputtered films of near-equiatomic TiNiX on (100) Si: Intrinsic and Extrinsic stresses and their modification by thermally activated mechanisms*, Phys. Stat. Sol. (a) **186** (2001) 17-39.

[168] A. Steegen, K. Maex, *Silicide-induced stress in Si: origin and consequences for MOS technologies*, Mater. Sci. Eng. R **38** (2002) 1-53.

[169] C.J. Tsai, K.H. Yu, *Stress evolution during isochronal annealing of Ni/Si system*, Thin Solid Films **350** (1999) 91-95.

[170] A.D. Johnson, M. Fanucchi, V. Gupta, V. Martynov, V.Galhotra, K. Clements, *"TiNi as a nano-actuator: experimental verification of excitation by electron-beam heating"*, 2003; http://www.innovation-on-demand.com/tini.htm

[171] F.E. Wang, S.J. Pickart, H.A. Alperin, *Mechanism of the TiNi martensitic transformation and the crystal structures of TiNi-II and TiNi-III phases*, J. Appl. Phys. **43** (1972) 97-112.

[172] F.E. Wang, B.F. DeSavage, W.J. Buehler, W.R. Hosler, *The irreversible critical range in the TiNi transition*, J. App. Phys. 39 (1968) 2166-2175.

[173] W.B. Cross, A.H. Kariotis, F.J. Stimler, *Nitinol characterization study*, NASA Report, **CR-1433** (1969).

[174] A.L. Roytburd, T.S. Kim, Q. Su, J. Slutsker, M. Wuttig, *Martensitic transformation in constrained films*, Acta Mater. **46** (1998) 5095-5107.

[175] Kremer Vakuumphysik, Chorbuschstr. 13, 50259 Pulheim, Germany, http://www.kremer-vakuumphysik.de

Appendix

APPENDIX A. PROPERTIES OF NiTiNOL

Transformation Properties

Transformation temperature.....–200 to 110 ºC

Latent heat of transformation.....5.78 cal/g

Transformation strain (for polycrystalline material)

for a single cycle .....8 %

for 100 cycles.....6 %

for 100 000 cycles.....4 %

Hysteresis.....30 to 50 ºC

Physical Properties

Melting point.....1300 ºC (2370 ºF)

Density.....6.45 g/cm^3 (0.233 lb/in^3)

Thermal conductivity

austenite.....0.18 W/cm * ºC (10.4 BTU/ft * hr * ºF)

martensite.....0.086 W/cm * ºC (5.0 BTU/ft * hr * ºF)

Coefficient of thermal expansion

austenite.....11.0×10^{-6}/ ºC (6.11×10^{-6}/ ºF)

martensite.....6.6×10^{-6}/ ºC (3.67×10^{-6}/ ºF)

Specific heat.....0.20 cal/g * ºC (0.20 BTU/lb * ºF)

Corrosion performance.....excellent

Electrical and Magnetic Properties

Resistivity

austenite.....approx. 100×10^{-6} ohms * cm (39×10^{-6} ohms * in)

martensite.....approx. 80×10^{-6} ohms * cm (32×10^{-6} ohms * in)

Magnetic permeability.....< 1.002

Magnetic susceptibility.....3.0×10^6 emu/g

Mechanical Properties

Young's modulus

austenite.....approx. 83 GPa (12×10^6 psi)

martensite.....approx. 28 a 41 GPa (4×10^6 to 6×10^6 psi)

Yield strength

austenite.....195 to 690 MPa (28 to 100 ksi)

martensite.....70 to 140 MPa (10 to 20 ksi)

Ultimate tensile strength (UTS)

fully annealed .....895 MPa (130 ksi)

work hardened.....1900 MPa (275 ksi)

Poisson's ratio.....0.33

Elongation at failure

fully annealed.....25 to 50 %

work hardened.....5 to 10 %

Hot workability.....quite good

Cold workability.....difficult due to rapid work hardening

Machinability.....difficult, abrasive techniques preferred

http://www.jmmedical.com/html/selected_properties.html

APPENDIX B. JCPDS cards (and simulations) used for the identification of the crystalline phases

Austenite (B2) (JCPDS card: 18-0899).

d (nm)	**Intensity (%)**	**(h k l)**	**2θ (º) *λ=0.0675 nm***	**2θ (º) *λ=0.154 nm***
0.211	100	1 1 0	18.400	42.800
0.150	40	2 0 0	26.077	61.978
0.122	60	2 1 1	32.065	78.147
0.106	10	2 2 0	37.168	93.327
0.095	30	3 1 0	41.711	108.68
0.087	20	2 2 2	45.931	125.86
0.080	70	3 2 1	49.826	148.04

Simulation: software PowderCell using Bragg-Brentano geometry, with variable slit and without anomalous dispersion. Radiation CuKα_{1+2}. Cubic structure CsCl type and spacial group Pm$\bar{3}$m.

d (nm)	**Intensity (%)**	**(h k l)**	**2θ (º) *λ=0.0675 nm***	**2θ (º) *λ=0.154 nm***
0.300	2.4	1 0 0	12.921	29.787
0.212	100.0	1 1 0	18.312	42.629
0.173	1.2	1 1 1	22.476	52.869
0.150	21.2	2 0 0	26.011	61.868
0.134	2.0	2 1 0	29.144	70.16
0.122	49.3	2 1 1	31.997	78.038
0.106	18.5	2 2 0	37.115	93.266

R-phase

Simulation: software PowderCell using Bragg-Brentano geometry, with variable slit and without anomalous dispersion. Radiation CuKα_{1+2}. Trigonal structure type and spacial group P3.

d (nm)	**Intensidade (%)**	**(h k l)**	**2θ (º) *λ=0.0675 nm***	**2θ (º) *λ=0.154 nm***
0.302	6.41	1 1 1	12.846	29.574
0.244	1.49	1 0 $\bar{2}$	15.907	36.804
0.215	95.82	1 1 2	18.109	42.083
0.212	100.00	3 0 0	18.302	42.55
0.203	2.53	2 0 2	19.118	44.527
0.184	1.01	2 2 0	21.164	49.54
0.174	1.30	0 0 3	22.424	52.67
0.151	28.63	2 2 2	25.858	61.389
0.129	1.11	1 0 -4	30.265	73.11
0.124	11.13	1 1 4	31.520	76.584
0.123	13.46	0 3 3	31.865	77.552
0.123	14.37	1 4 1	31.979	77.874

Martensite (B19') (JCPDS card: 35-1281).

d (nm)	**Intensity (%)**	**(h k l)**	**2θ (º) *λ=0.0675 nm***	**2θ (º) *λ=0.154 nm***
0.460	6	0 1 0	8.433	19.322
0.307	1	0 1 1	12.640	29.101
0.287	<1	1 0 0	13.530	31.193
0.257	13	1 $\bar{1}$ 0	15.092	34.882
0.235	11	1 0 1	16.500	38.234
0.231	2	1 1 0	16.795	38.940
0.230	54	0 2 0	16.913	39.222
0.218	100	1 $\bar{1}$ 1	17.804	41.364
0.206	54	0 0 2	18.859	43.915
0.202	94	1 1 1	19.275	44.926
0.201	26	0 2 1	19.381	45.186
0.190	1	1 $\bar{2}$ 0	20.420	47.727
0.188	<1	0 1 2	20.695	48.402
0.173	8	1 $\bar{2}$ 1	22.526	52.944
0.170	<1	1 2 0	22.957	54.024
0.167	<1	1 0 2	23.277	54.828
0.161	5	1 $\bar{1}$ 2	24.247	57.283
0.157	<1	1 2 1	24.860	58.846
0.154	1	1 1 2	25.352	60.110
0.153	26	0 2 2	25.436	60.327
0.153	1	0 3 0	25.487	60.457

Ti_2Ni (JCPDS card: 72-0442).

d (nm)	**Intensity (%)**	**(h k l)**	**2θ (º) *λ=0.0675 nm***	**2θ (º) *λ=0.154 nm***
0.654	16.9	1 1 1	5.921	13.538
0.400	0.1	2 2 0	9.675	22.194
0.341	0.1	3 1 1	11.350	26.088
0.327	5.0	2 2 2	11.857	27.270
0.283	0.7	4 0 0	13.699	31.590
0.260	7.0	3 3 1	14.935	34.510
0.231	29.3	4 2 2	16.798	38.948
0.218	100.0	5 1 1	17.826	41.415
0.200	25.6	4 4 0	19.421	45.281
0.191	4.3	5 3 1	20.320	47.480
0.189	8.7	4 4 2	20.611	48.196
0.179	0.1	6 2 0	21.739	50.984
0.173	0.8	5 3 3	22.550	53.005
0.171	1.5	6 2 2	22.814	53.666
0.163	1.7	4 4 4	23.843	56.259
0.159	1.9	7 1 1	24.588	58.153
0.151	1.3	6 4 2	25.785	61.226
0.147	4.4	7 3 1	26.479	63.027
0.142	0.6	8 0 0	27.600	65.968
0.138	1.3	7 3 3	28.252	67.699
0.137	0.1	6 4 4	28.467	68.271
0.133	17.5	8 2 2	29.310	70.539
0.131	5.0	5 5 5	29.929	72.219
0.130	0.9	6 6 2	30.132	72.776
0.127	0.3	8 4 0	30.934	74.985
0.124	2.4	7 5 3	31.524	76.628
0.124	3.5	8 4 2	31.718	77.172
0.121	0.1	6 6 4	32.485	79.340
0.119	0.6	9 3 1	33.049	80.956
0.116	0.1	8 4 4	33.972	83.634
0.114	8.2	9 3 3	34.515	85.234
0.111	1.9	10 2 0	35.404	87.892
0.109	2.1	9 5 1	35.928	89.484

Ni_4Ti_3 (JCPDS card: 39-1113).

d (nm)	**Intensity (%)**	**(h k l)**	**2θ (º) *λ=0.0675 nm***	**2θ (º) *λ=0.154 nm***
0.239	30	1 3 1	16.129	37.636
0.225	15	2 0 2	17.164	40.133
0.210	100	1 2 2	18.429	43.210
0.185	20	3 1 2	20.923	49.353
0.168	15	2 3 2	23.074	54.757
0.149	20	4 2 2	26.004	62.304
0.122	20	5 3 2	31.875	78.304

Ni_3Ti (JCPDS card: 75-0878).

d (nm)	Intensity (%)	(h k l)	2θ (º) *λ=0.0675 nm*	2θ (º) *λ=0.154 nm*
0.441	0.1	1 0 0	8.772	20.103
0.390	0.6	1 0 1	9.936	22.800
0.302	0.8	1 0 2	12.816	29.514
0.255	0.4	1 1 0	15.223	35.193
0.235	0.1	1 0 3	16.550	38.354
0.221	8.9	2 0 0	17.596	40.862
0.213	47.2	2 0 1	18.211	42.347
0.208	38.0	0 0 4	18.712	43.560
0.195	100.0	2 0 2	19.949	46.571
0.188	0.1	1 0 4	20.700	48.415
0.173	20.3	2 0 3	22.560	53.029
0.167	0.1	2 1 0	23.347	55.004
0.164	0.1	2 1 1	23.820	56.199
0.161	0.2	1 1 4	24.210	57.189
0.155	0.1	1 0 5	25.081	59.413
0.155	0.2	2 1 2	25.189	59.690
0.151	3.7	2 0 4	25.795	61.252
0.147	0.1	3 0 0	26.526	63.150
0.143	0.1	2 1 3	27.328	65.252
0.133	5.9	2 0 5	29.469	70.969
0.130	0.1	2 1 4	30.087	72.652
0.127	12.8	2 2 0	30.724	74.402
0.122	0.1	3 1 0	32.011	77.998
0.121	0.1	3 1 1	32.366	79.003
0.120	0.1	3 0 4	32.662	79.845
0.117	9.6	2 0 6	33.459	82.139
0.115	0.1	1 0 7	34.267	84.500
0.112	0.1	3 1 3	35.094	86.958
0.110	0.4	4 0 0	35.624	88.557
0.110	0.2	3 0 5	35.695	88.771
0.109	2.3	4 0 1	35.948	89.544

TiO_2 (JCPDS card: 87-0920).

d (nm)	Intensity (%)	(h k l)	2θ (º) *λ=0.0675 nm*	2θ (º) *λ=0.154 nm*
0.325	100	1 1 0	11.927	27.434
0.249	43.6	1 0 1	15.595	36.076
0.230	6.5	2 0 0	16.898	39.187
0.219	17.1	1 1 1	17.751	41.235
0.205	6.0	2 1 0	18.910	44.039
0.169	48.0	2 1 1	23.073	54.315
0.162	14.2	2 2 0	23.986	56.621
0.148	6.4	0 0 2	26.373	62.752
0.145	6.5	3 1 0	26.867	64.041
0.142	0.5	2 2 1	27.424	65.503
0.136	15.7	3 0 1	28.738	68.997
0.135	7.7	1 1 2	29.034	69.795
0.130	0.9	3 1 1	29.999	72.411

d (nm)	Intensity (%)	(h k l)	2θ (º) *λ=0.0675 nm*	2θ (º) *λ=0.154 nm*
0.127	0.2	3 2 0	30.720	74.392
0.124	1.6	2 0 2	31.489	76.530
0.120	0.9	2 1 2	32.654	79.822
0.117	3.1	3 2 1	33.524	82.327
0.115	2.1	4 0 0	34.179	84.240
0.111	0.8	4 1 0	35.264	87.470
0.109	4.9	2 2 2	35.947	89.540

MgO (JCPDS card: 78-430).

d (nm)	Intensity (%)	(h k l)	2θ (º) *λ=0.0675 nm*	2θ (º) *λ=0.154 nm*
0.243	12	1 1 1	15.954	36.932
0.210	100	2 0 0	18.442	42.906
0.149	45	2 2 0	26.196	26.196
0.127	5	3 1 1	30.821	30.821
0.122	11	2 2 2	32.228	32.228

TiN (JCPDS card: 74-1214).

d (nm)	Intensity (%)	(h k l)	2θ (º) *λ=0.0675 nm*	2θ (º) *λ=0.154 nm*
0.254	70	1 1 1	15.269	35.332
0.220	100	2 0 0	17.649	41.026
0.155	46	2 2 0	25.060	59.414
0.132	18	3 1 1	29.476	71.056
0.127	12	2 2 2	30.819	74.738
0.110	5	4 0 0	35.735	88.988

APPENDIX C. Sample preparation procedure for X-TEM observations

The sample ready for microscopy must be a disc of 3 mm in diameter, thinned and having a small hole in the centre.

The sample preparation starts whit the cutting of two pieces of 5×4 mm from the sample using a ultrasonic cutter (Fig. C.1). For this operation, the machine of Fig. C.2 is used.

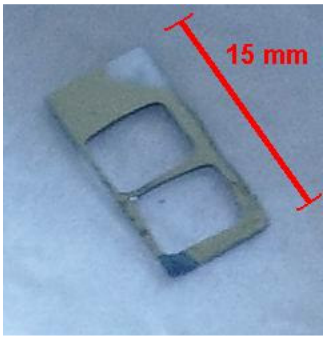

Fig. C.1: Ni-Ti/Si(100) sample after removing the 2 pieces of 5×4 mm for TEM preparation

(Cutting tool)

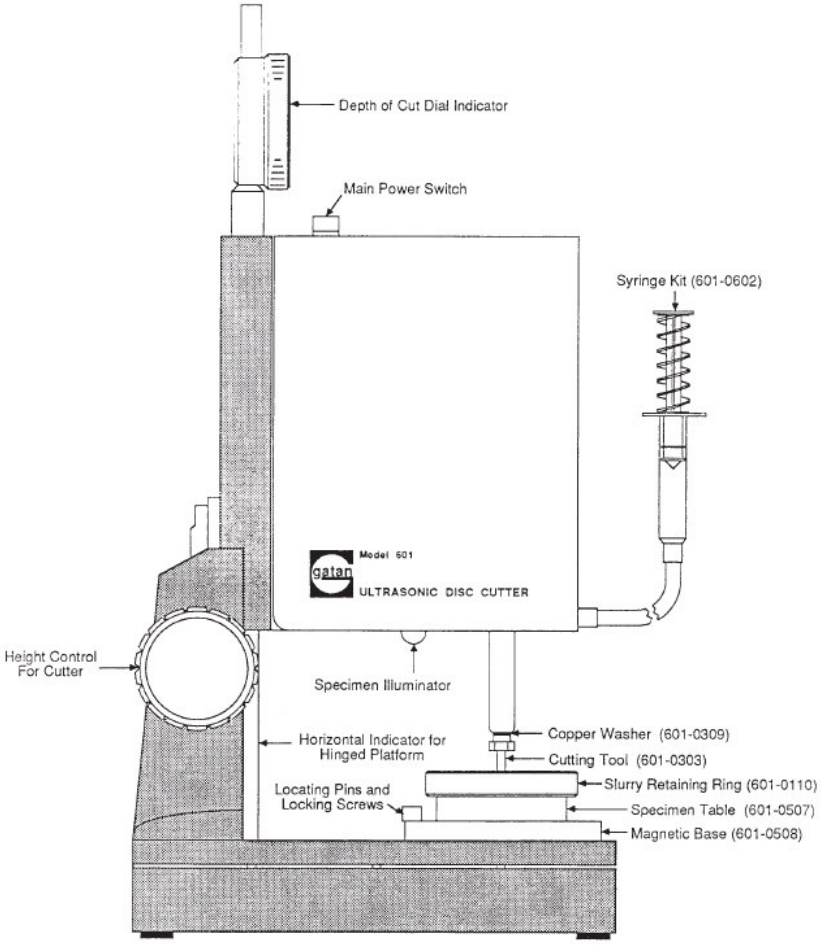

Fig. C.2: *Gatan 601* ultrasonic disc cutter.

The two pieces of the Ni-Ti sample and some Si dummy pieces from a wafer are then carefully cleaned in an ultrasonic bath: acetone → ethanol (better 96%) → acetone.

After, the pieces are glued together (Epoxidbasis, *Type G2* from *gatan*, 2 components, 1/10), like in Fig. C.3. The two pieces of the material to be investigated must be glued face-to-face, what means upper part contra upper part. Pieces of material of the same type (a dummy Si wafer in this case) are also glued in order to reach a final extension higher than 3 mm (total dimension).

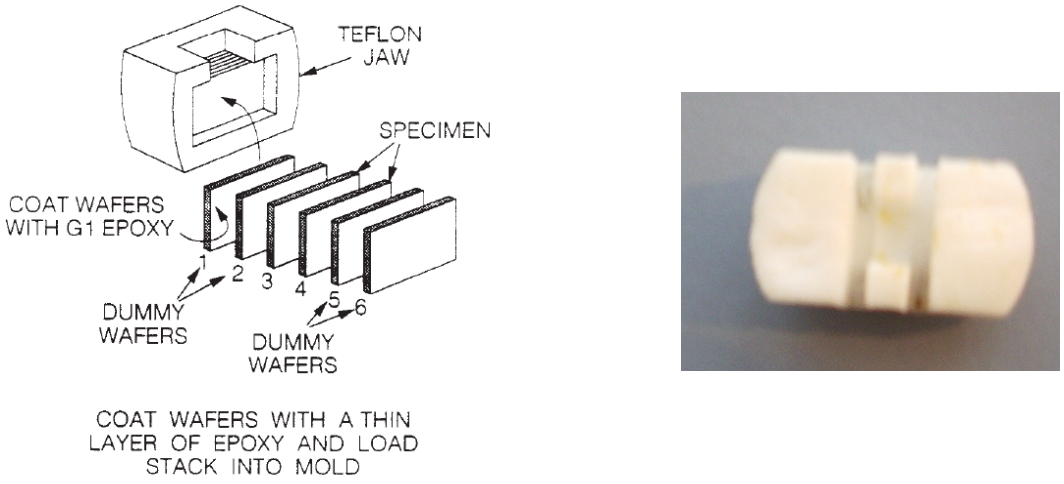

Fig. C.3: Teflon jaw and the schematic procedure for gluing.

The pieces are then pressed (Fig. C.4) and put on a heating plate (160°C) covered with a glass - all in a hotte due to the toxicity of the glue (Fig. C.5).

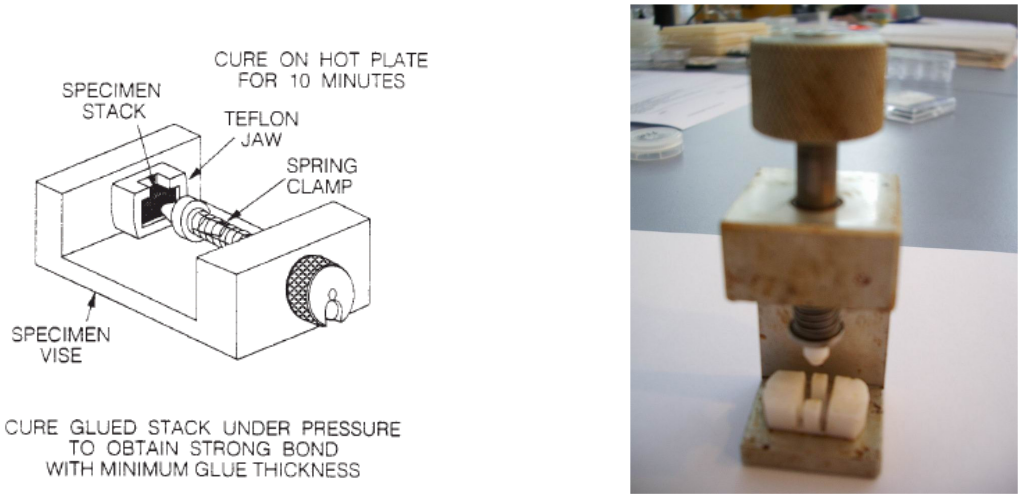

Fig. C.4: Mould and support used for the gluing procedure.

The glue used nowadays is very strong and, thus, it is not necessary to use anymore a Cu ring (like in Fig. C.6) for samples on Si wafers. In some other cases, it is necessary to border the sample in the ring (especially if the material is ductile and, therefore, no ultrasonic cutting is possible). In the present work, for the Ni-Ti films deposited on MgO single crystal substrates,

it was required the use of the Cu ring leading to an extra complexity for the whole sample preparation procedure.

Fig. C.5: The pieces pressed, on top of a heating plate (160°C) covered with a glass, in a hotte due to the toxicity of the glue.

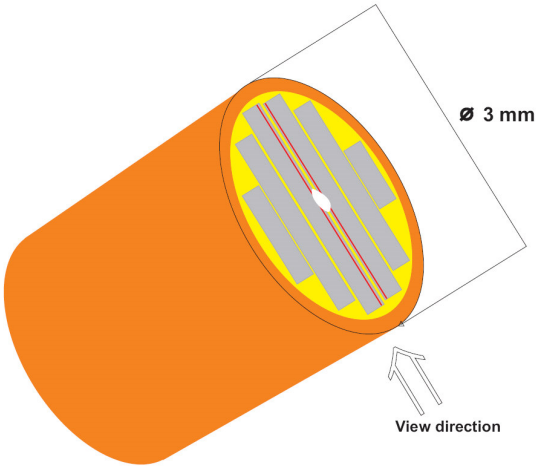

Fig. C.6: Cu ring used to involve the 2 samples pieces and the dummy pieces, in same especial cases. Ductile substrate or MgO, for example.

After the gluing process the resulting assemblage resembles a cube. The next step aims to obtain a plate with about 500 µm. For this operation, 2 cutting machines are available (Fig. C.7 and Fig. C.8). However, the one from Fig. C.7 offered better stability. The tungsten wire with a SiC suspension is kept on the accurate position due to the latter supports, which do not exist in the other machine shown in Fig. C.8.

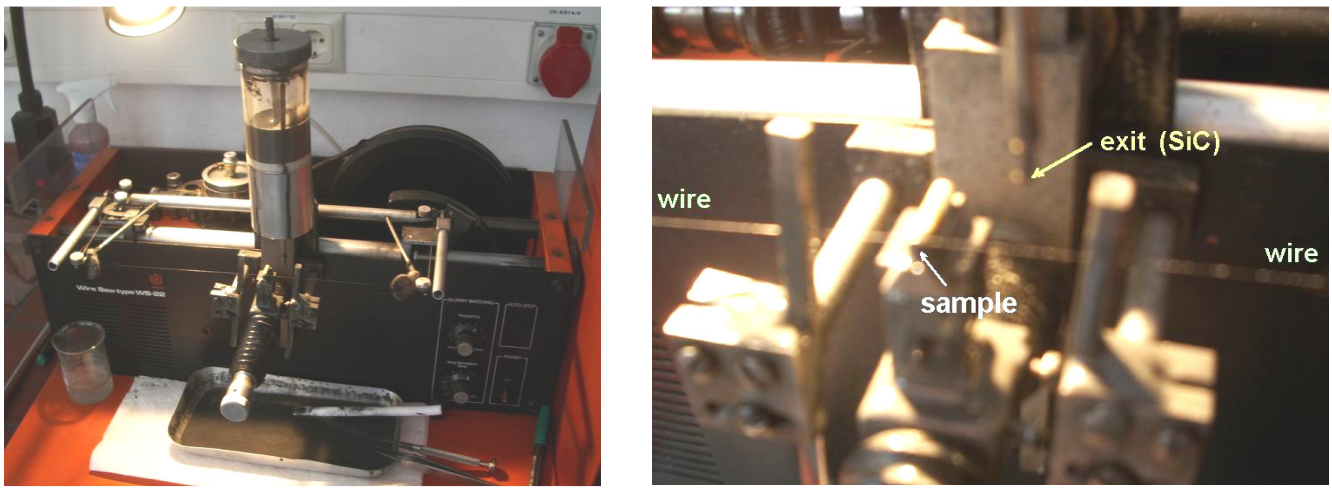

Fig. C.7: Cutting machine (using a wire).

The wire from the machine of Fig. C.7, as mentioned before, is made from tungsten with a diameter of 50 µm and a SiC suspension must be dropping during the cutting. A diamond wire of 30 µm is used on the other machine.

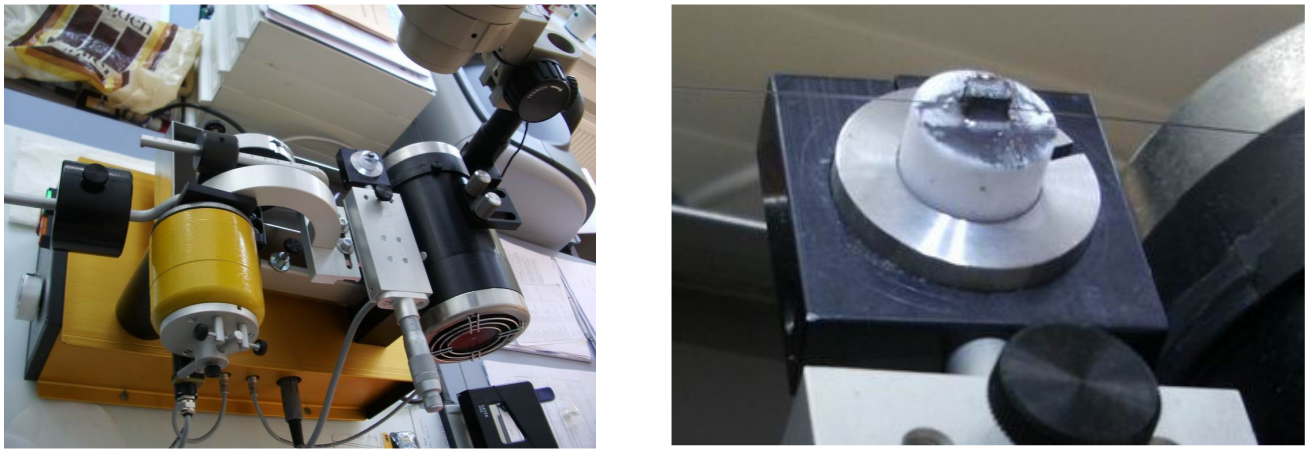

Fig. C.8: Cutting machine (using a wire).

It is important to point out that *the cutting is performed perpendicularly to the interfaces glued* (see Fig. C.3). The cutting operation takes approximately 1 h for a plate of 500 µm. Usually 4 plates are cut. The first one is not used because the surface exhibits imperfections. From the other 3, only one is prepared until the final step. In case the final sample does not allow a perfect observation in the microscope, two pieces are then still remaining.

Note: for the cutting with the machine from Fig. C.7, the cube is glued to a prism like the one in Fig. C.9. For the other machine, in Fig. C.8 it is visible the support to which the sample is glued. This glue is removable with acetone.

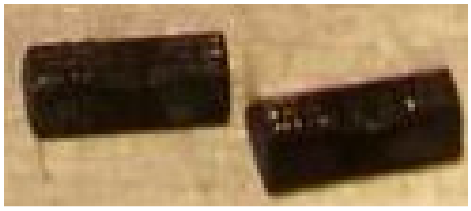

Fig. C.9: Prisms.

The plates with 500 µm are now glued on a glass plate with removable glue and subjected to ultrasonic cutting but now 3 mm round (Fig. C.10).

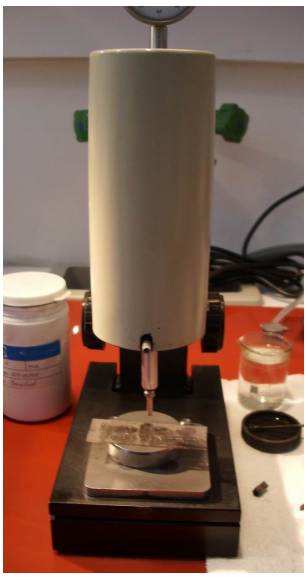

(Cutting tool)

Fig. C.10*: Gatan 601* ultrasonic disc cutter.

After the cutting (3 discs) they are heated up to 130°C in order to remove them from the glass (Fig. C.11). They are then cleaned in acetone ultrasonic bath.

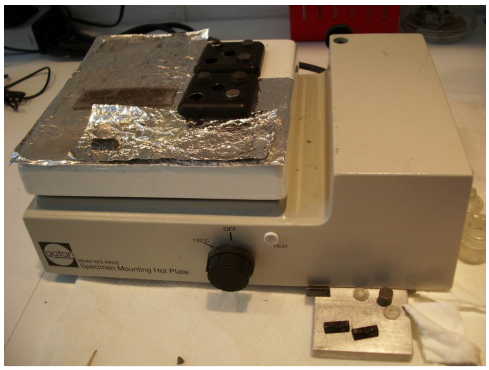

Fig. C.11: Heating plate.

The procedure continues with the polishing of one of the 3 mm discs, using the machine of Fig. C.12. For that the disc is glued (removable glue) to a metallic cylinder. Then the cylinder is introduced into the hole of the support of Fig. C.13(a). This support allows an adjustment of the position of the cylinder in z [Fig. C.13 (b)].

Fig. C.12: Polishing machine.

(a)

(b)

Fig. C.13: Bottom (a) and top (b) view of the sample support for the polishing machine of Fig. C.12.

The disc is polished from 500 µm up to 300 µm using a sand paper of 15 µm. The disc is then glued on the other side and it is polished again with the 15 µm sand paper but this time until it reaches a thickness of 180 µm. With a 10 µm sand paper the disc is thinned up to 130 µm. The final step to reach a thickness of 120 µm is performed with a 3 µm sand paper.

The disc of 3 mm diameter and a thickness of 120 µm is glued on a glass support in order to be subjected to a delicate polishing in the machine of Fig. C.14.

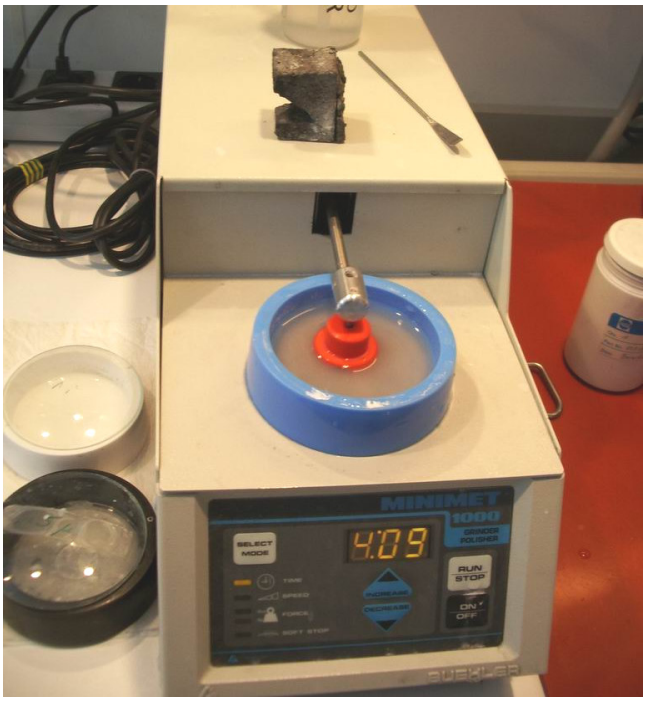

Fig. C.14: Polishing machine *(Minimet 1000)* - allows random movements for final polishing.

This machine performs random movements, which avoids preferential scratches on the sample (disc). Al_2O_3 of 5, 1 and 0.3 µm diameter are used (6 min/speed 10).

The following step is dimple-grinding in order to polish a calotte in the centre. For that the disc is glued on a polymeric cylinder. The better-polished face is glued directly on the cylinder. A Dimple Grinder *gatan 656* is used for this operation (Fig. C.15).

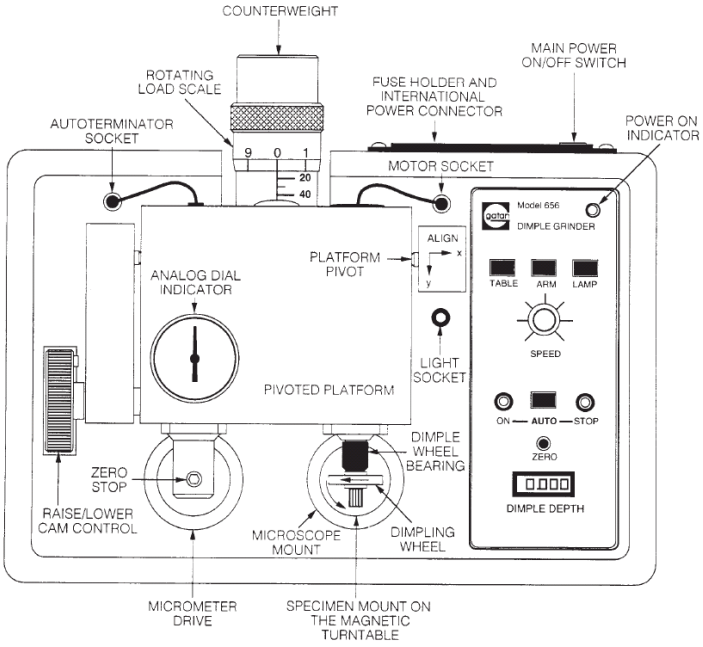

Fig. C.15: Dimple Grinder *(Gatan 656).*

A bronze wheel (∅ = 15 mm) with diamond paste polishes a calotte in the centre of the disc (Fig. C.16 and Fig. C.17). The support is also moving during this operation [Fig. C.18(a)].

Fig. C.16: View of the sample support *(yellow: diamond paste on top).*

Fig. C.17: Bronze wheel, with a diameter of 15 mm, rotating on the sample.

From the initial thickness of 120 µm to 30 µm a diamond paste of 6 µm is used. For the final depth of the crater (20 µm) the polishing is done with a 3 µm diamond paste. After it is cleaned with distillate water and alcohol.

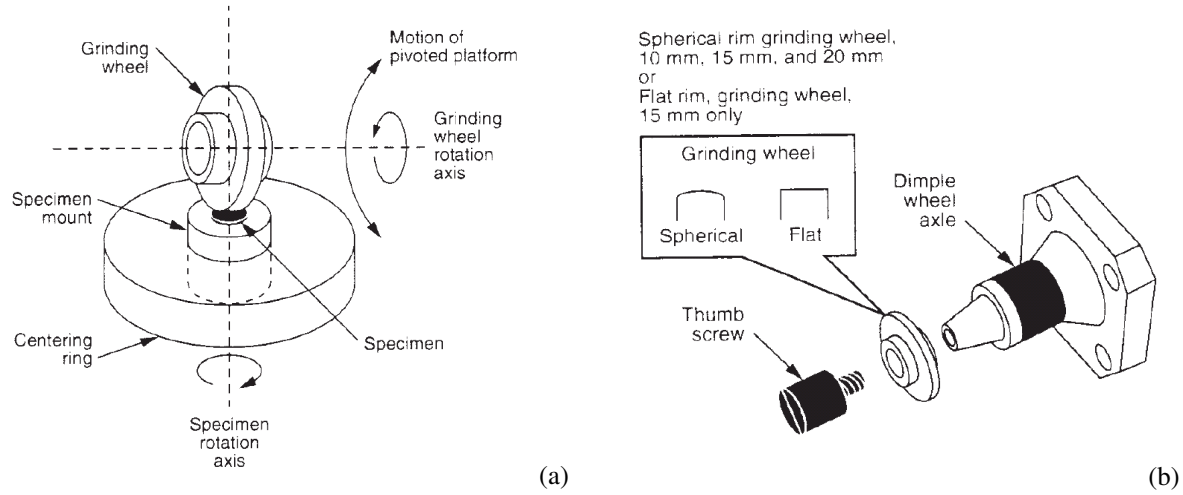

Fig. C.18: Perspective of the bronze wheel and the sample support (Dimple Grinder).

A final polishing step, with 0.05 µm Al_2O_3 and a felt-polishing ring of 15 mm (Fig. C.19), is performed, which does not change the 20 µm crater depth. The disc is then removed from the polymeric cylinder by heating up to 130°C and cleaned with *acetone→ alcohol→ acetone*. No ultrasonic bath is employed.

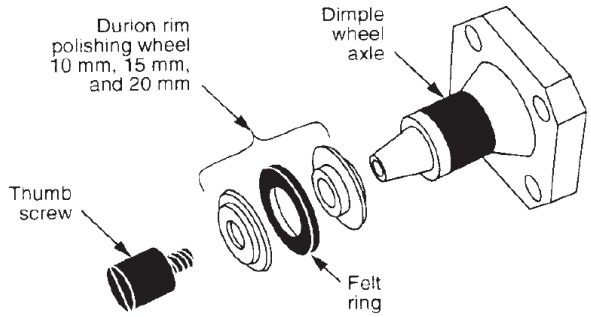

Fig. C.19: Perspective of the felt ring.

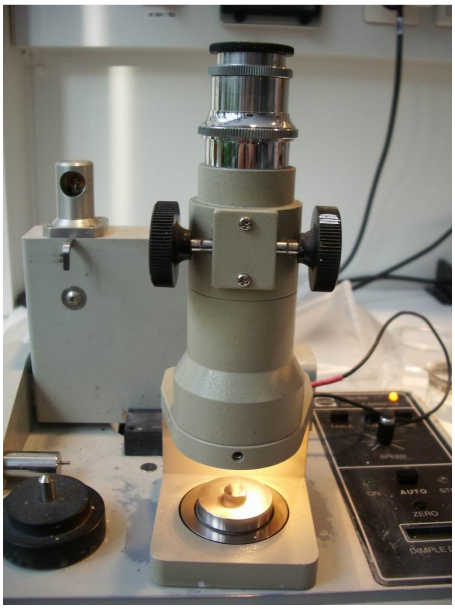

Fig. C.20: Microscope mounted in the machine.

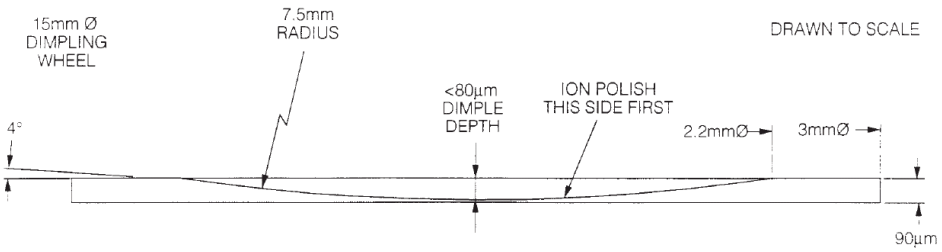

Note: To check the evolution of the crater, a microscope is mounted several times during the procedure; simultaneous check the thickness by a transmission light, from red to orange to yellow (Fig. C.20). This is the reason why the cylinder is made from polymer (a lamp is under the support).

Ion milling: (Ar, 4.5 keV) from the 20 µm up the state that a small hole arises in the centre.

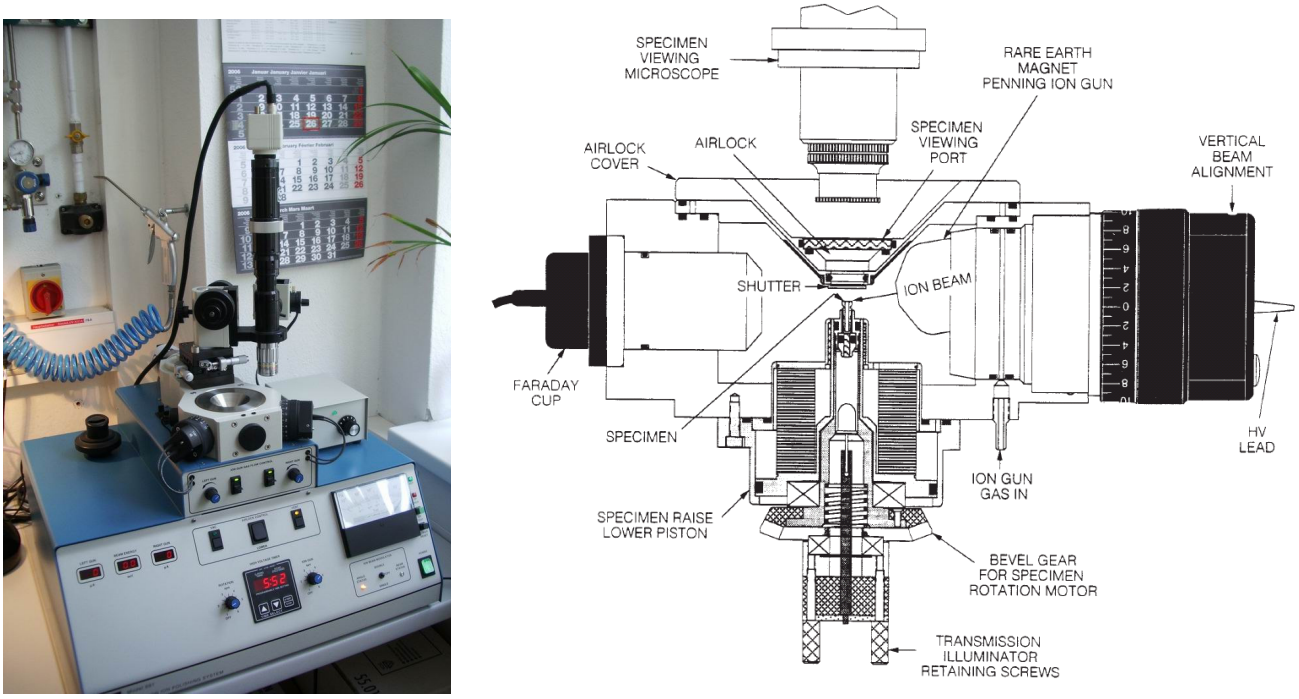

Fig. C.21: Picture and perspective view of the ion milling equipment.

Due to the sample holder design (Fig. C.22) and since the sample is rotating, the gun only sends the ions when the clamps are not on the way.

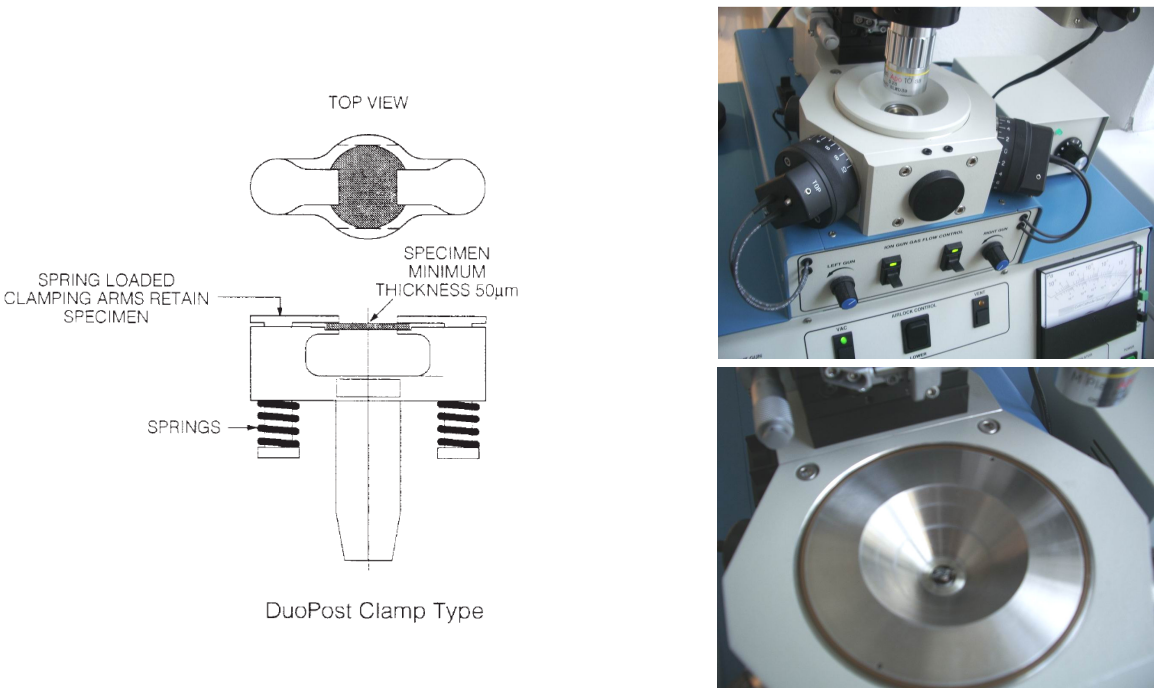

Fig. C.22: Sample holder (PIPS 691) and its location in the ion milling equipment.

TEM sample holder

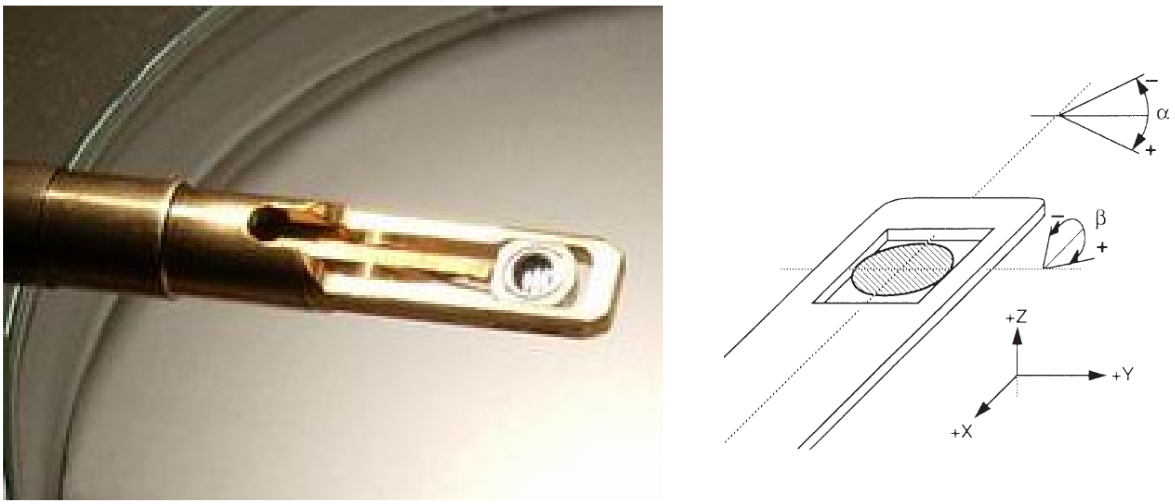

Fig. C.23: *Double tilt*-sample holder.